FORSCHUNGSZENTRUM ROSSENDORF FZR

WISSENSCHAFTLICH-TECHNISCHE BERICHTE
FZR-273
September 1999
ISSN 1437-322X

Institute of Safety Research

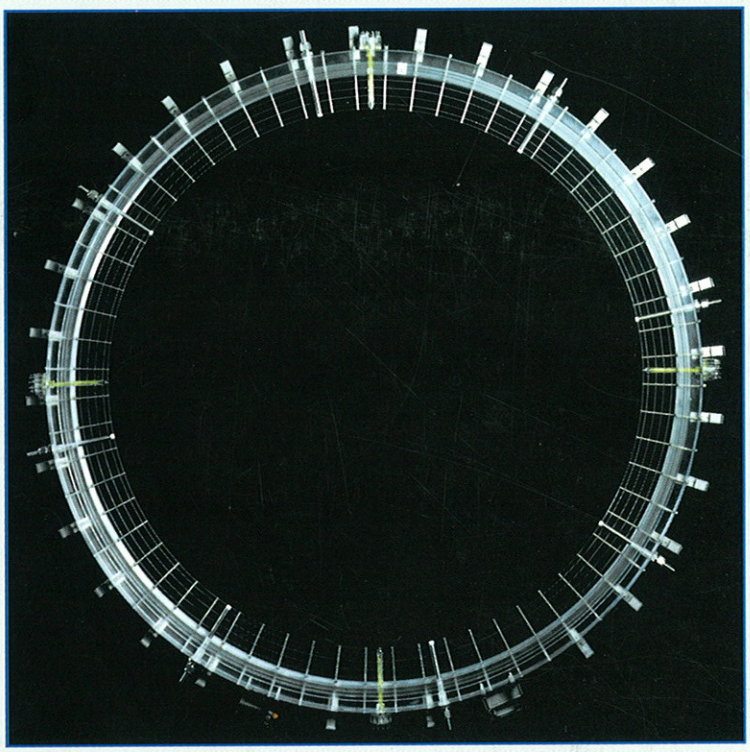

Report
January 1998 - June 1999

Cover photograph:
Grid sensor for concentration distribution measurements in the downcomer of a PWR model (ROCOM test facility)

Forschungszentrum Rossendorf e. V.

Postfach 51 01 19
D-01314 Dresden
Bundesrepublik Deutschland

Telefon +49 (3 51) 2 60 34 80
Telefax +49 (3 51) 2 60 34 40
E-mail weissfp@fz-rossendorf.de
Internet http://www.fz-rossendorf.de/FWS/

FORSCHUNGSZENTRUM ROSSENDORF
WISSENSCHAFTLICH-TECHNISCHE BERICHTE
FZR-273
September 1999

Institute of Safety Research

Report

January 1998 - June 1999

Editors:
Prof. Dr. F.-P. Weiß
PD Dr. U. Rindelhardt

CONTENTS

Preface

The Institute of Safety Research is one of the five scientific institutes of Forschungszentrum Rossendorf e.V. The Forschungszentrum Rossendorf is a member of the "Wissenschafts-gemeinschaft Gottfried Wilhelm Leibniz" and is funded by the Federal Ministry of Education and Research and by the Saxon Ministry of Science and Arts with 50 % each.

The research work of the institute aims at the assessment and increase of the safety and environmental sustainability of technical plants. The emphasis is put on the development and validation of mathematical and physical models for process and plant analysis, and of techniques for process and components monitoring. Subject of investigations are equally nuclear plants and installations of process industries.

To analyse the thermo-fluiddynamics of normal plant operation and of the behaviour during accidents, physical models and computer codes are developed for multi-phase and multi-component flows, and for the space and time dependent heat release (neutron kinetics, chemical kinetics).

The theoretical work is based on experimental investigations on chemical process kinetics and on transient two-phase flows. In the years to come, the institute will construct a multi-purpose test facility (TOPFLOW) to study transient flow phenomena. To better characterize the momentum, mass, and energy transfer between the phases and components sophisticated two-phase measuring equipment is developed.

Magneto-hydrodynamics (MHD) is a particular branch of the thermohydraulics research of the institute dealing with the control of electrically conducting fluids by external electromagnetic fields. MHD offers technological and safety relevant applications in semiconductor materials, metallurgy, and e.g. electrochemistry. The work is constitutional part of a common Innovationskolleg (innovative research activity) of the Technical University of Dresden and Forschungszentrum Rossendorf that is funded by Deutsche Forschungsgemeinschaft.

The efforts in materials safety are devoted to the behaviour of materials under neutron and gamma radiation. The susceptibility to irradiation induced embrittlement and the state after thermal annealing is assessed by fracture mechanical tests in dependence on the materials composition. The institute is specialized to the investigation of irradiated, radioactive material. Recently licensed laboratories are available to prepare and test radioactive specimens. The microstructural mechanisms of ductility reduction are revealed by highly resolving methods of structural analyses. Monte Carlo methods for radiation field calculation are developed and validated to get information about the irradiation fluences to which the components have been exposed. Starting from the estimated accident loads (pressure and temperature) and from the mechanical and thermal properties of the relevant components, the integrity of the plants and components is assessed by structural dynamic calculations. These calculations consider the thermal and mechanical interactions between the fluids and the components.

Together with the Institute of Radiochemistry, the institute investigates the chemical and physical phenomena ruling the transport of radionuclides in unsaturated zones of soil. The relevance of this topic is due to the wastes from Uranium mining in Saxony and Thuringia till the end of the eighties.

The work on decision analysis to support strategy finding for the environmental remediation from wastes were concluded. That topic could not satisfyingly be embedded into the research profile of the institute.

Together with the Technical University of Dresden and Hochschule für Technik, Wirtschaft und Sozialwesen (HTWS) Zittau/Görlitz the Institute of Safety Research constitutes one of the four remaining centres of competence for nuclear energy and nuclear safety research in Germany. It is the only one in East Germany and reagionally takes care for the conservation of the nuclear science and engineering competence. There are vital scientific links to the other centres of competence, particularily to the Gesellschaft für Anlagen- und Reaktorsicherheit and the Munich Technical University.

The institute takes part in coordinated research activities of the EU and in the German nuclear safety research programm of BMBF/BMWi. Among others we act as the leader of the western consortium in the safety research related TACIS project on the "Improvement of the Validation of Coupled Thermohydraulics, Neutron-Kinetics Code". Moreover, we are a member of the EU concerted action on the investigation of boron dilution transients in pressurized water reactors. The related research project is funded by BMWi. In this context, the institute constructed a 1:5 scaled model of a German pressurized water reactor for coolant mixing studies (ROCOM). This work is cofinanced by Vereinigung der Großkraftwerksbetreiber (VGB).

The following graphs give an overview about the sources and deployment of funding amongst the different research tasks. Between January 1998 and June 1999, 44 % of the total budget came from external sources, with 37 % from public research grants and with 7 % from research orders mainly by the industry.

Distribution of funding sources 1/1998 to 6/1999

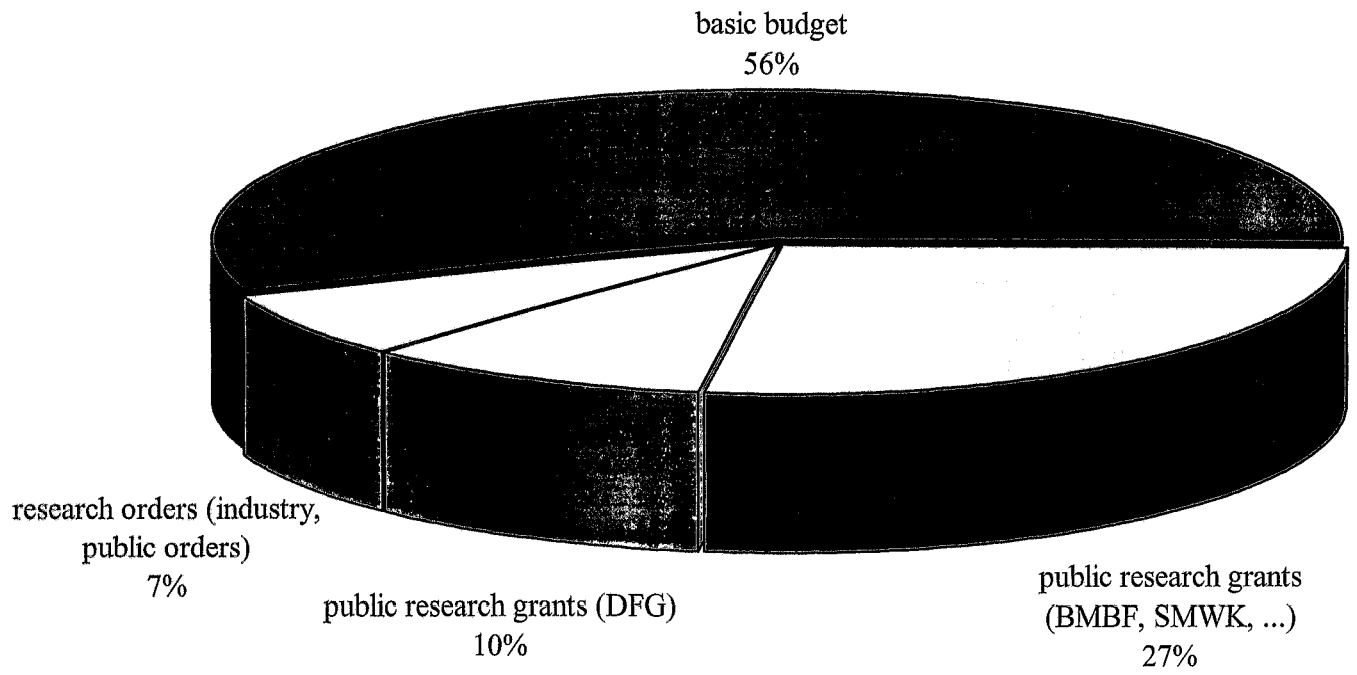

Deployment of funding on the various tasks/projects 1/1998 to 6/1999

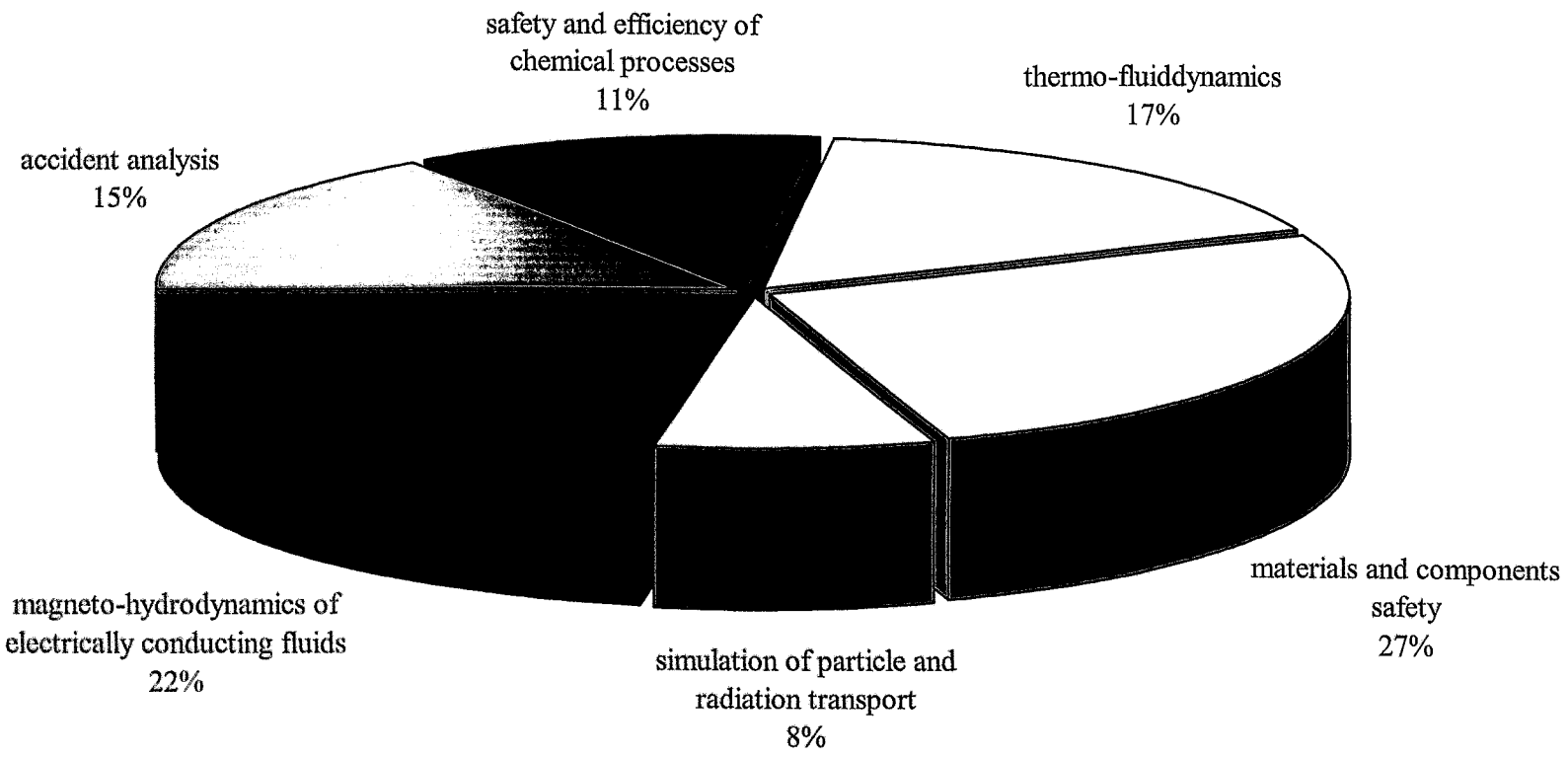

Selected Reports

WIRE-MESH SENSORS FOR TWO-PHASE FLOW INVESTIGATIONS

Horst-Michael Prasser

1. Introduction

In the annual report 1996 a new wire-mesh sensor for gas-liquid flows was presented [1]. It was used to visualise the cavitation bubble behind a fast acting shut-off valve in a pipeline with a time resolution of over 1000 frames per second for the first time. In the last two years the sensor was applied to an air-water flow in a vertical pipeline (inner diameter D=51.2mm) to study the flow structure in a wide range of superficial velocities. Besides the void fraction distributions, the high resolution of the sensor allows to calculate bubble size distributions from the primary measuring data. It was possible to study the evolution of the bubble size distribution along the flow path with growing distance from the gas injection (inlet length, L).

2. Working principle of the wire-mesh sensor

The function is based on the measurement of the local instantaneous conductivity of the two-phase mixture. The sensor consists of two electrode grids with 16 electrodes each, placed at an axial distance of 1.5 mm behind each other. The conductivity is measured at the crossing points of the wires of the two grids. This results in 16x16 sensitive points, which are equally distributed over the cross section (Fig. 1). In the corners of the rectangular measuring grid some of the sensitive points lie outside the boundary of the circular cross section and cannot be used. Therefore, the number of points taking part in the measurement is 242. The wires have a diameter of 120 µm.

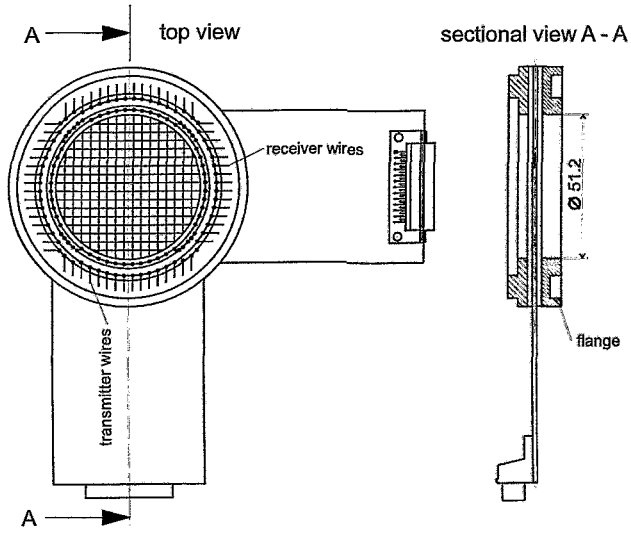

Fig. 1: Wire-mesh sensor (2 x 16 electrode wires)

For the conductivity measurement, one plane of electrode wires is used as transmitter, the other as receiver plane. During the measuring cycle, the transmitter electrodes are activated by a multiplex circuit in a successive order, as illustrated in Fig. 2 for an example of 2 x 4 wires. The time resolution achieved by the signal processing unit is 1200 frames per second. The spatial resolution is given by the pitch of the electrodes and equals 3 mm.

The measurement for one row is started by closing one of the switches S1-S4. The currents arriving at the receiver wires are transformed into voltages by operational amplifiers and sampled by individual sample/hold circuits. After an analogue/digital conversion the signals are recorded by a data acquisition computer and stored for each receiver electrode separately. This procedure is repeated for all transmitter electrodes.

During the activation of a single transmitter electrode all the other electrodes are kept on zero potential. This is done by low impedance input respectively output cascades (see Fig. 2). This special feature prevents a deterioration of the resolution by cross talk between parallel wires. In fact, the current from the activated wire flows towards all the other electrodes, but as the grounded wires cannot depart from zero potential there is no additional current from them to the given receiver wire. The network of grounded wires creates symmetry conditions, which prevent that the conductivity of the fluid far from the given crossing point can influence the locally measured value. In this way, the distribution of the electrical conductivity over the cross section occupied by the sensor is obtained row by row. After the last transmitter electrode has been activated, a two-dimensional matrix of 16 x 16 AD conversion results is available, which are proportional to the conductivity in the control volumes in the vicinity of all crossing points of two perpendicular wires. For more details about the signal acquisition see [2].

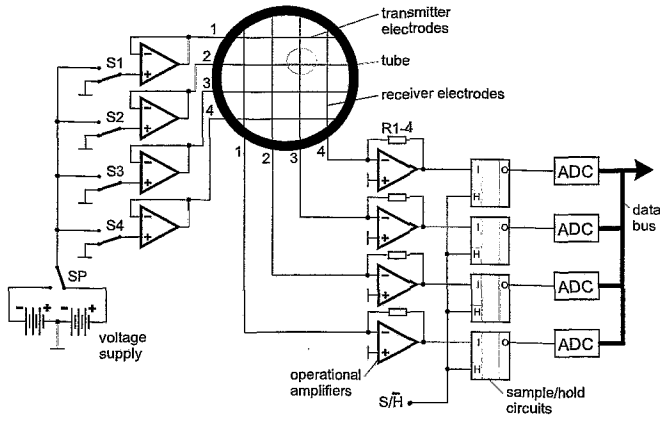

Fig. 2: Simplified scheme of a 2 x 4 wire-mesh sensor with signal acquisition system

3. Calculation of void fractions

During a calibration procedure, measurements for the situations "tube completely filled with liquid" and "tube completely filled with gas" are performed and the resulting matrices of AD conversion results are stored. The matrices acquired during the measurement of the two-phase flow are transformed into distributions of the void fraction by relating the individual measured components to the calibration values assuming a proportionality of local void fraction and electrical conductivity. The accuracy of the void fraction was tested by comparing line averages calculated from the wire-mesh data to the readings of a gamma-densitometer, which was located close to the wire-mesh sensor.

For that, the gamma-device (0.13 mCi Cs-137) was operated with an integration time of 120 s. This allowed to achieve a statistical accuracy of better than 1 %. The comparison to the gas fraction measured by the wire-mesh sensor is shown in Fig. 3. The dependency is linear within an error band of ± 5 % (related to the final value) in the following range of superficial velocities: J_{Air} 0.0024 - 12 m/s, J_{Water} 0.043 - 4 m/s.

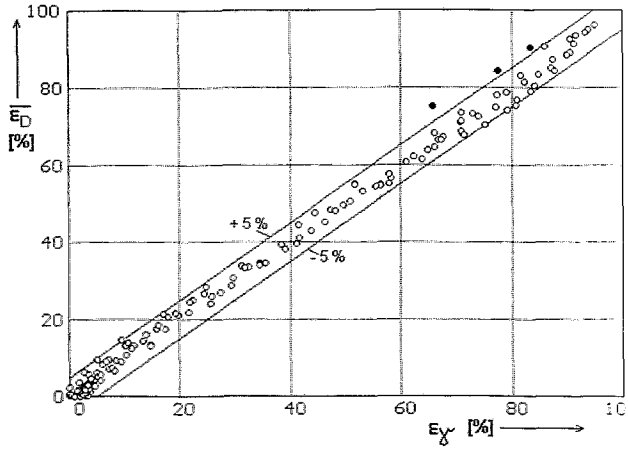

Fig. 3: Comparison between wire-mesh sensor and gamma-densitometer (black filled points: J_{Water}: 1.6 - 4 m/s; J_{Air}: 12 m/s)

4. Flow pattern visualisation

The output of the wire-mesh sensor consists of a time sequence of local instantaneous void fractions that characterise the presence of the gaseous phase in a grid of measuring positions in the cross section. These data sets can be used for a visualisation of the two-phase flow. With the help of a special software the individual gas fraction distributions can be displayed as a sequence of frames. Eulerian sectional views (pseudo side views) of the gas fraction distribution in the vertical center plane of the pipe can be obtained, if successive void fraction distributions over the diameter are plotted in a vertical stack, beginning from the top and moving downwards. When we assume that the gas bubbles travel with a constant velocity independently of their location in the cross section (radial velocity gradients are neglected), the phase velocity calculated from the average void fraction and the superficial gas velocity can be used to transform the time axis into a virtual z-axis.

Fig. 4 shows these sectional side views, obtained at different distances between air injection and wire-mesh sensor for a developed slug flow at J_{Water} = 1 m/s and J_{Air} = 0.48 m/s. The relation between horizontal and vertical dimensions of the bars in Fig. 4 are kept 1:1 with consideration the phase velocity of the gas, i.e. the shape of the gas bubbles, observed in the flow, is not distorted. In the presented experiment, the air was injected through 8 orifices in the wall of 4 mm diameter each. Therefore, the primary bubbles are therefore quite large. It has to be remarked that the side views represent a "frozen" flow pattern, characteristic for the given measuring position. In reality, the flow pattern continuously changes with growing height, e.g. at the sensor position of L = 30 mm above the injection we must expect the flow pattern of the next measuring position (L = 80 mm) at z=50 mm in the direction of the virtual z-axis, the flow pattern of the following position (L = 130 mm) at z=100mm, a.s.o..

The large primary bubbles are clearly visible at the distance of L = 30 mm. With growing height, they are more and more shifted towards the center of the pipe. Further, both coalescence and fragmentation occurs, leading to the appearance of bubbles either smaller or larger than the primary bubbles. In the end, slugs are formed. The characteristic shape of the slugs is very well reproduced by the sensor.

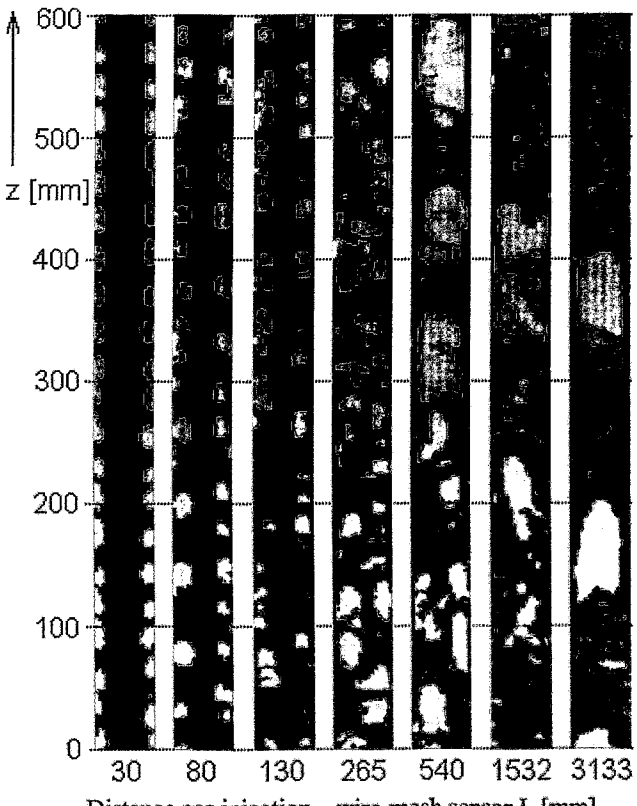

Fig. 4: Evolution of the flow pattern with growing distance from the air injection, J_{Water} = 1 m/s, J_{Air} = 0.48 m/s

5. Bubble size distributions

The high spatial and time resolution of the wire-mesh sensor allows to calculate bubble size distributions from the measured gas fraction distribution sequence. After the transformation of the time axis into the virtual z-axis, described in the previous section, the measured data can be treated as a three-dimensional instantaneous void fraction distribution $\varepsilon_{x,y,z}$ with a resolution given by the pitch of the electrode wires ($\Delta x = \Delta y = 3$ mm) in the x and y directions, and given by the phase velocity of the gas divided by the framing rate of $f_{meas} = 1200$ Hz in the z-direction ($\Delta z = 1.4$ mm in the example shown in Fig. 4). In the consequence, each bubble is mapped in several successive instantaneous void fraction distributions, delivered by the sensor (Fig. 5). The volume of an individual bubble V_{bub} can then be obtained by adding the local void fractions $\varepsilon_{x,y,z}$ of the grid points belonging to the selected bubble, multiplied by the magnitude of the control volume V:

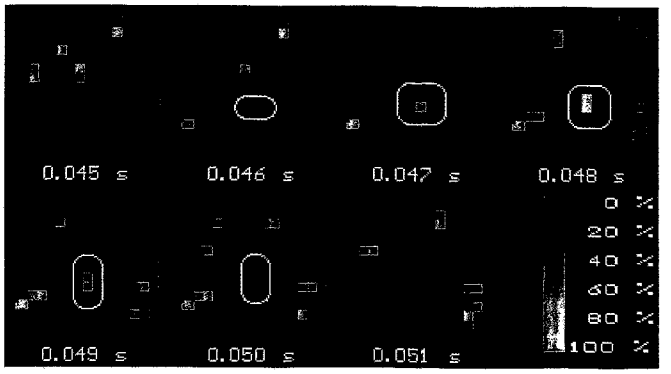

Fig. 5: Image of a selected bubble in a series of successive frames delivered by the sensor

$$V_{bub} = V \cdot \sum_{\varepsilon > \varepsilon_{min}} \varepsilon_{x,y,z} = \Delta x \cdot \Delta y \cdot \frac{J_{Air}}{\bar{\varepsilon}} \cdot \frac{1}{f_{meas}} \cdot \sum_{\varepsilon > \varepsilon_{min}} \varepsilon_{x,y,z} \qquad (1)$$

Here, the phase velocity of the gas is obtained from the superficial air velocity J_{Air} divided by the average void fraction $\bar{\varepsilon}$, which is determined by averaging the wire-mesh data. The summation is carried out by a recursive search procedure that starts at a grid position, where the void fraction is maximal. The summation must be terminated, when the boundary of the bubble is reached. Due to the presence of signal noise a termination threshold ε_{min} greater than zero must be defined. Otherwise, the recursive search could jump from one bubble to another via a channel of grid elements where the gas fraction is not accurately equal to zero. This would lead to an overestimation of the bubble volume. From the individual bubble volumes V_{bub}, equivalent bubble diameters D_{bub} were calculated:

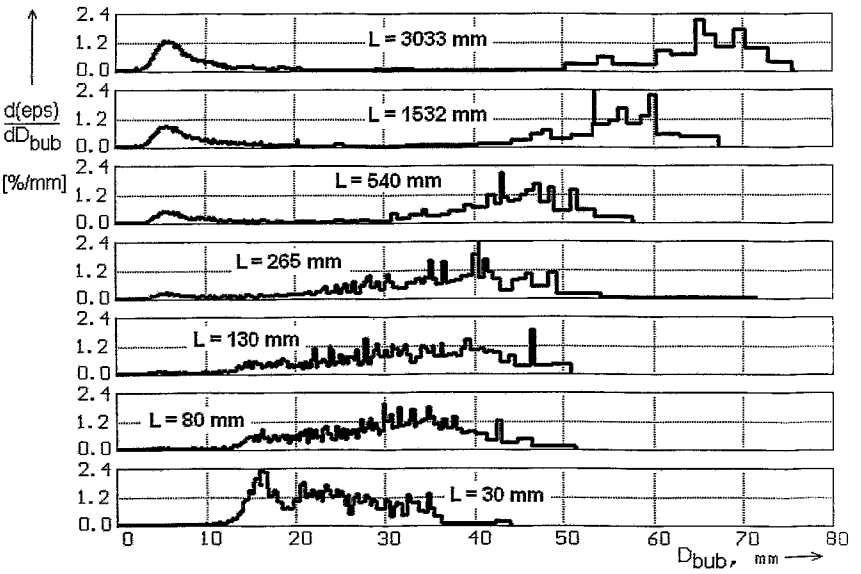

Fig. 6: Evolution of the bubble size distribution with growing distance L from the air injection, $J_{Water} = 1$ m/s, $J_{Air} = 0.13$ m/s

$$D_{bub} = \sqrt[3]{\frac{6}{\pi} \cdot V_{bub}} \tag{2}$$

Bubble size distributions were constructed by summarising the contribution of the bubbles of a given range of diameters to the integral volumetric gas fraction. These partial void fractions are plotted against the equivalent bubble diameter. In Fig. 6 the evolution of the bubble size distribution at the flow conditions of Fig. 4 is shown.

At z = 30 mm the maximum of the bubble size distribution corresponds to the size of the primary bubbles (D_0). With growing height, the coalescence leads to the appearance of a second peak at a diameter of $\sqrt[3]{2} \cdot D_0$. These are bubbles that origin from coalescence between pairs of primary bubbles. At z = 1532 mm, a characteristic bimodal distribution is observed, which indicates the transition to slug flow. The large bubble fraction is still further developing with increasing height. At the same time, bubbles smaller than the primary bubbles appear due to fragmentation.

6. Void fraction profiles

When the instantaneous two-dimensional void fraction distributions are averaged over a long period, void fraction profiles can be obtained. Fig. 7 shows the development of the profiles at the superficial velocities of J_{Water} = 1 m/s, J_{Air} = 0.13 m/s for three different air injection conditions.

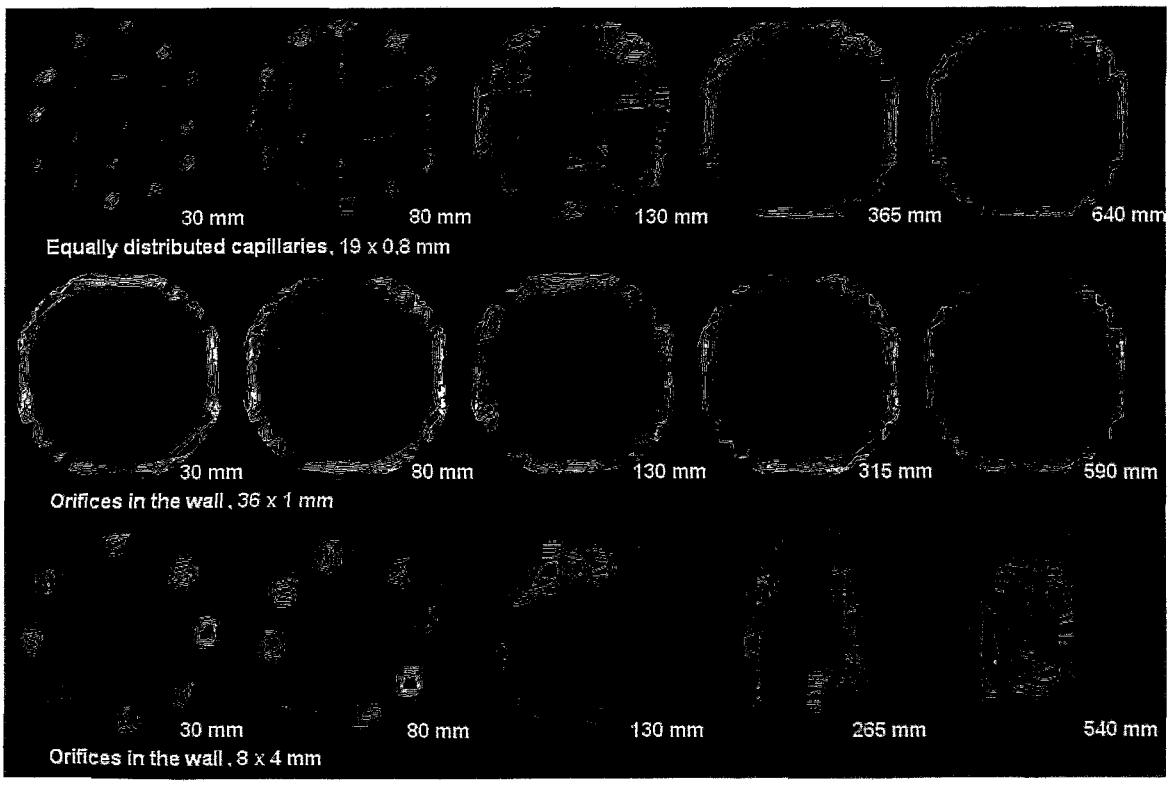

Fig. 7: Void fraction profiles averaged over 10 s for three different air injection conditions at different inlet length L, J_{Water} = 1 m/s, J_{Air} = 0.13 m/s

In case of 19 capillaries equally distributed over the cross section, at z = 30 mm a maximum of the void fraction is found at each individual position of an injecting capillary. With growing distance, the gas is pushed towards the wall by the lift force and a wall-peaked profile is formed. When the gas is injected through 36 orifices of 1 mm diameter, the peak at the wall is already formed by the mode of injection. A completely different behaviour is observed, when the gas is injected through large orifices of 4 mm diameter. Here, again each injecting orifice is visible in the void fraction distribution. But in contradiction to the injection by capillaries, the wall-peaking disappears with growing height, despite of the identical superficial velocities. The bubble size distributions are also significantly different even after a related inlet length of a approximately 60 L/D, as shown in Fig. 8.

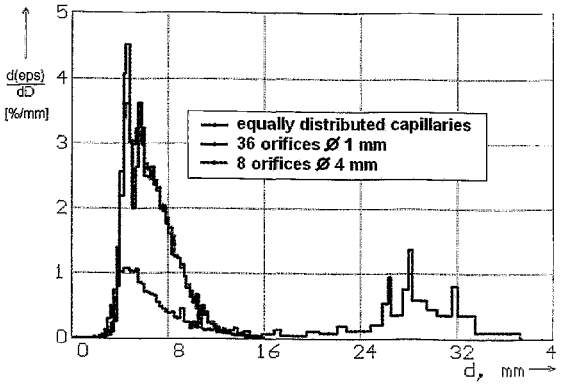

Fig. 8: Bubble size distributions at L ≅ 3100 mm (L/D ≅ 60) for three different air injection devices, J_{Water} = 1 m/s, J_{Air} = 0.13 m/s

7. Conclusion

The wire-mesh sensor provides detailed information about the structure of the two-phase flow. It is successfully used to visualise the air-water flow in a vertical pipeline. The comparison to gamma-densitometry has shown, that void fractions can be measured with good accuracy. From the primary measuring data it is possible to obtain void fraction profiles as well as bubble size distributions. Experiments were carried out to study the evolution of the flow structure with growing distance from the gas injection. A significant influence of the kind of the gas injection was found. The bubble size distributions clearly show the effect of coalescence and fragmentation. They can therefore be used for the development of bubble population models.

References

[1] H.-M. Prasser, A. Böttger, J. Zschau (1997), A New wire-mesh tomograph for gas-liquid flows, in F.-P. Weiß, U. Rindelhardt (Ed.), Annual Report 1996, Institute for Safety Research, FZR-190, 34-37

[2] H.-M. Prasser, A. Böttger, J. Zschau (1998), A new electrode-mesh tomograph for gas-liquid flows, Flow Measurement and Instrumentation 9, 111-119

A NEW CRITERION FOR THE BUBBLE SLUG TRANSITION IN VERTICAL TUBES

Andreas Schaffrath, Anne-Kathrin Krüssenberg, Horst-Michael Prasser

1. Introduction

The use of one dimensional (1D) system codes is very common in the design, optimization and safety analysis of nuclear power or chemical plants. These codes are based on the solution of a complete set of conservation equations for mass, momentum and energy for all phases. In complex structures three dimensional (3D) flow phenomena are often dominating. In this case, the 1D approximation requires constitutive laws, which describe the effect of the 3D processes on the mass, momentum and energy transfer integrated over the nodes of the 1D model. These correlations strongly depend on the geometry. They are found empirically and may have a comparatively narrow region of validity, i.e. they cannot be transferred to other boundary conditions without additional experiments. A particular problem of this kind is for example the scale-up from experimental test facilities up to the scale of the original plants.

The present work is aimed at the investigation of two-phase flow in a vertical pipe. Even under these very simple boundary conditions, strong 3D effects are observed. The distribution of the gas phase over the cross section varies significantly between the different flow patterns, which are known for the vertical two-phase flow. The paper presents experimental void fraction distributions obtained by a wire-mesh sensor in a wide range of superficial velocities of gas and liquid. The high resolution of the measurement allows to perform the analysis of the flow structure on a new qualitative level.

2. MTLOOP Test Facility and Test Procedure

For the study of two phase air-water and steam-water flows the MTLOOP test facility was constructed at Forschungszentrum Rossendorf. The facility has maximum operation parameters of 2.5 MPa and 225 °C (see Fig. 1). For the present investigations, the loop was operated with air at atmospheric pressure and 30 °C. The measurements were carried out at a vertical test section of 4 meters height and 51.3 mm inner diameter. Air was injected through systems of capillaries. The ends of these capillaries were equally distributed over the cross section of the pipe. The wire mesh sensor with 16 x 16 wires was located 3.5 m above the injection device, i.e. the inlet length was 70 L/D.

220 experiments were performed with superficial velocities of air between 0.0024 to 12 m/s and from 0.043 to 4 m/s for water respectively. The air flow rate was measured under normal conditions. The superficial velocity was calculated from a flow rate corrected according to the actual temperature and pressure at the location of the wire-mesh sensor. The pressure correction was necessary, because the pressure increasingly departed from atmospheric at higher flow rates due to the pressure drop in the pipeline. At each test point, the loop was operated under steady-state conditions.

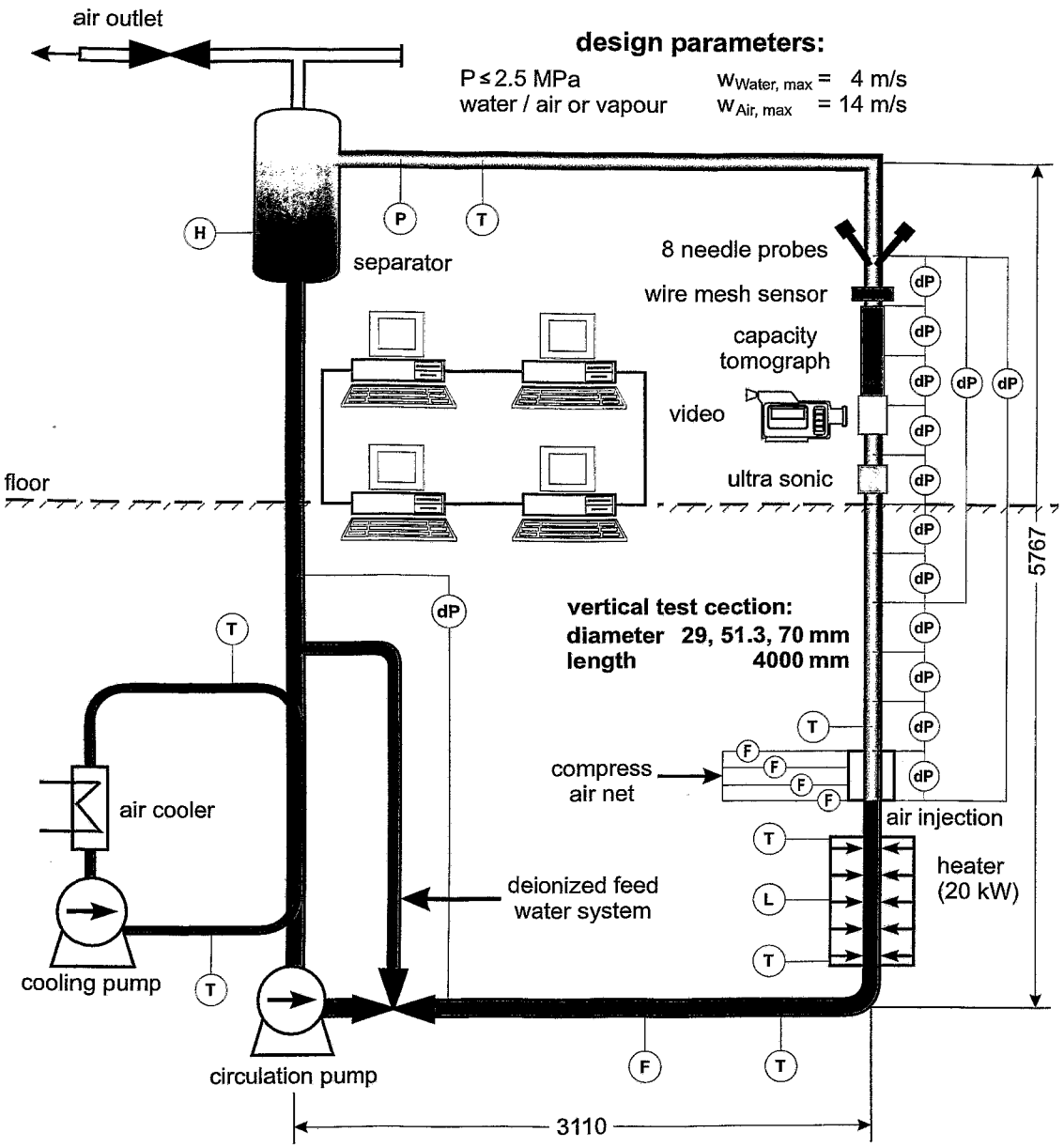

Fig. 1: MTLOOP test facility

The MTLOOP is equipped with several measurement systems (e.g. ultrasonic sensor, video camera, capacity tomography, wire mesh sensor and needle probes). The wire mesh was developed in Rossendorf [1,2]. A time resolution of the signal processing unit of up to 1200 frames per second is achieved. The spatial resolution is given by the pitch of the electrodes and is 3 mm.

3. New Criterion for Bubble-Slug Transition

The measuring data of the wire-mesh sensor can be used to create Eulerian sectional views (pseudo side views) of the flow. For this purpose, successive instantaneous void fraction distributions over the diameter are extracted from the measured two-dimensional distributions and plotted as a vertical stack along the time axis. Assuming a constant phase velocity of the

gas, which is given by the superficial gas velocity divided by the average gas fraction, the time axis can be transformed into an imaginary z-axis (see [3]). The result for the region of the transition from bubble to slug and from slug to annular flow is shown in Fig. 2. On the left side of the figure, the relations between the horizontal and the vertical dimensions of the side views is kept 1:1. That means, that the shape of the gas regions observed in the flow is not distorted. On the right side starting from J_{Air} = 0.75 m/s, the slugs become very long, so that the z-axis was shrunken by factor 5. The side view for J_{Air} = 0.75 is shown in both presentation modes, for orientation.

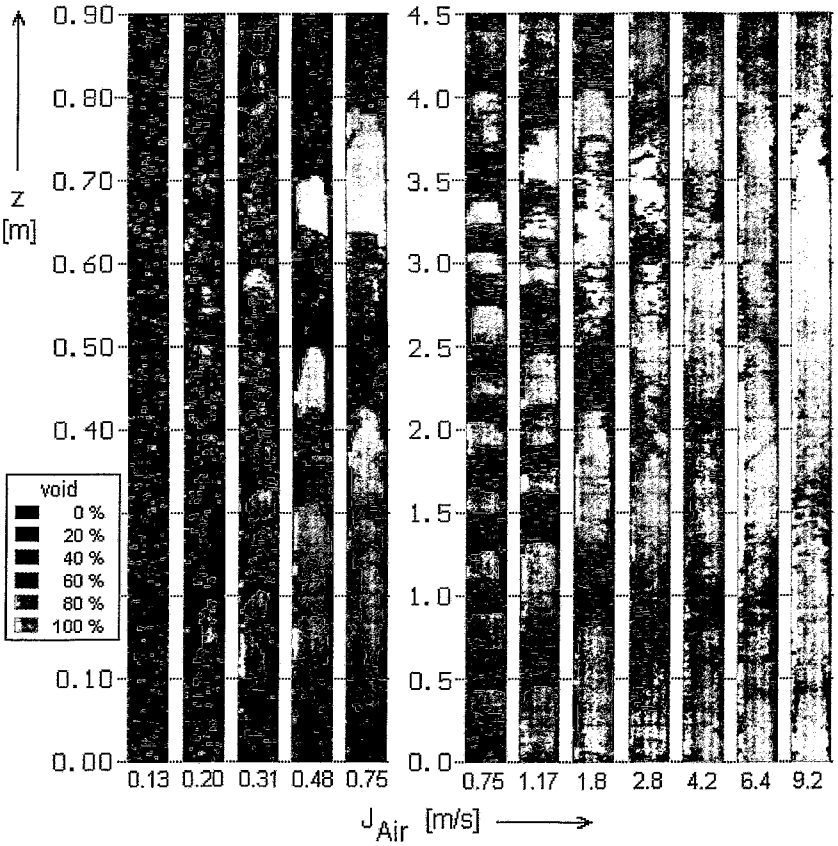

Fig. 2: Sectional side views of the flow pattern at different superficial velocities of air, transition from plug to annular flow, J_{Water} = const. = 1 m/s

At a superficial velocity of the water of 1 m/s, the transition to slug flow takes place at a superficial gas velocity between 0.31 and 0.48 m/s. When the gas flow rate is further increased, the transition to annular flow is observed. At the superficial gas velocity of 9.2 m/s, the flow is wispy annular.

The high spatial and time resolution of the wire-mesh sensor allows to calculate particle size distributions from the measured gas fraction distribution sequence. This was carried out for the flow regimes shown in Fig. 2 according to the method, which is described by Prasser in [3].

Fig. 3 shows the results for a stepwise increase of the gas flow rate (threshold ε_{min}=0.2, see [3]). The superficial velocity of the water was kept constant at 1 m/s, while the gas flow was increased from a superficial velocity of 0.033 to 0.75 m/s. It is clearly to be seen that the bubble size distribution changes from a monomodal (0.033 m/s $\leq J_{Air} \leq$ 0.08 m/s) distribution to a

bimodal one at a superficial gas velocity from 0.08 to 0.13 m/s. The bimodal distribution is characteristic for the transition to heterogeneous bubble flow. At J_{Air}=0.31 m/s the largest bubbles show an equivalent diameter of greater than 50 mm, i.e. they are bigger than the pipe diameter. These large bubbles are identical with the plugs observed in the pseudo side views in Fig. 2.

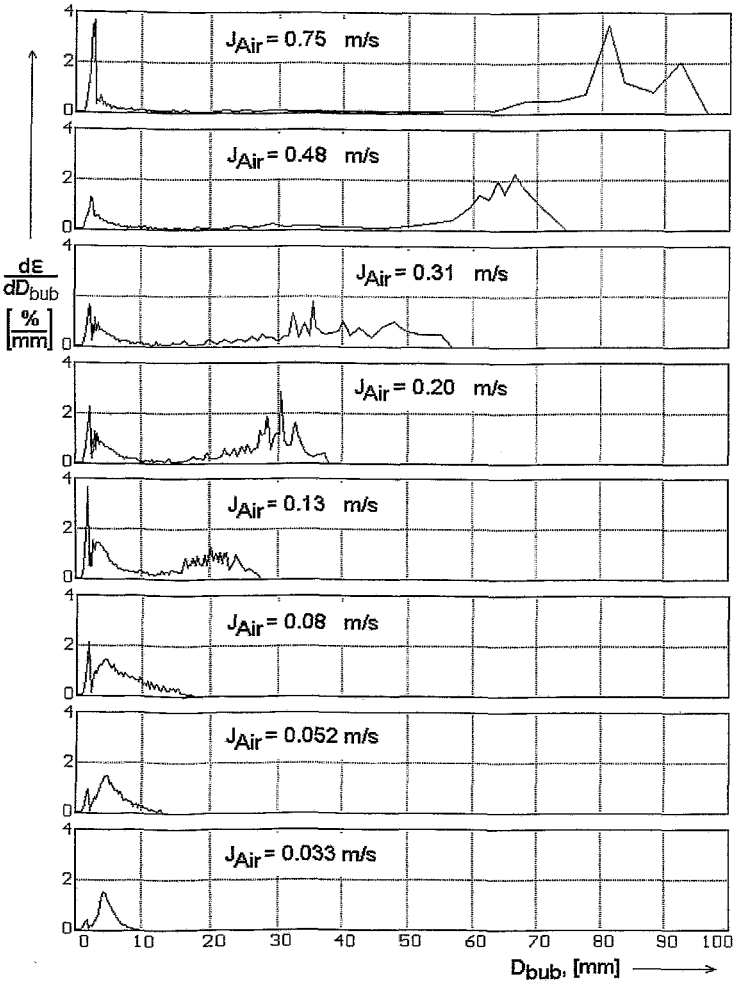

Fig. 3: Bubble size distribution at different superficial air velocities and J_{Water} = 1 m/s const. for a threshold of ε_{min}=0.2

From the analysis of the bubble size distribution, the following two criteria for flow pattern changes were formulated:

- the transition from homogeneous to heterogeneous bubble flow can be identified by the appearance of a bimodal bubble size distribution calculated from the wire-mesh data,
- the transition from bubble to plug flow takes place, when the largest bubbles in the bubble size distribution reach an equivalent diameter that is larger than the inner diameter of the pipe.

It is evident that the choice of the threshold has a strong influence on the shape of the bubble size distribution. With higher thresholds the transition from homogeneous to heterogeneous

bubble flow as well as from bubble to slug flow occurs at higher superficial air velocities. Detailed investigations on this subject will be performed in future.

In the left part of some of the curves in Fig. 3 there is a local minimum in the bubble size distribution at a diameter of 2.25 - 2.75 mm. This is an artefact caused by the finite resolution of the sensor. Indications of bubbles with a diameter less than 3 mm appear, if small bubbles do not fill the entire sensitive volume in the vicinity of the measuring point. This results in a higher error for small bubble volumes.

In Fig. 4 the measurements with the wire mesh sensor described in section 2 are plotted as superficial water velocity versus the superficial air velocity. The mentioned three different flow regimes bubble flow (monomodal distribution of bubbles), slug flow (bimodal distribution of bubbles), and the transition regime between these two flow patterns (characterized in fig. 4 as coalescence) are clearly identified.

4. Comparison with Existing Flow Regime Maps

The classification of the own experiments (see Fig. 4) is now compared with existing flow regime maps from literature (see. Tab. 1).

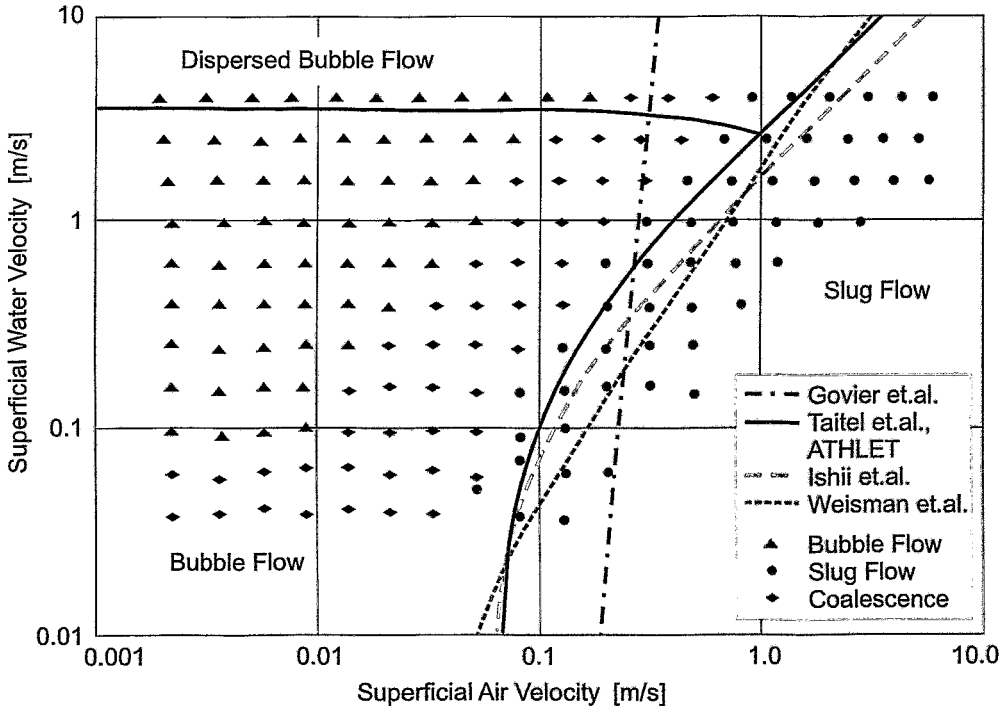

Fig. 4: Classification of own air/water flow experiments and comparison with existing flow pattern maps

The state-of-art in predicting the two-phase flow pattern is characterized by steady state flow-maps presented by different research groups. The flow classification is important, because the flow pattern decisively influences on the transport phenomena (e.g. pressure losses and heat transfer) [4]. Vertical two-phase flow is normally divided into four basic flow regimes and characterized as follows [5]:

- bubbly flow: small, discrete bubbles, which are normally distorted spheres, are surrounded by liquid,
- slug flow: slugs of liquid and bubbles are separated by regions of high vapor content (plug), which appears as large, spherical-capped bubbles and followed by a collection of smaller voids in bubbly form,
- churn flow: highly disordered (chaotic) flow regime in which the vertical motion of the liquid is oscillatory,
- annular flow: gas is flowing in the center of the tube and the liquid partially as a film along the walls and partially as droplets in the central gas bulk.

Table 1: Comparison of criteria for the transition of bubble flow to slug flow respectively bubble flow to intermittent flow transition

Author / Code	Investigated Flow Regimes	Abscissa	Ordinate	Criteria for the transition bubble – slug flow
Govier & Aziz [7]	bubble, plug, slug, churn, annular flow	$V^* = \frac{1-\dot{\varepsilon}}{\dot{\varepsilon}}$	J_L	$J_L \le 0.24 V^{*-1.1}$
Weisman & Kang [8]	bubble, intermittent, annular flow	J_l/ϕ_2	J_G/ϕ_l	$\frac{J_G}{\sqrt{gD}} > 0.45\left(\frac{J_G+J_L}{\sqrt{gD}}\right)^{0.78} \cdot (1-\cos\Theta)$ $\phi_l = \left(\frac{D}{0.0254}\right)^{n_w}(1-0.65\cos\Theta)$ $n_w = 0.26\,\varepsilon^{-0.17(J_L/0.305)}$ and $\phi_2 = 1$
Taitel, Bornea & Dukler [9]	bubble, dispersed bubble, slug, churn, annular flow	J_L	J_G	$J_L = 2.34\,J_G - 1.07 \cdot \frac{[g(\rho_L-\rho_G)\sigma]^{0.25}}{\rho_L^{0.5}}$
Ishii & Mishima [10]	bubble, slug, annular flow	ε J_L	J J_G	$\varepsilon = 0.3$ transition into coordinate system with superficial velocities $J_L = \left(\frac{3.33}{C_0}-1\right)J_G - \frac{0.76}{C_0}\left(\frac{g(\rho_L-\rho_G)\sigma}{\rho_L^2}\right)^{0.25}$
ATHLET (Steinhoff, [11])	bubble, churn turbulent bubble, slug, annular drop flow	ε	J	$\varepsilon < 0.1$ - bubble flow; $0.1 < \varepsilon < 0.3$ - churn turbulent bubble flow; $0.3 < \varepsilon$ - slug flow

It should be noticed that the transition between the different flow regimes does not occur suddenly and many extensions of this classification can be found in literature (e.g. subdivision of the annular flow regime into a wispy or nonwispy regime). For the prediction of flow patterns empirical and theoretical flow pattern maps have been developed [6].

Empirical flow pattern maps (e.g. Govier & Aziz [7]) are based on experimental investigation for a particular fluid (air-water or water-steam), geometry (in general diameter up to 50 mm) and pressure range (normally atmospheric pressure). The results are presented in different co-ordinate systems, but none of them is capable of making a proper prediction for all flow regimes. To overcome this problem Weisman and Kang [8] apply scaling parameters to various transitions. Because the classification of the flow regimes is subjective and mostly based on visual observations (and not on measurements) the agreement of the different flow maps is rather poor. Additionally, the application outside the scope is not possible.

Theoretical flow pattern maps (e.g. Taitel, Bornea and Dukler [9], Ishii and Mishima [10]) consider conditions which are necessary for the existence of each flow pattern and postulate mechanisms (e.g. interface friction, pressure gradients) associated with each transition. Therefore the effect of fluid properties and pipe sizes are considered. The result is a set of equations for the transition of the flow regimes. A comparison with experimental data shows a reasonable agreement.

In the present work the main attention was put on the transition from bubble to slug flow. The transition criteria presented in table 1 are transferred into a coordinate system with the superficial velocity of the air as abscissa and the superficial velocity of water as ordinate. The flow regime map of ATHLET [11], a 1D thermohydraulic code, developed by the Gesellschaft für Anlagen und Reaktorsicherheit (GRS) mbH, and own data are added to this comparison.

The flow map of Taitel, Bornea and Dukler and the model of ATHLET show the best agreement with the experiment. Ishii and Mishima indicate the transition at slightly higher superficial gas velocities. The correlation of Weisman and Kang overestimates the critical gas flow rate by a factor of 2 at medium superficial liquid velocities. The largest deviations were found for the correlation of Govier and Aziz, which overestimates the superficial air velocities for the transition at low superficial water velocities ($J_L < 0.2$ m/s) by a factor of 2 and underestimates it at high superficial water velocities ($J_L > 0.7$ m/s).

5. Summary

Experimental investigations of two phase air water flow were carried out in the MTLOOP facility at environmental conditions in a wide range of superficial velocities. The two-phase flow was studied by a wire-mesh sensor, a new device for high resolution local instantaneous conductivity measurements, which was developed by Forschungszentrum Rossendorf.

The high resolution of the void fraction measurements allows to determine the bubble size distribution by a recursive search procedure. From the individual bubble volumes, the equivalent bubble diameters are determined what allows to derive a bubble size distribution. From this analysis the quantitative criteria for flow pattern transitions were formulated. The transition from homogeneous to heterogeneous bubble flow is indicated by the appearance of a bimodal bubble size distribution. If the equivalent bubble diameter exceeds the tube diameter the transition from bubble to plug flow occurs.

The new criterion for the classification of the bubble slug flow transition were compared to existing flow pattern maps. The best agreement was found with Taitel, Bornea & Dukler and the code ATHLET.

References

[1] H.-M. Prasser, A. Böttger and J. Zschau, A new Electrode Tomograph for Gas-Liquid Flows, in F.-P. Weiss et. U. Rindelhardt (Ed.), Institute of Safety Research, Annual Report 1996, FZR-190, 34

[2] H.-M. Prasser, A. Böttger and J. Zschau (1998), Hochauflösende Gittersensoren für Gas-Flüssig-Strömungen, MSR Magazin 10, 12

[3] H.-M. Prasser, Wire-mesh sensors for two-phase flow investigations, in F.-P. Weiss et. U. Rindelhardt (Ed.), Institute of Safety Research, Annual Report 1998, FZR-268, 23

[4] S. Z. Rouhani and M. S. Sohal (1983), Two-Phase Flow Patterns: A Review of Research Results, Progress in Nuclear Energy 11, 219

[5] M. A. Vince and R. T. Lahey (1982), On the Development of an Objective Flow Regime Indicator, Int. J. Multiphase Flow 8, 94

[6] K. W. Quillan and P. B. Whalley (1985), Flow Patterns in Vertical Two-Phase Flow, Int. J. Multiphase Flow 11, 161

[7] G. W. Govier and K. Aziz, K. (1982), The Flow of Complex Mixtures in Pipes, van Nostrand Reinhold Company, New York, Cincinnati, Toronto, London, Melbourne

[8] J. Weisman and S. Y. Kang (1981). Flow Pattern Transition in Vertical and Upwardly Inclined Lines, Int. J. Multiphase Flow 7, 271

[9] Y. Taitel, D. Bornea and A. E. Dukler (1980), Modelling Flow Pattern Transitions for Steady Upward Gas-Liquid Flow in Vertical Tubes, AIChE Journal 26, 345

[10] K. Mishima and M. Ishii (1984), Flow Regime Transition Criteria for Upward Two-Phase Flow in Vertical Tubes, Int. J. Heat Mass Transfer 27, 723

[11] F. Steinhoff (1989), Thermo- und Fluiddynamikmodelle im Rechenprogramm DRUFAN und im Nachfolgeprogramm ATHLET zur Simulation von Separationsvorgängen und Gemischspiegelbewegungen in vertikalen Strömungskanälen - Teil1: Entwicklung der Modelle, Gesellschaft für Anlagen- und Reaktorsicherheit (GRS) mbH, Report GRS-A-1539

CFD SIMULATIONS OF A BUBBLY FLOW IN A VERTICAL PIPE

Eckhard Krepper

1. Introduction

Even at the very simple conditions of two phase flow in a vertical pipe, strong 3D effects are observed. The distribution of the gas phase over the cross section varies significantly between the different flow patterns, which are known for the vertical two-phase flow. The air water flow in a vertical tube having a diameter of 50 mm and a length of about 3 m was investigated in steady state tests for different liquid and gas superficial velocities. Several two phase flow measuring techniques were used. Applying a wire mesh sensor, developed in FZR, the void fraction could be determined over the whole cross section of the pipe. The working principle is based on the measurement of the local instantaneous conductivity of the two-phase mixture (see H.-M. Prasser et. al [1] (1999), [2] (1998), [3] (1999)). At the investigated flow velocities, the rate of the image aquisition is sufficient to record the same bubble several times. This enables to determine bubble diameter distributions. Applying two similar wire mesh sensors with a distance of 50 mm one above the other, the influence of the wire mesh to the flow could be investigated. No essential disturbances of the two-phase flow by the mesh could be found for the investigated flow regimes. Performing an auto correlation between the signals of both sensors, also profiles of the gas velocity were determined.

In the CFD code CFX-4.2 several two-phase flow models were available. Using the code, volume fraction profiles were calculated and compared to the measured results for bubble flow regimes, to investigate the capability of these models (see also Krepper and Prasser [4] (1999)).

2. The experiments

Different tests at nominal temperature conditions and nominal pressure with different superficial velocities of liquid and air were performed. Figure 1 shows the Taitel/Dukler diagram with the investigated tests marked in different flow regimes. For each test stationary conditions were settled.

In the regime of bubble flow, a well known region exists for which a void maximum near the wall is observed (marked yellow in Figure 1). At a gas superficial velocity of 0.01 m/s and water velocities less than 0.2 m/s a void maximum in the centre of the tube

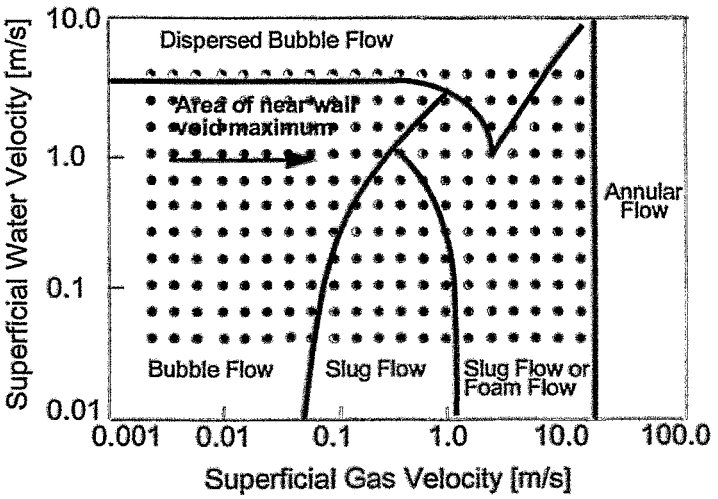

Fig. 1: Flow regime map (Taitel/Dukler) The performed stationary tests are marked by points

was found. Both decreasing the water velocity or increasing the gas velocity shifts the void maximum to the centre of the tube.

3. CFX-4.2 calculations

The CFX-4.2 calculations aimed at the assessment of the capability of the code to describe two phase bubbly flow. For different tests of bubbly flow the void profiles in the tube cross section were analysed. The development of the void profile in the tube in dependency on the distance to the air injection and on the injection mode was investigated, too.

For the calculations, the two fluid model implemented in CFX-4.2 was applied. The liquid phase was represented as continuous and the gas as disperse phase with a constant bubble diameter of 4 mm.

Figure 2 shows the measured bubble size distributions of the investigated flow regimes at different distances from the gas injection (see Prasser [1] (1999)). The results show, that this regime with the given superficial liquid and gas velocities can be modelled using a monodisperse approach for the bubble size. For other flow regimes bubble size distributions were detected, which indicate coalescence (see example in [1] (1999)).

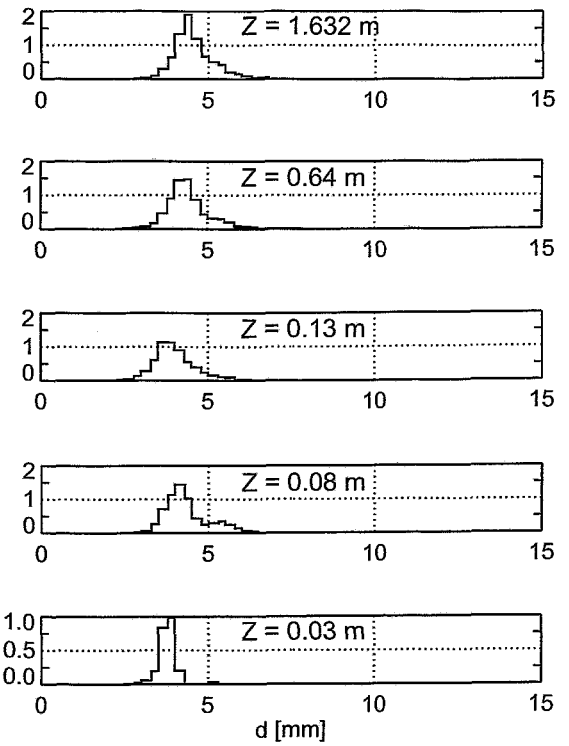

Fig. 2: Measured bubble size distribution at different distances above the gas injection
VL = 0.4 m/s; VG = 0.01 m/s

The drag force acting on the bubbles and the fluid were considered according to Ishii and Zuber [5] (1979). The particle induced turbulence was modelled according to Sato [6] (1975).

The establishment of the void profiles is mainly influenced by the "non drag forces", which act perpendicular to the flow direction. A spherical obstacle in a profiled flow undergoes a lift force $F_{\alpha lift}$ perpendicular to the flow direction (see Zun [7] (1980)).

$$F_{\alpha\text{lift}} = r_\beta \cdot \rho_\alpha \cdot C_L \cdot \vec{U}_\beta - \vec{U}_\alpha \times \nabla \times \vec{U}_\alpha$$

The index α denotes the liquid and β the gaseous phase. r is the volume fraction, ρ the density and U the velocity. For a solid sphere, a coefficient for $C_L = 0.5$ is calculated. For weakly viscous flows the bubble shape deviates from the spherical form. Therefore $C_L = 0.05$ was used.

The turbulent dispersion force acts towards an even gas fraction distribution:

$$F_{\alpha diff} = C_{TD} \cdot \rho_{\alpha} \cdot k_{\alpha} \cdot \nabla r_{\beta}$$

k is the turbulent kinetic energy. The coefficient C_{TD} was set to C_{TD}= 0.1.

According to the profiles of velocity, k and ∇r_{β}, found for a flow in a tube, these two components of non drag forces are directed towards the wall. Therefore, considering only lift and dispersion force, the gas fraction near the wall is overestimated. Antal et. al [8] (1991) proposed, additionally to consider a lubrication force which drives the bubbles away from the wall. This force is the consequence of the no-slip condition for the continuous phase at the wall. The asymmetric fluid flow, to which a bubble of a diameter d is exposed to at a distance of y_w, causes the lubrication force:

$$F_{\alpha lub} = \frac{r_{\beta} \cdot \rho_{\alpha} \left| \overrightarrow{U_{\beta}} - \overrightarrow{U_{\alpha}} \right|^2}{d} \cdot \max\left(C_1 + C_2 \cdot \frac{d}{y_w}, 0\right) \vec{n}$$

$\vec{n}$ denotes the normal vector at the wall. The coefficients were fitted to the experimental results and were set to C_1 = -0.0064 and C_2 = 0.016.

The flow of both phases was modelled as turbulent. The calculations were performed in a three-dimensional cylindrical domain with a radius of R= 0.025 m and a length of Z = 3.0 m corresponding to the vertical test section. The whole grid with non equally divided cell dimensions consisted of 50,000 cells. For the liquid phase a no-slip and for the gas phase a free-slip boundary condition were chosen at the wall. The inlet boundary condition at the lower end of the cylinder corresponded to an equal gas flow distribution over the cross section at the inlet. The fluid velocity profile, the liquid turbulent energy k and the liquid turbulent dissipation rate ε were set to a fully developed single phase flow. A pressure boundary condition was assumed at the outlet on the top.

During the calculations the default difference schemes were used. The inter-phase slip algorithm was applied. The calculations were performed as transients with constant boundary condition. A constant time step corresponding to the Courant time step was applied. The mass balance between the inlet and the outlet was checked during the transient (see Figure 3).

$$BALANCE = \frac{\dot{M}_{IN} - \dot{M}_{OUT}}{\dot{M}_{IN}}$$

The figure shows, that even small discrepancies in the gas mass balance disappeared only after a transient time which corresponds to the time that a disturbance needs to pass the tube length of 3 m. Increasing the time step by a factor of 4 resulted in larger mass balance deviations during the tran-

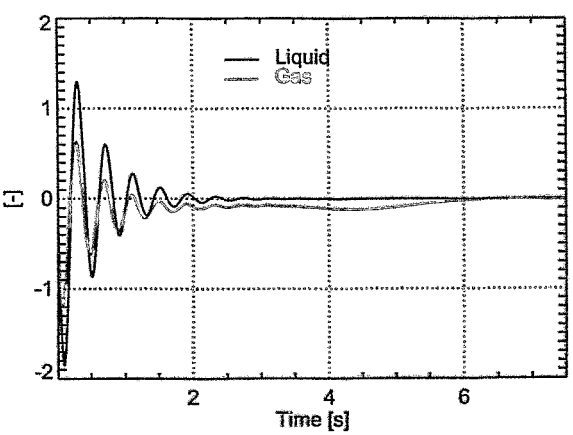

Fig. 3 : Relative liquid and gas mass balance between tube inlet and outlet
VL = 0.4 m/s; VG = 0.01 m/s

sient, but also converged to equalized balance after 7.5 seconds.

Figure 4 shows the calculated velocity profiles and the comparison to the experiment at about 3 m behind the air injection. A typical flow profile for the fluid is found. The gas velocity profile was experimentally determined by auto correlation of the signals of two wire mesh sensors arranged at a distance of about 50 mm.

Considering all three non drag forces, the calculated void profiles agree at least qualitatively with the measurements (see Figure 5). Injecting the gas from the bottom, the void fraction maximum immediately near the wall is established (see Figure 5 for Z = 0.1 m). With increasing distance from the air injection, the volume fraction maximum is shifted away from the wall (see Figure 5). These relations were observed in the tests, too.

Figure 6 shows the different contributions of the non drag forces. A positive value means the direction towards the wall. Corresponding to a liquid velocity profile found in a vertical tube, the lift force is directed towards the wall. Only near the wall the turbulent dispersion force which depends on the profiles for k and ∇r_β is directed towards the centre of the tube. The lubrication force acts away from the wall, but only immediately near the wall. Therefore the description of a flow regime with a volume fraction in the tube centre will not be possible considering only these three forces and assuming a monodisperse bubble size distribution.

Figure 7 shows the measured void fraction profiles for a test series with a liquid superficial velocity of 1.0 m/s. The gas superficial velocity for the different tests is increased from 0.01 to 0.125 m/s. The establishment of a second

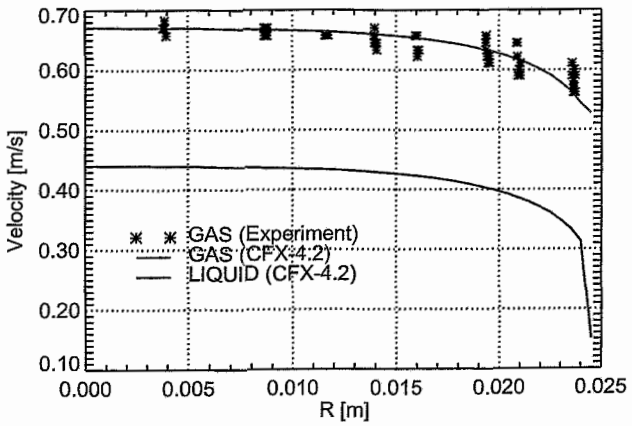

Fig. 4: Measured and calculated velocity profiles near the top of the tube
VL = 0.4 m/s; VG = 0.01 m/s

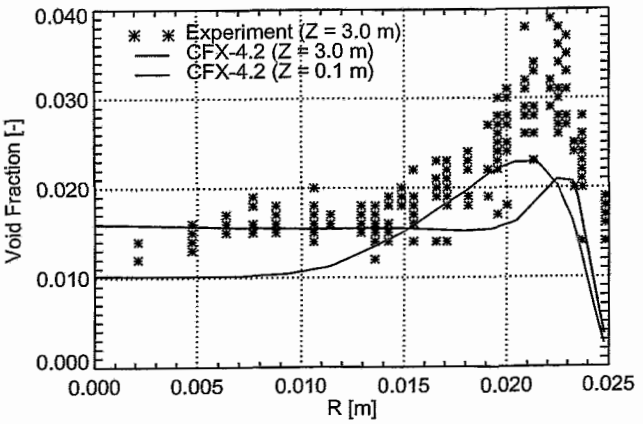

Fig. 5: Measured and calculated gas volume fraction profiles at different distances from the gas inlet
VL = 0.4 m/s; VG = 0.01 m/s

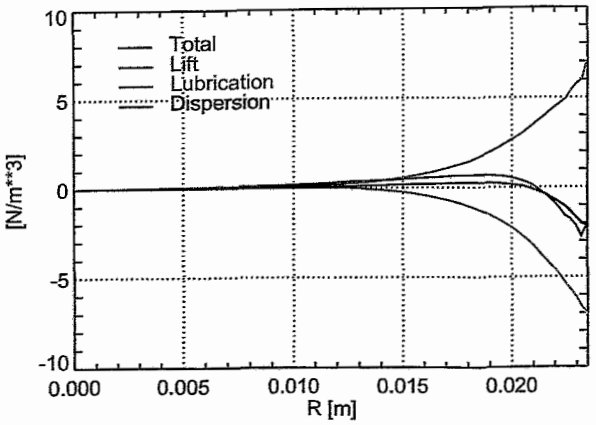

Fig. 6: Components of the considered non drag forces
VL = 0.4 m/s; VG = 0.01 m/s

void maximum in the tube centre is seen in the experiments. For larger gas velocities this second maximum is enlarged and dominates the whole profile. Figure 8 shows the calculated results. The figure shows, that with increasing gas velocity the near wall void maximum is overestimated, but the second maximum in the centre does not develop. The reason might be found in the occurrence of bubble coalescence and bubble diffraction, which is not considered in the models. For these flow regimes different bubble classes have to be considered. Larger bubbles having dimensions in the order of the tube diameter will be exposed to other forces than modelled here.

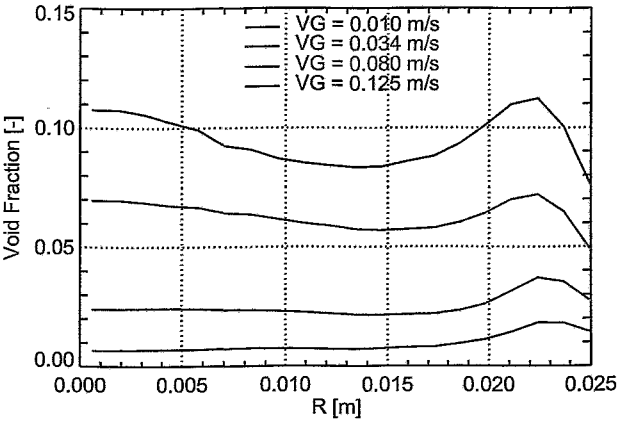

Fig. 7: Measured void fraction profiles for a liquid superficial velocity of VL = 1.0 m/s

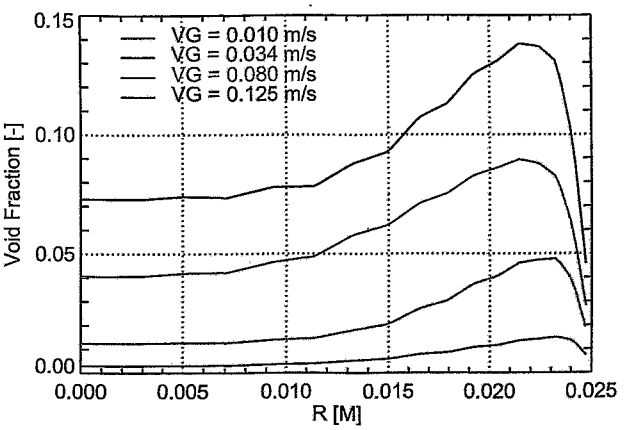

Fig. 8: Calculated void fraction profiles for a liquid superficial velocity of VL = 1.0 m/s

4. Summary and conclusions

For the calculation of void profiles in a vertical upward bubbly flow, the consideration of the non drag forces is essential. The two phase models implemented in the code version CFX-4.2 can describe void profiles with a near wall void maximum, when the model constants are well fitted to the tests. The investigated tests show the limits of the assumption of a single bubble diameter. Model extensions are necessary which consider the bubble diameter distribution due to bubble coalescence and bubble diffraction. The consideration of bubbles having a size in the order of the tube diameter requires the development of new bubble force models. The experiments at the measuring techniques test loops yield valuable information for the development and validation of such models.

References

[1] H.-M. Prasser (1999), Wire-mesh sensors for two-phase flow investigations, F.-P. Weiß, U. Rindelhardt (Ed.) Forschungszentrum Rossendorf, Institute of Safety Research, Annual Report 1998

[2] H.-M. Prasser, A. Böttger, J. Zschau (1998), A new electrode-mesh tomograph for gas-liquid flows; Flow Measurement and Instrumentation 9, pp. 111-129

[3] E. Krepper, A. Krüssenberg, H.-M. Prasser, A. Schaffrath (1999), High Resolution Void Fraction Measurements for the Validation of Flow Maps and CFD Codes, 2nd International Symposium on Two-Phase Flow Modelling and Experimentation, Pisa 1999, Proceedings Vol. III, pp. 1371-1378

[4] E. Krepper, H.-M. Prasser (1999), Measurements and CFX-Simulations of a Bubbly Flow in a Vertical Pipe, CFX International Users Conference, Friedrichshafen, Juni 1999

[5] M. Ishii, N. Zuber (1979), Drag coefficient and relative velocity in bubbly, droplet or particulate flows; AIChE Journal Vol. 25(1979)5, 843-855

[6] Y. Sato, Sekoguchi, K. (1975), Liquid velocity distribution in two phase bubble flow; Int. J. Multiphase Flow 2(1975), p. 79

[7] I. Zun (1980), The transverse migration of bubbles influenced by walls in vertical bubbly flow; Int. J. Multiphase Flow 6, pp. 583-588

[8] Antal, S.P., Lahey Jr., R.T., Flaherty, J.E. (1991), Analysis of phase distribution in fully developed laminar bubbly two phase flow; Int. J. Multiphase Flow 17(1991)5,635-652

INVESTIGATION OF COOLANT MIXING IN PRESSURIZED WATER REACTORS AT THE ROSSENDORF MIXING TEST FACILITY ROCOM

Gerhard Grunwald, Thomas Höhne, Horst-Michael Prasser, Karlheinz Richter, Frank-Peter Weiß

1. Introduction

During the so called boron dilution or cold water transients at pressurized water reactors too weakly borated water or too cold water, respectively might enter the reactor core. This results in the insertion of positive reactivity and possibly leads to a power excursion. If the source of unborated or subcooled water is not located in all coolant loops but in selected ones only, the amount of reactivity insertion depends on the coolant mixing in the downcomer and lower plenum of the reactor pressure vessel (RPV). Such asymmetric disturbances of the coolant temperature or boron concentration might e.g. be the result of a failure of the chemical and volume control system (CVCS) or of a main steam line break (MSLB) that does only affect selected steam generators (SG) [1-3]. For the analysis of boron dilution or MSLB accidents coupled neutron kinetics/thermo-hydraulic system codes have been used. To take into account coolant mixing phenomena in these codes in a realistic manner, analytical mixing models might be included. These models must be simple and fast running on the one hand, but must well describe the real mixing conditions on the other hand. One possibility is to use pre-determined mixing matrices mapping the contribution of each cold leg to each fuel assembly at the reactor core inlet [2]. The coolant mixing in the downcomer and lower plenum depends

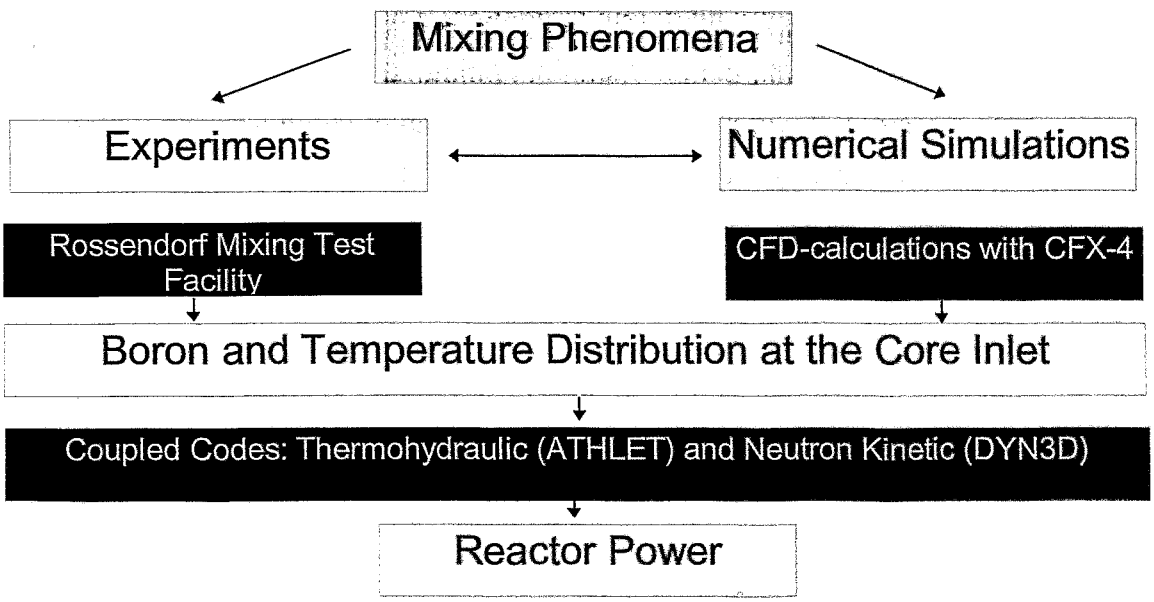

Fig. 1: Systematic of investigations in mixing phenomena

significantly on the construction of the reactor vessel and on the instantaneous flow conditions. The models and assumptions for coolant mixing description to be used in the coupled codes must be validated against experimental data and detailed computational fluid dynamics (CFD) calculations. Therefore the Institute for Safety Research of Forschungszentrum

Rossendorf has constructed a 1:5 mixing test facility ROCOM (**Ro**ssendorf **Co**olant **M**ixing Model) representing the geometry of the German Konvoi type pressurized water reactor. Later on tests on the future European Pressurized Water Reactor (EPR) are planned. The numerical simulations are based on the CFD-Code CFX-4.2. [4].

The scheme in Figure 1 shows the systematics of transient analyses reaching from mixing tests and numerical simulations of the mixing up to the reactor dynamics calculations providing the reactor power and other safety relevant parameters [5].

2. The test facility

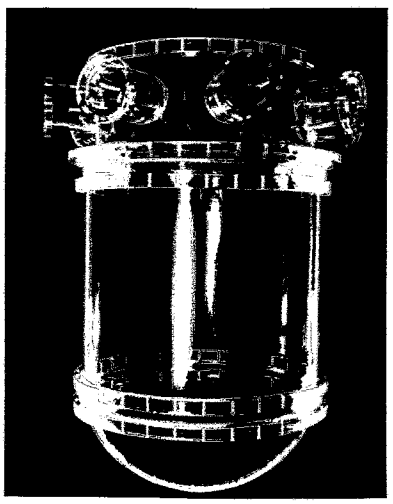

Fig. 2: RPV Plexiglas® Model

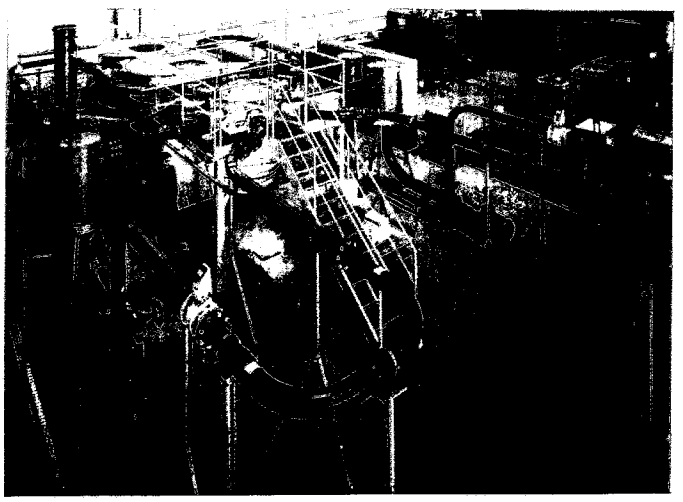

Fig. 3: Test facility ROCOM

Table 1 compares the relevant parameters of the model with those of the Konvoi type reactor.

Table 1: Comparison original PWR - 1:5 scaled mixing model: coolant medium water, 20°C

Dimension	Unit	Original	Model 1:5
diameter of the pressure vessel	mm	5000	1000
height of the pressure vessel	mm	~12 000	~2400
inlet nozzle diameter.	mm	750	150
downcomer gap	mm	315	63
general mass flow of the coolant	m^3/h	92 000	1400
mass flow per loop	m^3/h	23 000	350
speed at inlet nozzle	m/s	14.5	5.5
speed at the downcomer	m/s	5.5	2.1
Re inlet nozzle	-	$8.4*10^7$	$8.3*10^5$
Re downcomer	-	$2.7*10^7$	$2.5*10^5$
Re Original / Re Model	-	1	~100

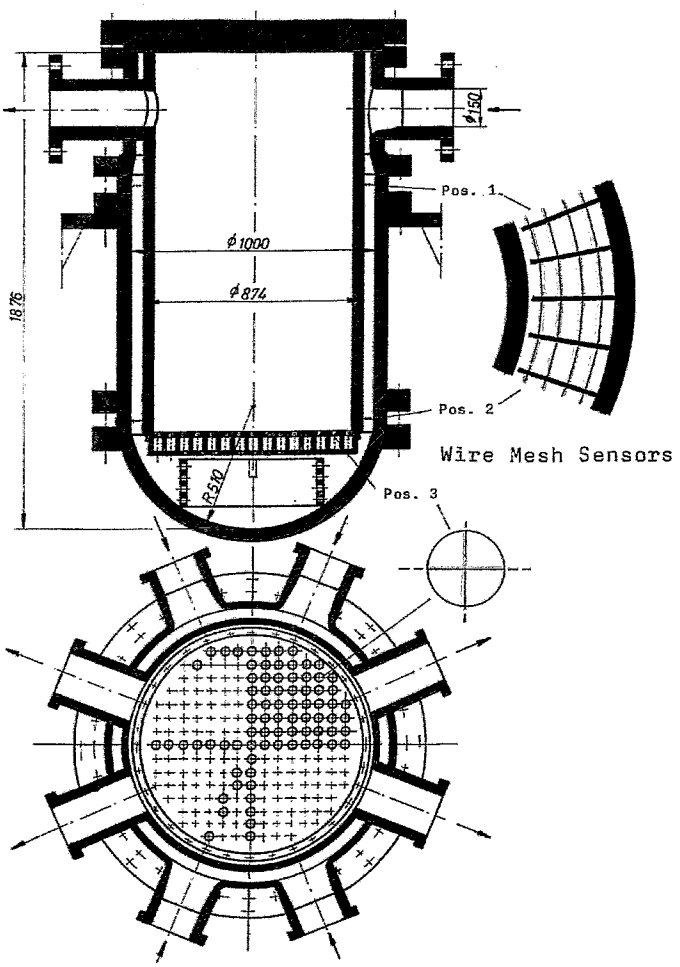

Fig. 4: View of the Plexiglas® model

As mixing is less influenced by the absolute temperatures and by the static pressure but by density differences and flow velocity the vessel of the 1:5 scaled test facility could be made of Plexiglas® and is operated at ambient pressure with cold water (Fig. 2) This allows flow visualisation and LDA velocity measurements.

The test facility is furnished with 4 separately controllable coolant pumps (Fig. 3) to be able to simulate different flow conditions from nominal coolant flow rate to natural convection and pump start-up.

To study the mixing phenomena plugs of salt water are injected into deionate in the RPV through one of the cold legs. The salt significantly changes the conductivity of the water what can be measured by conductance methods. In the facility, the so called wire mesh sensors are applied. The working principle of the mesh sensors is explained in „Wire-mesh sensors for two-phase flow investigations" of this annual report and in [6].

There is one sensor at the lower core support structure, two are in the downcomer and one in one cold leg (see Fig. 4). The extensive instrumentation with these sensors permits a high resolution of the concentration field in the RPV in space and time. The sensors are shown in detail in Fig 5-7. The downcomer sensors and those in the cold leg have 16x16 measurement points each. The sensor at the core bottom yields 193 points at the same time. This means, there is one concentration measurement at the bottom of each fuel element.

All sensors provide 200 measurements per second and work in the conductivity range of 10-500 µS/cm. In the experiments, a time resolution of 20 measurements per second is sufficient, i.e. 10 individual measurements are averaged.

Fig. 5: Sensor DC

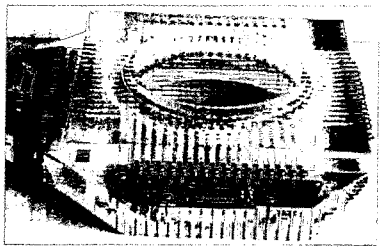

Fig. 6: Sensor inlet nozzle

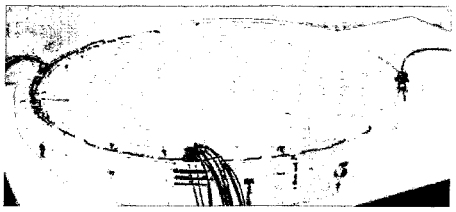

Fig 7: Sensor core inlet

The mixing measurements in the reactor model are realised by the following steps: First the test facility is filled with low conductivity water (deionat). The wanted flow field is adjusted by controlling the main coolant pumps. After this, the injection pumps forward a plug of salted water continuously or discontinuously to the mixer in one of the cold legs. The concentration profile is measured by the wire mesh sensor in that cold leg. All processes, including the measurement of the mass flow, temperature, pressure, the tracer injection and the water cleaning with ion exchangers are computer controlled.

The screen panels of the computerised process control system is shown in Fig. 8. It is based on the software package DELPHI™ -4.

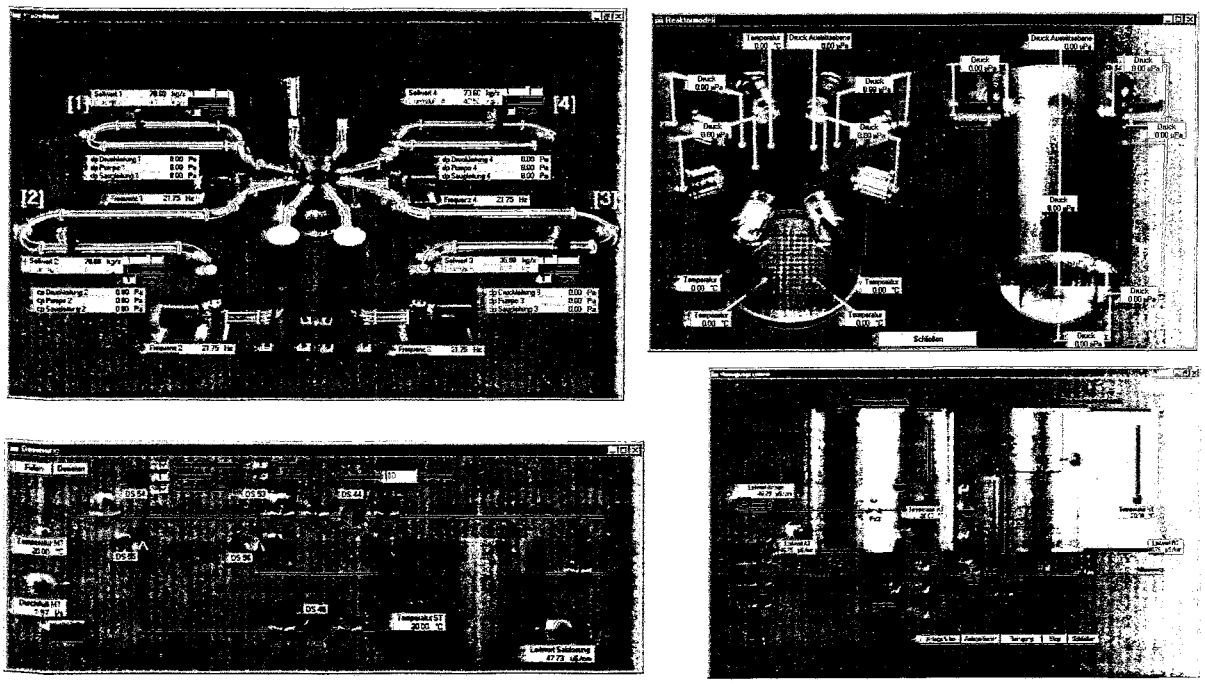

Fig. 8: Process control system of the mixing test facility

5. Experimental Results

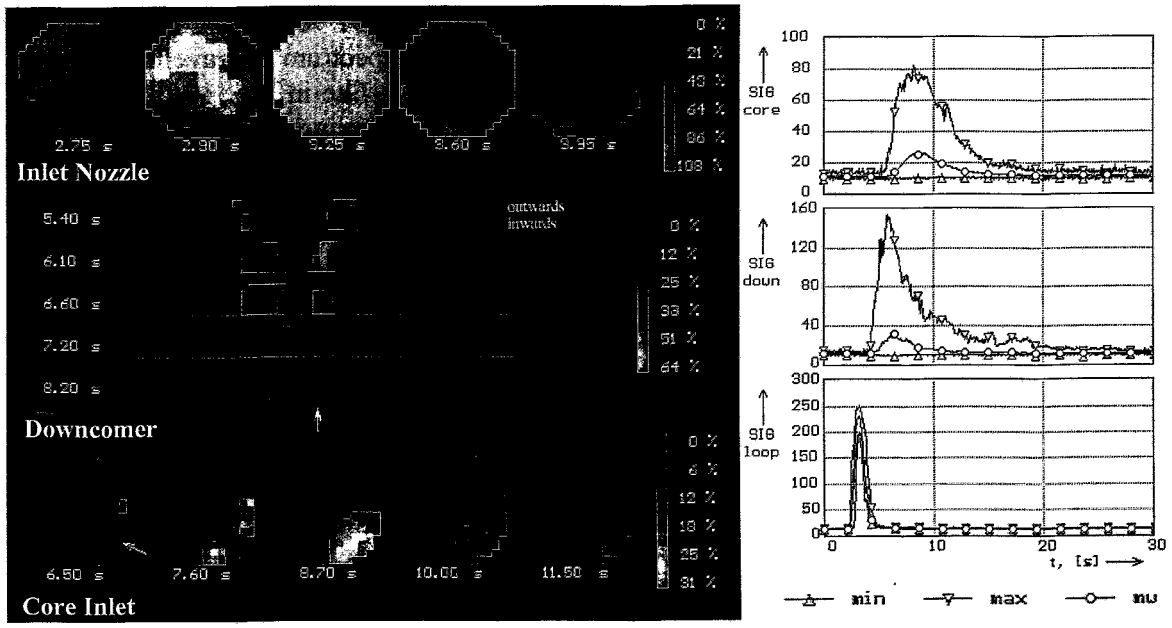

Fig. 9: Injection of a salted water plug into one loop at nominal conditions

Figure 9 shows the concentration distribution in space and time after the injection of a short salted water plug in one loop at nominal conditions, i.e. all four pumps were operating at full speed. Conductivity distributions are shown at the inlet nozzle, at the end of the downcomer and at the core inlet. The arrows are indicating the direction of the injection. The mass flow rate was 50 m^3/h in all 4 loops and the tracer injection lasts 0.7 seconds (1 litre salted water).

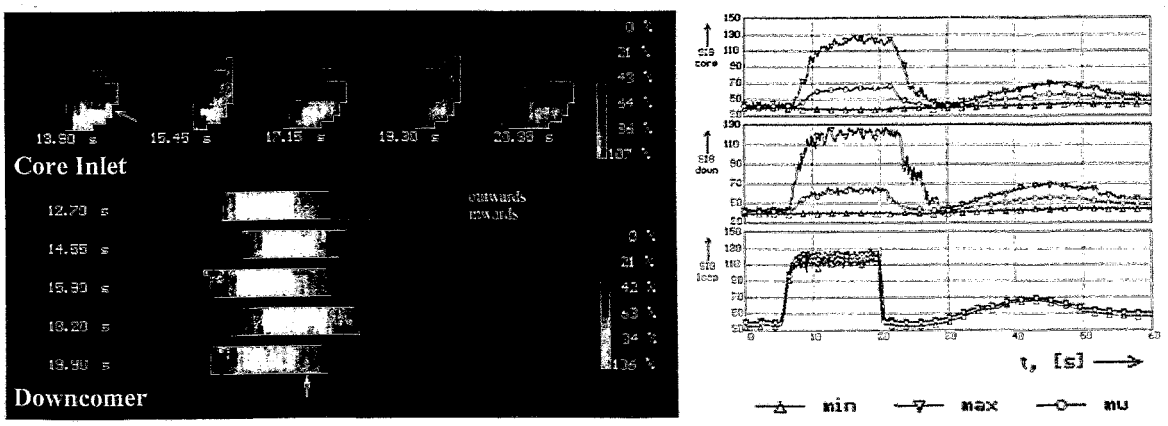

Fig. 10: Constant injection of a salted water plug into one loop at nominal condition

The diagrams show three time dependencies of the conductivity at the wire mesh sensors: instantaneous values of the maximum, the minimum and the averaged conductivity over the measuring planes at the core inlet sensor (core), the downcomer sensor (down) and the inlet nozzle sensor (loop). The sensor in the inlet nozzle confirms the good mixing of the salt water by the injection device. In the downcomer and at the lower plenum, the mixing is incomplete. At the moment when the plug is entering the downcomer sensor and also at the core inlet, two

maxima are clearly to be seen. This phenomenon is caused by a re-circulation area below the inlet nozzle. Later on, these two maxima are merging together. The highest concentration level at the core inlet is found at the periphery. It reaches only 31 % of the concentration at the reactor inlet, which is caused by mixing due to the wide spectrum of travelling times in the vortexes of the downcomer. When the plug is big enough, like in Fig. 10 (injection: 22 liters in 15 seconds, mass flow rate per loop: 100 m^3/h), the maximum concentration at the core inlet corresponds to the concentration at the inlet nozzle, i.e. there are several fuel element positions, which are supplied with practically unmixed water from the disturbed loop. At the same time, the minimum concentration remains at the initial level, i.e. the majority of the measuring points are not reached by the water from the plug. In the process shown in Fig. 10, the injection conditions were constant for 14 s seconds. Despite of this, the concentration distribution shows characteristic azimuthal oscillations with a period of about four seconds, which are caused by the vortexes in the downcomer. The diagrams also show the second arrival of the plug after one turn around through the loops.

6. Outlook

To simulate real accident scenarios and for code validation an extensive test programme is planned. The experimental results will be compared against CFD calculations for analysing the dependencies of the power output of the reactor on the temperature and/or boron distribution. The classification of the tests is shown in Table 2.

Table 2: Classification of the Mixing Experiments

Group	Experimental Objects
A	Mixing under steady state conditions
B	Mixing under quasi-steady state conditions
C	Pump start-up scenarios
D	Steady state or transient flow regimes as an input for an analytical model using transfer functions
E	Start of natural circulation
F	Influence of internals on the flow field

References

[1] R. Hertlein, (1998), UPTF TRAM Test Phase C3, 1. EUBORA Project Meeting, 21-23 Oct., Vantaa, Finland

[2] P. Dräger (1987), Makroskopische Kühlmittelvermischung in Druckwasserreaktoren, Dissertation TH Zittau

[3] G. Ulrych und E. Weber (1983), Neuere Ergebnisse zur Kühlmittelströmung in Druckwasserreaktoren, Atomkernenergie-Kerntechnik 42, 217

[4] CFX-4.2 User Manual (1997), AEA Technology

[5] U. Grundmann, S. Kliem, U. Rohde (1997), The coupled code complex DYN3D/ATHLET- application to main steam line break analysis, Proc. M&C and SNA '97, Saratoga Springs, New York, USA, October 6-9

[6] H.-M. Prasser, A. Böttger, J. Zschau(1998), A new electrode-mesh tomograph for gas liquid flows, Flow Measurement and Instrumentation 9, 111-119

CFD SIMULATION OF COOLANT MIXING IN A VVER-440 TYPE REACTOR

Thomas Höhne and Ulrich Rohde

1. Introduction

Complex computer codes modeling the whole reactor system including 3D neutron kinetics in combination with advanced thermohydraulics plant models become more and more important for the safety assessment of nuclear reactors. Such codes only are capable of estimating the feedback effects in a realistic way, for instance reactivity initiated accidents with strongly asymmetric neutron flux distribution in the core caused by a perturbation in one of the primary circuit loops. At Forschungszentrum Rossendorf (FZR), Institute of Safety Research, both the hexagonal and the Cartesian versions of the 3-dimensional neutron kinetics code DYN3D were coupled with the advanced thermohydraulics system code ATHLET [1]. The 3-dimensional reactor core model DYN3D [2] has been developed at FZR to improve the simulation of reactivity initiated accidents, where space-dependent effects in the reactor core are relevant. These are, e. g. steam line breaks or boron dilution transients. Since a 1D thermohydraulics code and a 3D reactor core model are coupled, there is a need for an interface between the different spatial resolutions. This interface simulates 3D mixing in the RPV by relating the 2D concentration and temperature fields at the core inlet to the 1D concentration and temperature profiles in the single loops.

In the past, an analytical model for the description of coolant mixing in the RPV of VVER-440 reactors based on the analytical solution of the Navier-Stokes equations in the potential flow approximation has been developed to replace the non-conservative approach of homogeneous mixing inside the RPV. This model is included in the coupled code DYN3D/ATHLET [2]. Another way to calculate the 3D flow distribution in the downcomer and the lower plenum is the use of the results of computational fluid dynamics (CFD) codes. At present, the direct coupling of CFD and thermohydraulics system codes is impossible due to the high demands on computation time in the CFD-calculations. Therefore, simplified mixing models validated by CFD calculations are still important for use within coupled codes.

The VVER-440 (440 MW), a standard Russian reactor operating in several east European countries was considered for analyzing the flow field and mixing processes. There exist two versions of VVER-440 type reactors (V-230 and V-213). In the V-213 there is an elliptical sieve construction in the lower plenum. In this paper, only the V-230 without elliptical sieve is considered. The 3D flow distribution in the downcomer and the lower plenum of the VVER-440 reactor is calculated by means of the CFD code CFX-4 [3] for operational conditions. The CFX-calculations are compared with the experimental data and the analytical mixing model.

2. Calculation of mixing processes with a CFD code

2.1 Model assumptions, geometry preparation and grid generation

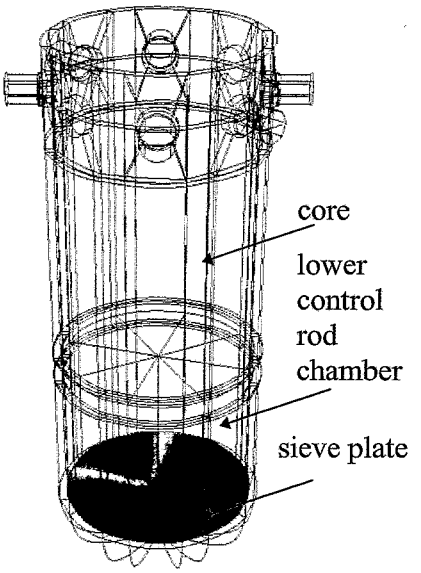

Fig. 1: Computational grid (VVER-440)

For the coolant flow simulation in the downcomer and lower plenum of a VVER-440 type reactor an incompressible fluid was assumed for the coolant flow. The turbulence was modeled using the standard k-ε approximation. The calculations were done on a SGI Origin 200 (1 GB RAM, 4x R 10000 180 MHz, 64 Bit CPU) workstation platform. For the calculations, a grid model of the VVER-440 RPV has been developed (see Fig. 1). The parameters of the discretization are given in Table 1. In order to receive an optimal net griding for the later flow simulation one must consider the following items: Checking grid number in special regions to minimize numerical diffusion, refinement of the griding in fields with strong changes of the dependent variables, adaptation of the griding to estimated flow lines, generation of nets as orthogonal as possible (angle >20°).

Table 1: Discretizations of the Reactor Type VVER-440

PWR	No. of blocks	No. of patches	No. of grid cells
VVER-440	236	912	159800

Inlet boundary conditions were set at the inlet nozzles as given velocity and temperature. The outlet boundary conditions were set to pressure controlled at the core inlet. In the case of the VVER-440 / V-230 a control rod chamber exists below the core, which is separated from the lower plenum by a sieve plate. It was not possible to simulate the whole core with the fuel elements, control elements etc. The sieve plate is modeled as a porous region. The porosity value γ for perforated plates is determined by relating the area of orifices to the total area of the sieve plate . The body forces B are added to the momentum equation (1), to take into account distributed friction losses in the sieve plate. Using the Cartesian coordinate system, the momentum equation is written:

$$\text{(j=1,2,3)} \qquad \rho\left(\frac{\partial U_j}{\partial t} + U_i \frac{\partial U_j}{\partial x_i}\right) = B_j - \frac{\partial}{\partial x_i}\tau_{ij} \tag{1}$$

$$B = B_F - \left(R_C + R_F|\overline{u}|\right)\overline{u} \tag{2}$$

In the equation (1) U_j are the components of velocity and τ is the shear stress, in equation (2) B_F, R_C and R_F are the coefficients of the body force dependence on the velocity. In our

model, only the second order contribution of the body forces according to relation (2) is used. The corresponding coefficient is obtained from measured values for the flow resistance at the perforated plate of the VVER-440.

2.2 Results of steady state calculations of the VVER-440 in comparison with experimental results and an analytical model

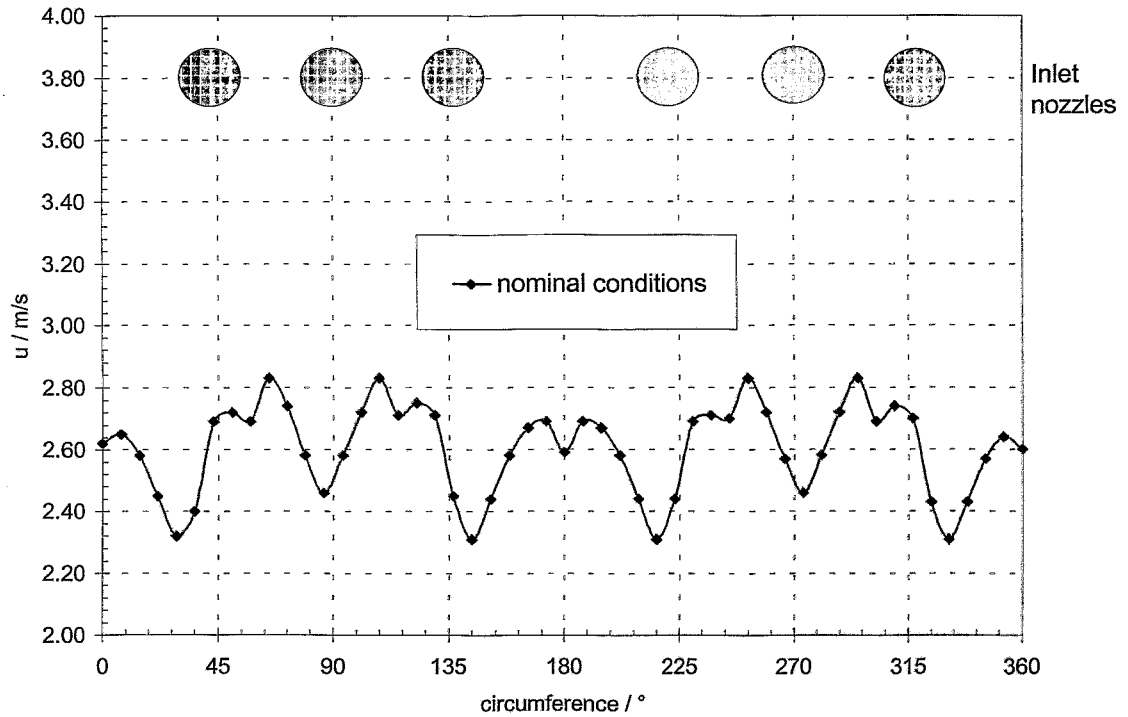

Fig. 2: Flow fields in the downcomer of the VVER-440 at nominal conditions

The CFD-calculations of the downcomer and lower plenum of the VVER-440 / V-230 were performed under the conditions of equal nominal coolant velocities at all 6 inlet nozzles assuming an arbitary temperature perturbation in one of the loops.

The results widely confirmed the validity of the analytical mixing model of Dräger [5]. The flow field in the downcomer is shown in Fig. 2. While in Western type reactors (PWR Konvoi) recirculation areas exist below the inlet nozzles [4], almost no vortices are found in the VVER-440. The velocity field is nearly parallel in the downcomer what confirms the applicability of the potential flow approximation.

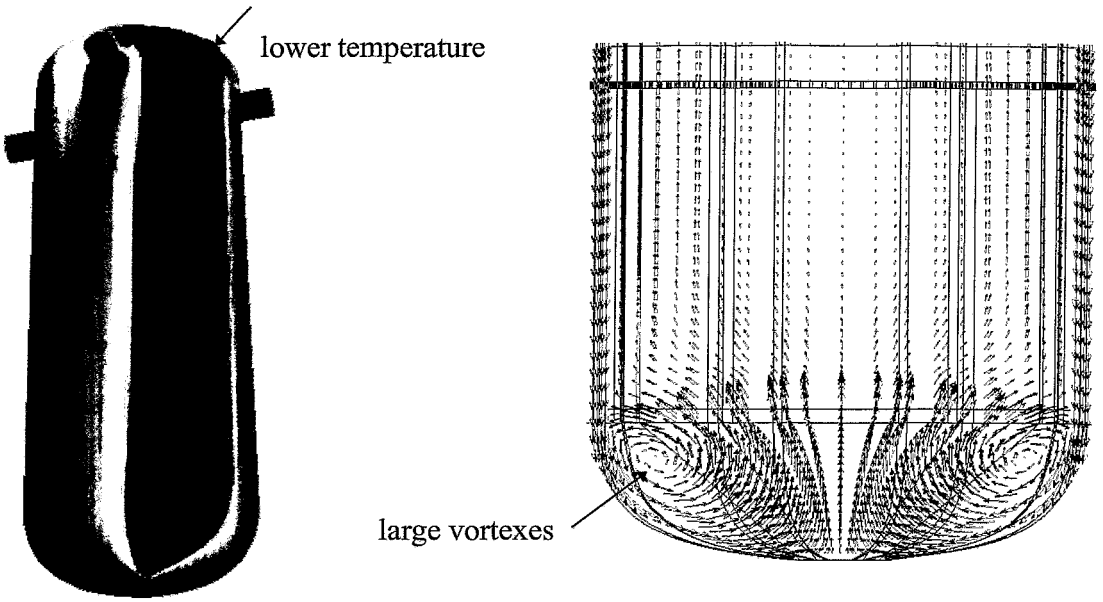

Fig. 3: Temperature distribution in the downcomer (main steam line break scenario) and flow field in the lower plenum at nominal conditions

This is a special feature of VVER-440 type reactors which is due to the inlet/outlet nozzles construction, downcomer geometry and high number (6) of loops. However, a maximum velocity exists at azimuthal positions between the inlet nozzles. The almost parallel flow in the downcomer leads to a low mixing rate what can be seen from the temperature distribution.

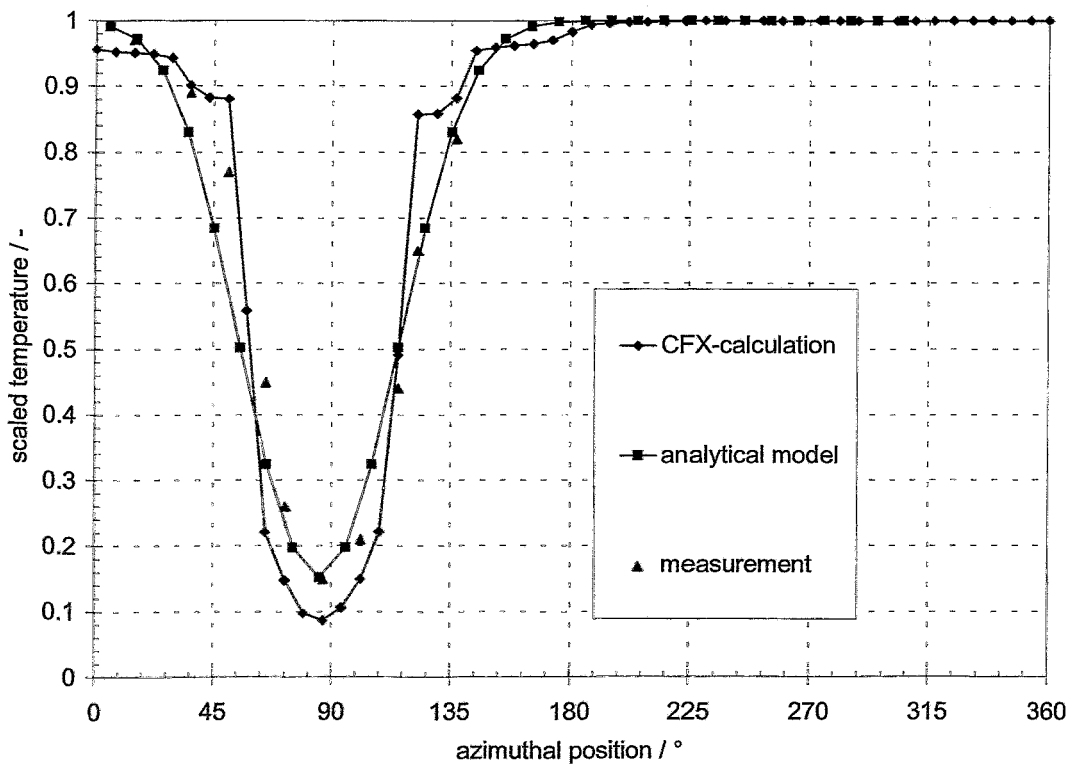

Fig. 4: Scaled temperature distribution at the end of the downcomer of a VVER-440

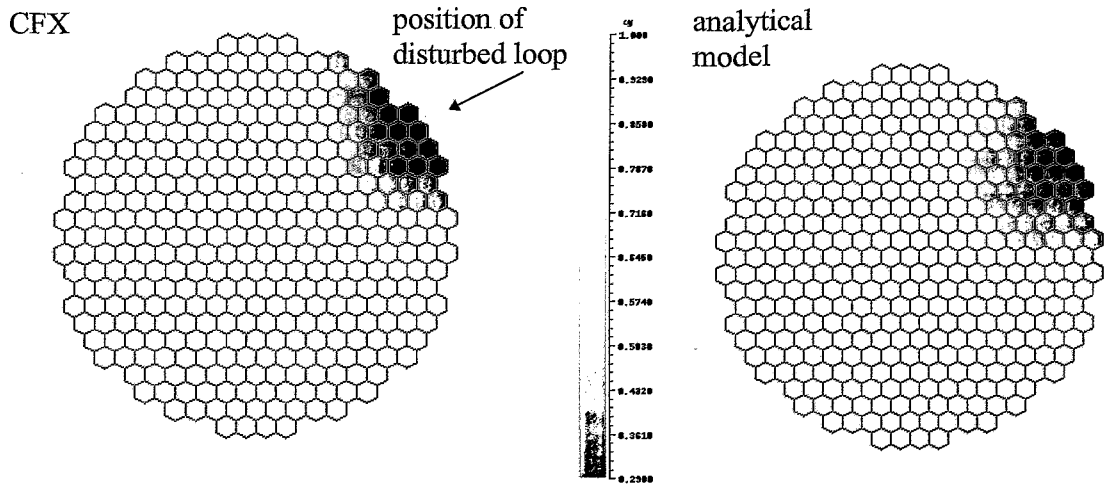

Fig. 5: Scaled temperature distribution at the core inlet (CFX, analytical model)

In the lower plenum of the VVER-440, large vortices exist (Fig. 3). The perforated plate is controlling the size and location of the vortices and therefore also the mixing of the coolant. The maximum velocity at the core inlet is situated at the outer core radius. To compare the measurements, the analytical model and numerical simulations with CFX results an

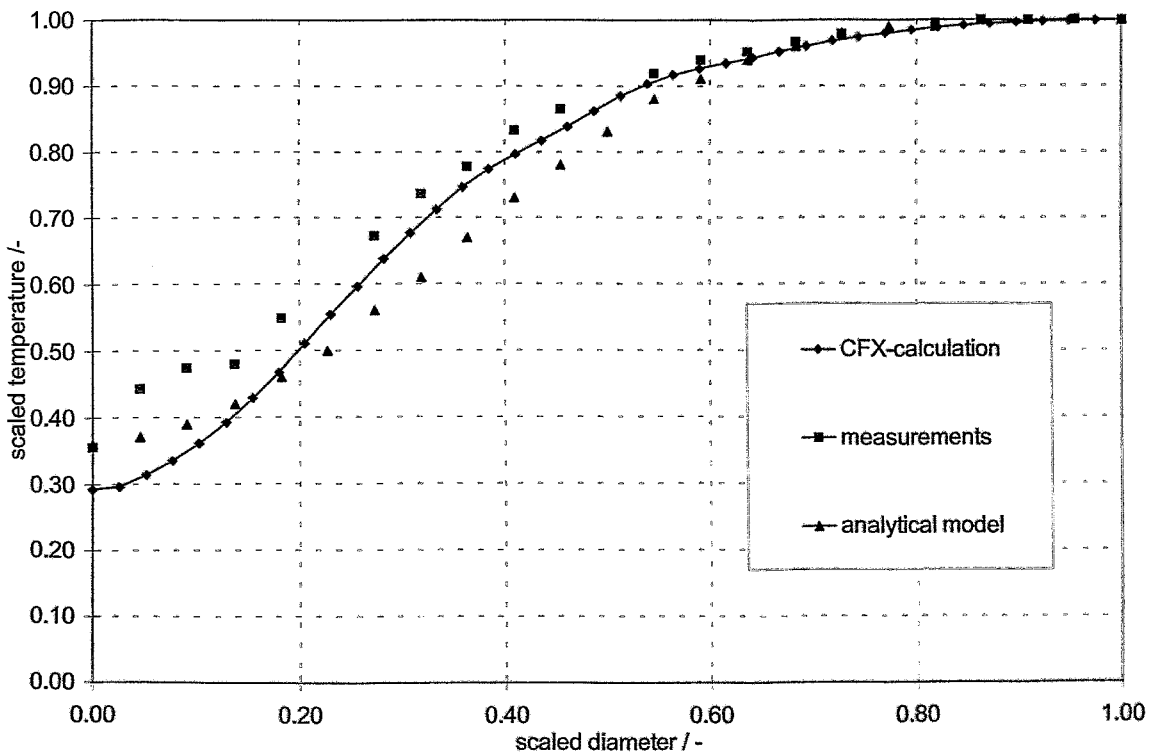

Fig. 6: Scaled temperature distribution at the core inlet

experiment at the scaled air operated model of the VVER-440 at TH Zittau [5] was considered. In the experiment, all loops were in steady state operation, one of the six loops was operating at lower temperature. These conditions correspond to a main steam line break scenario (MSLB).In Fig. 4 the temperature distribution at the downcomer outlet is shown. A relatively sharp sector of cold water is located below the inlet nozzle. Figs. 5 and 6 show the scaled temperature distribution at the core inlet of the VVER-440. At nominal conditions the numerical simulation using CFX provides similar results like the analytical model based on potential theory. While Fig. 5 shows the 2D distribution at the core inlet, in Fig.6 the distribution is shown along the core diameter starting from the position of the disturbed loop. The CFD-calculation gives the lowest mixing rate, which can be seen from the greater difference between maximum and minimum scaled temperatures. However, sector formation can be clearly seen in all models (see Fig. 5). The lowest mixing rate is situated near the core edge with the value 30%.

3. Outlook

Transient CFD-calculations with changing inlet boundary conditions are to be accomplished as the next step to simulate real accident scenarios. Further investigations are necessary to model internals. To validate the CFX-4 code it is necessary to compare the results with experiments for different reactor types, e.g. with experiments at the 1:5 scaled Plexiglas® model of the PWR Konvoi at Forschungszentrum Rossendorf (FZR). To analyze the dependencies of the power output of the reactor on the temperature and/or boron concentration distribution an interface between CFD models and the neutron kinetic code DYN3D has to be set up at the core inlet region.

References

[1] Burwell, M.J., Lerchl, G., Miro, J., Teschendorff, V., Wolfert, K. (1989) The Thermalhydraulic Code ATHLET for Analysis of PWR and BWR Systems. In: NURETH-4, Proceedings Fourth International Topical Meeting on Nuclear Reactor Thermal-Hydraulics, Vol. 2, Karlsruhe, 1234

[2] U. Grundmann, S. Kliem, U. Rohde (1997), The coupled code complex DYN3D/ATHLET-application to main steam line break analysis, Proc. M&C and SNA '97, Saratoga Springs, New York, USA, October 6-9

[3] CFX-4.2 User Manual (1997), AEA Technology

[4] G. Ulrych und E. Weber (1983), Neuere Ergebnisse zur Kühlmittelströmung in Druckwasserreaktoren, Atomkernenergie-Kerntechnik 42, 217

[5] P. Dräger (1987), Makroskopische Kühlmittelvermischung in Druckwasserreaktoren, Dissertation TH Zittau

NEW 3D NODAL METHOD HEXNEM FOR IMPROVING THE ACCURACY OF THE HEXAGONAL VERSION OF THE CODE DYN3D

Ulrich Grundmann

1. Introduction

The nodal expansion method (NEM) used in the hexagonal version of the code DYN3D is based on the node averaged values of fluxes in the node volume and averaged values of fluxes and currents at the interfaces of the nodes [1]. The 3-dimensional diffusion equation is split into a 2-dimensional equation in the hexagonal plane solved with the help of Bessel functions and a 1-dimensional equation in axial direction solved by polynomial expansion. The two the equations are coupled by the transversal bucklings. The accuracy of this method is sufficient for the VVER-440 where the assembly pitch is 14.7 cm. The assemblies of the VVER-1000 have a larger pitch of 24.1 cm. Comparisons with mathematical benchmarks for the VVER-1000 show a maximal deviation of powers in the order of 5%. The new nodal expansion method HEXNEM presented here uses a different flux expansion in the nodes. In addition to the averaged values at the interfaces of the hexagon the values at the corner points are included. It is shown that the accuracy is improved particularly for the VVER-1000 problems.

2. Description of the Method

Using standard notation the 3-dimensional 2-group neutron diffusion equation in the node n is given by

$$-\nabla D_g^n \nabla \Phi_g(\boldsymbol{r}) + \Sigma_g^n \Phi_g(\boldsymbol{r}) = S_g^n(\boldsymbol{r}) \tag{1}$$

with

$$S_1^n(\boldsymbol{r}) = \frac{1}{k_{eff}} \sum_{g=1}^{2} \nu\Sigma_{f,g}^n \Phi_g^n(\boldsymbol{r}) \quad \text{and} \quad S_2^n(\boldsymbol{r}) = \Sigma_{1\to 2}^n \Phi_1(\boldsymbol{r}) \tag{2}$$

The one- and 2-dimensional equations of the node n are obtained by integration over the hexagonal area F_{hex} or the height a_z of the box with the volume $F_{hex} \cdot a_z$. After integration over the z-direction for each energy group one obtains the 2-dimensional equation (the group index g and node index n are omitted in the following) for the axially averaged flux $\Phi(x,y)$

$$-D\left(\frac{\partial}{\partial x^2} + \frac{\partial}{\partial y^2}\right)\Phi(x,y) + \Sigma\Phi(x,y) = S(x,y) - L^z(x,y) \tag{3}$$

with the transversal leakage term

$$L^z(x,y) = -\frac{D}{a_z} \int_{z_0}^{z_1} \frac{\partial^2}{\partial z^2} \Phi(x,y,z)\,dz \tag{4}$$

for any z_0 and $z_1 = z_0 + a_z$. The integration over the hexagon F_{hex} gives the one-dimensional equation for the radially averaged flux $\Phi(z)$

$$-D\frac{d^2}{dz^2}\Phi(z)+\Sigma\Phi(z)=S(z)-L^r(z) \tag{5}$$

The average value of transversal leakage $L^r(z)$ is given by

$$L^r(z)=-\frac{D}{F_{hex}}\int_{F_{hex}}\left(\frac{\partial^2}{\partial x^2}+\frac{\partial^2}{\partial y^2}\right)\Phi(x,y,z)dF \tag{6}$$

The solution of the equations (3) and (5) in the nodes is described in the following. The flux in the hexagonal plane is expanded using polynomials $w_i(x,y)$ up to the 2nd order and exponential functions being the solutions of the homogeneous equation (3)

$$\Phi(x,y)\approx\sum_{i=0}^{5}c_i w_i(x,y)+\sum_{k=1}^{6}a_{s,k}\exp[B(e_{s,k}\boldsymbol{r})]+\sum_{k=1}^{6}a_{c,k}\exp[B(e_{c,k}\boldsymbol{r})] \tag{7}$$

with $\boldsymbol{r}=(x,y)$. The unity vectors $e_{s,k}, e_{c,k}$ show in the directions of the midpoints of the sides and to the corners (see fig. 1). The buckling B is given by

$$B=\sqrt{\frac{\Sigma}{D}} \tag{8}$$

The chosen polynomials $w_i(x,y)$ fullfill the following conditions

$$\frac{1}{F_{hex}}\int_{F_{hex}} w_i w_j dF = N_i^2\delta_{ij} \tag{9}$$

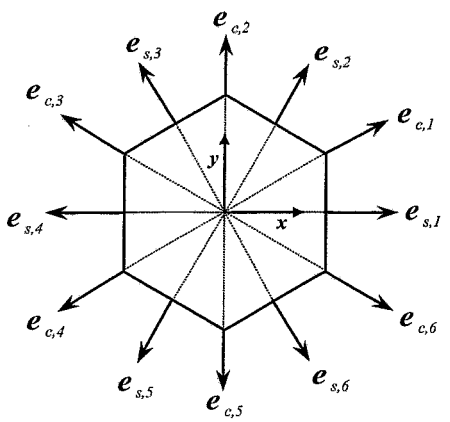

Fig. 1: Vectors $e_{s,k}, e_{c,k}$ of directions

with Kronecker's symbol δ_{ij} and the normalization factors N_i. The source terms and the transversal leakage terms of (3) are approximated by the polynomials. The coefficients of the leakage terms are obtained from the averaged leakage of the considered box and the values of the neighbouring hexagons. The coefficients of the source are given by the updated coefficients of the fluxes of the last outer iteration. Inserting expansion (7) into the diffusion equation (3) the coefficients c_i are obtained from the coefficients of polynomial expansions at the right hand side. Defining the partial currents by

$$J^{\pm}=\frac{1}{2}\left[\frac{\Phi}{2}\pm(\boldsymbol{eJ})\right] \quad \text{with } \boldsymbol{J}=-D\nabla\Phi \tag{10}$$

for any direction from (7) $\boldsymbol{e}=\boldsymbol{e}_{s,k},\boldsymbol{e}_{c,k}$ one obtains the equation system

$$\begin{aligned} \boldsymbol{J}_s^{\pm} &= \boldsymbol{P}_s^{\pm}\boldsymbol{C} + \boldsymbol{Q}_{ss}^{\pm}\boldsymbol{A}_s + \boldsymbol{Q}_{sc}^{\pm}\boldsymbol{A}_c \\ \boldsymbol{J}_c^{\pm} &= \boldsymbol{P}_c^{\pm}\boldsymbol{C} + \boldsymbol{Q}_{cs}^{\pm}\boldsymbol{A}_s + \boldsymbol{Q}_{cc}^{\pm}\boldsymbol{A}_c \end{aligned} \tag{11}$$

where $\boldsymbol{C}, \boldsymbol{A}_s, \boldsymbol{A}_c$ are the vectors of the coefficients $c_i, a_{s,k}$ and $a_{c,k}$, respectively. The side averaged partial currents and the partial currents at the corners form the vector $\boldsymbol{J}_s^{\pm}$ and $\boldsymbol{J}_c^{\pm}$, respectively. Caused by the symmetry of the problem each of the 6x6 matrices has only a few different elements. Each of the matrices $\boldsymbol{P}_s^{\pm}, \boldsymbol{P}_c^{\pm}$ consist of 6 different elements $\boldsymbol{Q}_{ss}^{\pm}, \boldsymbol{Q}_{cc}^{\pm}$ of 4, and $\boldsymbol{Q}_{sc}^{\pm}, \boldsymbol{Q}_{cs}^{\pm}$ of 3 elements. The $\boldsymbol{A}_s, \boldsymbol{A}_c$ are determined by a direct calculation of the inverse matrices of the (12x12) equation system (11) for given incoming partial currents $\boldsymbol{J}_s^-, \boldsymbol{J}_c^-$ and $\boldsymbol{C}$. Eliminating the $\boldsymbol{A}_s, \boldsymbol{A}_c$ in the equations (11) for the outgoing partial currents $\boldsymbol{J}_s^+, \boldsymbol{J}_c^+$ it is possible to express the $\boldsymbol{J}_s^+, \boldsymbol{J}_c^+$ by means of the incoming partial currents $\boldsymbol{J}_s^-, \boldsymbol{J}_c^-$, and the coefficients of the polynomial expansion $\boldsymbol{C}$:

$$\begin{aligned} \boldsymbol{J}_s^+ &= \boldsymbol{V}_s\,\boldsymbol{C} + \boldsymbol{W}_{ss}\boldsymbol{J}_s^- + \boldsymbol{W}_{sc}\boldsymbol{J}_c^- \\ \boldsymbol{J}_c^+ &= \boldsymbol{V}_c\,\boldsymbol{C} + \boldsymbol{W}_{cs}\boldsymbol{J}_s^- + \boldsymbol{W}_{cc}\boldsymbol{J}_c^- \end{aligned} \tag{12}$$

These matrices have the same structure as the matrices of (11). The different elements can be calculated at beginning of the iteration. At the interface between two hexagons, the incoming partial currents $\boldsymbol{J}^-$ are equal to the outcoming currents $\boldsymbol{J}^+$. For the corners of three hexagons 1,2 and 3 (number in parentheses), the following interface condition is derived:

$$\{J_{c,1}^+(1) - J_{c,1}^-(1)\} + \{J_{c,3}^+(2) - J_{c,3}^-(2)\} + \{J_{c,5}^+(3) - J_{c,5}^-(3)\} = 0 \tag{13}$$

The described 2-dimensional method with the zero transversal leakage term in (3) was verified separately in [3] with the help of benchmark solutions obtained by Chao et. al. [2].

A analogous procedure as in the 2-dimensional case above is used for the solution of the equation (5), i. e. the flux is $\Phi(z)$ expanded into polynomials until second order and exponential functions

$$\Phi(z) \approx \sum_{i=0}^{2} c_i^z w_i^z(z) + a_1^z \exp(Bz) + a_2^z \exp(-Bz) \tag{14}$$

A quadratic approximation of the source term and the leakage is used in (14). The coefficients of the radial leakage are calculated from the averaged radial leakage of the box and the values of the upper and lower boxes. The coefficients of the source are given by the updated coefficients of the fluxes from the last outer iteration. Inserting expansion (14) into the diffusion equation (5) the coefficients c_i^z are obtained. Using a similar procedure as for the 2-dimensional case the outgoing partial currents at the bottom and top of the node are expressed by the c_i^z and the incoming partial currents in axial direction:

$$\begin{aligned} J_{z_0}^+ &= v_0^z c_0^z - v_1^z c_1^z + v_2^z c_2^z + w_1^z J_{z_1}^- + w_2^z J_{z_0}^- \\ J_{z_1}^+ &= v_0^z c_0^z + v_1^z c_1^z + v_2^z c_2^z + w_2^z J_{z_1}^- + w_1^z J_{z_0}^- \end{aligned} \tag{15}$$

An inner and outer iteration scheme is applied to solve the equation system for all nodes of the core. In the inner iteration process it is assumed that the fission and scattering sources in (3) and (5) are approximated by the polynomials with coefficients given from the last outer iteration. Based on the coefficients of the right hand side source terms and the coefficients of the leakage terms the polynomial coefficients c_i and c_i^z of the flux expansions are determined by inserting (7) and (14) into the diffusion equations (3) and (5), respectively. Using these coefficients the outgoing partial currents are calculated for each node by means of the expressions (12) and (15) from the given incoming currents. The incoming currents are determined from the outgoing currents of the neighbouring nodes using the interface conditions between the nodes or the boundary conditions at the core border.

After few (3 - 5) inner iterations the coefficients of the source terms are updated from the flux expansions (7) and (14) by using (9) and equivalent conditions for the polynomials of (14). The new source terms are used for the next outer iteration step. A Chebychev extrapolation scheme is applied to accelerate the outer iteration.

3. Results

Two 3D steady state benchmark problems were calculated with one node per assembly in horizontal direction and $\Delta z = 25\,\text{cm}$ (VVER-440) or $\Delta z = 35.5\,\text{cm}$ (VVER-1000). The problems have a 30 degree symmetry. Fig. 1 shows the axial configuration of the VVER-440 with the half inserted control rods of bank K6. The calculation was carried out with axial and radial reflector assemblies. The deviations Δk_{eff} of the eigenvalue k_{eff}, the maximum and averaged value of the relative deviations of nodal powers and assembly powers from reference solution of Maraczy [4] are presented in table 1 for the DYN3D method and the HEXNEM method. The comparison of the HEXNEM assembly powers with the results of reference solution [4] can be seen in fig. 2. The positions of the half inserted control rods of bank K6 are identical by the assemblies with a thicker boundary (no. 1 and 7). In case of the VVER-440 with the smaller assembly pitch of 14.7 cm the accuracy of the DYN3D method is sufficient for practical applications. The HEXNEM method even shows an improvement of the results in this case.

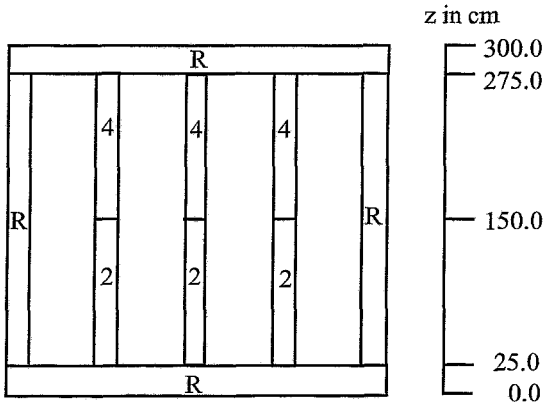

Fig. 2: Axial configuration of the VVER-440 (4 = absorber, R = reflector, 2 = fuel)

Table 1: VVER-440: Comparison of DYN3D and HEXNEM results with the reference:

VVER-440 Benchmark	DYN3D $\Delta k_{eff} = 40$ pcm		HEXNEM $\Delta k_{eff} = 1$ pcm	
	Max. (%)	Av. (%)	Max. (%)	Av. (%)
Nodal powers	2.7	0.93	0.8	0.17
Assembly powers	1.1	0.52	0.4	0.08

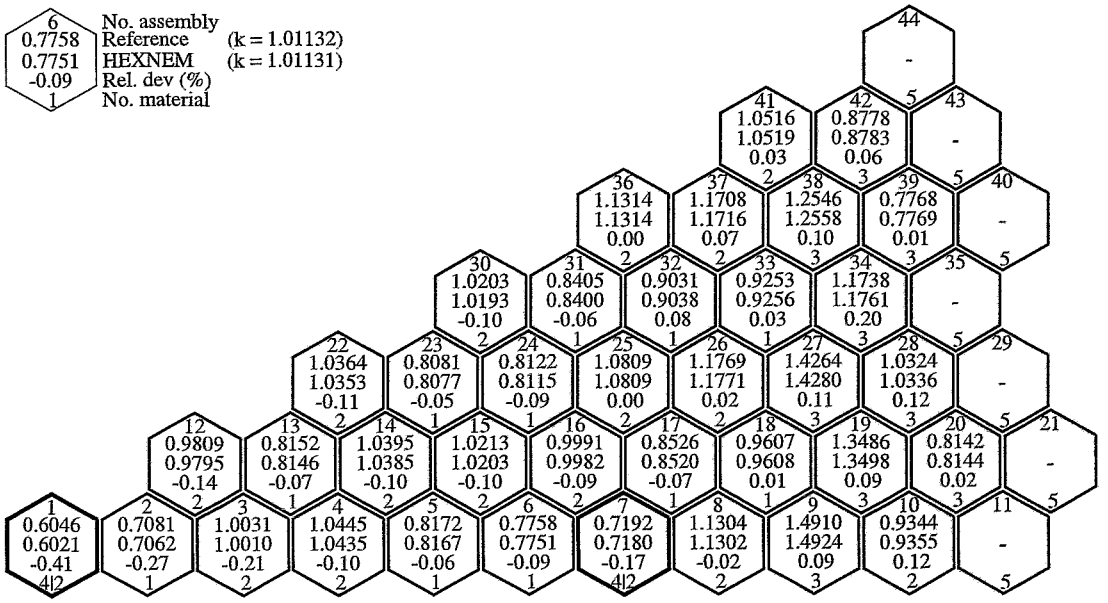

Fig. 3: Comparison of assembly powers for the VVER-440 Benchmark

The accuracy is more improved by the HEXNEM method for the VVER-1000 (pitch 24.1 cm). The 3D AER benchmark for the VVER-1000 is a problem with half inserted cluster and and a half cluster in the central fuel assembly. The axial configuration is shown in Fig. 3. The results of the detailed comparison with the reference values published by Kolev in [5] can be seen in table 2. Fig. 4 compares the normalized assembly powers for each assembly. The HEXNEM results for the VVER-1000 problem show a significant improvement of the results compared with the DYN3D method.

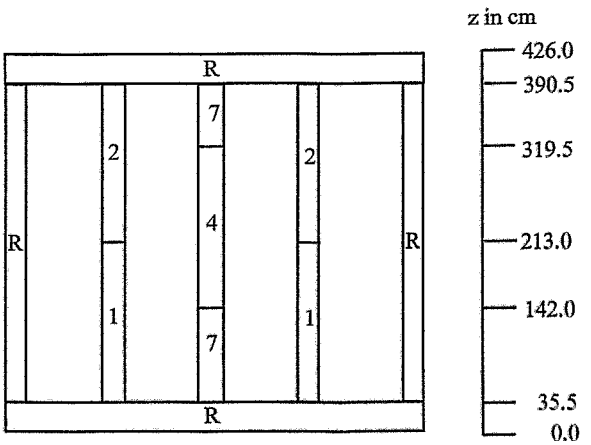

Fig. 4: Axial configuration of the VVER-1000 (1,7 = fuel, 2,4 = fuel with absorber rods, R = reflector)

Table 2: VVER-1000: Comparison of DYN3D and HEXNEM results with the reference:

VVER-1000 Benchmark	DYN3D Δk_{eff} = 62 pcm		HEXNEM Δk_{eff} = 14 pcm	
	Max. (%)	Av. (%)	Max. (%)	Av. (%)
Nodal powers	5.2	1.83	2.2	0.60
Assembly powers	3.0	1.53	0.8	0.33

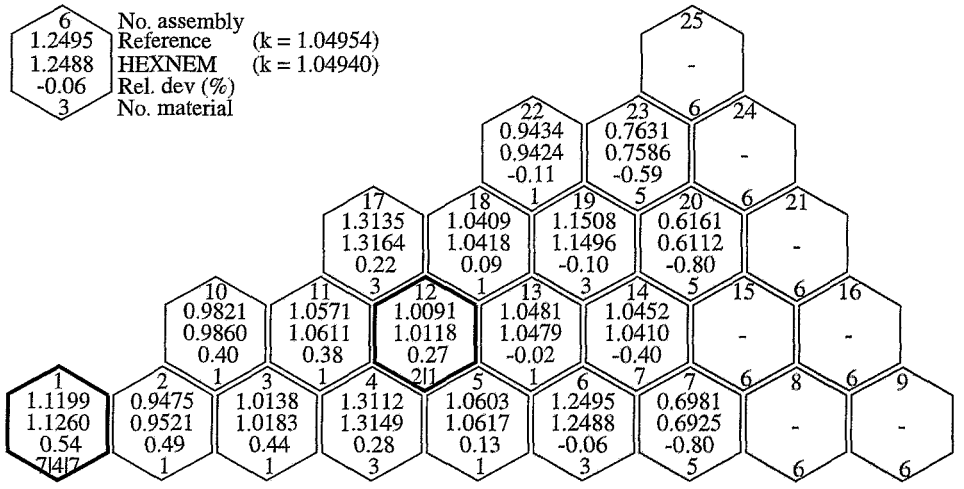

Fig. 5: Comparison of assembly powers for the VVER-1000 Benchmark

4. Conclusions

The new nodal method HEXNEM for hexagonal geometry which includes the corner point fluxes shows a better accuracy for problems with large fuel assembly pitch as in the VVER-1000 reactors. Considering the future implementation of the method into the code DYN3D the use of the corner point fluxes together with the average values on the sides of the hexagon gives the possibility to apply the flux reconstruction method of DYN3D presented in without additional reconstruction of corner fluxes. Concerning the further development of the method the assembly discontinuity factors (ADF) can be taken into account in a simple way. The energy group wise solution scheme combining polynomial expansion and exponential functions can be extended to a larger number of energy groups.

References

[1] U. Grundmann, U. Rohde (1989), DYN3D/M2 - a Code for Calculation of Reactivity Transients in Cores with Hexagonal Geometry, Proceedings of IAEA Technical Committee Meeting on Reactivity Initiated Accidents (pp. 257-302), Wien or Report FZR 93-01, Research Center Rossendorf (1993)

[2] Y. A. Chao and Y. A. Shatilla (1995), Conformal Mapping and Hexagonal Methods - II: Implementation in the ANC-H Code, Nucl. Sci. Engng., 121, 210

[3] U. Grundmann, F. Hollstein (1999), A Two-Dimensional Intranodal Flux Expansion Method for Hexagonal Geometry, accepted for publication in Nucl. Sci. Engng.

[4] Cs. Maraczy (1995), A Solution of Seidel's 3D Benchmark for VVER-440 with the DIF3D-FD Code, Proceedings of 5th Symposium of AER (pp. 287 - 296), KfKI Atomic Energy Research Institute Budapest

[5] N.P. Kolev, R. Lenain, C. Fedon-Magnaud (1997), Solutions of the AER 3D Benchmark for VVER-1000 by CRONOS, Proceedings of 7th Symposium of AER (pp. 650 - 665), KfKI Atomic Energy Research Institute Budapest.

IMPROVEMENT OF THE VERIFICATION OF COUPLED THERMOHYDRAULICS / NEUTRON KINETICS CODES: DYN3D-ATHLET TRANSIENT CALCULATIONS

Sören Kliem, Siegfried Mittag, Ulrich Rohde, André Seidel, Frank-Peter Weiß

1. Introduction

The main objective of the PHARE project SRR1/95 is the validation of coupled thermal-hydraulics - neutron kinetics codes, that are currently used for modelling the behaviour of the Russian pressurized water reactors VVER. Short descriptions of two transients, measured in the Loviisa-1 VVER-440 and the Balakovo-4 VVER-1000, respectively, have been presented in [1]. DYN3D burnup and steady-state calculations for the states before the transients and their comparison with measurements have also been described in [1]. The present report contains the main results of the simulation of both measured transients by the coupled code DYN3D-ATHLET [2].

Two different versions of coupling the three-dimensional core model DYN3D to the thermal-hydraulic system code ATHLET are available and have been used for the calculations. In the external coupling, the whole core model DYN3D (neutron kinetics, thermal-hydraulics, and fuel rod model) is coupled to ATHLET by interfaces at the core bottom and top. In the internal coupling, only the neutron kinetics of DYN3D is implemented into ATHLET.

2. Loviisa-1 VVER-440 transient

The transient was caused by the power drop of one of the two turbo-generators from nominal value down to house load level.

2.1 Boundary conditions

After transient initiation, the power was reduced by inserting the control rod group No. 6 [1]. On the basis of the documented measured control rod positions, a time table for the control rod positions was derived (fig. 1). A standard VVER-440/213 ATHLET input deck was adapted to the specific design conditions of the Loviisa-1 NPP [3]. For the calculation, the measured pressure in the main steam header (MSH) was used as a boundary condition. A

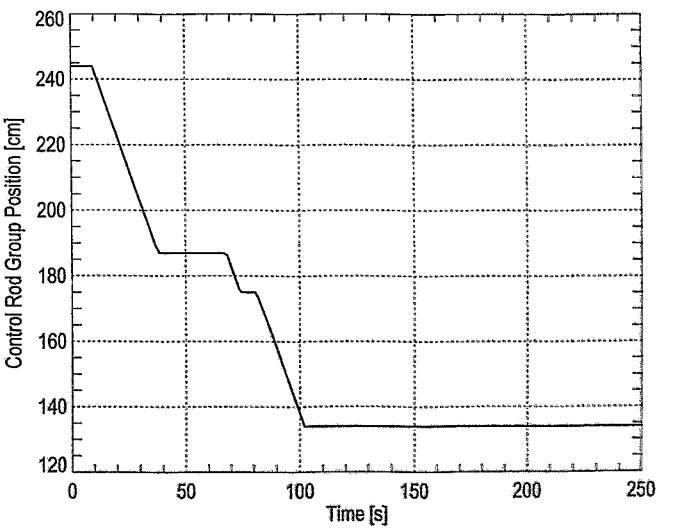

Fig. 1: Control rod group position

controller was introduced into the input deck, which regulates the calculated steam mass flow in a way that the pressure in the calculation follows the measured values (fig. 2). Further, the measured feed water mass flow rate was provided as a code input. The approach of fixed boundary conditions was chosen, because the main task of the project is the simulation of the physical behaviour of the reactor, especially of the core and the primary circuit. The simulation of the plant controllers is of secondary interest.

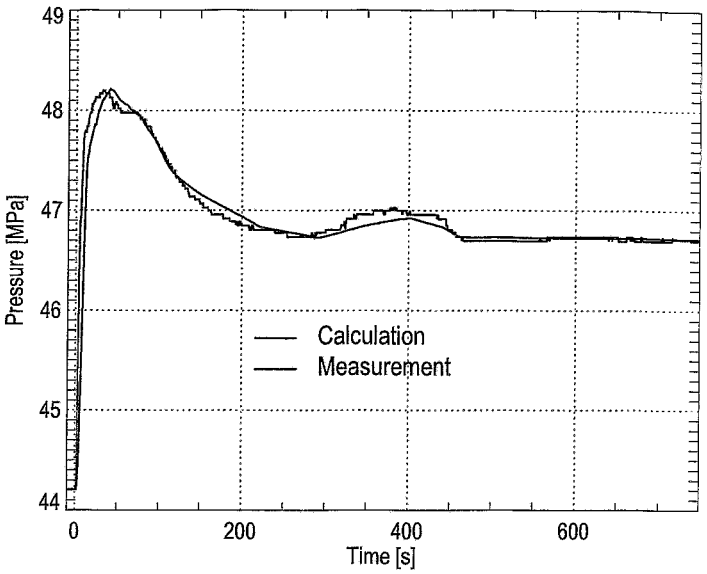

Fig. 2: Main steam header pressure

2.2 Comparison of the main parameters

The external coupling of DYN3D to ATHLET was applied to the calculation. During the transient, two main movements of the control rod group No. 6 are modelled, up to t = 38 s and from t = 70 s on. Between these two movements, the calculated power level is about 5 % lower than the measured one (fig. 3). This can be due to the control rod efficiency, to the measurement error of the neutron power at a reduced power level, or to uncertainties in the control rod position measurement. (The measurement information on rod positions allows only to determine a corridor with an upper and a lower boundary, between which the current control rod group must be located). The second insertion of the control rod group led to a power level reduction down to about 60 % of the nominal power. After this decrease, the power controller worked in the automatic regime, keeping the given power level constant. In the calculation, the power drops a bit deeper (to 57 %) at the end of the second movement. But due to the temperature feedback effects, the power rises up to 60 % (at about 200 s) and remains nearly constant until the end of the transient.

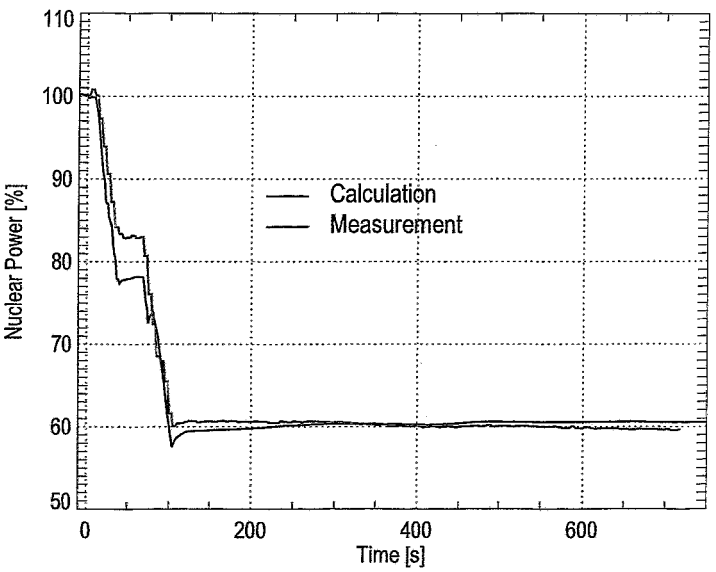

Fig. 3: Nuclear power

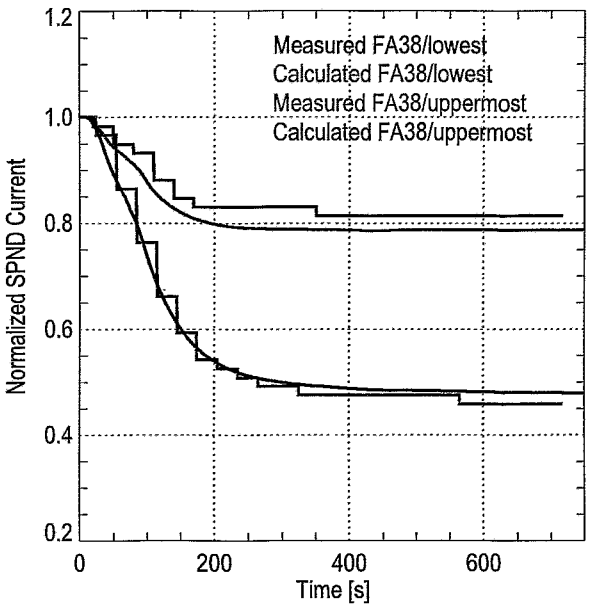

Fig. 4: Normalized SPND currents

Thermal neutron fluxes calculated by DYN3D were compared to the in-core self-powered neutron detector (SPND) currents, that have been measured during the transient. SPND detectors are located in four fuel assemblies in the 60-degree core symmetry sector, at the heights of 50, 100, 150 and 200 cm from the bottom of the core. An example of two measured and calculated SPND currents (assembly No.38, at the heights of 200 and 50cm), normalised to the values at the beginning of the transient, is presented in fig. 4. As the control rod group is inserted only to the middle of the core (see fig. 1), the neutron flux drops much deeper in the uppermost layer (200 cm) than in the layer near to the core bottom (50 cm). There is a good agreement between measured and simulated SPND signals. The deviation in the upper part of the core part is smaller than in the lower region. A similarly satisfying agreement has been reached at the positions of the other 14 SPNDs.

In Fig. 5, the calculated hot leg temperature is compared with the average of the temperatures measured in the six hot legs. During the transient, no significant asymmetrical effects are observed. The six measured values differ by 2.0 K and 1.6 K in the initial and final state, respectively, which is within the measurement accuracy. The calculated hot leg temperature shows a very good agreement with the curve of the averaged temperatures measured during the transient. The new stationary value is very close to the measured one.

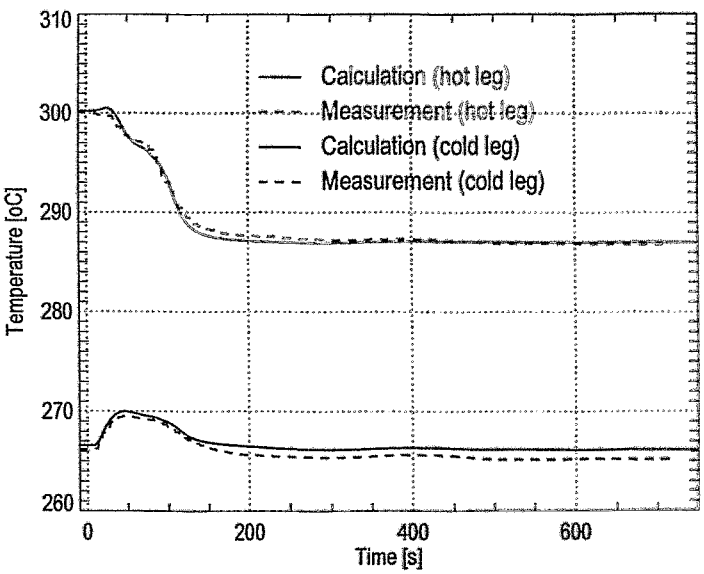

Fig. 5: Hot and cold leg temperatures

The cold leg temperature is determined by the hot leg temperature and the heat transfer to the secondary circuit. The initial and transient cold leg temperature shows a very good agreement between calculation and measurement (fig. 5). At the end of the transient, the calculated value is about 1 K higher. Again, this deviation is lower than the differences between the six measured cold leg temperatures.

The sensitivity of the dependence of the cold leg temperature on the secondary side pressure can be observed by comparing fig. 5 to fig. 2. A rising steam header pressure means an increasing saturation temperature, which leads to a decreasing heat transfer in the steam generator. The result is a rising cold leg temperature. Vice versa, a falling steam pressure causes a decrease in cold leg temperature. Obviously, there is also a strong correlation between hot and cold leg temperatures: although the steam pressure is higher in the final state (compared to the state before the transient), the cold leg temperature is somewhat lower, due to a decreased hot leg temperature that is caused by the power reduction.

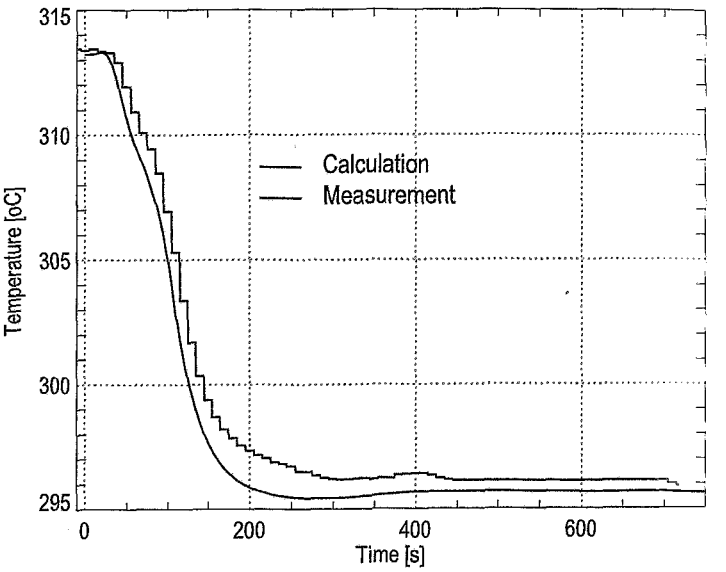

Fig. 6: Maximum fuel assembly outlet temperature

The maximum assembly outlet temperature in the calculation belongs to assembly No. 23. The comparison with the measured data is shown in fig. 6. There is almost total agreement at the beginning and during the transient. At the end, the measured temperature is slightly higher. This temperature is a local parameter that is mainly determined by the power distribution in the reactor core. At least in the stationary state before the transient, this temperature behaviour corresponds to the power in assembly 23 [1], where the measured power is slightly underestimated by DYN3D. Unfortunately, no transient SPND measurement data are available for this hottest assembly.

3. Balakovo-4 VVER-1000

The transient was initiated by the failure of one of the two working feed water pumps at nominal power.

3.1 Boundary conditions

Two seconds after the pump failure, the control rod group No. 1 was dropped into the core within four seconds. Group No. 10 was inserted at the operational speed of 2 cm/s [1]. A time table based on measured control rod positions was used as input for the neutronics calculation. A standard VVER-1000/320 ATHLET input deck was adapted to the specific conditions of the Balakovo NPP [5]. The measured pressure in the main steam header and the feed water mass flow [6] were applied as boundary conditions for the calculations.

3.2 Comparison of the main parameters

Both versions of coupling have been used in the calculations. The results for the nuclear power and primary circuit temperatures are compared to the measured values.

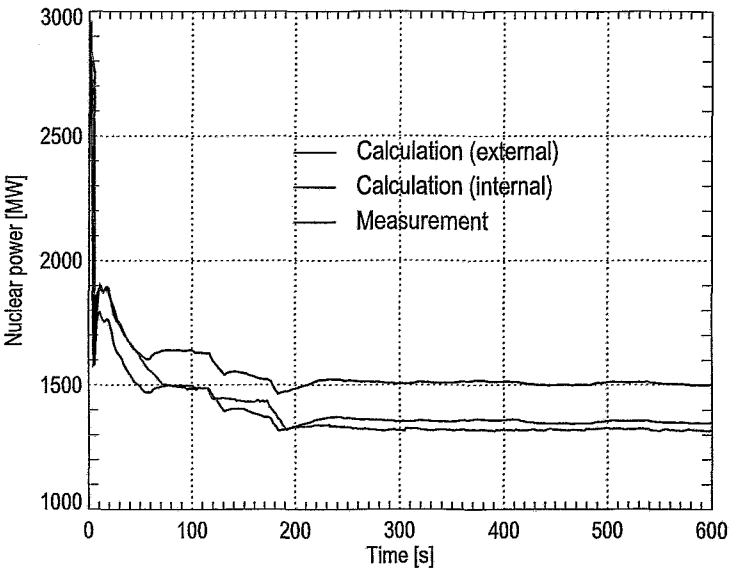

Fig. 7: Nuclear power

The sharp decrease of nuclear power, mainly caused by dropping control rod group 1, is well described by the calculations (fig.7). In the following, fuel and moderator temperature feedback effects lead to a power increase, which is better modelled by the internal-coupling version. The slow insertion of the control rod group 10 is the reason for further power level reduction. From t = 70 s on, the measured power is in good agreement with the results from the external-coupling calculation. At the end of the transient, the internal-coupling version overestimates the measurement by some 150 MW (10 %).

The deviation in the nuclear power, observed between the two coupling versions, is caused by the different treatment of the heat transfer in the gas gap between fuel pellets and fuel rod cladding. In the internal-coupling calculation, the heat transfer coefficient (HTC) is always kept constant, as the present ATHLET model does not allow to calculate the HTC. But in reality, the HTC decreases during the transient, because, due to fuel temperature reduction, the width of the gas gap increases. In the external coupling calculation however, this behaviour of the HTC is computed by the fuel rod model implemented in the DYN3D code. The worse heat transfer from fuel to cladding and coolant causes a fuel temperature that is higher than in the case of internal coupling. A higher fuel temperature increases the effect of the negative Doppler feedback, which leads to lower reactivity and lower power level.

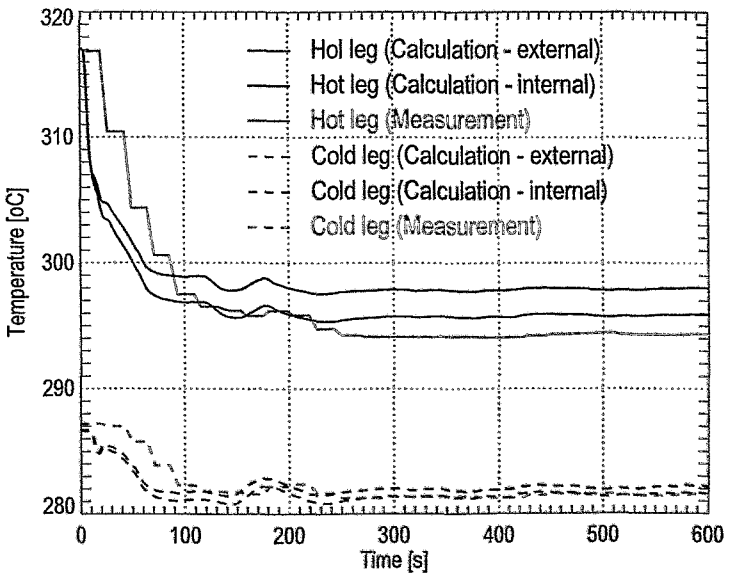

Fig. 8: Hot and cold leg temperature

The aforementioned power differences, are reflected in the primary circuit temperatures: a higher power leads to an increased hot leg temperature (cf. fig.8, end of the transient). For the comparison, the measured data from the hot legs and cold legs of the four loops were averaged, respectively. The temperature difference between the four hot and cold legs is not higher than 1.8 K and 1 K, respectively. In fig. 8, there is a time shift between calculated and measured temperature curves during the transient. This shift can be explained by a time delay in the thermocouple measurement, which (by contrast to the Loviisa-1 transient, fig. 5) has not been taken into account in the calculation, due to lack of information on the Balakovo-1 thermocouple properties.

4. Conclusions

Generally, a good agreement between calculated and measured thermal-hydraulic parameters has been achieved for both the VVER-440 and the VVER-1000 transient. The validation work carried out in the framework of the PHARE SRR1/95 project demonstrates that the coupled code DYN3D-ATHLET is capable of simulating real transients in both VVER reactor types. Both coupling versions produce acceptable results. Some deviations can be explained by uncertainties in the measurement parameters (control rod positions, differences in cold leg temperatures of different loops). The external coupling provides a more accurate modelling of the nuclear power transient behaviour, due to the more refined treatment of heat transfer in the DYN3D fuel rod model.

In the near future, the results calculated by the other coupled codes involved in the SRR1/95 project [1] will be compared to the measurements and to the DYN3D-ATHLET results.

References

[1] Sören Kliem, Siegfried Mittag, Ulrich Rohde, André Seidel, Frank-Peter Weiß (1998), CEC PHARE Project SRR1/95 - Improvement of the verification of coupled thermo-hydraulics / neutron kinetics codes: DYN3D burnup and steady state calculations, in F.-P. Weiß, U. Rindelhardt (Ed.), Institute of Safety Research - Annual report 1998, Rossendorf

[2] U. Grundmann, D. Lucas, S. Mittag and U. Rohde (1995), Weiterentwicklung und Verifikation eines dreidimensionalen Kernmodells für Reaktoren vom Typ WWER und seine Ankopplung an den Sörfallanalysecode ATHLET, Rossendorf, Report FZR-84

[3] K.-D. Schmidt (1998), Preparation of an ATHLET input data set of VVER- 440/213 for the Loviisa-NPP, Garching, Technical Report GRS/SRR/195/R7.1A

[4] H. Kantee (1998), Drop of one turbine to house load level experiment on Loviisa-1 NPP, Loviisa, Technical Report IVO/SRR/195/LOV1.1

[5] W. Luther (1998), Preparation of an ATHLET data set of VVER-1000, Balakovo NPP, unit 4 for the calculation of the experiment - turn off 1 MFW- pump, Garching, Technical Report, GRS/SRR195/REV1.0

[6] S. Danilin (1998), Experimental data of the transient caused by the turning off one feed water pump from working two (VVER-1000, Balakovo NPP, Unit 4), Moscow, Technical Report KI/SRR195/ED2.0

PLUME AND FINGER REGIMES DRIVEN BY AN EXOTHERMIC INTERFACIAL REACTION

Alexander Grahn and Kerstin Eckert[1]

1. Introduction

Studies of convection in fluids, like Rayleigh-Bénard- [1] or Bénard-Marangoni convection [2] have strongly influenced our understanding of pattern formation and turbulence. In these systems energy is supplied by an external temperature difference applied across a given vertical length scale. However, this situation is not representative for a variety of systems occurring in nature. Here, the dynamics is driven by internal sources of energy and the selected length scale is a part of the solution of the problem. The study of such systems is interesting from both a fundamental point of view and with respect to potential applications of basic research. Promising candidates for such studies are systems involving chemical reactions. Consumption of educts and the release of reaction enthalpy are sources of solutal and thermal gradients. Hydrodynamic instabilities, driven by these gradients, can drastically alter the chemical reaction rate [3]. We demonstrate that a rather simple interfacial neutralization reaction can develop an unexpected coupling of different hydrodynamic instabilities (for details we refer to [4]).

2. Experimental set-up and chemistry

The experiments were performed in a two-layer system, placed in a Hele-Shaw-cell (Fig. 1). The gap width was $d = 0.1$ cm. Visualization of the patterns was done by means of a shadowgraph technique. The two-layer-system inside the cell consisted of a lower aqueous layer (water and base) and an upper organic layer (isobutyl-alcohol and carboxylic acid). The viscosity of the organic solvent is four times higher than that of water. Since water and isobutyl-alcohol have a certain solubility (12 % at $T = 25$ °C) saturated solutions were prepared before filling. Saturation was to prevent interfacial turbulence arising from counterdiffusion of the solvents into each other. The respective densities are 0.987 g/cm^3 (upper layer) and 1.016 g/cm^3 (lower layer, including the base concentration). The density of both phases increases with increasing acid concentration. While the concentration of the base B in the water was fixed to $c_B = 1$ mol/l, different concentrations c_{HA} of the acids have been used ($c_{HA} = 0.04$ to 0.08 g/l or equivalently 0.5 to 2 mol/l).

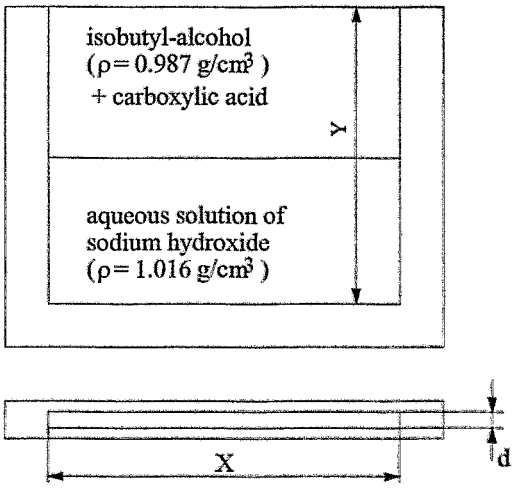

Fig. 1: The two-layer system in the Hele-Shaw cell. The given densities refer to the saturated phases.

[1] Institute for Thermofluid Dynamics, TU Dresden, Germany

The basic reaction is the neutralization of carboxylic acid by a base, sodium hydroxide, close to the interface. Precondition of this reaction is the dissociation of both species, i.e.,

$$HA + H_2O \rightarrow A^- + H_3O^+ \quad (1)$$

$$B + H_2O \rightarrow H^+ + OH^-. \quad (2)$$

sodium hydroxide as a strong base is completely dissociated, the dissociation degree of the weak organic acids is smaller than 1 %. If a hydronium ion H_3O^+, formed by dissociation, encounters a OH^- ion, neutralization takes place, i.e.,

$$H_3O^+ + OH^- \rightarrow 2\,H_2O. \quad (3)$$

The enthalpy released by this reaction amounts to -57 kJ/mol.

3. Observations

The system displays three basic regimes (Fig. 2). The initial one (Fig. 2a) is dominated by rising *plumes* in the upper organic layer. The plumes are emitted from an unstable boundary layer (b.l.) above the interface. We assume that they consist of warmer fluid with lower acid concentration. The intensity of the plume regime is most distinct in the formic-acid system and decreases with increasing chain length. The duration is of the order of minutes.

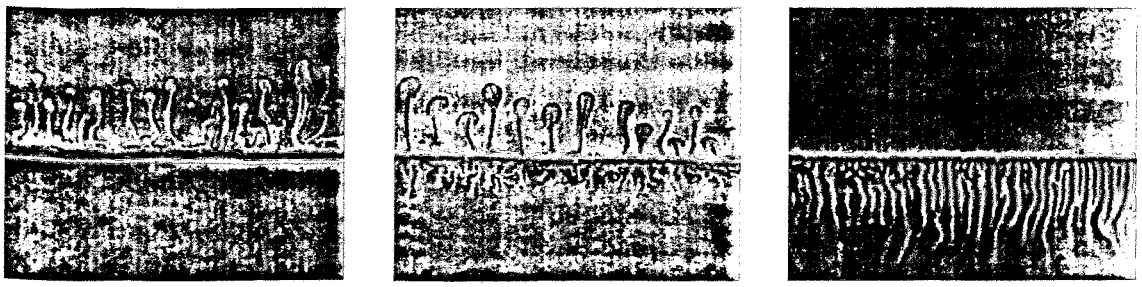

(a) (b) (c)

Fig. 2: The three basic regimes. (a) Rising plumes, (b) plumes and irregular fingers, (c): nearly regular fingers in the lower.

The intermediate regime (Fig. 2b) is characterized by plumes in the upper layer and by an irregular formation of fingers in the lower layer. The onset of the fingers starts the earlier the longer the acid chain length is. The duration of this second regime is of the order of 1 hour. In its course the upper layer plume regime becomes increasingly disorderd till it fades away.

In the final regime (Fig. 2c) the system displays an array of regularly spaced *fingers*. In the fingers warmer fluid, rich in acid/acetate ions, moves downwards. In between the fingers colder fluid, which should have a higher hydroxide concentration, moves in the opposite direction towards the interface. This is a double diffusive instability arising from the different diffusivities of heat and mass. Since heat diffuses 100 times faster than mass, the convective motion is driven by the horizontal concentration difference between the rising and falling fluid columns. Next we analyse the upper-layer motions by studying the advancing of the Plumes with time (Fig. 3). This is done by tracing the head positions of the plumes in the

digitized shadowgraph images and averaging over the plume ensemble. Usually approx. 10 plumes are taken into account. We find that the velocity of the upper layer plume ensemble decreases with increasing chain length of the carboxylic acid.

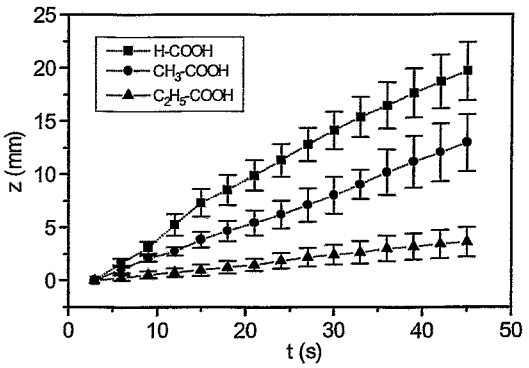

Fig. 3: Advancing of the plume ensemble with time for three diffusing acids.

To determine the wavenumber as the characteristic horizontal length scale of the finger structure we apply the one-dimensional Fourier transformation to lines parallel to the interface. The corresponding power spectra are shown in Fig. 4. At equal molar concentrations all three systems display nearly the same wave numbers k. After 90 min we find $k = (3.9 \pm 0.3)$ mm^{-1}. We could not detect a significant dependence on the gap width (0.5, 1.0 and 2.0 mm).

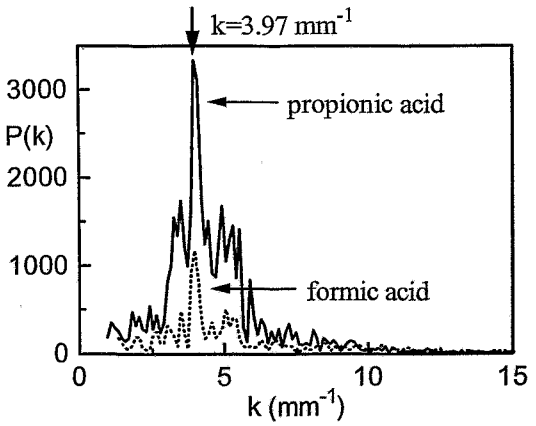

Fig. 4: One-dimensional power spectra of the fingers, C_{HA}=1 mol/l. For the sake of clarity the acetic-acid system has been omitted.

4. Discussion

The engine of the dynamics is the diffusion of acid from the upper into the lower layer. The acid diffusion leads to an unstable density stratification at both sides of the interface since heavier fluid lies above lighter fluid. Convection in the form of plumes, emitted from the concentration boundary layer, sets in (Fig. 1a). The neutralization reaction provides a local heating and an additional decrease of the density of regions close to the interface. Consequently, the effective Rayleigh number, governing the stability of the boundary layer of the upper phase, is higher. Solutal plumes move faster due to additional thermal buoyancy in the systems with reactive mass transfer.

However, the temperature gradient has a stabilizing effect on the boundary layer below the interface. The destabilizing concentration gradient is superimposed by the stabilizing temperature gradient. This configuration leads to double-diffusive instability which is known from thermohaline convection in oceans, responsible for the exchange of salt and heat between surface and deeper water layers. The nature manages both effects by switching to the finger instability to provide a very efficient mixing. Both plume and finger instability are responsible for the self-sustained dynamics observed in the experiment for more than 2 hours. We expect that numerous interfacial reactions are accompanied by the formation of fingers and plumes. Since both instabilities lead to an efficient mixing they can strongly accelerate diffusion-controlled interfacial reactions. Thus, the understanding of the hydrodynamics offers a possibility to control this reaction type.

5. References

[1] M. C. Cross and P. C. Hohenberg (1993), Pattern formation outside equilibrium, Rev. Mod. Phys. 65, 851-1112

[2] K. Eckert, M. Bestehorn and A. Thess (1998), Square cells in surface tension driven Bénard convection: experiment and theory, J. Fluid Mech. 356, 155-197

[3] T. S. Sherwood and J. C. Wei (1957), Interfacial Phenomena in Liquid Extraction, Ind. Eng. Chem. 49, 1030-1034

[4] K. Eckert and A. Grahn (1999), Plume and Finger Regimes Driven by an Exothermic Interfacial Reaction, Phys. Rev. Lett. 82, 4436-4439

SchaumPET – A SETUP FOR POSITRON EMISSION TOMOGRAPHY (PET) INVESTIGATION OF FOAM IN A BUBBLE COLUMN

Frank Hensel and Horst-Michael Prasser

1. Introduction

The paper describes the current status of a Positron Emission Tomograph dedicated to the investigation of the behavior of foam in a bubble column. It is planned to use the device for studying foam generation, foam stability and transport phenomena in the liquid phase.

In earlier work, the importance of turbulent contributions to the dispersion of a tracer in a bubbly flow was investigated (Hensel, [1]). In this paper, the coefficients of dispersion were determined for a flow in a narrow rectangular tank. The bubble flow was generated either by injecting air or by a catalytic decomposition of hydrogen peroxide at a platinum coated rod in the bottom of the tank. Sodium fluoride solution enriched with ^{18}F was used as tracer and added into the liquid phase in the beginning of the experiment. The annihilation radiation was registered by a double-head PET detector array. Turbulent dispersion coefficients were obtained by evaluating the spreading of the tracer cloud in the bubble flow. Using the commercial CFD code CFX-4, a numerical simulation of the experimental setup was carried out (Hensel and Rohde, [2]).

In the present work, a dedicated detector system optimized for the instrumentation of a cylindrical bubble column is developed. The main part of the equipment, like scintillator crystals, photo multipliers, pre-amplifiers and power supplies were taken from the decommissioned medical tomograph POSITOME 3p, which was in use in the Institute of Bioinorganic and Radiopharmaceutical Chemistry for some years.

2. Objectives

Positron Emission Tomography is an imaging technique originating from nuclear medicine. It is mainly applied as an in vivo non invasive tool by which metabolic activities can be investigated. The typical PET positron emitters like ^{11}C, ^{13}N, ^{15}O and ^{18}F can substitute naturally occurring isotopes in a wide range of organic compounds. Two γ-quanta originate from the annihilation of the positrons departing in back-to-back direction from the point of annihilation, which is for the most applications close to the place of the positron emission (Fig. 1). The coincident arrival of the two γ-quanta at the detector system is used to indicate the event line, i.e. the positron emission is assumed to have happened at the connecting line of those two detectors, which registered a γ-quantum simultaneously.

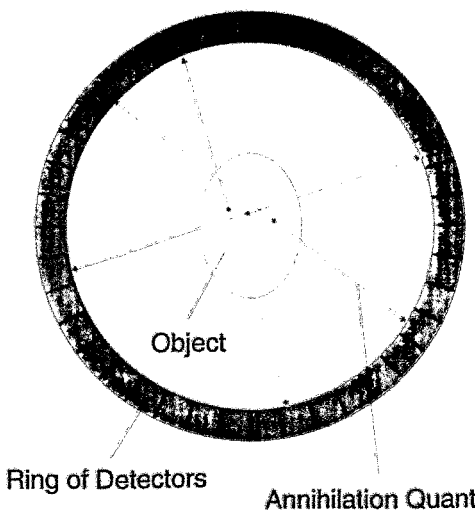

Fig. 1: Principle of coincidence detection in Positron Emission Tomography

For the calculation of the activity distribution inside the measuring volume, tomographic image reconstruction methods are used.

Besides medical imaging, industrial and engineering applications are known, including the investigation of chemical processes like catalysis (Jonkers et al., [3]) and flow monitoring in an oil reservoir rock (van den Bergen et al. [4]).

The results of earlier work have shown that PET is an appropriate technique for investigating transport phenomena in liquid-gaseous two-phase flows. Therefore it was decided, to develop and construct a PET detector system for a bubble column. It is planned to use the tomograph for the investigation of transport processes in bubble flow and especially in the foam layer forming at the top.

3. Construction of the detector system

In order to visualize the transient transport process in the column in three dimensions, the detector system consists of eight detector rings, which are stacked above each other with an axial distance of 50 mm. Each ring contains 16 BGO (bismuth germanate) scintillator crystals with a rectangular front surface of 18 x 30 mm. The crystals are 30 mm thick, which provides an intrinsic efficiency for the detection of the 511 keV annihilation radiation of about 93 %.

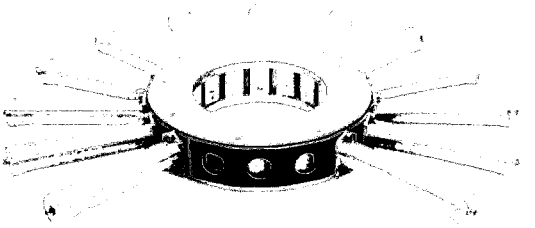

Fig. 2: Partially assembled detector ring with crystal container and photomultipliers

The crystals are placed into a light-tight container ring. The photomultipliers are connected to the back surface of the crystals. For a good optical contact a special optical grease is used. Fig. 2 shows this housing without the inner aluminum ring, which protects the front faces of the crystals from extraneous light (see Fig 3).

The ring is mounted on a cylindrical base plate, together with the pre-amplifiers (Fig. 3). In the final assembly, eight rings are stacked above each other. The opening in the center of the base plates accommodates the bubble column or other measuring objects. The minimum axial distance between the detector planes is 50 mm. It can be increased by additional spacers. In the standard configuration, the control volume is therefore 400 mm high and the maximum diameter of the measuring object is 120 mm. For radiation protection, the construction will be completed

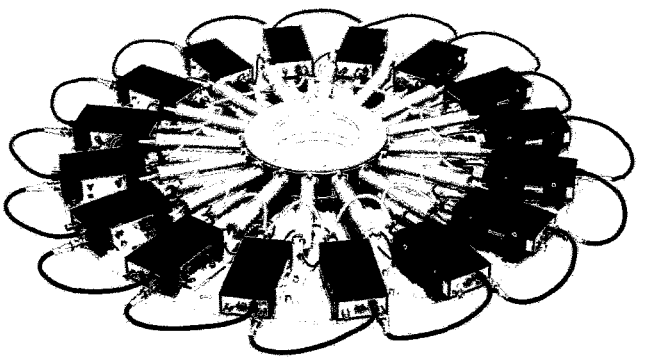

Fig. 3: Base plate with detector ring, photomultipliers, pre-amplifiers and power supply wires

by lead bricks and other absorbing elements. A simplified sketch of the detector assembly is shown in Fig. 4.

4. Signal acquisition

After amplifying, the signals undergo an energy discrimination to suppress scattered γ-quanta. In the first step, the 16 detectors of each ring will be connected to individual coincidence logic circuits, i.e. the 3D tomogram will be constructed from 16 individual 2D reconstructions. In the future it is planned to create a unified coincidence block for all 128 detectors in order to allow a real 3D tomography. This will also allow to increase the resolution in axial direction, because intermediate layers between neighboring detector planes can be involved into the image reconstruction.

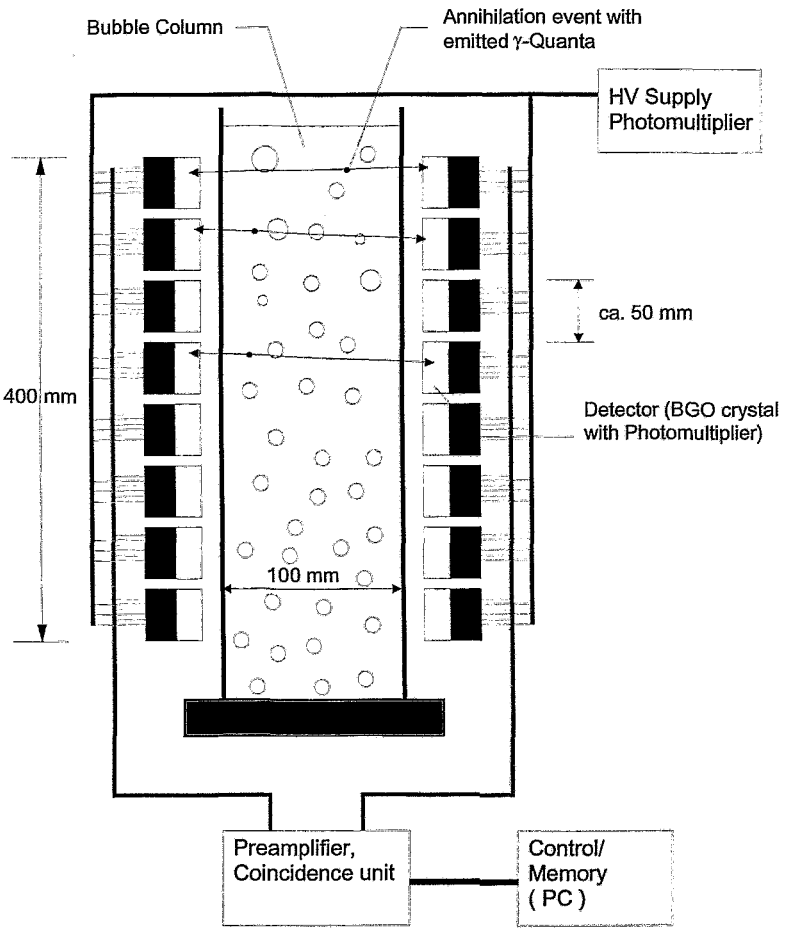

Fig. 4: Sketched overview of the setup of SchaumPET

5. Experimental capabilities

At first, it is planned to repeat the experiments on turbulent mixing of a tracer in the liquid of the two-phase flow [1, 2]. For this purpose, the bubble column will be aerated from a sparger in the bottom . An aqueous solution of $Na^{18}F$ will be injected into the center of the control volume. We assume that the detector system will allow to achieve a measuring rate of better than 1/s, so that it should be possible to measure the spreading of the tracer and to quantify the turbulent dispersion coefficient.

A great advantage of PET is, that for the investigation of foam, the surface active compound can be labeled. Here, wet unstable foams are of special interest, because they often lead to unwanted conditions for the operation of chemical reactors. For example in [5, 6], the influence of different aliphatic alcohols on the emergency depressurization of a batch reactor was studied. For this reason, we plan to label alcohols like propanol, butanol or pentanol with ^{11}C. In the same context, the carbon acids with 4-8 carbon atoms are also of interest [7]. In principle, it is possible to label more complicated compounds, such as industrial surfactants, but this requires special development efforts concerning the synthesis methods. When the surface active compound is equally distributed in the liquid at the beginning of the gas supply, the dynamics of the enrichment process in the top of the column can be studied. It is also possible to

irrigate the foam layer either with the clear solvent or with the bulk solution to study the processes during foam destruction.

Moreover, the device can be used for any other experiment, where the apparatus fits into the control volume of the tomograph (e.g. extraction columns, migration of pollutant in the soil, loading of ion exchangers, adsorption on catalyst or filter packages). It is also possible to label gases, like $^{11}CO_2$, ^{11}CO or $S^{18}F_6$.

6. Conclusions

A 3D PET tomograph for bubble columns and foam studies is under development. In the present stage, the construction of the detector assembly is finished. The pre-amplifiers are being optimised, particularly concerning the slew rates, and the coincidence logic is in the phase of design. The application for a license according to German radiation protection rules is in preparation. The device will be operated in one of the active laboratories of the nuclear chemistry building of the FZR. We expect the first experiments (with $Na^{18}F$ labelled liquid) in autumn 1999.

7. References

[1] Hensel, F. (1997), Studies of liquid-gaseous two-phase systems by positron emitting radiotracers, Appl. Radiat. Isot. 48 (10-12), 1485.

[2] Hensel, F. and Rohde, U. (1998), Measurement and Simulation of the turbulent Dispersion of a radioactive Tracer in a two-phase flow System. In: Rahman, M. et al.: Advances in Fluid Mechanics II. Conference AFM98, Udine 1998, Paper book, ISBN 185312589X, 283-292.

[3] Jonkers G. et al. (1992), Surface catalysis studied by in situ positron emission. Nature 63, 355

[4] van den Bergen E.A. et al. (1989), Industrial Applications of positron emission computed tomography. Nucl.Geophys. 3, 407

[5] D. Lucas, H.-M. Prasser, T. Kern: Die thermische Zersetzung von Wasserstoffperoxid als Modellreaktion für die Druckentlastung, 4. Fachtagung Anlagen-, Arbeits- und Umweltsicherheit, Köthen, 5./6. November 1998, Preprints P9

[6] D. Lucas: Brick – A 1-D Tool for Transient Multiphase Vessel Flow Simulations based on a new Particle Method, 2nd intern. symposium „Two-Phase Flow Modelling and Experimentation", Pisa, 23-26 May 1999, proceedings vol. 3, pp. 1657-1664.

[7] Malysa K., Miller R., Lunkenheimer K.: Relationship between foam stability and surface elasticity forces: fatty acid solutions, Colloids and Surfaces. 53 (1991) 47-62

This work is funded by the Deutsche Forschungsgemeinschaft, contract Pr 488/5-1

CALORIMETRIC INVESTIGATION OF THE FORMATION OF GRIGNARD REAGENTS

Günther Hessel, Günther Hulzer[1], Holger Kryk, Peter Palitzsch[1], Wilfried Schmitt, Nurelegne Tefera, Frank-Peter Weiss

1. Introduction

In the fine-chemical and pharmaceutical industry, Grignard reagents are of enormous importance as an initial stage of numerous organic syntheses. Due to the spontaneous heat release during the initiation of this strongly exothermic reaction, Grignard reactions dispose of considerable harzard potentials. Therefore, the knowledge of thermodynamic and thermokinetic parameters is one of the prerequisites for safe formation of Grignard reagents in production plants. In literature, measurement values of the molar reaction enthalpy have only been known for a few Grignard compounds. Up to now the calorimetric investigation of Grignard reactions has been carried out at reflux conditions to control the spontaneous heat release by means of hot cooling (cooling by evaporation). However, calorimetric measurements under reflux conditions are connected with a higher error (about ± 30%) than in closed systems (about ± 10%) due to additional heat losses and the evaluation of the heat of reflux. To obtain more accurate results, these studies on the formation of Grignard reagents were carried out in a closed reaction calorimeter for the first time.

2. Preparation of Grignard reagents

Reactions between organic halides and solid magnesium are the most common method to prepare Grignard reagents. As a model reaction, the direct reaction between the bromobenzene derivative and solid magnesium was studied. The brutto reaction equation can be written as follows

$$\underset{\text{bromobenzene derivative}}{R-Br} + \underset{\text{magnesium}}{Mg(s)} \xrightarrow{THF} \underset{\text{organomagnesium bromide}}{R-Mg-Br} \qquad (1)$$

To initiate the formation of Grignard reagents, the organometallic compound (R-Br) has to be solvated by the tetrahydrofurane solvent (THF). Additionally, active centres (radicals) have to be formed on the magnesium surface. When forming the Grignard reagent (R-Mg-Br), the magnesium radical is inserted between the rest of the organic molecule (R) and the bromine (Br). After an induction time, the Grignard reaction seems to go autocatalytically. That means when a critical amount of the Grignard reagent was formed, new active centres are exposed and subsequently the rate of reaction increases exponentially. The runaway reaction is only stopped when one reactant is consumed. Since Grignard reactions are highly exothermic, a thermal explosion could occur if a large amount of organic halides was added during a long induction time. The reasons for non-reproducible and long induction times or even uninitiated Grignard reactions could be:

[1] Arzneimittelwerk Dresden GmbH (AWD)

- trace amounts from water, oxygen or alcohol which immediately react with the Grignard reagent or with magnesium to form insoluble hydroxide or alkoxide salts that coat the surface of the metal
- magnesium with an oxide film which must be penetrated for reaction with the organic halide.

For safety reasons an experiment should be terminated if the maximum permitted amount from the organic halide did not initiate the Grignard reaction.

3. Performance of calorimetric measurements

The studies were carried out in the RC1 reaction calorimeter equipped with the pressure vessel HP60 and an anchor stirrer. For on-line concentration measurements the Fourier-Transform-Infrared (FTIR)-spectrometer ReactIR 1000 was used (Fig.1). To improve the accuracy of the calorimetric measurements, the experiment was divided into two stages:

- initiation reaction at the boiling point of the THF solvent
- main reaction at the isothermic reaction temperature

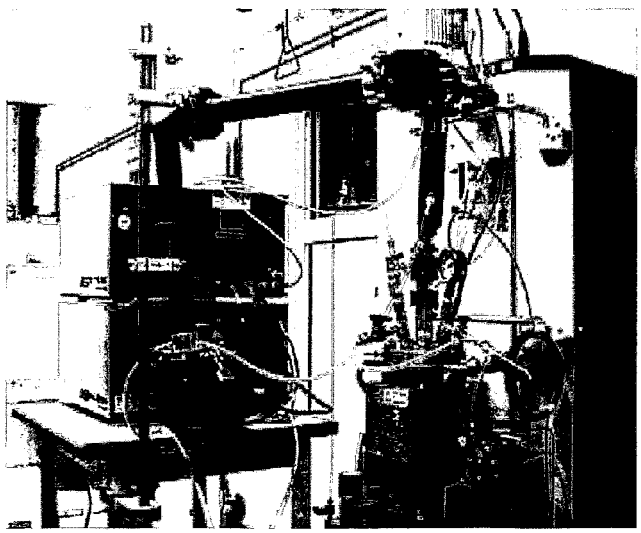

Fig. 1: RC1 reaction calorimeter with FTIR-spectrometer

First, the total amounts of magnesium shavings and anhydrous THF solvent were added into the reactor under agitation (1000 rpm) and degassed with nitrogen. To initiate the Grignard reaction, the mixture has to be heated up to 70°C. When this temperature was kept constant, part of bromobenzene derivate was added gradually up to initiating the formation of the Grignard reagents (see Fig. 2). After this initiation process the reaction mixture was cooled down to the desired temperature of the main reaction. To determine the heat of reaction and kinetic parameters, the stage of the main reaction was performed under isothermal conditions (see Fig. 3).

4. Results and discussion

The formation of the Grignard reagent was studied with respect to the initiation behaviour, the heat of reaction and kinetic parameters. In Fig. 2, the initiation is depicted for the used semi-batch process. This initiation process can be characterised by the so-called induction time (t_{ind}), the period of initiation (t_{ini}) and the released heat of reaction (Q_r). The induction time is defined by the duration of dosing up to initiating the Grignard formation, while the period of initiation corresponds to the duration of heat production. Well-reproducible induction times were obtained when the pure bromobenzene derivative was added with a constant rate of dosing into the reactor containing the total amount of magnesium and tetrafurane at 70°C and a stirrer speed of 1000 rpm. The initiation of the Grignard reaction can be recognised both by

the decreasing concentration of the bromobenzene derivative and by the increasing concentration of the Grignard reagent shown in Fig. 2.

Some seconds later the heat release rate also increases gradually and then after about 4 minutes it rises steeply. The rapid rise in the heat release rate and in the concentration of the Grignard reagent can also be detected by a steep increase in pressure because a closed reactor vessel was used for the calorimetric measurements. Depending on the accumulated amount of bromobenzene derivative and on the power of the jacket cooling, the period of initiation will last over about 10 minutes.

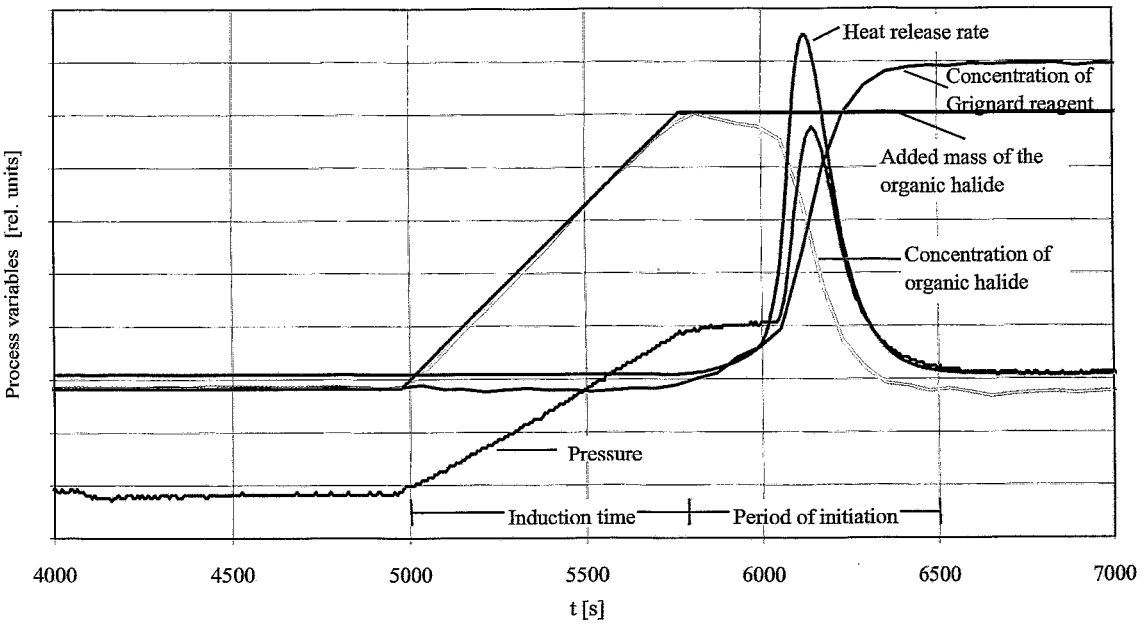

Fig. 2: Profiles of process variables during the initiation of the Grignard reaction at 70°C.

To determine the molar reaction enthalpy and kinetic parameters, the stage of the main Grignard reaction was carried out in semibatch operation under isothermal conditions. Figures 3 shows profiles of several selected process variables during the isothermal period. By gradually adding the bromobenzene derivative, the heat release rate could almost be kept constant. As shown by the profile of concentration of the bromobenzene derivative, an accumulation of the reactant was prevented. The increase in pressure mainly resulted from the increasing filling volume. The measured heat of reaction Q_r and the molar reaction enthalpy ΔH_r are listed in Tab. 1 at different isothermal reaction temperatures. An influence of the reactor temperature on the heat release rate was not stated in the range from 40 °C to 70 °C as shown in Fig. 4.

As a result of the calorimetric measurements, a mean molar reaction enthalpy per mole bromobenzene derivative was determined:

$$\Delta H_r = (270 \pm 6)\, kJ/mol \quad .$$

To model the Grignard reaction kinetics of the main reaction stage, the above experiments were adopted. This shows that the main reaction stage is only controlled by the dosing rate of the bromobenzene derivative.

Table 1: Heat of reaction and molar reaction enthalpy of the Grignard reaction for different reactor temperatures

Experiment	Tr [°C]	N_{BBD} [1)] [mol]	Qr [kJ]	ΔHr [kJ/mol]	$\overline{\Delta H_r}$ [kJ/mol]
BA14	40	0,4332	117,9	272,2	
BA15	40	0,4332	115,8	267,3	
BA16	40	0,4332	118,0	272,5	270,7
BA17	50	0,4332	115,1	265,6	265,6
BA11	60	0,4332	120,0	277,1	
BA12	60	0,2513	68,6	272,9	
BA13	60	0,4332	118,7	274,0	274,7
BA7	70	0,4813	128,4	266,9	
BA9	70	0,4332	115,5	266,5	
BA10	70	0,4332	117,9	272,2	268,5

[1)] Mole of bromobenzene derivative

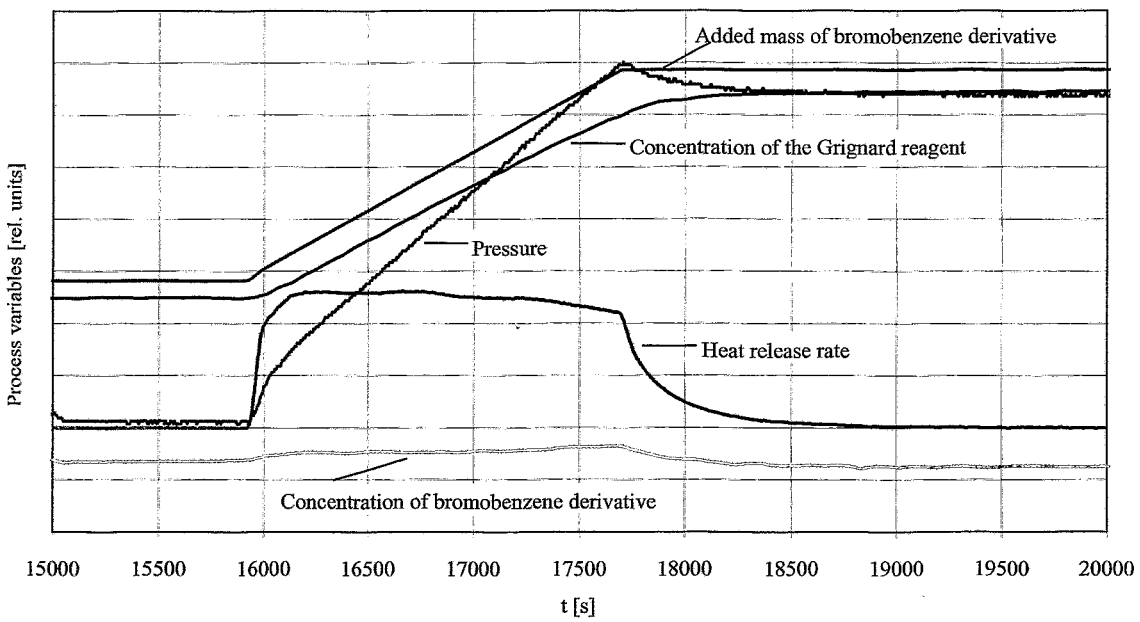

Fig. 3: Profiles of process variables during the main Grignard reaction under isothermal conditions

Therefore, the following rate equation for this type of reaction can be assumed:

$$r = k\,[R-Br]^{\alpha}\,[Mg]^{\beta}$$

For modelling this process, the experiment was conducted in a quasi batch mode (Fig. 5). From these experiments the following model parameters were determined using the Batch-CAD program RATE (Tab. 2).

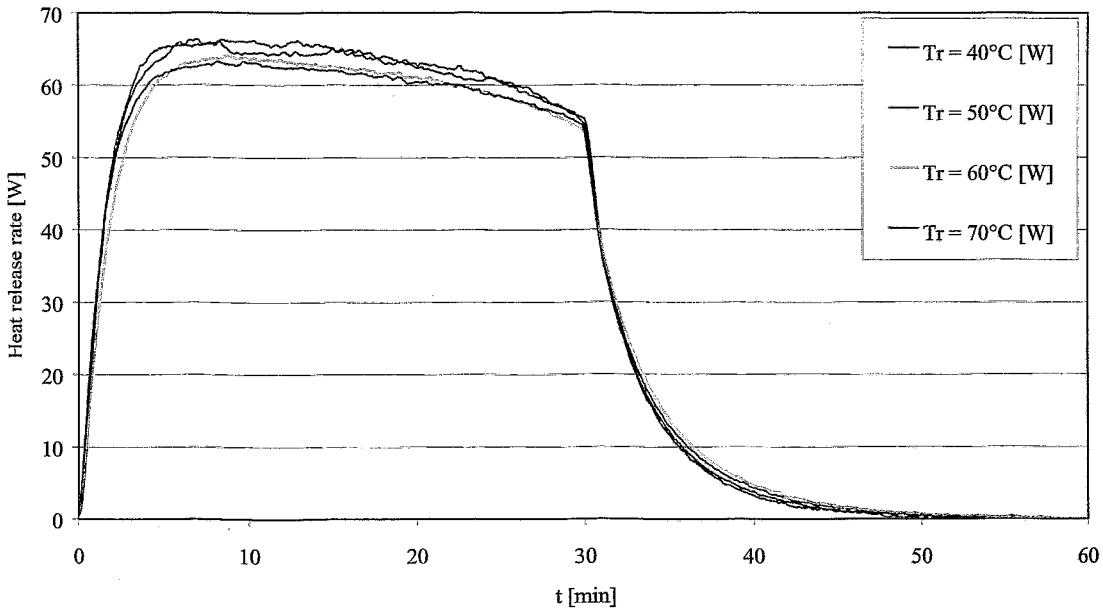

Fig. 4: Influence of the reactor temperature on the heat release rate during the main reaction.

Table 2: Grignard reaction of the bromobenzene derivative with Mg at 40°C.

Reaction stage	k [l/mol s]	k / [Mg]
2	$1.5720 \cdot 10^{-2}$	$1.5542 \cdot 10^{-2}$
3	$1.2557 \cdot 10^{-2}$	$1.9348 \cdot 10^{-2}$
4	$0.9092 \cdot 10^{-2}$	$2.1678 \cdot 10^{-2}$
5	$0.6472 \cdot 10^{-2}$	$2.3670 \cdot 10^{-2}$

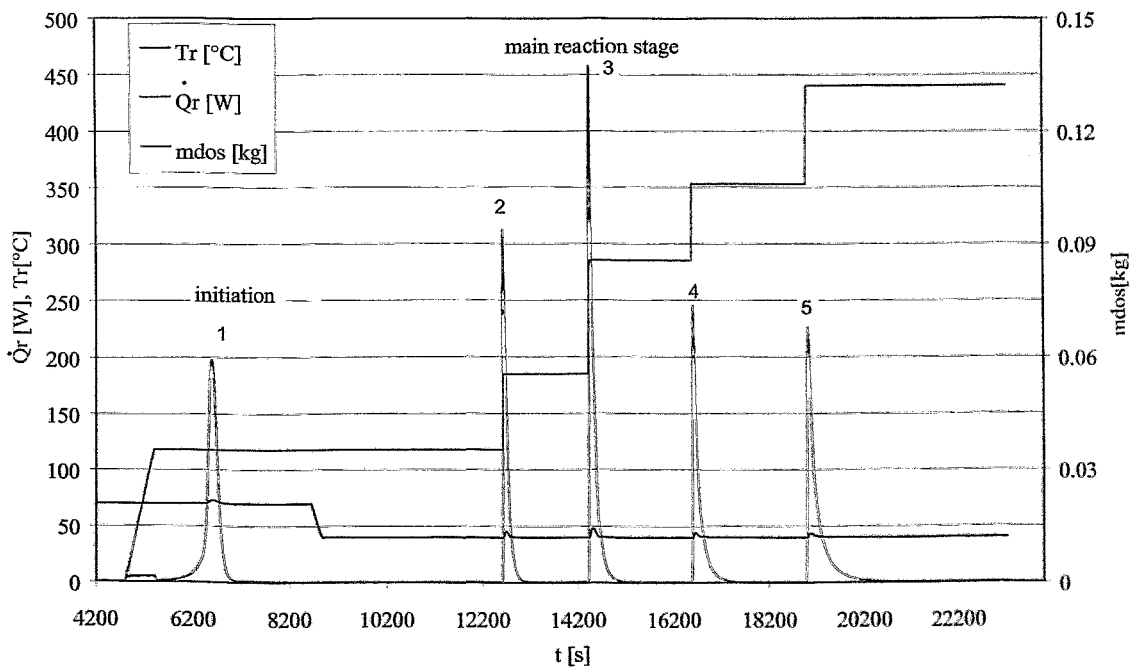

Fig. 5: Grignard reaction in the quasi batch mode

Figure 6 compares the model and experimental results for the second reaction stage. There is a good agreement between model and experiment for the first three main reaction stages. So, the reaction is of the first order $\alpha = 1$ in the concentration of the bromobenzene derivative and of zero order $\beta = 0$ in the concentration of Mg. When the concentration of Mg decreases (stage 5), the rate of reaction depends on the concentration of Mg. The reaction order is then found to be $\beta = 0.5$. Further investigation is necessary to study the influence of temperature on the rate of reaction during the quasi batch regime.

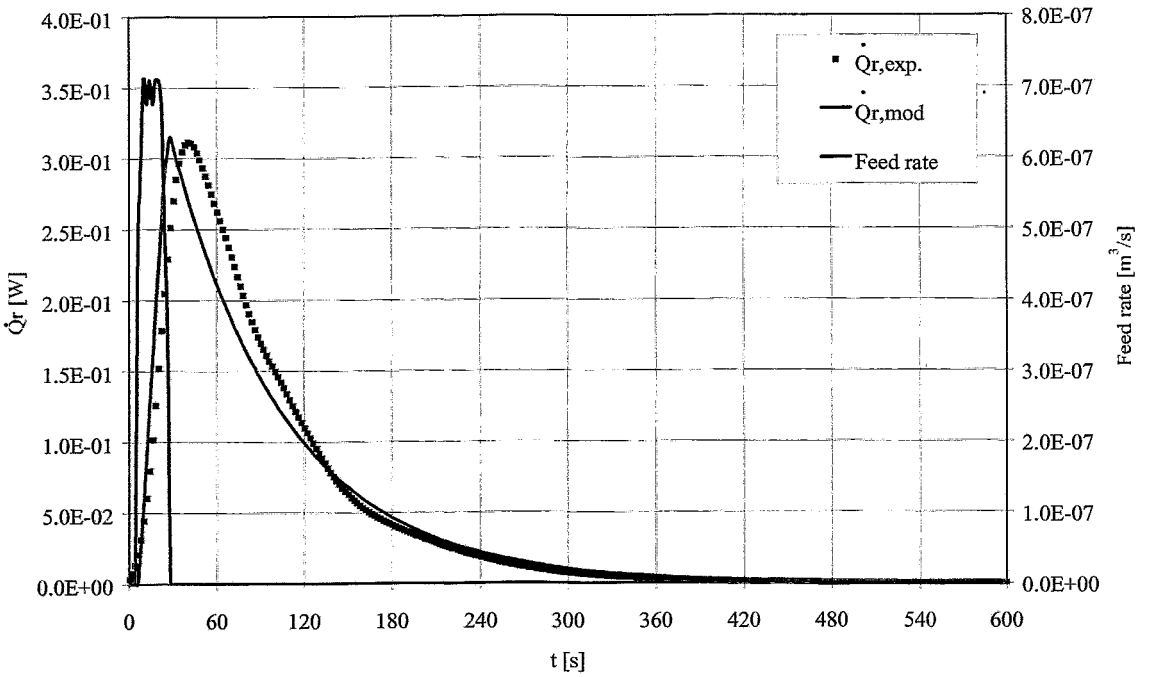

Fig. 6: Comparison between model and experiment results (stage 2).

5. Conclusions

A novel technique was applied to determine of the thermodynamic and kinetic parameters of Grignard reactions. Instead of operating under reflux conditions which are commonly used to control the spontaneous strongly exothermic initiation of Grignard reactions, the calorimetric measurement was carried out in a closed reactor pressure vessel. In that way the increase of the reactor temperature and the pressure can be used for detecting the initiation of the Grignard formation as shown by the comparison with the on-line profiles of the concentration of the Grignard reagent measured simultaneously by FTIR-spectroscopy. Results showed that the molar reaction enthalpy of a Grignard reagent could be determinated by a closed reactor vessel more accurately than under reflex conditions.

VALIDATION OF THE BRICK CODE WITH DATA FROM PRESSURE RELIEF EXPERIMENTS IN CASE OF RUNAWAY REACTIONS

Dirk Lucas

1. Introduction

Usually batch or semi-batch reactors are used for exothermic reactions. Often the reaction systems and the process control change. For this reason they imply a high risc potential. The reliable design of the emergency pressure relief system is very important to guarantee the safe operation of such reactors.

For the one-dimensional transient simulation of pressure relief processes the new BRICK code was developed [1,2]. The code was verified by many test cases including comparisons with analytical solutions for special cases. Examples for the validation of the code by depressurization experiments with water/steam are given in [1,2]. But to apply the code to the design of pressure relief systems of batch reactors it has to be validated for realistic reaction systems. Up to now 3 different systems were used for the validation, which represent 3 different situations. The first reaction is the esterification of methanol and acetic anhydride. In this case the pressure is caused by the evaporation of the components. The second is the decomposition of ammonium peroxydisulphate, where the pressure mainly builds up from the release of oxygen and the third is the thermal decomposition of hydrogen peroxide. This is a so called hybrid system, what means, that the increase of pressure results from the production of gas as well as from the evaporation.

2. Experiments

Data of pressure relief experiments for the esterification of methanol and acetic anhydride as well as for the decomposition of ammonium peroxydisulphate were available by courtesy of Wilhelm-Jost-Institut Hamm. The reactor has a height 1 meter and a diameter of 0.6 meter. This corresponds to a volume of 280 litres. For both reaction systems the kinetics of the reactions were investigated by calorimeter experiments at the Inburex GmbH Hamm. The data are also kindly placed at our disposal.

The most important parameter for these experiments are listed in the tables 1 and 2. For the esterification an initial composition of 38,6 wt-% methanol and 61,4 wt-% acetic anhydride was used. The initial concentration of ammonium peroxydisulphate was 35 wt-%.

Table 1: Calorimeter experiments - Inburex GmbH Hamm

Parameter	Esterification	Decomposition
Volume of the test cell	110 ml	120 ml
Mass of reaction mixture	73 g	75 g
Filling	70 %	70 %

Table 2: Pressure relief experiments - Wilhelm-Jost-Institut Hamm

Parameter	Esterification	Decomposition
Diameter of the orifice	13 cm	10 cm
Filling	90 %	80%

Small scale experiments with the thermal decomposition of hydrogen peroxide were done at our institute [3]. A 1.95 litre vessel was filled with 1 litre of 5, 10, 15, 17.5 and 20 wt-% H_2O_2 solution. Discharge orifices of 0.7 mm, 1 mm and 2 mm were used. The decomposition was initiated by an external heating. Experiments were carried out with a complete decomposition before starting the relief as well as with a relief during the runaway.

3. Esterification of methanol and acetic anhydride

In a first step, calculations for the calorimeter experiment were done. In this experiment the reaction is completed without pressure relief. After the completed reaction there is a slight decrease of temperature and pressure because of the loss of heat. Using a heat-transfer coefficient of 6 W/(m^2 K), the temperature decrease of the calculation agrees with the experiment. This is the only parameter adapted for the calculation. A very good agreement of the time dependent temperature and pressure curves was achieved. This means the modules for chemical

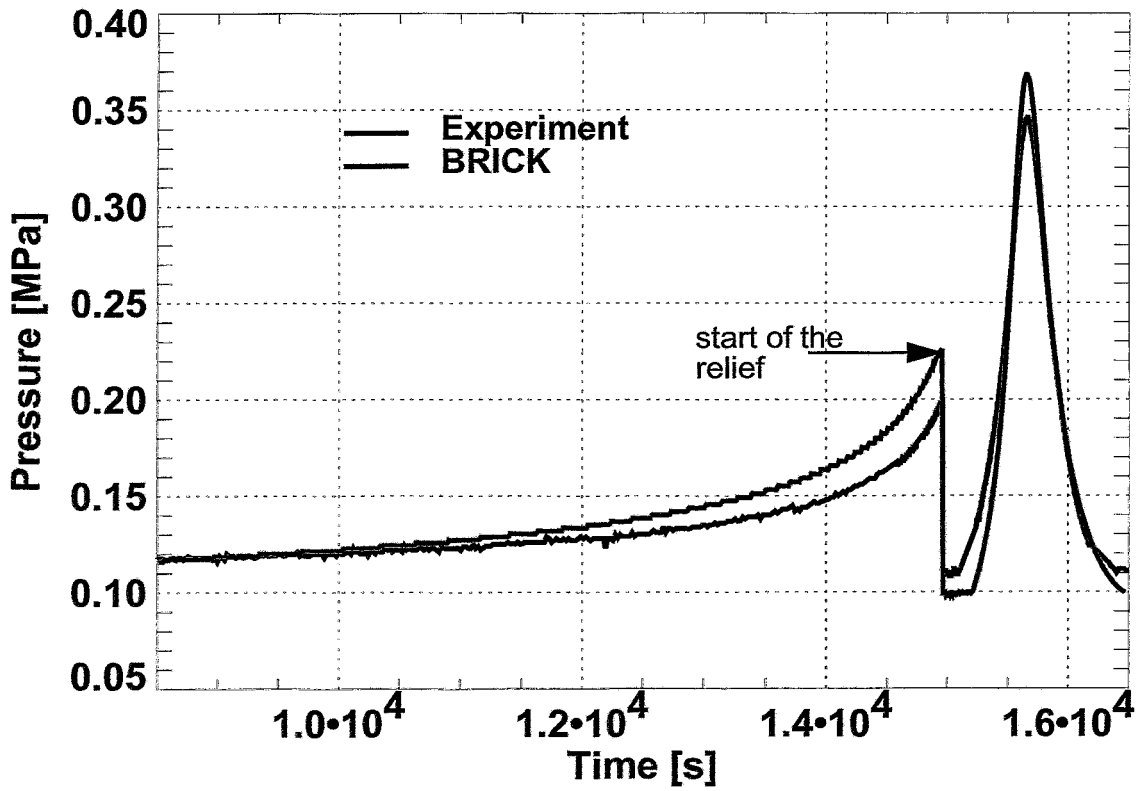

Fig. 1: Comparision of measured and calculated pressure in case of the 280 litre pressure relief experiment with the runaway esterification of methanol and acetic anhydride

reaction, phase transfer as well as for the calculation of material properties work well for this case.

Fig. 1 shows a comparison of the experimental and calculated pressure for the 280 litre pressure relief experiments. The pressure relief was started in the calculation, when the experimental starting temperature of the experiment was achieved. After starting the relief the pressure decreases rapidly to ambient pressure. However the cooling caused by evaporation is not sufficient to stop the reaction. For this reason the temperature even increases after the relief. The pressure peak caused by the runaway reaction is higher than the opening pressure. This is reflected very well by the calculation. The increase of pressure before starting the relief was mainly caused by the expansion of the liquid phase and the corresponding compression of the non-condensible gas. Since here the pressure is only a function of the temperature, material properties and the amount of the non-condensible gas (assumption of an ideal gas), it can be calculated analytically. Also other parameters like the location of the top level of the liquid phase were compared with analytical calculations. The agreement of all these analytically calculated values and the values obtained by the BRICK code confirm the right implementation of the model in the code. Differences between experiment and calculation may be caused by non-ideal behaviour of the fluid.

The most important element of uncertainty in the calculation is the modelling of heat transfer to the outside of the vessel. The influence of the heat transfer is shown in fig. 2. Here only the pressure peak after starting the relief is shown (compare time scales of fig 1 and 2). The red curve shows the pressure without any heat removal from the liquid. In case of the green curve, the vessel wall is considered, but no heat transfer to the outside of the vessel is assumed. The assumption of a constant heat transfer coefficient to the outside is more realistic. The best agreement between experimental and calculational results was achieved with a heat transfer

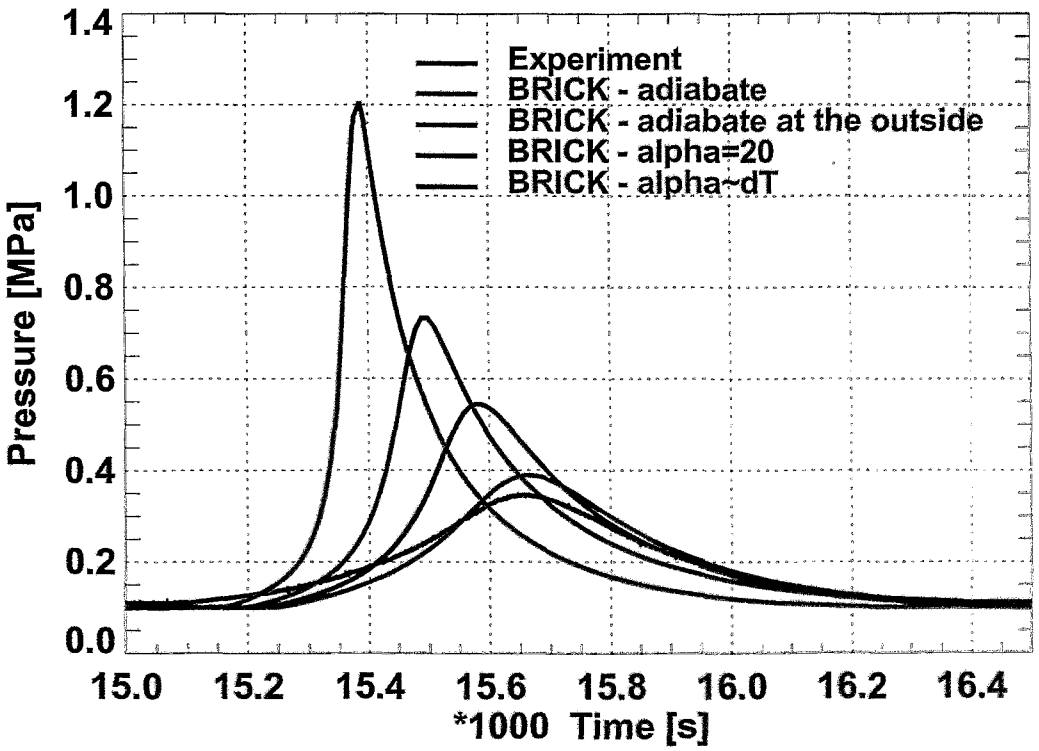

Fig. 2: Case studies for the influence of the heat transfer for the 280 litre pressure relief experiment with the runaway esterification of methanol and acetic anhydride

coefficient, which is proportional to the difference of the temperatures of the outside vessel wall and the environment. That indicates a non-linear behaviour of the heat transfer. However a physically based modelling was not possible, because the conditions of the outside cooling of the vessel are not well known. For the calculations only one node was considered. That means, a point model is used for the balance of energy, but the phase distribution is considered in the calculation over the vessel height.

4. Decomposition of ammonium peroxydisulphate

Due to the lack of material data for ammonium peroxydisulphate the calculations were done using data for hydrogen peroxide. According to the calorimeter experiments, an initial mass fraction of 7% hydrogen peroxide was used in the calculation, what means approximately the same mole fraction as in the case of a 35 wt-% ammonium peroxydisulphate solution. With this assumption an ideal agreement of the experimental and calculated time dependent pressure and temperature curves was achieved for the calorimeter experiments.

Fig. 3 shows a comparison of the measured and calculated pressure curve for the 280 litre pressure relief experiment. The pressure peak caused by the runaway does not reach the opening pressure in this case. There is a significant difference in the pressure increase before the relief. The reason for this difference is not clear. Analytical estimations confirmed the calculated increase of pressure. The runaway happens a little bit later in the calculation than in the experiment. Again the uncertainty of the heat transfer may be a reason for that.

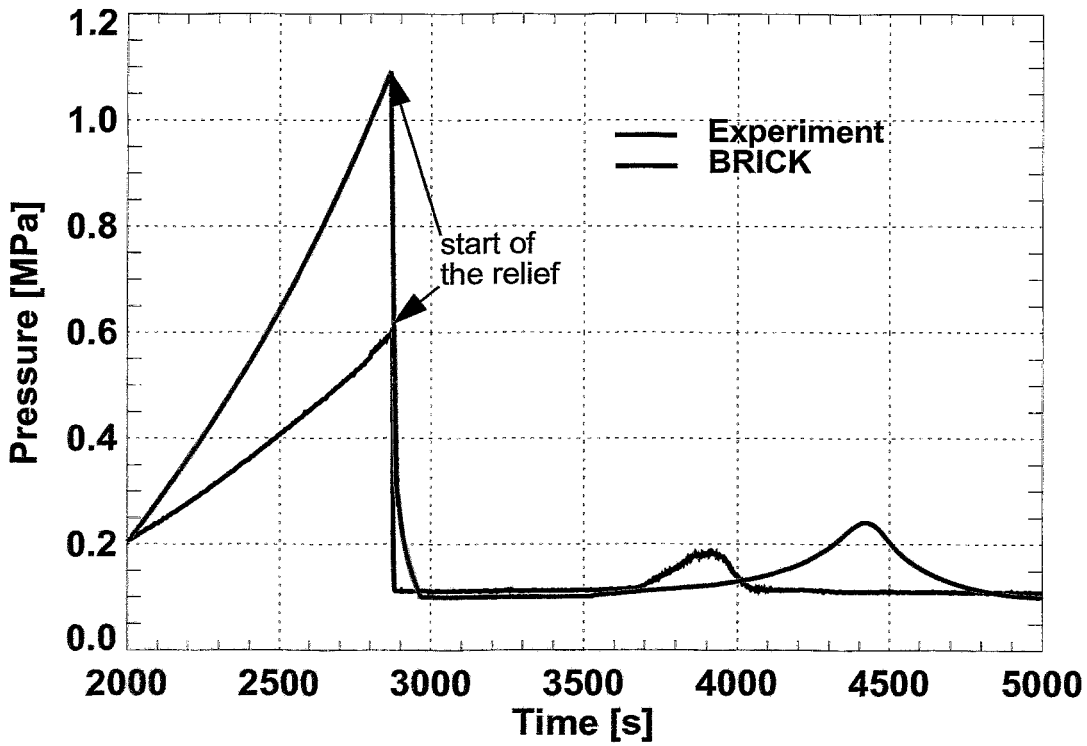

Fig. 3: Comparision of measured and calculated pressure in case of the 280 litre pressure relief experiment with the runaway decomposition of ammonium peroxydisulphate

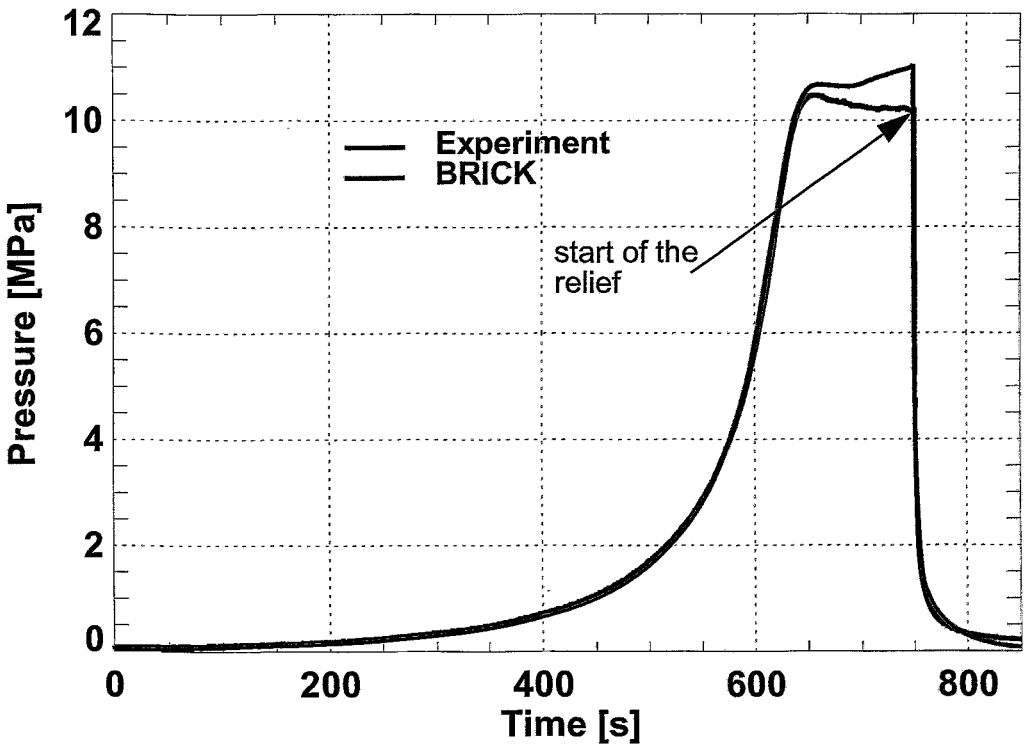

Fig. 4: Comparision of measured and calculated pressure in case of the 1.95 litre pressure relief experiment with the runaway decompostion of hydrogen peroxide (complete reaction)

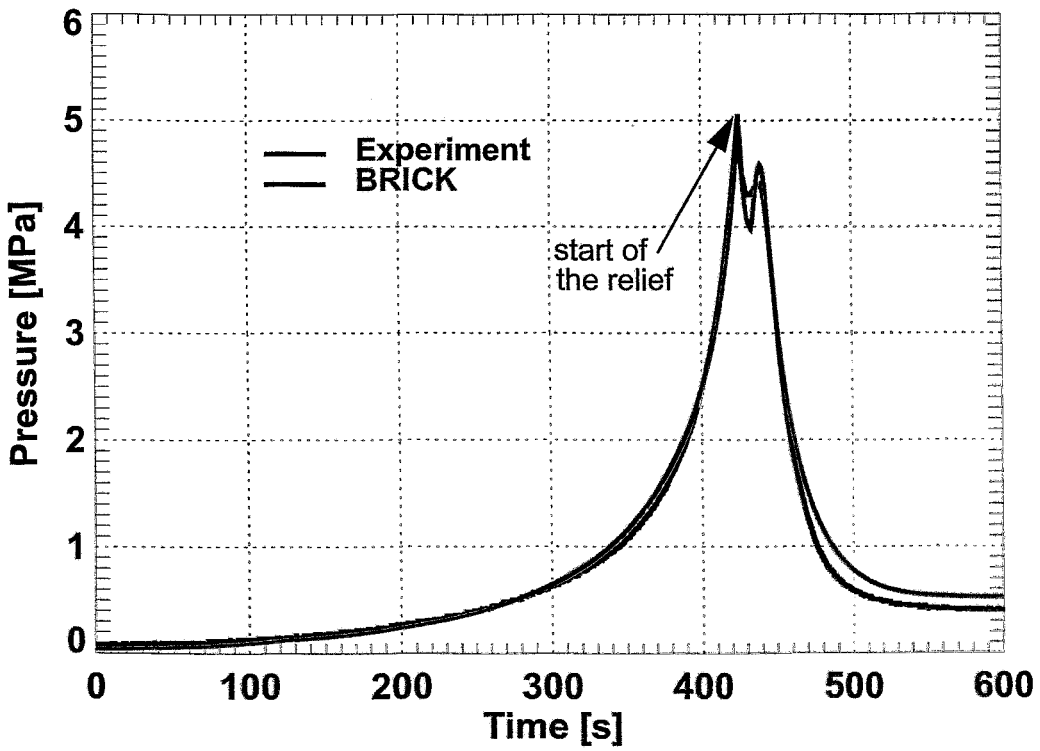

Fig. 5: Comparision of measured and calculated pressure in case of the 1.95 litre pressure relief experiment with the runaway decompostion of hydrogen peroxide (Relief at 5 MPa)

5. Decomposition of hydrogen peroxide

Fig. 4 and 5 show the pressure as a function of time for an experiment with a complete reaction before starting the relief and an experiment with a pressure relief, which was started at a pressure of 5 MPa. In the first case a 2 mm orifice and in the second case a 0.7 mm orifice was used. In both cases a good agreement was achieved. The pressure recovery after starting the relief was obtained in the experiment and also in the simulation with the BRICK code. The heating of the vessel was an additional element of uncertainty. The heating power of the vessel wall was adapted in the calculation.

6. Conclusions

Comparisons of the parameters calculated by the BRICK code with analytical solutions, which may be obtained for some simple cases, showed, that the code works correct. The agreement of the calculated and measured parameters as a function of time is satisfactory in most cases. The main uncertainty in the calculation is the modelling of the heat transfer from the vessel to the environment. Improvements are necessary. In addition, models for the axial heat transfer both in the fluid and in the wall should be implemented.

References

[1] D. Lucas (1999a), BRICK - A1-D Tool for transient Multiphase Vessel Flow Simulations based on a new Particle Method, 2nd International Symposium on Two-Phase Flow Modelling and Experimentation, Pisa, Italy, May 23-26, 1999, Proceedings, Volume 3, pp. 1657-1664

[2] D. Lucas (1999b), BRICK - ein 1-D-Simulationstool für Mehrphasenströmungen in Behältern, Chemie-Ingenieur-Technik 71, Heft 7

[3] D. Lucas, H.-M. Prasser, T. Kern (1998), Die thermische Zersetzung von Wasserstoffperoxid als Modellreaktion für die Druckentlastung, 4. Fachtagung Anlagen-, Arbeits- und Umweltsicherheit, Köthen, 5./6. November 1998, Preprints P9

This work was supported by the Volkswagen-Stiftung.

COMPOSITION EFFECTS ON THE IRRADIATION EMBRITTLEMENT OF VVER REACTOR PRESSURE VESSELS

Jürgen Böhmert, Alexander Kryukov[1], Yuri Nikolaev[1], Dimitri Erak[1]

1. Introduction

The irradiation embrittlement of the pressure vessels of the VVER Russian type reactors is highly safety-relevant. One of the most important parameters which influences the level of embrittlement is the composition of the steel. Especially copper, phosphorus and nickel are considered as harmful [1]. Whereas the effect of copper is repeatedly proved and is already part of the legal guides for predicting the irradiation embrittlement [2], the influence of phosphorus and nickel is still a matter of investigation. Above all high nickel content of 1.5 to 2 % which is contained in the weld metal of some VVER 1000-type reactors is controversially assessed [3]. Finally the existence of synergistic effects of the several alloy elements is completely obscure. That is why an extensive irradiation programme was started. In the framework of this programme, 19 mock-up alloys with systematically varied content of copper, phosphorus and nickel are irradiated under typical VVER-operating conditions. The mechanical properties of these alloys are tested after irradiation and post-irradiation annealing in order to establish common trends of chemical composition effects on the behaviour under neutron irradiation and after thermal recovery.

For a first step, 8 alloys were selected. The selection of the alloys aimed at maximum variation of these 3 elements. This step is finished.This paper reports on the results obtained from these alloys.

2. Experimental

The composition of the 8 investigated mock-up alloys is given in Tab. 1. The alloys were fabricated under the same conditions in an industrial small-scale production. The final thermal treatment complies with the heat treatment of the VVER 1000-type reactor pressure vessel steel. The alloys exhibit a ferritic microstructure. Their grain size is different. Particularly the Ni-rich alloys have a fine grain. From these alloys Charpy-V standard specimens and small tensile specimens were machined. The specimens were irradiated at the surveillance positions of the VVER 440 reactors ROVNO 1 and KOLA 3 over one reactor cycle. Both reactors differ in the core design and, thus, in the neutron flux (ROVNO 1: 0.4×10^{12} n/cm^{2}s; KOLA 3: 3.0×10^{12} n/cm^{2}s [E>0.5 MeV]). Fluence of 10×10^{18} n/cm^2 (= F_1) and 80×10^{18} n/cm^2 (= F_2) [E>0.5 MeV] were reached respectively. The irradiation temperature was about 270 °C.

[1] Russian Research Center „Kurchatov Institute" Moscow

Table 1: Chemical composition of the mock-up alloys (in wt.-%; Fe balance)

Code	C	S	Cu	P	Ni	Si	Mn
A	0.01	0.004	0.015	0.002	0.01	0.15	0.39
B	0.01	0.005	0.42	0.012	0.01	0.24	0.49
C	0.01	0.004	0.12	0.010	1.98	0.09	0.35
D	0.01	0.004	0.12	0.012	1.10	0.12	0.41
E	0.01	0.004	0.12	0.039	1.13	0.20	0.41
F	0.01	0.004	0.42	0.012	1.19	0.21	0.47
G	0.01	0.004	0.11	0.013	0.012	0.37	0.48
H	0.01	0.004	0.11	0.039	0.010	0.24	0.49

The specimens were tested by Charpy-V impact testing and tensile testing in the unirradiated state and the irradiated state. Before testing, a part of the specimens was annealed at 475° C/100 h after the irradiation. The ductile-brittle transition temperature was determined from the impact energy-temperature curves. The transition temperature is related to consumed impact energy of 47 J according to the Russian guide. The Russian guide uses the following relations:

$$\Delta TT_{irr} = TT_o - TT_{irr} = A_{irr} \sqrt[3]{F} \qquad (1)$$

TT_o or TT_{irr} are the transition temperatures in the initial state and after irradiation to the fluence F (F in 10^{18} n/cm^2 [>0.5 MeV]). A_{irr} characterizes the radiation sensitivity and depends on the content c (in wt-%) of copper and phosphorus

$$A_{irr} = 800\ (C_p + 0.07\ C_{Cu}) \qquad (2)$$

3. Results

In every case, irradiation clearly affects the mechanical properties. The strength parameters (ultimate tensile stress, yield stress) increase, the ductility (uniform elongation, total elongation, upper shelf energy) is reduced and, the transition temperature is shifted to higher values. The effect on the transition temperature is the bigger the higher the content of copper (B, F), phosphorus (E, H) and nickel (C-F) and the higher the fluence (Fig. 1).

Comparing the shift ΔTT_{irr} of the Ni-poor alloys (A, B, G, H) for the fluence F_1 and F_2, it does not seem that ΔTT_{irr} follows the relation as expected according to (1). This could result from a flux effect. A such effect is described for VVER 440-type weld metal on the base of surveillance results [4]. For comparable differences in the flux and similar level of fluence a constant shift of 40 °C to higher temperature is observed if the flux is lower. The related correction is depicted in Fig. 1 as well (red-marked points corrected).

To evaluate the composition effect the correction was used and all results were related to the fluence level F_1 by means of equation (1).

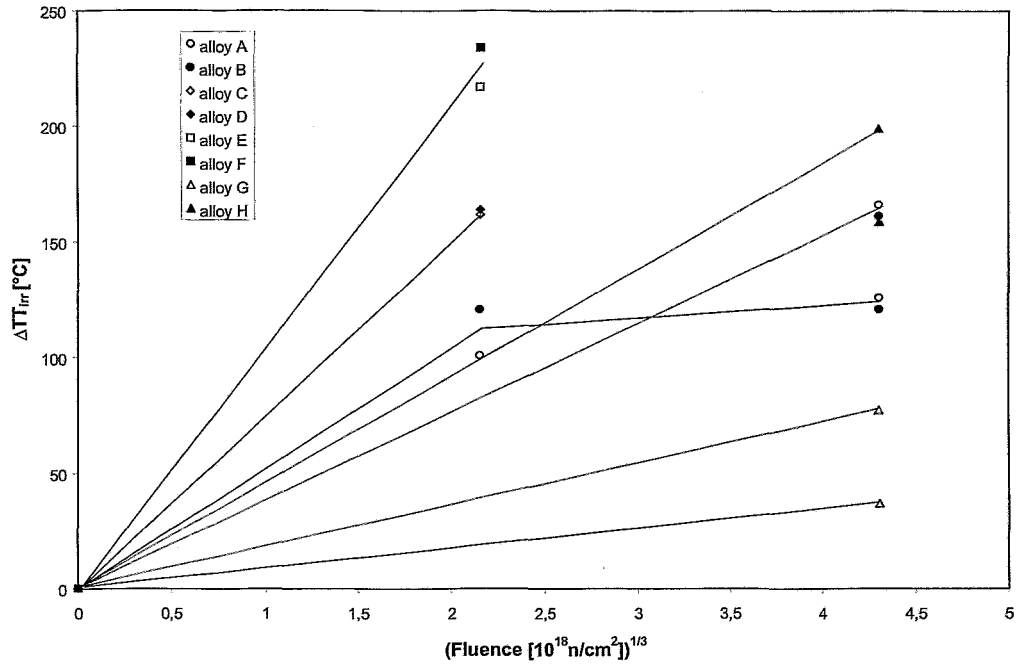

Fig. 1: Irradiation-induced shift ΔTT_{irr} of the transition temperature (red-marked points corrected)

Fig. 2 shows the influence of the composition on the transition temperature shift more clearly. Apart from the expected copper effect, phosphorus and nickel affect the transition temperature in the same way. For Ni-poor alloys the shift seems to follow the prediction of the Russian guide for weld metal as the Figs. 3 and 4 show. Nickel produces an additional shift of the transition temperature which hardly depends on the Ni content in the investigated range between 1.1 and 2 %. It amounts to about 120 °C at a fluence of 10 x 10^{18} n/cm^2 and at a flux of 0.4 x 10^{12} n/cm^2 s [E > 0.5 MeV].

A surprisingly strong effect occurs at the very pure alloy A (A contains only Mn and Si apart from marginal residues of other elements). This is not understandable from the composition point of view and gives a hint that other irradiation defects with different efficiency as dislocation barriers are formed in a pure α-iron matrix. Thus, the interaction of the solute atoms, such as copper, phosphorus or nickel, and the primary irradiation defects (vacancies, interstitials) plays an essential role in the mechanism of the irradiation embrittlement.

An influence of the composition on the annealing behaviour can also be proven (Fig. 5). For low copper or phosphorus content, annealing at 475° C/100 h removes the irradiation-induced changes of the mechanical properties completely. If the content of these elements, however, is high, then a residue of 20 to 25 % of the changes survives. Nickel has no influence on that. The pure alloy A again drops out of the trend and exhibits an „overrecovery".

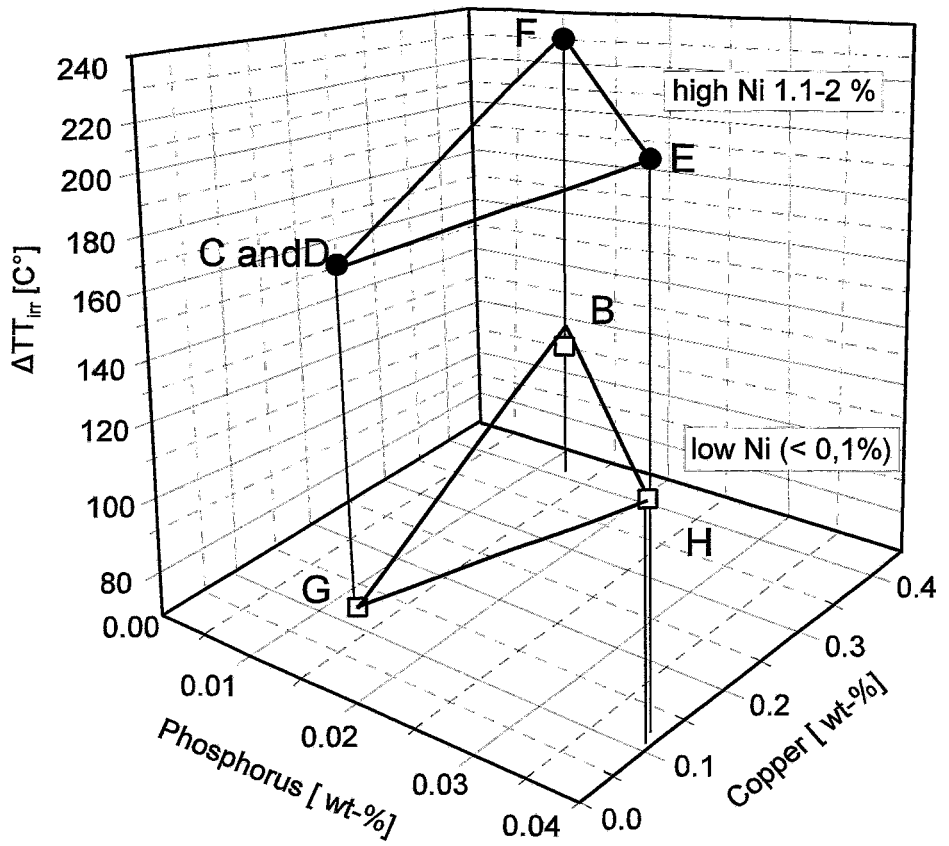

Fig. 2: Chemical composition effect on the irradiation-induced shift ΔTT_{irr} of the transition temperature

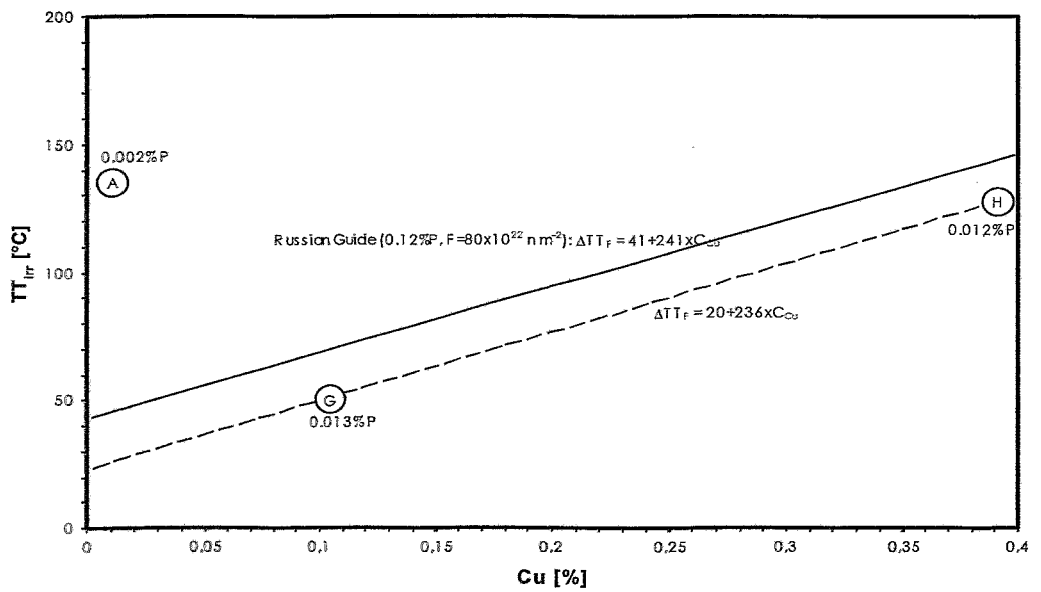

Fig. 3: Phosphorus effect on the irradiation sensitivity for mock-up alloys with low copper

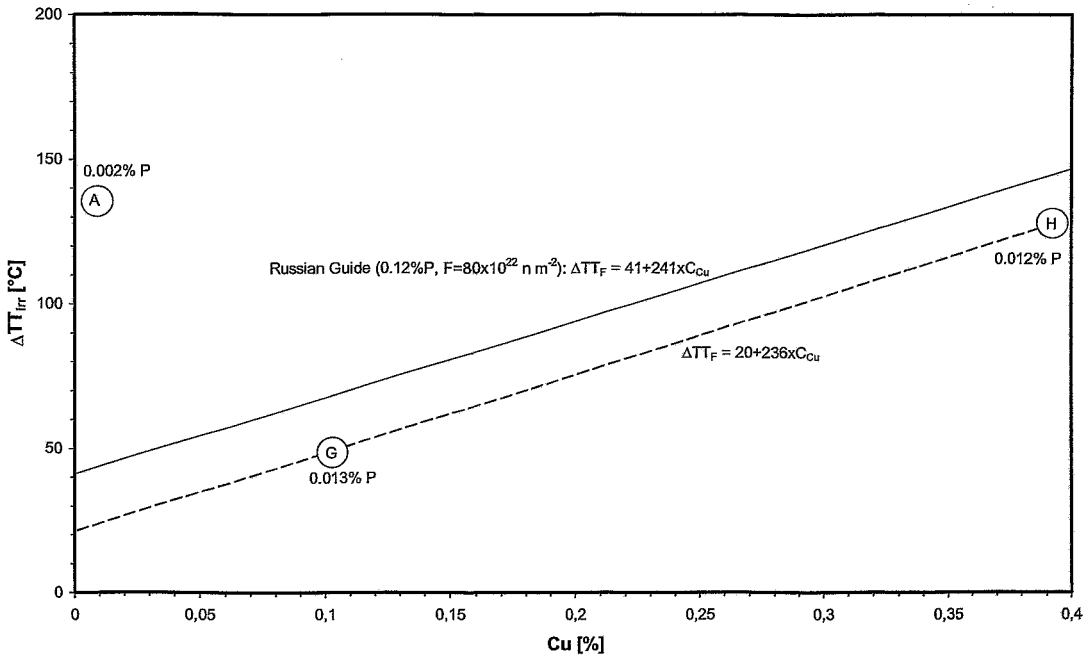

Fig. 4: Copper effect on the irradiation sensitivity for mock-up alloys with low phosphorus

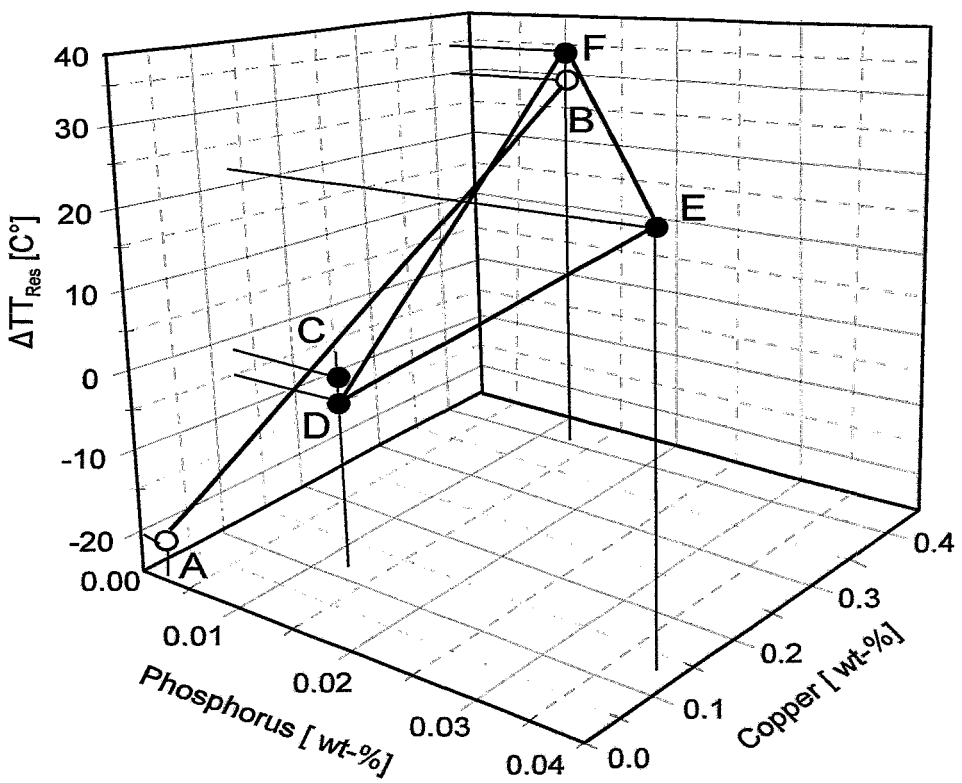

Fig. 5: Chemical composition effects on the residual shift ΔTT_{Res} of the transition temperature (• high Ni, ◦ low Ni)

4. Conclusion

The paper presents the first results of an extensive irradiation programme to characterize how the chemical composition affects the irradiation embrittlement. The harmful effect could be proven not only for copper but also for phosphorus and nickel. As the alloys exhibit a ferritic microstructure, the effect can only result from the interaction between the solute atoms and the primary irradiation defects in the iron matrix. The agreement between the results obtained with the Ni-poor alloys of this study and those achieved by the surveillance programmes with weld metal indicates that the irradiation behaviour of VVER 440-type weld metals is not essentially influenced by the metallurgical state but by the chemical composition. The recently valid guide seems to provide a useful assessment of the embrittlement for high flux levels. Ni has a clearly negative effect and must be considered for VVER 1000-type material. However, the results of this study do not suggest an increase of the irradiation sensitivity with the Ni content within the range of 1.1 to 2.0 % as often assumed. In this stage of investigation synergistic effects have not yet been proven. The programme is to be continued and completed by microstructural analysis. This is in preparation.

References

[1] L.E. Steele (1970), Critical Aspects of Neutron Irradiation Embrittlement of Pressure Vessel Steels and Welds, Symposium on the Technology or Pressure Retaining Steel Components, Vail Village, 1970, M.S. Weckler (Ed.), Nuclear Metallurgy, 6, 270

[2] P. Petrequin (1996), A Review of Formals for Predicting Irradiation Embrittlement of Reactor Vessel Materials, AMES-Report No. 6, Paris, EUR 16455

[3] M. Brumovsky, C.Y. Rieg (1995), Problems in a Standard Surveillance Programme of WWER-1000 Reactor Pressure Vessels in Irradiation Embrittlement and Mitigation, Proc. of a IAEA Specialist's Meeting, Espoo (Finland), IWG-LMNPP 95/5, Vol. II

[4] A.M. Kryukov (1998), The State of the Art of WWER-type RPV: Radiation embrittlement and Mitigation, Proc. of the Specialist's Meeting on Irradiation Effects and Mitigation, Vladimir (Russia)

IRRADIATION RESPONSE OF VVER PRESSURE VESSEL STEELS: FIRST RESULTS OF THE RHEINSBERG IRRADIATION PROGRAMME

Jürgen Böhmert, Hans-Werner Viehrig, Holger Richter

1. Introduction

An extensive irradiation programme was performed at the VVER 2 of the Rheinsberg nuclear power plant between 1983 and 1990. Almost 2000 specimens made from 37 various heats of preferentially VVER pressure vessel steels were irradiated in different irradiation rigs during one reactor cycle each.

The programme should considerably enhance the data base for irradiated materials. Mainly, the influence of detrimental elements, such like phosphorus or copper, and the metallurgical treatment should be analyzed. The final goal was to contribute to the validation of the predictive formula describing the neutron embrittlement as they are formulated in the Russian guides.

The prototype reactor VVER 2 is especially suitable as irradiation facility because the neutron fields and the temperature condition are comparable with the VVER 440. Moreover, the large cross section of the high flux channels allows to irradiate large and numerous specimens.

The programme comprises two parts. A first part is a German-Russian cooperation project. In this part Materialprüfanstalt Stuttgart and Forschungszentrum KFA Jülich were also involved. A second part was designed and prepared by Zentralinstitut für Kernforschung Rossendorf which was the predecessor for Forschungszentrum Rossendorf (FZR).

Testing of the specimens was delayed as the FZR's hot cell laboratories had been reconstructed. Since 1998 the FZR has had new hot cell laboratories with facilities for preparation and testing of irradiated specimens. In these laboratories the specimens of the first part of the irradiation programme were tested. Some results of the tests are presented in the following.

2. Experimental

The material tested by FZR [1] consists of

- 4 heats from VVER 440-type base metal 15Kh2MFA (15CrMoV 2) (code: R1, R2, R3, D25)
- 2 heats from VVER 1000-type base metal 15Kh2NMFAA (15CrNiMoV2) (code: R16, R17) and
- 1 heat from VVER1000-type weld metal 10KhGNMAA) (10CrMnNiMo 1) (code: R19) [1].

Most of the heats have a rather low content of the harmful elements copper and phosphorus (Tab. 1). Hence the irradiation sensitivity should be low. From each heat, Charpy V-notch standard and precracked specimens were available in the unirradiated, the irradiated and partly the post-irradiation annealed state.

The specimens were taken from the 1/4 to 3/4 thickness position and in L-S, T-S, L-T and T-S orientation. The specimens were placed in open irradiation rigs in the high flux irradiation positions (target channels) with direct contact to the coolant (255 °C inlet temperature). The mean neutron flux rate was 2.6 10^{12} $cm^2 \cdot s$ [E>1MeV]. The fluences of different specimens of one set vary up to a factor of 2. Therefore, the results of the tests were corrected to the same mean fluences. Both the details of the irradiation and the correction procedure are given in [2].

The Charpy impact tests were performed with an instrumented impact pendulum in the temperature range of -150 °C to +300 °C. Testing of the precracked specimens is based on the master curve concept according to ASTM E 1921-97 using the multiple temperature method [3]. The specimens were loaded by three-point bending with a servo-hydraulic test system „MTS 810-Test Star" in a nitrogen cooled environmental chamber.

3. Results

The two VVER 440 base metal heats (R1 and R3) excepted, in general all investigated materials exhibit a high toughness in the unirradiated state. Particularly the Charpy toughness parameters of the VVER 1000 base metal are excellent. As usual the toughness of the weld metal is lower but sufficient according to the Russian specification. Definitely, irradiation within the investigated fluence range from 23.2 to 138 $\cdot 10^{18}$ /cm^2 [E > 0.5 MeV] affects a clear degradation of the toughness. Irradiation shifts the ductile-brittle transition temperature to higher temperatures, lowers the upper shelf energy and extends the transition range. Figs. 1 and 2 illustrate this phenomenon for heats of VVER 440 base metal and of VVER 1000 weld metal. Using the Russian procedure [1] for the evaluation of the irradiation sensitivity

$$\Delta TT = A_F \cdot \sqrt[3]{F} \qquad (1)$$

an irradiation embrittlement coefficient A_F can be estimated from the fluence F (in $10^{18}/cm^2$ [E > 0.5 MeV) and the measured transition temperature shift $\Delta TT = TT_F - TT_o$. Tab. 1 summarizes the calculated values for A_F. The values range from 3.4 for a 15Kh2MFA heat (R1) to 47.5 for the weld metal (R19). This means that for typical end of life fluences $\geq 10^{20}$ /cm^2 [E>0.5 MeV] the transition temperature shifts range between 20 and ≥220 °C. Whereas a shift of 20 °C proves an excellent irradiation resistance, a shift of more than 250 °C is not acceptable even if the transition temperature is very low in the initial state.

Table 1: Irradiation embrittlement coefficients A_F

material	code	Cu / weight-%	P / weight-%	Φ_{mean} [x 10^{18} ncm^{-2}]	ΔTT_{48J} [°C]	A_F
15Kh2MFA	R1	0.10	0.011	43.6	12	3.4
	R2	0.12	0.014	80.7	32	7.4
	D25	0.11	0.017	127.6	99	19.7
	R3	0.12	0.024	47.5	47	13.1
15Kh2NMFAA	R16	0.07	0.012	46.0	65	18.1
	R17	0.13	0.013	72.7	119	28.5
10KhNGMAA	R19	0.05	0.008	65.1	191	47.5

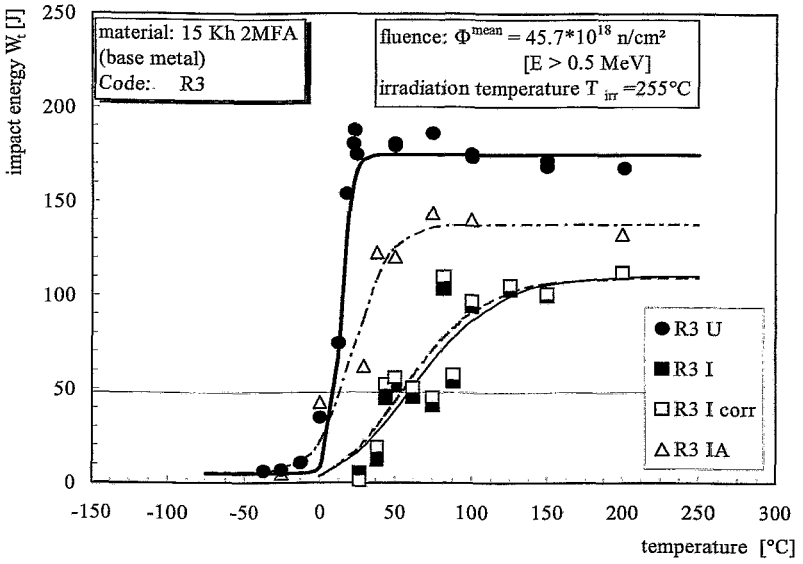

Fig. 1: Charpy V impact energy temperature curves of VVER-440 base metal (R3) in the as-received (U), irradiated (I) and annealed (IA) state

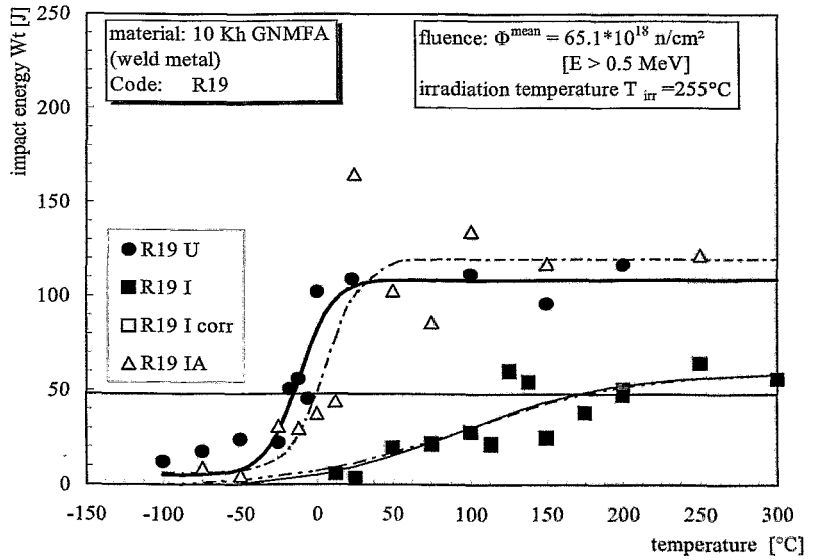

Fig. 2: Charpy V impact energy temperature curves of VVER-1000 weld metal (R19) in the as-received (U), irradiated (I) and annealed (IA) state

The irradiation embrittlement coefficient A_F depends on the material composition and the irradiation temperature. The Russian guide is based on the following rules [2]:

$$A_F = 800\ (\%\ P + 0.07\ \%\ Cu) \qquad (2a)$$

for weld metal, WWER-440, $T_{irr} = 270$ °C

$$A_{FT} = A_{F\,270} + K\,(T_{270} - T_{irr}) \qquad (2b)$$

with K = 0.2 for base metal and K = 0.4 for weld metal

maximum values for VVER 440, T_{irr}=270 °C maximum values for VVER 1000, T_{irr}=290

$A_F \leq 15$ weld metal $A_F \leq 20$ weld metal

≤ 18 base metal ≤ 23 base metal (2c)

For the different materials the transition temperature shifts are calculated using equations (1) to (2a-c) and compared with the measurements. The comparison is shown in Fig. 3. On the base of the Russian guidelines always conservative predictions are obtained apart from the weld metal (R19). The very high irradiation embrittlement sensitivity of material R 19 is not correctly predicted. As the material meets the Russian specification regarding both the chemical composition and the heat treatment, this irradiation response is unexpected. Also the microstructure does not give a clue for the irregularity. R19 is a weld material. Weld metal is considered to have the highest susceptibility to embrittlement. Nevertheless, the finding cannot be explained consistently what is a proof for our lack of adequate knowledge on the phenomenon.

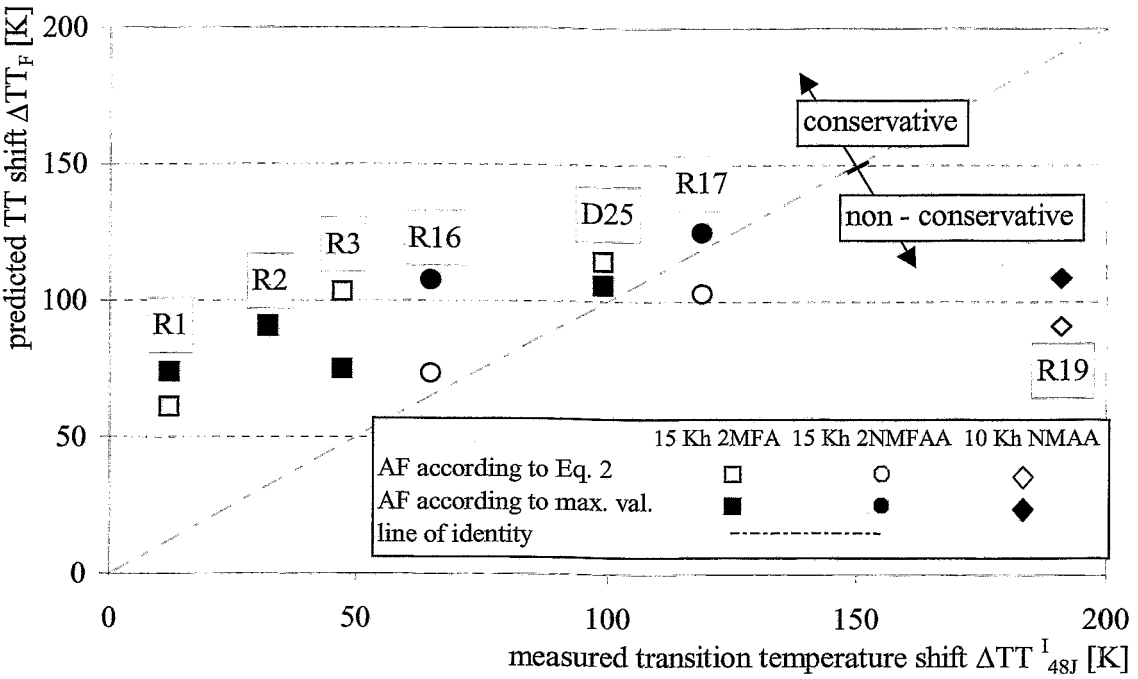

Fig. 3: Transition temperature shift due to irradiation related to a Charpy V-impact energy of 48 J - comparison between predicted and measured values

An annealing treatment to recover the thoughness has become a must for the old VVER-440 s. There are well-tried annealing technologies but, unfortunately, their efficiency has not yet been sufficiently validated. The effect of annealing can be described by a recovery parameter R defined as relative change of the transition temperature TT or the upper shelf energy USE

$$R = \frac{P_{irr} - P_{ann}}{P_{irr} - P_{unirr}} \; 100 \; [\%] \qquad (3)$$

where P_{irr}, P_{ann}, P_{unirr} are the concerning Charpy impact test parameters (TT, USV) in the unirradiated, the irradiated or the annealed state.
After 100 h annealing at 475° C the recovery parameter R is shown in Fig. 4. Both "over-recovery" and incomplete recovery can be observed. From the safety point of view the results are favourable: the heats with the highest irradiation sensitivity reveal complete recovery. One should notice that the transition temperature shift of heat 16 is hardly recovered by annealing.

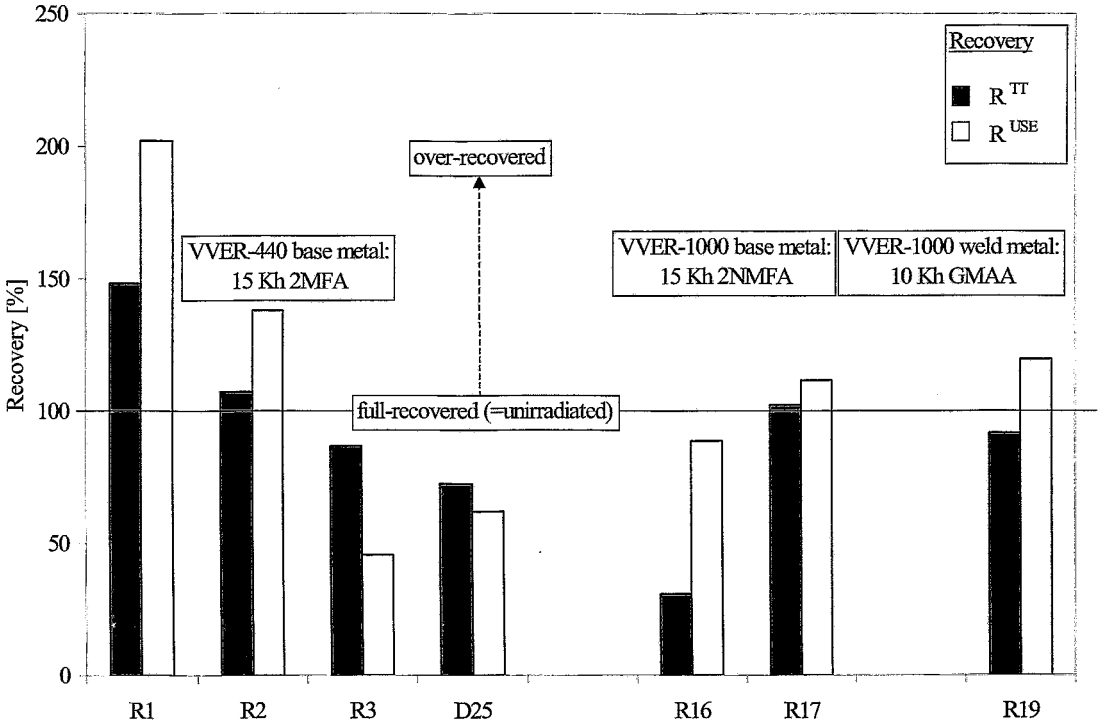

Fig.4: Recovery of Charpy V parameters

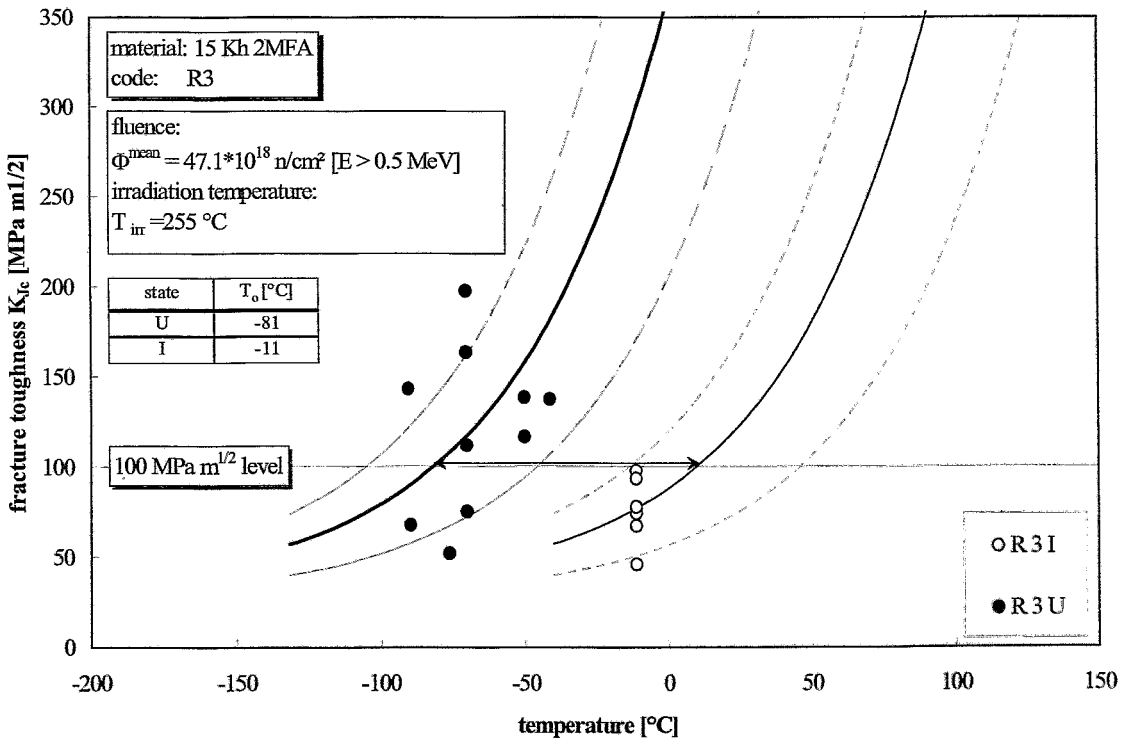

Fig. 5: Fracture toughness, K_{Jc}, - temperature curve for heat R3 from VVER-440 steel in the unirradiated (U) and irradiated (I) state

Heat 16 only differs from the other heats in the small grain size and the shorter tempering at lower temperature.

Fracture mechanics parameters were determined using the master curve concept [4]. The master curve is a commonly valid fracture toughness-temperature curve. The position on the temperature axis is defined by a material-dependent reference temperature T_0. Fig. 5 presents the fracture toughness - temperature curve (mean curve with 5 and 95 % probability boundaries) for heat R3 in the unirradiated and irradiated state. Irradiation shifts the curve to higher temperature. The shift is larger than the transition temperature shift measured by Charpy impact tests. In other cases both characteristic temperature shifts are approximately comparable with each other. Predictive formula which describe the influence of the irradiation on fracture mechanics parameters for VVER steels have not yet been available. Nevertheless, the Charpy transition temperature shift seems to provide a useful estimation for the irradiation-induced changes of the fracture mechanics response, too.

4. Conclusion

For 7 heats from VVER 440 and 1000 reactor pressure vessel steels, the change of the Charpy impact parameters and the master curve reference temperature T_0 due to irradiation and annealing could be determined.
As a rule, the irradiation behaviour meets the prediction of the Russian guides in a conservative manner and is not critical from the safety point of view. However, there are surprising non-conservative results after both irradiation and annealing. Such outliers are suspect and we have not yet been able to explain the effect. Microstructural investigations are planned to clarify the abnormal behaviour.

References

[1] H.-W. Viehrig, J. Böhmert, H. Richter (1999), Common German/Russia Irradiation Experiment at Rheinsberg NPP - Results of the Mechanical Testing, Proc. of a IAEA Specialist's Meeting on Irradiation Embrittlement and Mitigation, IAEA, Madrid

[2] H.-W. Viehrig, Barz, H.-U. Barz, J. Boehmert, B. Boehmer (1997), Consideration of neutron flux gradients for sophisticated evaluation of irradiation experiment, Proc. of the IAEA Specialists Meeting, Vladimir, Russia,, Sept. 1997, IWG-LMNPP-97/2, Vienna, pp. 230

[3] H.-W. Viehrig, J. Boehmert (1999), Some Issues by Using the Master Curve Concept, 15th International Conference on Structural Mechanics in Reactor Technology, SMiRT-15, August 15-20, Seoul, Korea

[4] K. Wallin (1997), Small Specimen Fracture Research Characterisation-State of the Art and Beyound, Proc. of the Advances in Fracture Research, ICF 9, B.L. Karihaloo, Y.M. Mai, M.I. Ripley, R.O. Ritchie (Eds.), pp. 2333-2344, Amsterdam

FINITE ELEMENT ANALYSIS OF A BWR FEED WATER DISTRIBUTOR UNDER EXTREME TRANSIENT PRESSURE LOAD

Eberhard Altstadt, Hermann Ohlmeyer[1], Frank Otremba[1], Frank-Peter Weiss

1. Introduction

The break of a feed water line outside of the containment is a hypothetical accident scenario for German boiling water reactors (BWR). Fig. 1 shows a simplified scheme of the this scenario. It is assumed that the pressure in the feed water system drops to ambient pressure within a few milliseconds. The feed water distributor (FWD) consists of four hydraulically separated ring lines supported at the feed water nozzles of the RPV. The cross section of the FWD ring lines is rectangular (inner height 210 mm, inner width 155 mm, wall thickness 10 mm). Figure 2 shows a 3D-view of the FWD in the region of RPV inlet nozzle. The feed water is normally sprayed into the reactor pressure vessel (RPV) through a number of small nozzles with a rather high flow resistance, located at the top wall of the FWD. Therefore in the case of a feed water line break the pressure within the RPV drops not as fast as the pressure of the feed water system. Thus for a short time the FWD is exposed to high difference pressure between its outer and its inner surface. The maximum pressure peak is 62 bar. The linear stress analysis shows that the ring line is one of the locations where large deflection and large strain is to be expected (Fig. 3). Within this paper the non-linear behaviour of the FWD ring line is investigated.

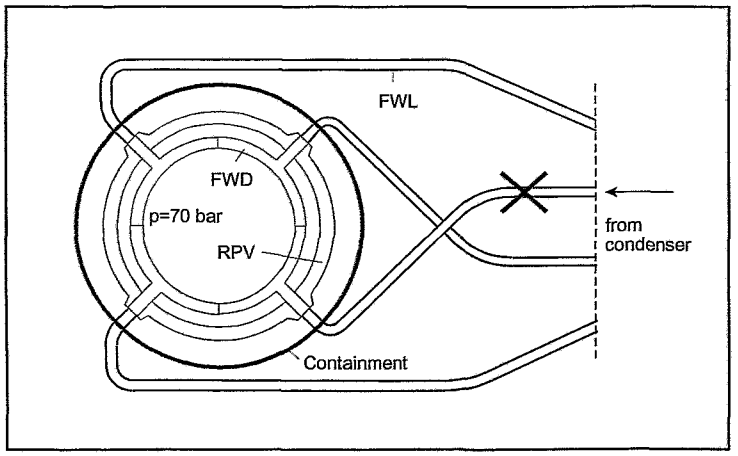

Fig. 1: Scheme of reactor pressure vessel, feed water distributor (horizontal section) and feed water lines

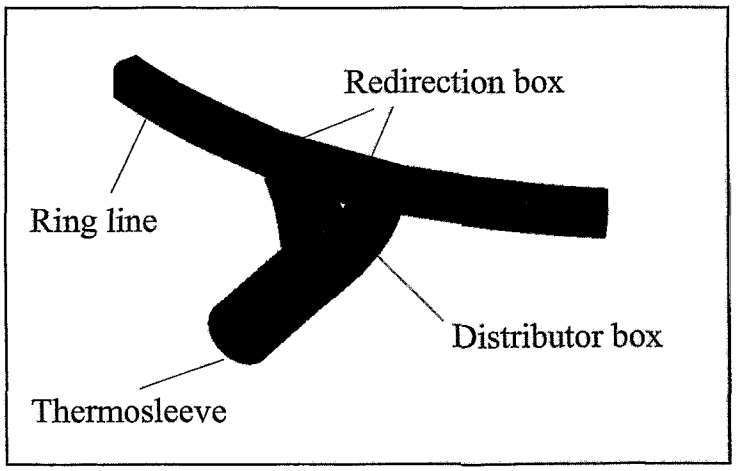

Fig. 2: Feed water distributor (region of RPV nozzle)

[1] Hamburgische Elektrizitätswerke AG

2. Mechanical phenomena and solution method

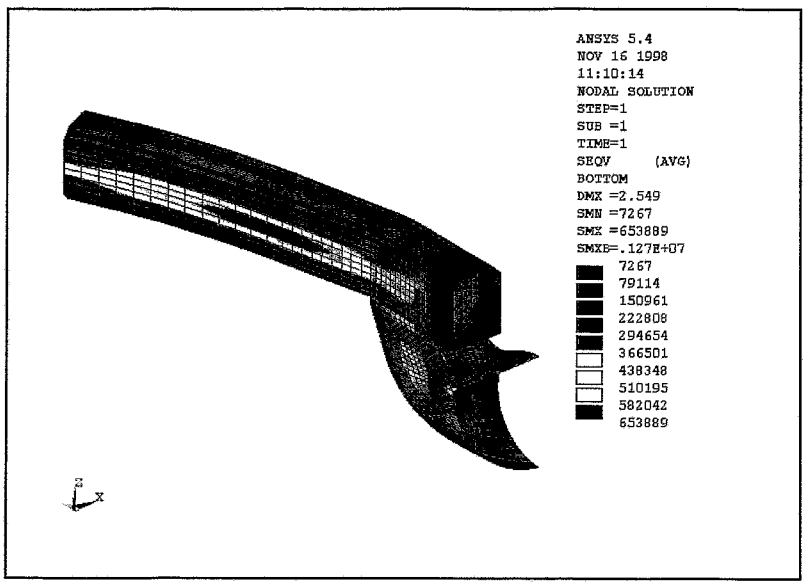

Fig. 3: Equivalent stress (kPa) in the FWD at maximum pressure load. Linear analysis.

Figure 3 shows the distribution of the equivalent stress at maximum pressure calculated with a linear shell model. Due to the high pressure load the elasticity limit of the FWD (austenitic steel) is clearly exceeded. Hence the mechanical stress analysis must consider the on non-linear material behaviour. An elastic-plastic material law with an isotropic hardening rule is adopted (section 3).

Furthermore the problem is geometrically non-linear because large strain and large deflection have to be expected. Due to the fact that the load is imposed by external pressure the deflection process is connected with instabilities (buckling). The buckling process of the FWD ring pipe is illustrated in Figure 4. The height of the cross section of the ring line is larger than the width, so the vertical walls are bended to the inside and the horizontal walls to the outside. The pressure upon the horizontal walls leads to additional negative membrane stress in the vertical walls and thus causes a stress weakening. As a consequence, the ring line tends to buckling. This process is unstable until the opposite horizontal walls get in contact. This phenomenology can be characterized by the load-displacement curve shown in Fig. 5 (p is the external pressure and u the deflection of the vertical wall).

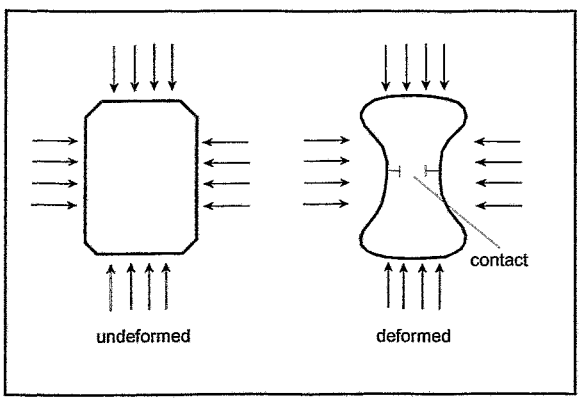

Fig. 4: Buckling of the FWD ring line

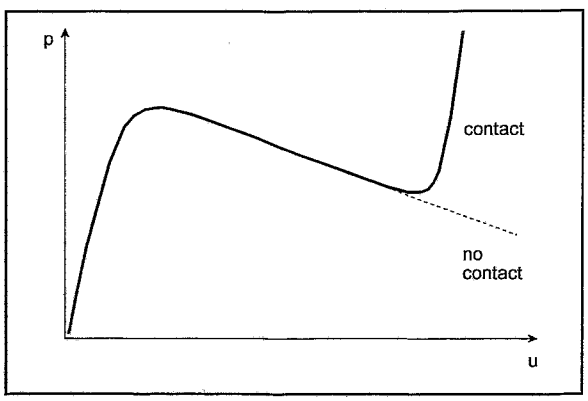

Fig. 5: Load-deflection curve for buckling

Due to these instabilities special mathematical tools are required to get a converging solution. Like for all non-linear problems the load must be applied in small steps even in a static analysis. Equilibrium iterations are performed at every load step to solve the equations. For stable load-

deflection behaviour the classical Newton-Raphson procedure is an adequate algorithm (Zienkiewicz,1977):

$$\underline{\phi} = \underline{K}(\underline{u}) \cdot \underline{u} - \underline{f}_a = \underline{0} \tag{1}$$

$$\underline{f}_r^{(i)} = \underline{K}^{(i)}(\underline{u}^{(i)}) \cdot \underline{u}^{(i)} - \underline{f}_a \tag{2}$$

$$\underline{f}_r(\underline{u}^{(i)} + \Delta\underline{u}^{(i)}) = \left[\frac{\partial \underline{\phi}}{\partial \underline{u}}\right]_i \Delta\underline{u}^{(i)} + \underline{f}_r(\underline{u}^{(i)}) = \underline{0} \tag{3}$$

$$\Delta\underline{u}(i) = \left[\underline{K}_T^{(i)}\right]^{-1} \underline{f}_r^{(i)} \tag{4}$$

$$\underline{u}^{(i+1)} = \underline{u}^{(i)} + \Delta\underline{u}^{(i)} \tag{5}$$

$$\underline{f}_r^{(i+1)} = \underline{K}^{(i+1)} \underline{u}^{(i+1)} - \underline{f}_a \tag{6}$$

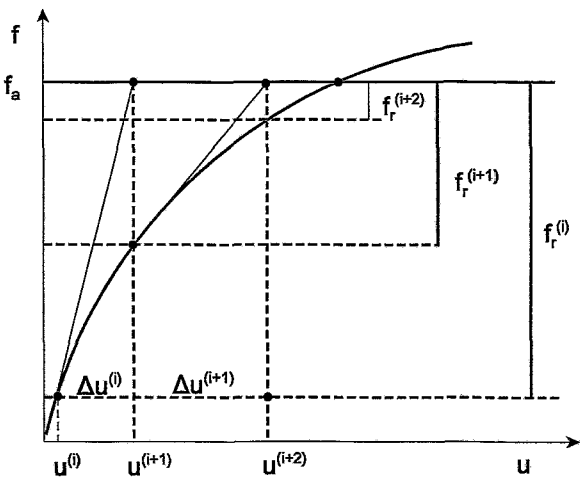

Fig. 6: Newton-Raphson procedure

The Newton-Raphson procedure (equations 1-6) iterates the equilibrium at each load step. $\underline{K}$ is the stiffness matrix of the FE-model, $\underline{K}_T$ the tangent siffness matrix, $\underline{u}$ the vector of the nodal degrees of freedom (deflection), $\underline{f}_a$ is the vector of the apllied loads at the current load step and i the iteration index. Figure 6 shows a simplified scheme of that procedure for a one degree of freedom model. The solution is converged if the vector of residual forces $\underline{f}_r$ is sufficiently small (equilibrium between applied loads and internal forces).

However, if the load-deflection curve exhibits instability points (negative slope) the classical Newton-Raphson algorithm does not work. This is illustrated in Fig. 7. A numerical algorithm to solve problems with instabilities is the arc-length method (Kolar and Kamel, 1986). The basic idea of this method is to control the gradual application of the load by a relative load factor λ in such a way that the distance between two iterations points in the load-deflection space is limited by an arc length radius. Thus the load can be increased and decreased during the progress of the equilibrium iterations. Figure 8 illustrates this strategy. The second equation of the calssical Newton-Raphson procedure (eq. 2) is modified as follows:

$$\underline{f}_r^{(i)} = \underline{K}^{(i)}(\underline{u}^{(i)}) \cdot \underline{u}^{(i)} - \lambda \underline{f}_a \tag{7}$$

The load factor λ is determined from the additional condition:

$$l_i^2 = \Delta\lambda_i^2 + \beta^2 (\Delta \underline{u}_n^{\,i})^T (\Delta \underline{u}_n^{\,i}) \tag{8}$$

where li is the arc-length radius and β a scaling factorto consider the different units of load and deflection, n is the load step index and i the iteration index.

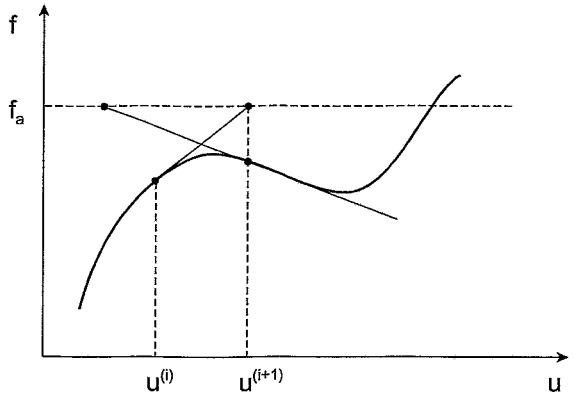

Fig. 7: Divergence of the classical Newton-Raphson procedure at instability points

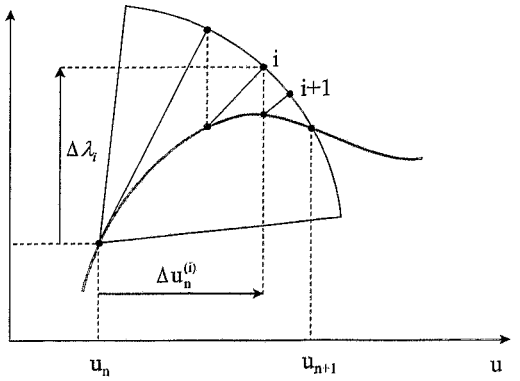

Fig. 8: Arc-length procedure

The arc-length method is only applicable to static analyses. If the load is time dependent in such a way that the dynamic forces of the structure cannot be neglected, a non-linear transient analysis is to be performed. In this case the inertia and damping forces have to be included into the equilibrium iterations of the classical Newton-Raphson procedure. The residual force vector then reads:

$$\underline{f}_{r,n}^{(i)} = \underline{M}\,\underline{\ddot{u}}_n + \underline{B}\,\underline{\dot{u}}_n + \underline{K}^{(i)}(\underline{u}_n^{(i)}) \cdot \underline{u}_n^{(i)} - \underline{f}_{a,n} \tag{9}$$

with $\underline{M}$ being the mass matrix, $\underline{B}$ the damping matrix and n the time index. Equilibrium iterations are performed for each time step of the analysis. For the time integration the Newmark method is adopted (Bathe, 1982).

3. Finite element model and loading

3.1 Elements

The FWD is modelled using the FE code ANSYS®. Various models are available. The first analyses were done using a shell model of the complete 90° segment of the FWD (curvator, redirection box and ring line, Fig. 1). This model is only useful for linear static and dynamic calculations. In the non-linear large strain analyses no convergent solutions could be obtained. Therefore the model was separated into one model for the curvator and one model for the ring line. For the ring line a shell model and a volume model can be used. The volume model was used because of the missing convergence with shell elements (see section 4). All element types have plasticity, large strain, large deflection and stress stiffening capabilities. To cope with the dependence of the stiffness of the structure on the deflection an updated Lagrangian formulation is used (Mattiasson, et. al. 1986). Contact elements are used to model the touching of the two opposite vertical walls of the ring line.

3.2 Material

The material behaves elastic-plasticly with multi-linear isotropic hardening. The initial yield stress is about 180 MPa, the tensile strength is about 680 MPa, the fracture strain is 0.44 (true stresses and strains).

To describe the plastic material behaviour within the 3-dimensional stress state the flow rule of Huber, von Mises and Hencky is employed (Zienkiewicz, 1977):

$$\Phi = \sigma_e^{\,2} - \sigma_F^{\,2}(\varepsilon^{pl}) = 0$$

$$\sigma_e^{\,2} = \frac{1}{2}\left[(\sigma_x - \sigma_y)^2 + (\sigma_y - \sigma_z)^2 + (\sigma_z - \sigma_x)^2 + 6 \cdot (\tau_{xy}^{\,2} + \tau_{yz}^{\,2} + \tau_{zx}^{\,2})\right] \tag{10}$$

where σ_e is the equivalent stress, σ_F the current yield stress and ε^{pl} the plastic equivalent strain. If equation (10) is fulfilled the material is subjected to a plastic strain that can be calculated from the von-Mises flow law:

$$d\varepsilon_{kl}^{pl} = d\Lambda \cdot \frac{\partial \Phi}{\partial \sigma_{kl}} \quad ; \qquad d\Lambda = \frac{d\varepsilon_e^{pl}}{2\sigma_F} \tag{11}$$

The plastic strain increment $d\varepsilon_{kl}^{pl}$ is directed perpendicular to the flow area described by eq. 10. Therefore, eq. 11 is also refered to as normal rule.

3.3 Load

The load on the FWD is the pressure on its outer surface (pressure difference between RPV and feed water system). The pressure is time dependent and exhibits a spatial distribution. Figure 9 shows the pressure distribution for the time when the maximum pressure occurs (t=0.045 s). In Figure 10 the progress of the pressure load is shown at the curvator over the time.

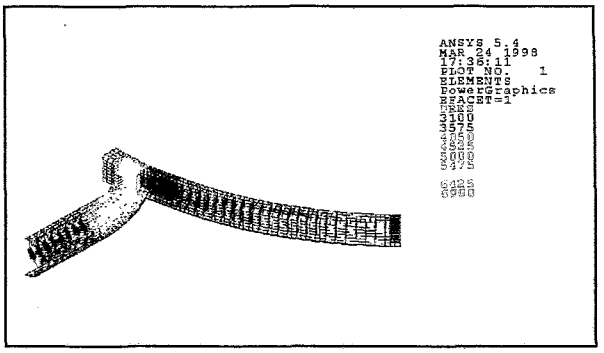

Fig. 9: Pressure distribution at the FWD (kPa)

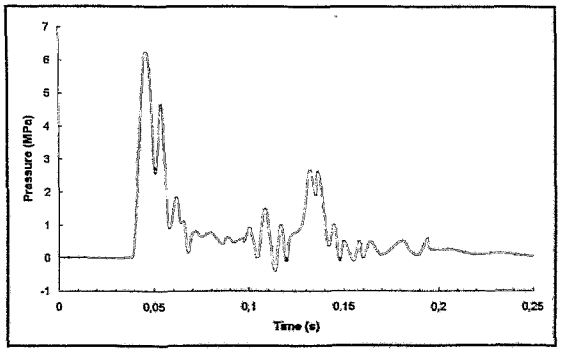

Fig. 10: Pressure at the curvator vs. time

For static analyses the pressure distribution at t=0.045 s (maximum pressure) is used as load (Fig.9). For transient analyses the time dependent distribution between t=0.04 s and t=0.056 s is used.

$$p(\vec{x},t) = p(\vec{x}) \cdot \lambda(t) \quad ; \qquad 0 \le \lambda(t) \le 1 \tag{12}$$

where $p(\vec{x})$ is the distribution of the pressure according to Fig. 9 and $\lambda(t)$ a relative load factor which corresponds to the pressure curve of Fig. 10 between t = 0.04 s and t = 0.056 s.

4. Results

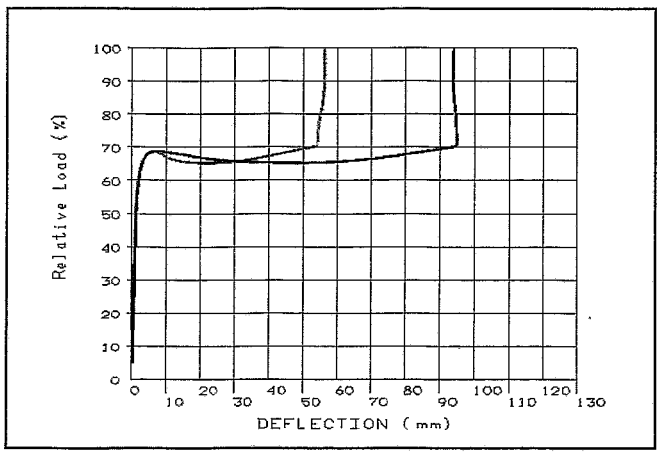

Fig. 11: Static analysis of the ring line. Load deflection curve for nodes at the inner wall (green) and the outer wall (blue) at azimutal position 15°.

As stated in section 3.1 the non-linear mechanical analysis for the FWD has to be carried out with separate models for the curvator and for the ring line, because a convergent solution could not be obtained with the shell model for the complete structure. For the ring line the best results were achieved with volume elements. First the static analysis is discussed. Figure 11 shows two load deflection curves. The relative load factor (eq. 12) is drawn vs. two nodal displacements. The green curve is for the node at the inner vertical wall of the FWD ring line, half height at an azimutal position 15° from the nozzle. The blue curve is for the node displacement of the outer vertical wall at the same axial and azimutal position. Up to about 50% load the curves are linear with a rather steep slope. This is the range of elastic deformation (high stiffness). If the relative load factor gets higher then 50% the plastic deformation starts to develop. The point of instability is around 68% of load. The instability is a result of the stress weakening of the vertical walls (Fig. 4). At about 50 mm deflection of the outer node (blue curve Fig. 11) and 20 mm deflection of the inner node (green) the structure becomes stable again. This is a consequence of the hardening of the material (increasing yield stress due to plastic strain). At about 95 mm deflection of the outer node and 54 mm of the inner node the first contact between the opposite wall takes place. This leads to a high stiffness of the structure again (extremly steep slope). The slope of the blue curve is even higher than 90°, because of the increasing contact region between the walls.

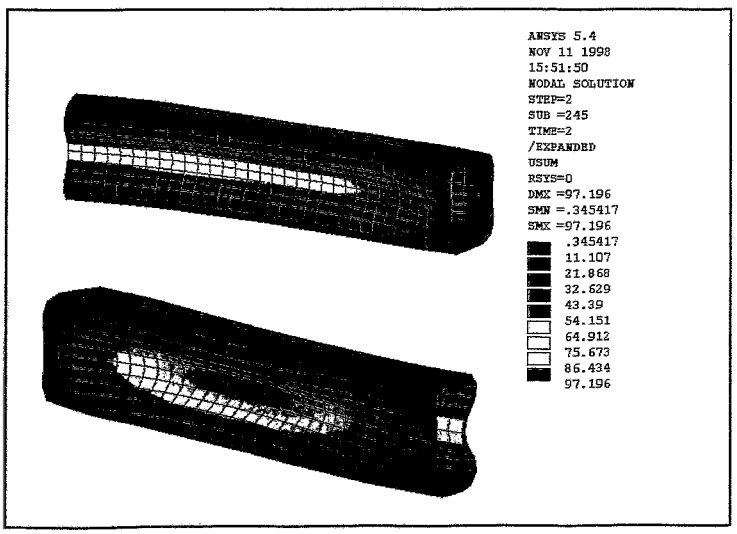

Fig. 12: Deflection (mm) of the ring line at 100% load. Static calculation, volume model. View to the inner wall (upper figure) and to the outer wall (lower figure).

Fig. 12 shows the deflection of the structure at 100% load and Figure 13 the plastic equivalent

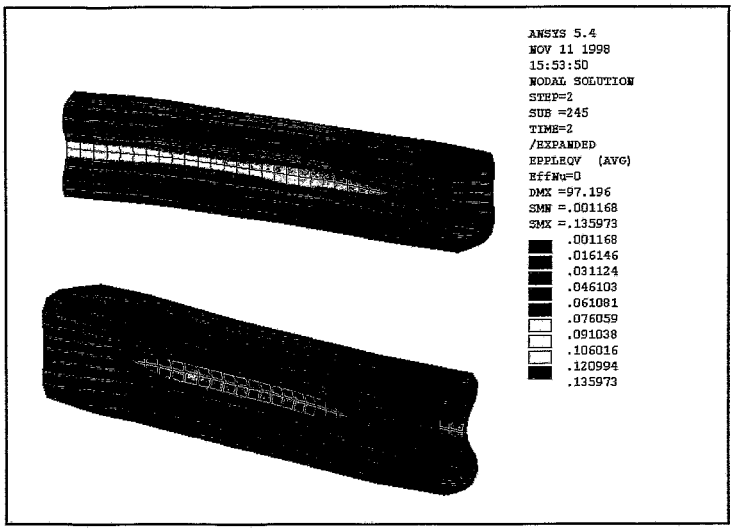

Fig. 13: Plastic equivalent strain of the ring line at 100% load. Static calculation, volume model. View to the inner wall (upper figure) and to the outer wall (lower figure).

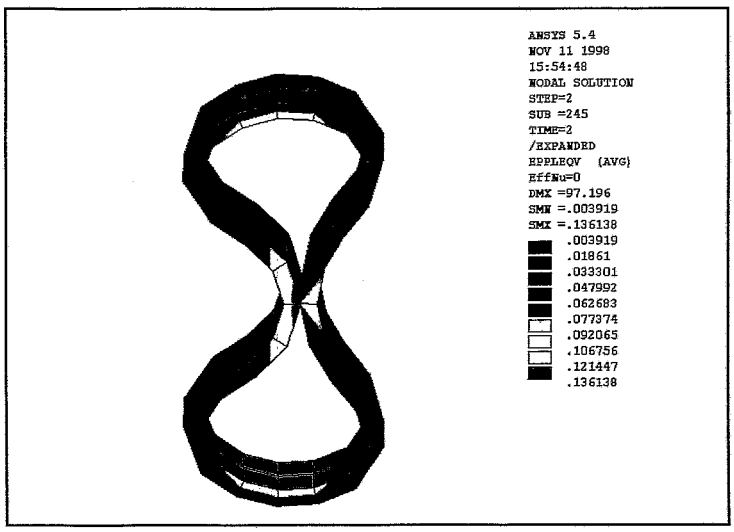

Fig. 14: Plastic equivalent strain of the ring line at 100% load. Static calculation, volume model. View to the ring line cross section at 15 °. Left side is outer wall.

strain. Inspite of the large deflection the maximum strain (0.14) is clearly below the fracture strain (0.44). Figure 14 shows a detail of the strain distribution to demonstrate that there is contact between the opposite walls. The maximum deflection of the outer wall is larger than that of the inner wall. The maximum equivalent stress is about 320 MPa. This agrees to the σ-ε curve of the FWD steel (Fig. 9). The static calculation with the shell model exhibits a worse convergence in comparison with the volume model. At a relative load factor greater than 58% the solution is not convergent.

For the transient calculation the deflection and the relative load factor are displayed versus time (Fig. 15). The relative load factor (blue) corresponds to the part of the pressure curve in Fig. 12 between 0.04 s and 0.056 s. It is to be seen that there is a remarkable time delay between the maximum pressure peak and the response of the structure. At 100% load there is only a deflection of 15 mm at both vertical walls. This is a consequence of the intertia of the material which acts as an additional resistance in the beginning of the deformation. But at the time of the maximum pressure peak there is a high velocity of deformation, and the kinetic energy promotes a further deflection even when the load is already decreasing again. The motion is only stopped when contact between the walls takes place. The maximum deflection and the maximum strain are very similar to those of the static calculation. The maximum strain is 0.13. The maximum deflection of the outer wall is 85 mm and that of the inner wall is 70 mm. The corresponding values from the static calculation are 97 mm and 58 mm. This means that the deformation of the ring line cross section calculated in the transient analysis is not as skew than that calculated in the static analysis. According to the maximum stresses and strains the static solution is sufficiently precise.

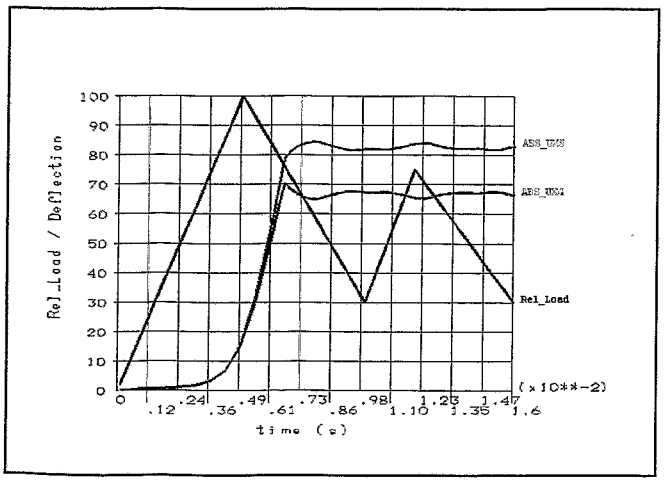

Fig. 15: Transient analysis of the ring line. Deflection curves vs. time for nodes at the inner wall (red) and the outer wall (green) at azimutal position 15°. Relative load vs. time (blue).

5. Conclusions

Within the considered scenario - break of a BWR feed water line - the ealsticity limit of the feed water distributor is exceeded. Hence the stress analysis has to be done with consideration of material and geometrical non-linearity. Within a static analysis the arc-length procedure is an adequate numerical tool to handle instabilities occuring with the buckling of the FWD ring line. However, a convergent solution up to 100% load could only be obtained with volume elements. The shell elements which were also used proved not to be sufficiently stable. The results of the transient analysis show that there is a time delay between maximum load and maximum deflection. The maximum stresses and strain do not differ significantly between static and transient solution. Inspite of the large deformation the FWD ring line the maximum strain remains clearly below the break limit.

References

Hughes, T.J.R. (1987), The Finite Element Method - Linear Static and Dynamic Finite Element Analysis. Prentice-Hall International Editions.

Zienkiewicz, O.C. (1977), The Finite Element Method, Maidenhead, McGraw-Hill Book Company.

Kolar, R. and H.A. Kamel (1986), On some efficient solution algorithms for nonlinear finite element analysis. In: Finite Element Methods for Nonlinear Problems, Heidelberg, Springer-Verlag Berlin, Editors P. Bergan, K.J. Bathe and W. Wunderlich.

Bathe, K.J.(1982), Finite Element Procedures in Engineering Analysis, Prentice-Hall, Englewood Cliffs.

Mattiasson, K., A. Bengtsson, A. Samuelson (1986), On the accuracy and efficiency of numerical algorithms for geometrically nonlinear structural analysis. In: Finite Element Methods for Nonlinear Problems, Heidelberg, Springer-Verlag Berlin, Editors P. Bergan, K.J. Bathe and W. Wunderlich.

THE INFLUENCE OF FLUID-STRUCTURE INTERACTION UPON THE VIBRATIONS OF VVER-1000 TYPE REACTORS

Eberhard Altstadt, Matthias Werner, Sergey Perov [1]

1. Introduction

For vibration monitoring of nuclear reactors which became a standard procedure of plant surveillance it is important to know the dynamical behaviour of the reactor pressure vessel (RPV) and its internals. The vibrations of structures which contain a fluid or which are surrounded by a fluid can considerably be influenced by the interaction between fluid and structure. It is well understood that the influence of the fluid-structure interaction (FSI) is especially strong in the case of a narrow gap filled with the fluid (Paidoussis [1]).

FSI problems can be treated in different ways. One group of methods is based on approximate 1D or 2D analytical solutions (Chen and Rosenberg [2]; Paidoussis and Pettigrew [3]). Though very effective, these methods are commonly restricted to simple geometries (e.g. straight pipes, cylindrical shells, annular gaps, rectangular tanks etc.) because they are based on global approaches for the coupled equations of motion. The theory for analytical approaches of cylindrical structures was described by Altstadt et al. [4,5]. There it was shown that this approximation can be used in two ways:

- recalculation of the shell mode eigenfrequencies obtained without FSI by a factor (correction of the „dry" shell model)
- development of a fluid-structure element (FSE) for annular gaps

The second group of methods is based on numerical solutions. The structure is modelled using the finite element technique, whereas the fluid can be modelled by finite elements (FE) or finite volumes. Because of the local approach there are almost no restrictions related to the geometry of the system. The problem is the coupling between the fluid model and the structural model because the fluid equations are based on the Eulerian representation and the structural equations on the Lagrangian representation. In most cases the models are based on different codes so that the coupling can be realized only externally. The fluid pressure at the interface is applied to the structure as surface load and the structural motion at the interface is applied as boundary condition to the flu[1]id. This requires a data exchange between the models in each time step. As a consequence the computer time needed is much higher than for pure structural analyses or pure fluid analyses. Thus the external coupling of FE codes and CFD codes is practically limited to a moderate model size (depending on the computer performence). The internal coupling of fluid and structure equations employing the Arbitrary Lagragian-Eulerian (ALE) formulation is still under development (Nomura and Hughes [6]).

An alternative method to analyse FSI systems with complex geometry is the modelling of the fluid using displacement based finite elements with appropriate material properties. This is possible for slightly compressible fluids and if the fluid equations can be linearized (i.e.

---

[1] Bauman Moscow State Technical University, Russia

neglecting the convective acceleration). In this paper the FE method is applied to model the reactor pressure vessel (RPV), the core barrel (CB), the thermal shield (TS), the core, the upper core support structure and the coolant of a VVER-1000 reactor. The eigenfrequencies and mode shapes are calculated with and without FSI. To prove that this method is working well, it is at first applied to a fluid-shell test system which was used by Chen and Rosenberg [2]. Additionally, some simple analytical approaches to consider FSI with cylindrical structures are discussed.

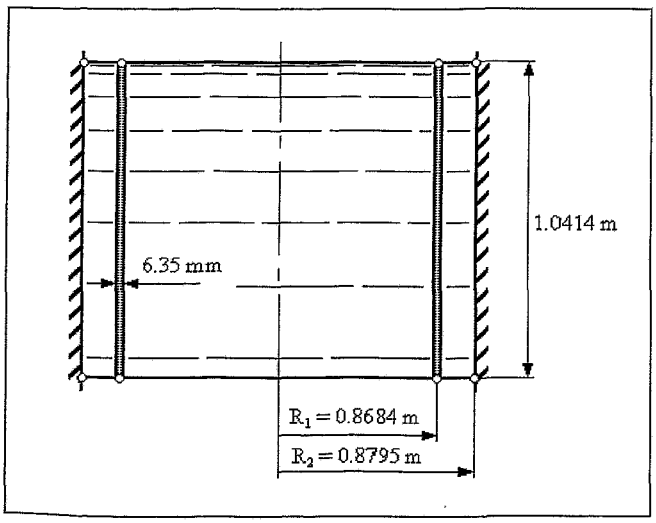

Fig. 1: The Fluid-shell test system by Chen and Rosenberg [2]

2. Numerical investigation of a fluid-shell test system

Figure 1 shows the fluid-shell system investigated by Chen and Rosenberg [2]. A hinged cylindrical shell is surrounded by an outer fluid and contains an inner fluid. This test system was selected because the outer fluid gap is rather narrow and the diameter to gap width ratio corresponds approximately to that of PWR internals. Chen and Rosenberg developed a semi-analytical solution for the eigenfrequencies of this system based on Fluegge's shell theory and a potential approach for the fluid. This solution is refered to as „exact solution" in the following.

For this shell-fluid system the FE model was developed to prove the numerical method to be sufficiently precise especially in view of the extreme narrow outer fluid gap. The FE code ANSYS was used. The external fluid gap is modelled with only one layer of FLUID80 elements over the gap width. Therefore, it is important that the nodes of the fluid elements and the nodes of the shell are only coupled in radial direction. Figure 2 shows the eigenfrequencies for the circumferential

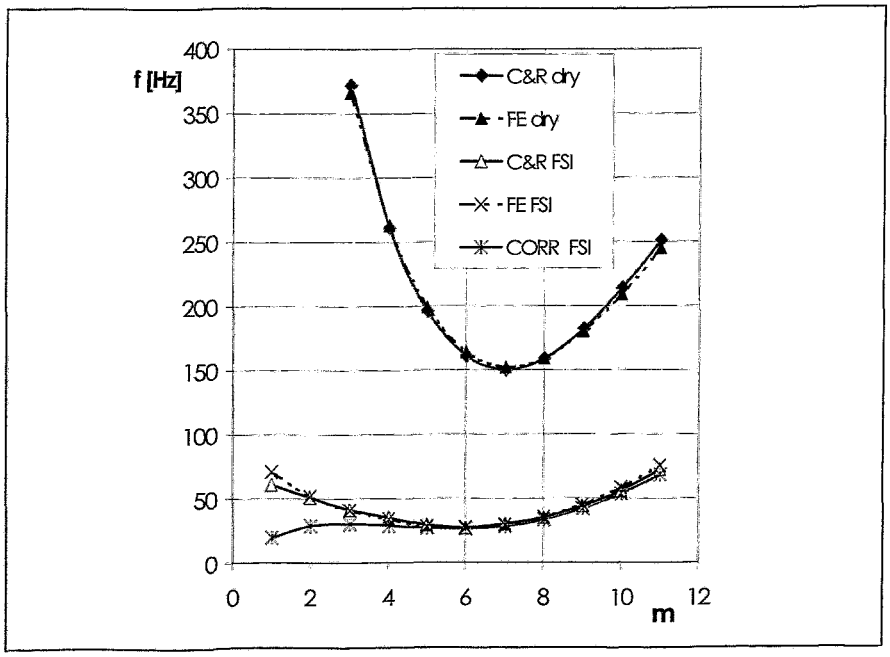

Fig. 2: Comparison of the eigenfrequencies for the fluid-shell test system

modes m = 1 ... 11. In this case the axial mode number is n=0.5. That means, the shapenof motion of the test cylinder corresponds to a sinus-halfwave in the axial direction. The upper two curves are for the dry shell (no fluid), the lower curves are for the shell fluid system. The modes m=1 and m=2 for the dry case are not displayed because their frequencies are above 500 Hz. The agreement between the exact solution and the FE solution is very good in both cases. The largest error of about 10 % appears for the mode m=1 (beam mode) for the case with fluid. In view of the fact that this mode is lowered about 10 times due to the FSI (from about 700 Hz to 70 Hz) this is still an excellent agreement.

Table 1: Eigenfrequencies of the fluid-shell test system [Hz]

Mode number	DRY	FSI	
	FE solution	FE solution	Approximate solution [4,5]
1	700	71	19.7
2	516	51.6	28.8
3	366	41	30.4
4	263	34	28.9
5	199	28	27
6	164	27.2	26.5
7	152	29.4	28.3
8	159	35.4	33.5
9	180	44.8	42.2
10	209	58.3	53.8
11	245	75.6	68.5

Table 1 shows the eigenfrequencies of the FE-solution, and the approximate solution for the FSI case. The approximate solution overestimates the influence of FSI, especially such modes where the dry shell frequency is rather high (m=1,2). This is due to the assumption that there is no repressed flow in the axial direction.

3. Vibration modes of the VVER-1000 reactor pressure vessel internals

Figure 3 shows a principal scheme of the VVER-1000 RPV and its internals. Two FE models were developed for the vibration analysis: a 3D shell-volume model and a 1D beam model. The shell-volume model consists of the RPV, the CB and the TS (meshed with shell elements) and the coolant in the downcomer and in the gap between CB and TS (meshed with volume elements). The RPV head, the core, and the upper core structure are represented in a simplified way by beams and pointed masses. The coupling between fluid elements and structural shell elements is shown in Fig. 5. At the TS wall also the vertical DOFs are coupled, because the TS wall exhibits small circumferential ribs (Fig. 3, detail). The beam model comprises the RPV with internals and the RPV head (modelled by beam and pipe elements, Fig. 4). The FSI in the downcomer and in the CB-TS gap is represented by the FSEs discussed in [4]. This global model can of course only describe the bending and vertical modes of the system.

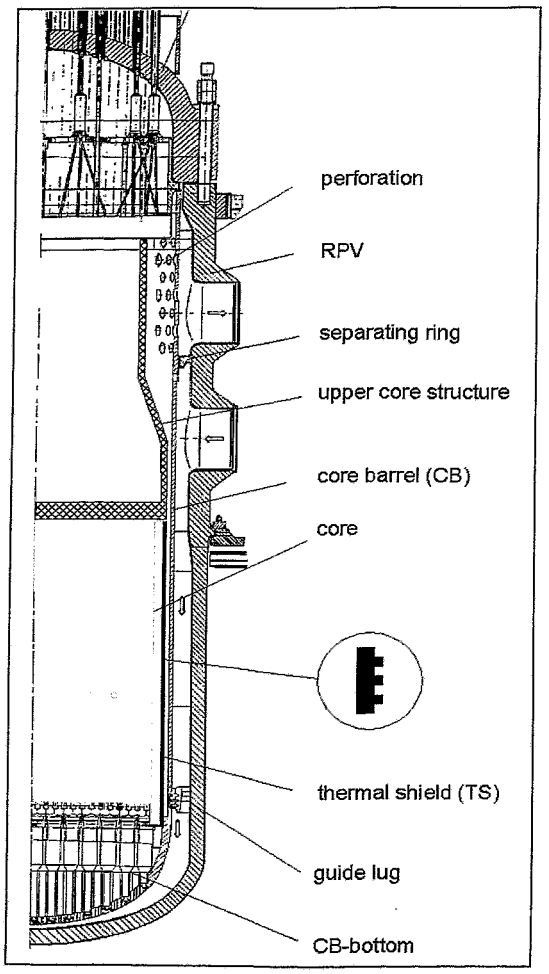

Fig. 3: Scheme of the VVER-1000 pressure vessel internals

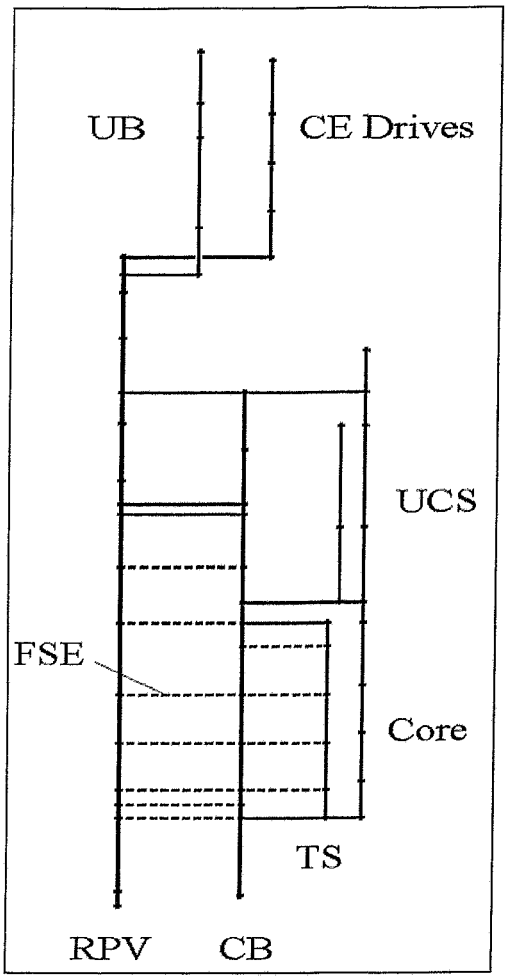

Fig. 4: Global vibration model (beam model) with FSE

Table 2 shows the eigenfrequencies of the FE shell model of the RPV with its internals without and with coolant. The results for the approximate consideration of the FSI are listed in the 3rd column. To show the influence of the guide lugs on the bending modes of the CB, two cases are considered: 1. guide lugs are not in contact with the CB slots and 2. full contact between guide lugs and CB slots. The shell modes do not depend on the fixation of guide lugs due to the extremely stiff bottom of the CB.

Table 2: Eigenfrequencies [Hz] and mode shapes of the shell model

No fluid FE	With fluid FE	With fluid Approx.	Shape of modes
13.8	9.7	-	CB, m=1 (no guide lugs)
41.2	33.5	-	CB, m=1 (with guide lugs)
58	8.5	-	TS, m=1
61.6	9.8	(12.8)	TS, m=2
62.4	13.6	12.1	CB, m=3
77.2	22.2	19.6	CB, m=4

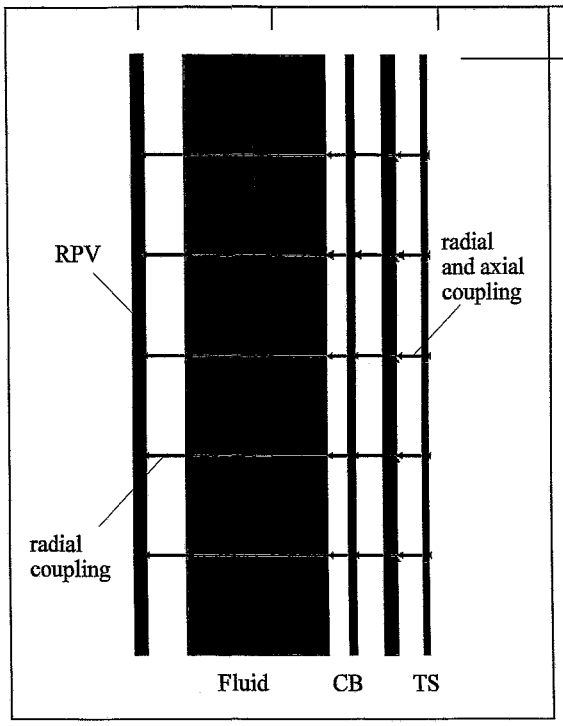

Fig. 5: Coupling between shell elements and fluid volume elements

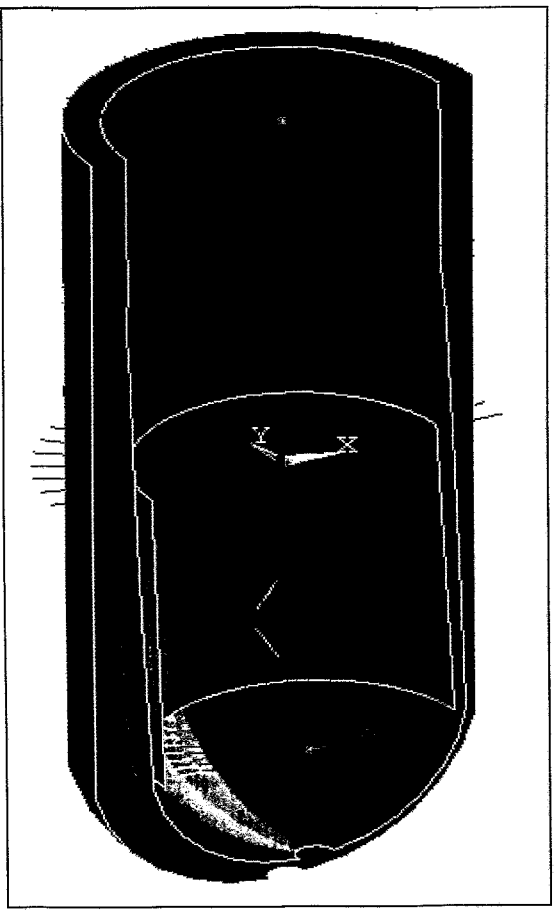

Fig. 6: Vibration mode CB, m=1 at 9.7 Hz (without guide lugs) calculated with the FE model. The color indicates the radial displacement

The FE solution demonstrates that all eigenfrequencies are significantly shifted down due to the FSI. As an example Fig. 6 shows the bending mode (m=1) of the CB without contact of guide lugs.

The modes m=2 of TS and CB have the same eigenfrequency (9.8 Hz, FE solution) if the fluid is present. In fact these modes are coupled and merge into one mode. Therefore, the frequencies of the approximate solution for these modes are set in brackets in Table 2. The modes m=1 (bending modes) cannot be calculated with the approximate solution because these modes depend on the masses of the CB internals (core, core supporting structures). These internals cannot be considered within the approximate solution.

Table 3 shows a comparison of the beam modes of the RPV with internals calculated by the shell-volume model and by the beam model respectively.

Table 3: Comparison of eigenfrequencies [Hz] for shell and beam models

No Fluid			With Fluid		
Shell model	Beam model	Shape of modes	Shell model	Beam model	Shape of modes
41.2	42.9	CB-beam	8.5	8.3	TS-beam
58.7	60.3	TS-beam	33.5	26.5	CB-beam

The deviation between the eigenfrequencies of the dry models (without coolant) is rather small, thus it can be stated, that the beam model describes the bending modes of the shell structure correctly. The accuracy of the FSI representation in the beam model depends on the vibration mode, the agreement between the TS-beam modes are very good whereas for the CB-beam modes there is a deviation of about 20 %. The reason for this is that the TS wall is not smooth but exhibits small circumferential ribs. Thus the axial fluid motion is prevented at that wall and the influence of the FSI is stronger than at a smooth wall. Since the FSE is based on the assumption that no repressed axial fluid motion takes place, it represents the FSI in the TS-CB gap pretty well. In contrast to that, the CB and the RPV wall are smooth, so that the FSE overestimates the influence of FSI in the RPV-CB gap.

4. Conclusions

The FE modelling provides an accurate description of the FSI in gaps. The free slip condition at interface between fluid and structural nodes is essential. Analytical approximate solutions for cylindrical annular gaps can efficiently be used to correct the shell mode eigenfrequencies obtained without FSI, and to represent the FSI in structural beam models by a fluid-structure element. The analytical approach slightly overestimates the influence of FSI. The FSI considerably influences the eigenfrequncies of the shell modes and the beam modes of the CB and TS of VVER-1000 reactors. The RPV itself has no shell modes in the frequency range up to 100 Hz due to its large wall thickness. For the same reason the influence of FSI on pendulum or bending modes of the RPV itself is insignificant.

References

[1] M. P. Paidoussis (1998), Fluid-Structure Interactions - Volume 1: Slender Structures and Axial Flow. Academic Press.

[2] S. S. Chen, G. S. Rosenberg (1975), Dynamics of a coupled shell-fluid system, Nuclear Engineering and Design 32, pp. 302-310

[3] M. P. Paidoussis, M. J. Pettigrew (1979), Dynamics of Flexible Cylinders in Axisymmetrically Confined Axial Flow. Journal of Applied Mechanics Vol. 46, pp. 39-45

[4] S. Perov, E. Altstadt, M. Werner (1999), The influence of fluid-structure interaction upon the vibrations of VVER-1000 type reactors

[5] E.Altstadt, G. Grunwald, M. Scheffler, f.-P. Weiß (1997), Analytische Modellierung mechanischer Schwingungen von Primärkreiskomponenten des Druckwasserreaktors WWER-440 mit finiten Elementen,Rossendorf, Report FZR-172

[6] T. Nomura, T.J.R. Hughes, (1992): An arbitrary Lagrangian-Eulerian finite element method for interaction of fluid and a rigid body. Computer Methods in Apllied Mechanics and Engineering 95 , pp. 115-138

MODELLING THE RPV LOWER HEAD UNDER THE LOAD OF A SEGREGATED METAL-OXIDE CORIUM POOL

Hans-Georg Willschütz

1. Introduction

For future nuclear power plants it is demanded that there are no consequences for the environment and the population even in the closest vicinity of the plant during and after every possible accident scenario [1]. This includes the hypothetical scenario of a severe accident with subsequent core meltdown, corium relocation and formation of a melt pool with internal heat sources in the reactor pressure vessel (RPV) lower head (LH). Some reactor concepts have the aim to arrest the melt in the lower head removing the decay heat by external water flooding [2, 3]. In other concepts a dry reactor pit is designed and after the vessel failure a core catcher shall assure the long term stabilization of the corium within the containment.

For both strategies investigations on the transient behaviour of the RPV are necessary. Two kinds of vessel failure can be distinguished: thermal and structural failure. Thermal failure means that the heat flux through the vessel wall becomes so high that the steel solidus temperature at any position of the vessel outside is exceeded. Structural failure means that a combination of thermal and mechanical loads causes the failure, e. g. the wall thickness of the vessel is reduced by thermal ablation and at the same time the internal pressure and the gravitational forces induce creeping with subsequent creep failure.

Different melt configurations can be assumed. They can be distinguished by the melt masses released into the LH, the melt composition, the segregation behaviour of the oxidic and the metallic component, and the density and the distribution of the internal heat sources. One of the most dangerous accident scenarios for a pressurized water reactor (PWR) assumes the relocation of a melt mass in the range of 200 Mg or more which is segregated into some 150 Mg of the heavier oxidic component at the bottom and some 50 Mg of a metallic melt above (cf. Fig. 1). The oxidic melt is surrounded by an oxidic crust due to the high solidification temperature of the oxide. The internal heat sources are mainly in the oxidic component, but due to the geometric configuration and the different fluid properties the highest heat fluxes and the major thermal ablation is expected between the metallic layer and the vessel wall. This phenomenon is called focussing effect.

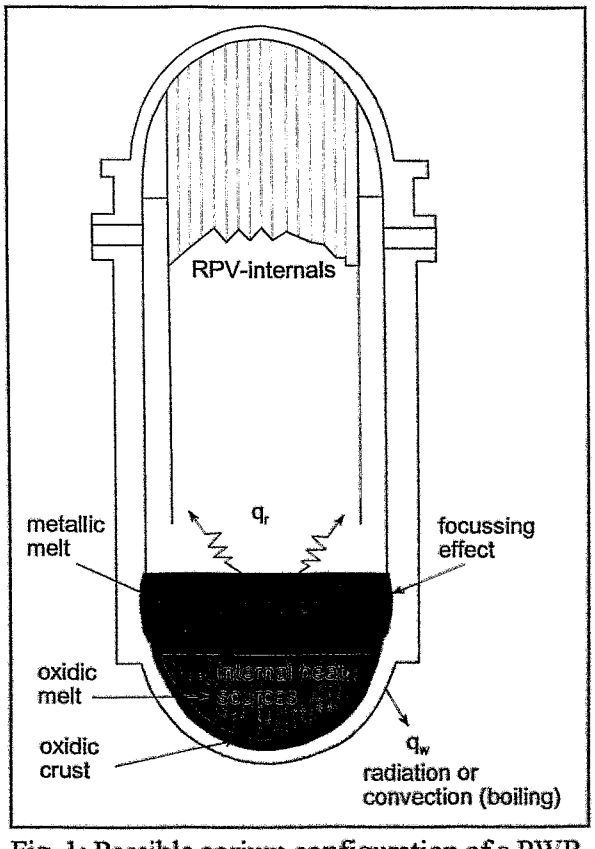

Fig. 1: Possible corium configuration of a PWR.

An in-vessel-scenario of a PWR has been assumed and modelled with ANSYS/ Multiphysics. Using this Finite Element (FE) code package it is possible to simulate the velocity and temperature field for a fluid region and the corresponding temperature field within the surrounding solid structures. This thermo-fluiddynamic calculation can be coupled with a mechanical FE-model of the solid structures to analyse the stress and possible creeping forced by the mechanical and thermal loads. In this report, the recent modelling approach and the results obtained with the code ANSYS/Multiphysics are discussed. An outlook on the further development is given.

2. Description of the thermo-fluiddynamic model

Due to computational limitations 2D simulations of the problem were performed with ANSYS. An axisymmetric model was developed comprising the LH of the RPV with a two component melt. An oxidic crust is considered between the oxidic melt and the metal layer and between the oxide and the LH. The problem domain is meshed with the element type *fluid141*, these are quadrilateral elements with four nodes, one in each corner. For the considered problem each node has 6 degrees of freedom (DOF): temperature T, pressure p, horizontal velocity v_x, vertical velocity v_y, turbulent kinetic energy k, and turbulent kinetic energy dissipation rate ε. The problem domain was meshed with 3400 elements. For further information how to model this problem with ANSYS/Multiphysics in detail the reader is referred to the code description [4] and a comparable problem described in the FZR-report [5]. In the following, the boundary conditions and material properties are described. All quantities in the model are SI units (m, kg, s); temperatures are given in K.

2.1 Initial and boundary conditions

For the initial state of the calculations it is assumed that the corium is located in the lower head (see Fig. 2). The total mass of the oxidic components is 152 Mg and 51 Mg for the metallic components. Both phases have segregated, are separated by an oxidic crust, and have an initial temperature of T_0=2275 K. Internal heat sources are modelled with constant values of 200 kW/m^3 within the metallic pool and 1,500 kW/m^3 for the oxidic pool. At the upper surface of the metallic pool and at the inner free surface of the RPV wall radiation heat transfer is modelled with an ambient temperature of 1400 K and an emissivity of 0.4. At the RPV outside flooding is assumed and a simple convection model is applied with a heat transfer coefficient of 1000 W/m^{2}K and a bulk temperature of 373 K (cf. Fig. 2). The initial temperature of the vessel wall is set to 673 K. At the beginning the fluid is standing still.

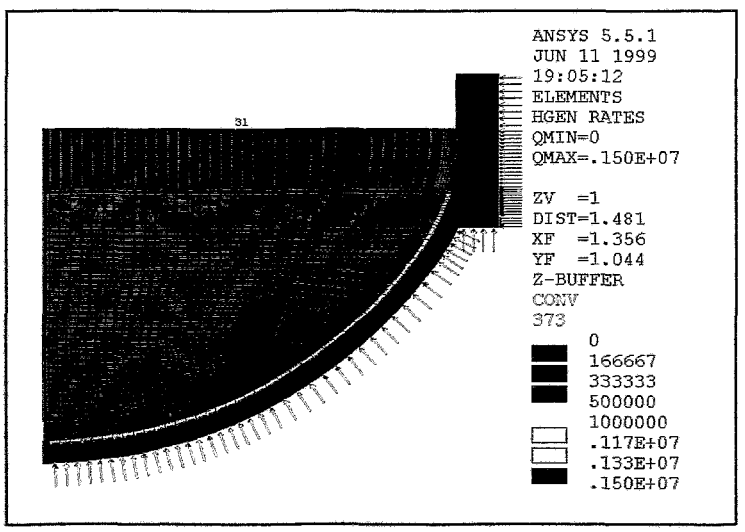

Fig. 2: Thermal boundary conditions of the FE-model.

2.2 Material properties

The material properties have to be defined for two fluids and two solids: the oxidic and the metallic melt components, the solid oxidic crust, and the RPV steel. Over the considered temperature range, the dynamic viscosity of the liquid components is assumed to be constant at $\mu_{met}=2.5\cdot10^{-3}$ Pa·s for the metallic phase and $\mu_{oxi}=25.0\cdot10^{-3}$ Pa·s for the oxide. The temperature independent thermal conductivity is set to $\lambda_{met}=20.0$ W/mK and $\lambda_{oxi}=2.21$ W/mK for the two components. Also the heat capacity is modelled with constant values of $c_{p,met}=750$ J/kgK and $c_{p,oxi}=602$ J/kgK for the metal and the oxide respectively. The Oberbeck-Boussinesq-approximation cannot be chosen for the temperature dependency of the density in ANSYS. With the usual Boussinesq-approximation the density becomes constant in all equations except for the buoyancy term of the equation of motion. Contrary to this, the temperature tracking of density is considered in all equations in the ANSYS-model for both components. For the calculations reference densities of $\rho_{0,met}=6450$ kg/m^3 and of $\rho_{0,oxi}=9060$ kg/m^3 have been defined at the assumed initial temperature of the melt configuration of $T_0=2275$ K. The volumetric coefficient of expansion was set to $\beta=5.0\cdot10^{-5}$ 1/K for both components. The thermal properties of the oxidic crust are the same as those of the liquid oxide. Mechanical properties are not defined, because the oxide is not considered in the mechanical model. For the solid steel parts of the model the temperature dependent material properties have been set to typical values of a ferritic steel: the thermal conductivity ranges from $\lambda_{fer}(T=293\ K)=44.5$ W/mK to $\lambda_{fer}(T=1700\ K)=26.5$ W/mK and the heat capacity changes between $c_{p,fer}(T=293\ K)=463$ J/kgK and $c_{p,fer}(T=1700\ K)=625$ J/kgK.

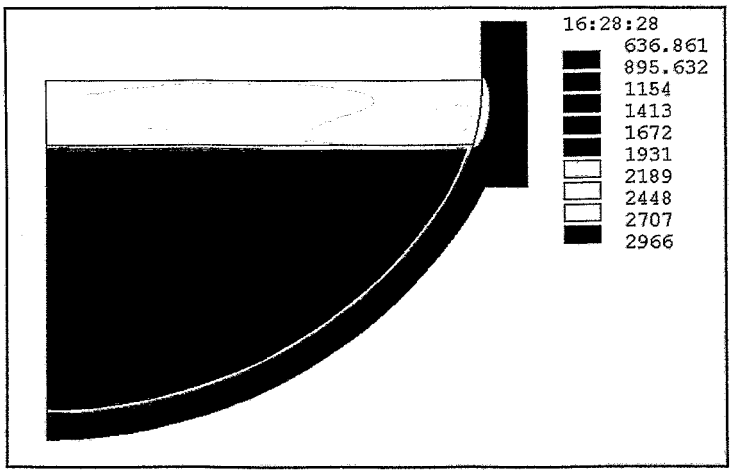

Fig. 3: Temperature field after t=3000 s. Temperatures in K.

3. Transient thermo-fluid-dynamic calculation

Due to the large variation of physical properties within the calculational domain the simulation results in a numerically ill conditioned problem. Therefore, the FE-mesh and the solution options have to be set carefully to get converging and reasonable solutions.

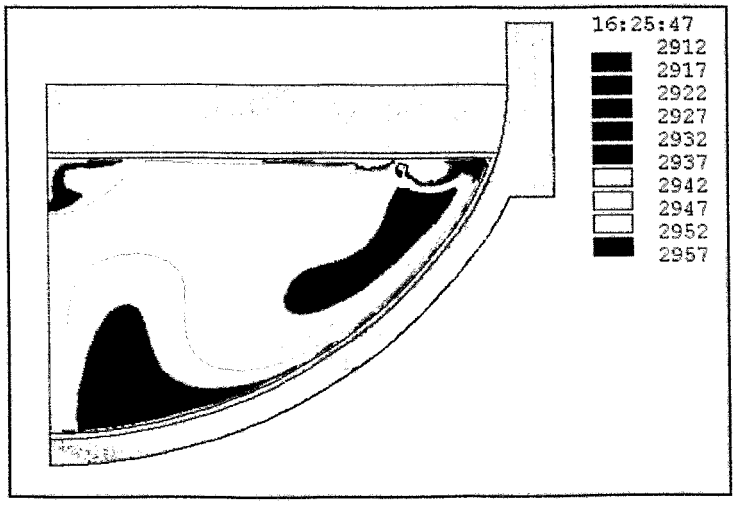

Fig. 4: Temperature field after t=3000 s within the oxidic phase. Temperature scale adjusted. Temperatures in K.

For the transient thermo-fluid dynamic calculation a time step of Δt=1.0 s was used. Due to the large result files generated for a transient calculation and the long calculation time, at present only a time range up to 5000 s has been simulated. Until this time the melt configuration shows a transient behaviour (see Fig. 3): the oxidic layer is heated up due to the internal heat sources and the bad heat transfer whilst the metallic layer cools down due to the radiation heat transfer at the free surface and the strong convection heat flux into the vessel wall. Although melting is not modelled within this stage of the simulations the focussing effect can be confirmed for this melt configuration. Because of the very large temperature range between the outside of the vessel wall and the hot oxidic melt the contour plot in Fig. 3 shows a homogenous temperature within the oxide. In Fig. 4 the temperature range has been adjusted to show the temperature distribution within the oxide in detail. The temperature and the velocity field (cf. Fig. 5) within the oxidic pool do not show the same behaviour than it was observed in experiments with comparable internal Rayleigh numbers (10^{15} - 10^{17}) (e. g. [6, 7]). On the one hand this can be caused by different physical properties and boundary conditions. On the other hand the numerical model could be too coarse - especially near the vessel wall - or the applied k-ε-turbulence model [8] has to be modified to get more accurate results. Therefore, post-test calculations of these single fluid experiments are planned to validate the CFD-part of the simulation.

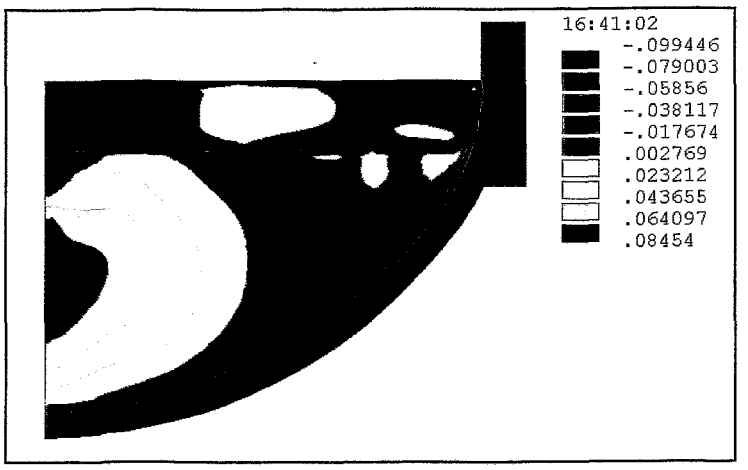

Fig. 5: Vertical velocities [m/s] after t=3000 s.

4. Modelling the creep process

For the mechanical calculations isotropic material behaviour is assumed. The Young's modulus was defined between E(T=293 K)=210 GPa and E(T=1700 K)=7.3 GPa. The thermal expansion coefficient ranges from α(T=293 K)=10.6·10^{-6} 1/K to α(T=1700 K)=15.6·10^{-6} 1/K. After the transient calculation of the temperature field within the corium and the vessel wall a transient calculation of the creep process can be performed applying the temperature field as a body load to the solid vessel structure. In Fig. 6 the temperature field after t=3600 s is shown for the mechanical model.

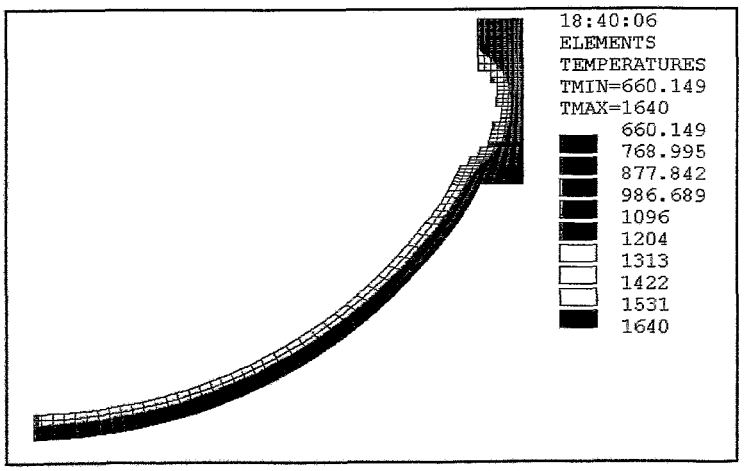

Fig. 6: Temperature field [K] as body load for the transient mechanical calculation of the creep behaviour.

Using the Element-Birth-and-Death option all RPV-wall elements with temperatures above

1700 K have been killed. That means these elements do not contribute to the stiffness of the model. For test calculations the temperature field has been applied statically for a time range up to 24 h. In future calculations the temperature field will be read and applied periodically. A primary creep equation provided by ANSYS has been activated:

$$\Delta\varepsilon_{Cr} = C_1\ \sigma^{C_2}\ t^{C_3}\ e^{-(C_4/T)}\ \Delta t \qquad (1)$$

where $\Delta\varepsilon_{Cr}$ is the creep strain increment during the time step Δt at the total transient time t,the current stress σ, and temperature T. The constants in the equation have been set to values regarding the expected temperature and stress range in accordance to the results found by GRS [9, 10] in the field of structural analysis methods. According to the applied conditions the transient calculation has been performed in 108 time steps with a step width of Δt=800 s. The creep ratio for each substep is calculated according to equation (1). First calculations showed that the RPV is in such a good condition - assuming the thermal loads after t=3600 s for the whole time range - that it can even withstand a typical normal operation pressure of a PWR of 16.4 MPa. Fig. 7 shows the equivalent stresses after a transient calculation time of t=3600 s. Considering the results of this simple model it can be stated that the maximum equivalent stresses at the outer side of the vessel are below the maximum tensile strength of a typical RPV steel at the corresponding temperatures. Figure 8 shows the vertical displacement of the lower head after a time of 24 h if the temperature and pressure load are assumed to be constant. Noting that the model is fixed in vertical direction at the upper section line, a maximum displacement of 76 mm can be found at the centre of the RPV bottom. However, this calculation does not take into account the further heat-up of the RPV wall during the creep process.

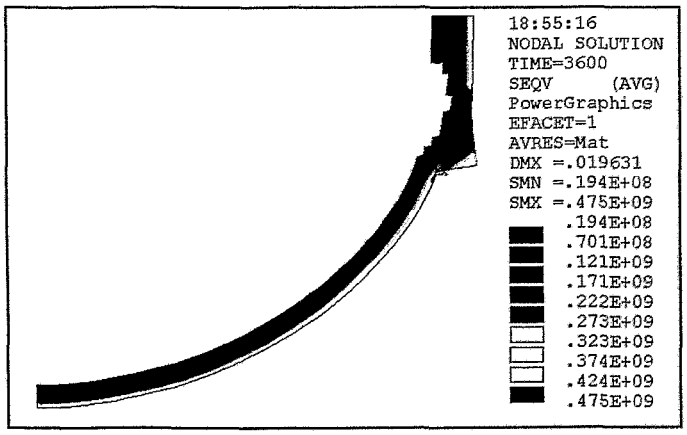

Fig. 7: Equivalent van-Mises-stress [Pa] after t=3600s.

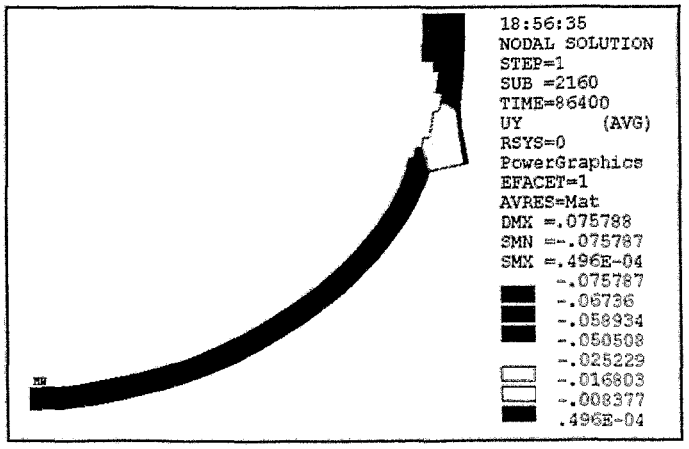

Fig. 8: Vertical displacement [m] after t=24 h.

5. Further development and outlook

The present stage of model development shows that it is possible to simulate the transient behaviour of a RPV under the conditions of different corium pools using ANSYS/Multiphysics. The great advantage of this modelling approach consists in the flexible and fast coupling of the CFD-simulation and the structural analysis. Due to computational

limitations it seems not to be possible to perform 3D-calculations within the next future. The further development can be divided into two parts: the thermodynamic and the structural model improvement. For the CFD-model a validation to comparable experiments is necessary. This can result in the necessity to adjust the turbulence model or even to implement a Low-Reynolds-k-ε-model. Furthermore the development of a melting and solidification model is planned. For the structural part the implementation of new creep models regarding especially the transient temperature and stress conditions has to be finished. A good validation of the whole FE-model will be possible by performing calculations of the FOREVER (Failure Of REactor VEssel Retention) experiments [11]. These are scaled experiments simulating a RPV LH with a corium pool inside under medium pressure loads.

References

[1] H. Alsmeyer; H. Werle (1994), Kernschmelzkühleinrichtungen für zukünftige DWR-Anlagen, KfK-Nachrichten, 26, pp. 170-178

[2] T. G. Theofanous, C. Liu, S. Addition, S. Angelini, O. Kymäläinen, T. Salmassi (1997), In-vessel coolability and retention of a core melt, Nucl. Eng. Des., 169, pp. 1-48.

[3] N. I. Kolev, I. Roloff-Bock (1999), Potential for external cooling of boiling water reactors during postulated severe accidents with melt relocation, proceedings of the Jahrestagung Kerntechnik '99 (pp. 287-295), München

[4] ANSYS Code Manual, Release 5.5 (1998), ANSYS Inc., Houston, USA

[5] H.-G. Willschütz (1999), CFD-Calculations to a Core Catcher Benchmark, Rossendorf, Report FZR-257

[6] F. J. Asfia, V. K. Dhir (1996), An experimental study of natural convection in a volumetrically heated spherical pool bounded on top with a rigid wall, Nucl. Eng. Des., 163, pp. 333-348

[7] J. M. Bonnet, J. M. Seiler (1999), Thermal hydraulic phenomena in corium pools: the bali experiment, Proceedings of the 7th International Conference on Nuclear Engineering, ICONE-7057, Tokyo

[8] B. E. Launder, D. B. Spalding (1974): The Numerical Computation of Turbulent Flows. Computer Methods in Applied Mechanics and Engineering 3, pp. 269-289

[9] D. Azodi, P. Eisert, P. Gruner, U. Jendrich, W. M. Kuntze (1995), Beitrag zur Methodenentwicklung für erweiterte Strukturanalysen des Reaktordruckbehälters von Siedwasserreaktoren bei Belastungen jenseits der Auslegungsgrenzen, Abschlußbericht, Köln, GRS-A-2264

[10] D. Azodi, P. Eisert, P. Gruner, U. Jendrich, W. M. Kuntze (1996), Verifizierung und internationaler Vergleich von Strukturanalysemethoden zur Beschreibung des Verhaltens des Reaktordruckbehälters bei Belastungen jenseits der Auslegungsgrenzen, Abschlußbericht, Köln, GRS-A-2338

[11] B. R. Sehgal, R. R. Nourgaliev, T. N. Dinh, A. Karbojian, J. A. Green, V. A. Bui (1998), FOREVER experiments on thermal and mechanical behaviour of a reactor pressure vessel during a severe accident, OECD/CSNI Workshop on In-Vessel Core Debris Retention anCoolability, Garching, Germany.

FLUIDDYNAMIC WATERHAMMER SIMULATIONS WITH CONSIDERATION OF FLUID-STRUCTURE INTERACTION

Thomas Repp

1. Introduction

The design rules for pipe systems of nuclear installations require that also fluid dynamic loads have to be examined (KTA 3201 and 3211 [1], RSK-L. 4.1.1-3,4 [2]). These loads are the result of transient pressure changes, developing due to the acceleration and slow down of the fluid masses. In the past, results were obtained only from fluid dynamic calculations or simulations without consideration of the fluid-structure interaction (FSI) or only by considering the structural influence to the fluid. In the last decade, one-dimensional programs were introduced to simulate the influence of the structure to the fluid but not to explore the feedback from the fluid to the structure (Borchsenius and Bornemann [3]). The topic of this project is to investigate the influence of the dynamic fluid-structure interaction in pipes on the pressure in the fluid and on the reaction loads on the structure to show whether the commonly used formula are conservative or not and when it is necessary to consider the FSI especially with fully-coupled 3D-Codes.
The project this report is based on is included in the initiative for competence maintenance in nuclear technology which is carried by the Verein Deutscher Elektrizitätswerke e.V. (VDEW e.V.) and the German Ministry of Research (BMBF).

2. Theoretical Background

A pressure wave may arise when a valve is closed very fast. Before the valve the fluid masses are slowed down and because of this acceleration a pressure wave occurs which propagates in the pipe with sound velocity (see Fig. 1). It is reflected at the open end of the pipe (change of sign but not of the amplitude) or at a wall or a closed pipe end (no change of sign and same amplitude). When the wave hits a wall considerable mechanical loads may occur. This phenomenon is called a waterhammer.

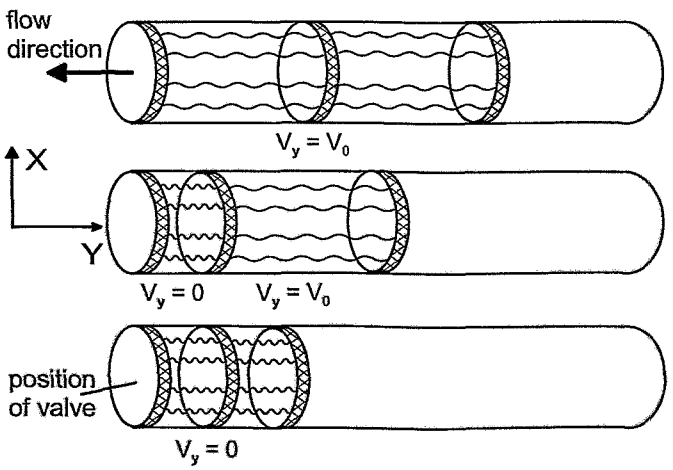

Fig. 1: Fluid compression

Commonly the Joukowsky equation is used to determine the amplitude of the pressure wave.

$$\Delta p = \rho \, c \, \Delta v \tag{1}$$

The Joukowsky equation (1) shows that the pressure change Δp only depends on the density ρ, the sound velocity c, and the change of the fluid velocity Δv. For rigid pipe walls, the sound velocity can be calculated by

$$c_{rigid} = \sqrt{\frac{E_F}{\rho}} \tag{2}$$

with the bulk modulus E_F, being the elasticity of the fluid which is in the range of $2{,}1 * 10^9 \, N/m^2$, and the density ρ in the range of $1000 \, kg/m^3$. To consider the influence of the elastic walls upon the propagating pressure wave in the Joukowsky approximation, the sound velocity is modified according to

$$c_{elastic} = \sqrt{\frac{\frac{E_F}{\rho}}{1 + \frac{E_F}{E_M} \frac{d}{s} K}} \tag{3}$$

Eq. (3) is called the extended Joukowksy formula, which includes also material properties of the structure, like the Young's modulus E_M, the inner diameter d, the thickness of the pipe s and additionally the factor K ($0 \leq K \leq 1$), which depends on the geometry and the fixing of the pipe structure. The K factor is clearly defined only for certain kinds of fixing and in general only for straight pipes (Tijsseling [4]). It is not clear whether the pressure amplitude can be described for pipes with high ratios of the pipe diameter to the pipe wall thickness and with build-ins like pipe bends. It is also unknown whether the maximum pressure amplitude gives enough information to exactly predict the stresses and strains in the pipe structure. But is clear that the locations of the maximum stress and strain cannot be predicted by equations (1) - (3). For that a 3-dimensional simulation is needed.

3. 3D-modeling using ADINA

The simulations are performed using the program system ADINA®, which is a fully coupled fluid and structure code. It is possible to perform transient 1- and 2-phase flow simulations under consideration of dynamic fluid-structure interaction. For the simulation of a waterhammer only 1-phase flow simulation is needed. Even if cavitation occurs, the pressure wave is induced after the condensation of the vapor phase. The interface between the fluid and the structure is modeled with FSI-elements at the structure and special FSI-boundary conditions at the fluid wall. Both together transfer the fluid pressure as load to the structure and the new structural geometry to the fluid within every iteration of every time step. As convergence criteria the relative displacement and stress residuals are used (ADINA R&D [5]). With a fully incompressible fluid it is not possible to simulate pressure waves with a finite sound velocity. Therefore, ADINA® offers the special feature to model slightly compressible fluids. Up to now straight pipes and pipe bends with water flow have been examined with regard to pressure and stress changes within a certain time after the valve closure.

The pressure amplitude, the stress and the strain of the pipe were calculated depending on the ratio of the wall thickness to the diameter and of the diameter to the bend radius. In case of the straight pipe the initial conditions are the pressure level and the axial fluid velocity in the whole volume. In case of the pipe bend the pressure and the fluid velocity obtained from a transient calculation is used as initial condition. The valve closure is simulated by a transient slow down of the fluid velocity at the position of the valve. As boundary condition for the pipe wall it is assumed that the fluid velocity normal to the wall is equal to the local structural velocity. In general, the structural motion causes a change of the pressure in the fluid and due to the fluid reaction forces stresses and strains in the elastic pipe wall. At the location of the valve no translational motion is permitted. The model of the bended pipe consists of the bend and two short straight pipes at its ends. The model is axially fixed at the open ends. The straight pipes are only added to minimize the influence of the support onto the stresses. Therefore, the pressures and stresses are only analyzed at the curved part.

4. Results of the simulations

Figure 2 shows the pressure amplitude over the time for a straight pipe (initial fluid velocity 5 m/s, time of slow down 0,005 ms, inner diameter 0,1 m, wall thickness 3 mm, length 1m) at defined locations of the pipe (see right side of Fig. 2). The extended Joukowksy equation yields $\Delta p = 6{,}275$ MPa (see straight horizontal line in Fig. 2). The maximum pressure is more than 10 % higher than the value predicted with the extended Joukowksy equation. The difference between the averaged pressure amplitude (disregarding the over oscillations) and the analytical solution is smaller than 2,5 %. It can be stated that the average pressure amplitude agrees well with the result of the extended Joukowsky equation.

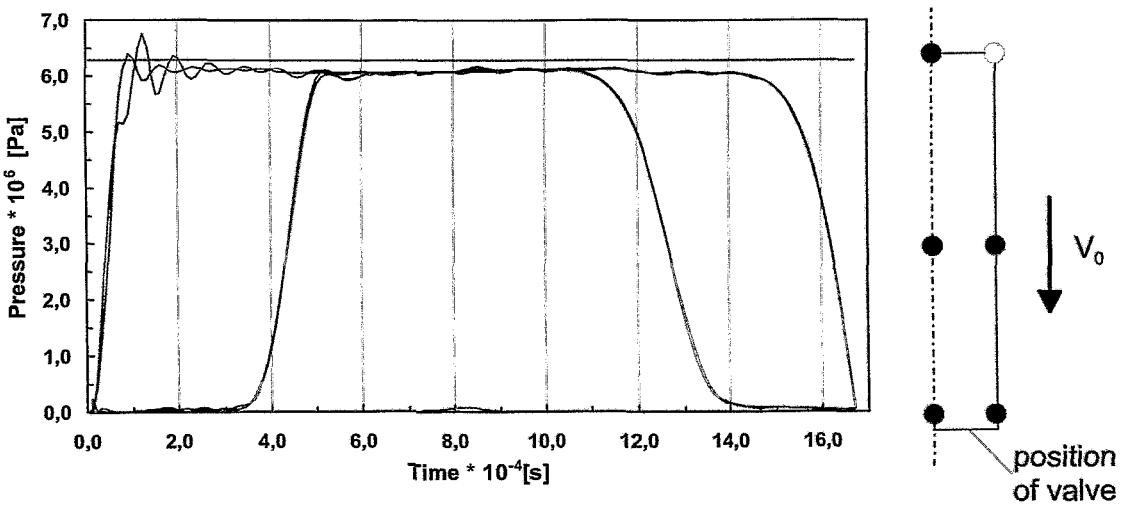

Fig. 2: Pressure over time on the pipe axis and pipe wall (with FSI)

Figure 3 shows the von-Mises-stress for the straight pipe under dynamic pressure load. The static stress because of the static pressure level is not regarded in the simulations and therefore generally needs to be added. Neglecting the oscillations the local maximum stress amplitude is at the same level as the static stress in the same pipe if it was exposed to a static pressure as predicted with the extended Joukowsky equation (straight line at 109 MPa). At maximum pressure (at 0,1 ms) also the maximum von-Mises-stress is found (see Fig. 2 and 3).

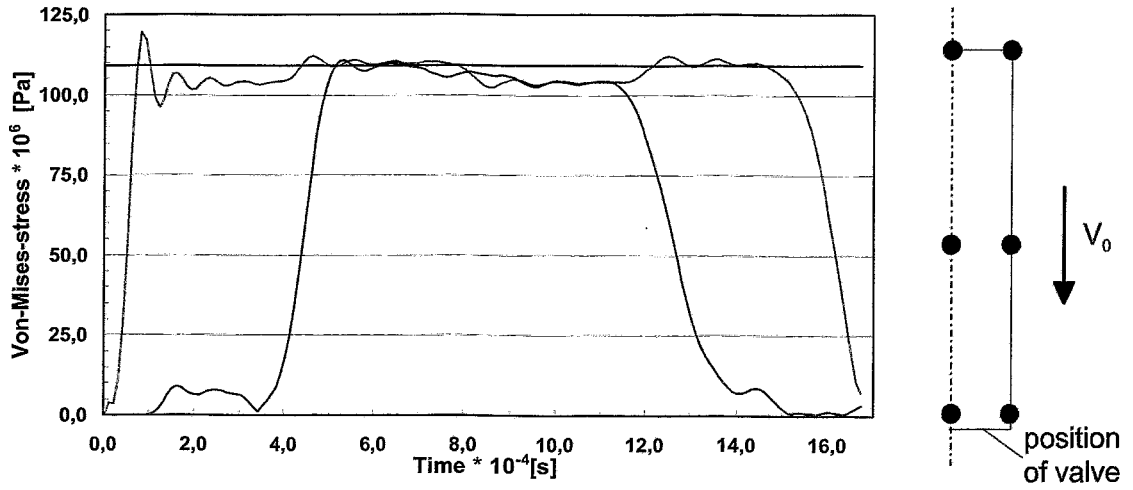

Fig. 3: Von-Mises-stress over time at the inner pipe wall

The response of a pipe bend to a waterhammer differs significantly from that of a straight pipe. Figure 4 shows the pressure amplitude in a pipe bend (initial fluid velocity 5 m/s, slow down time 0,05 ms, inner diameter 0,1 m, wall thickness 2,6 mm, bending radius 0,27 m, bend length 0,424 m) at the inner and outer bend radius under 0°, 45°, and 90°. Additionally the pressure amplitude predicted with the extended Joukowksy equation (horizontal line) is shown. The analytical result is conservative compared with the simulation. But there are unneglectable differences comparing the pressure at the inner and outer bend radius.

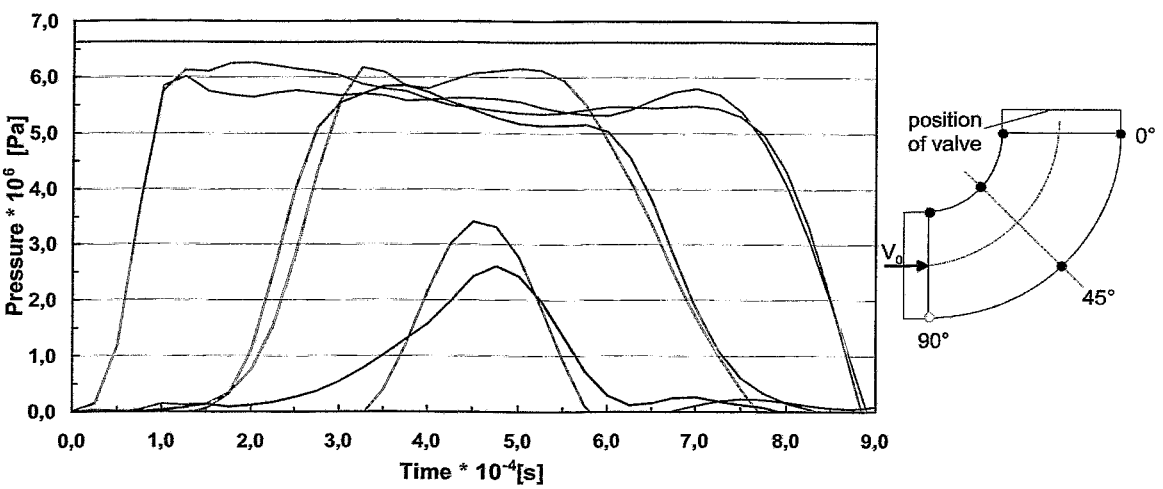

Fig. 4: Pressure over time at specified locations in a pipe bend

Figures 5 and 6 show the maximum Von-Mises-stress for the same pipe bend under dynamic load and under static load (equal to the maximum pressure amplitude predicted with extended Joukowsky). The maximum equivalent static stress is more than 50 % lower than the maximum dynamic stress within the investigated time range. The maximum stress is found at the end of the pipe bend.

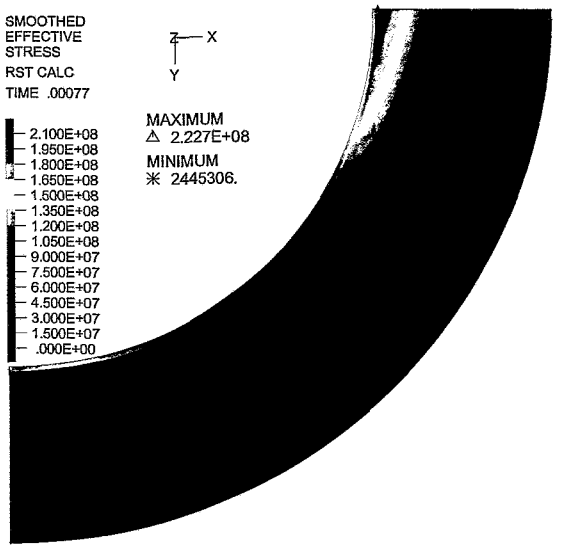

Fig. 5: Maximum von-Mises-stress [Pa] for a calculated pressure wave (accord. to Fig. 4)

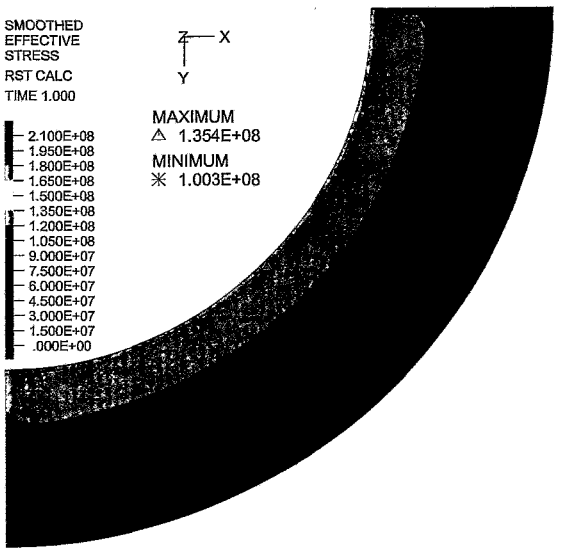

Fig. 6: Von-Mises-stress [Pa] for a static internal pressure according to eq. (1)

Figure 7 shows the decrease of the pressure amplitude (maximum pressure minus static pressure) in dependance on the slow down in a straight pipe for two selected fluid velocities. The maximum pressure, in this case regarded without FSI, is proportional to the initial fluid velocity and strongly decreases with increasing closure time. The start of the decrease is proportional to L (L = length of pipe). For L = 1 m a critical valve closure time $t_{critical}$ = 1,34 ms is found.

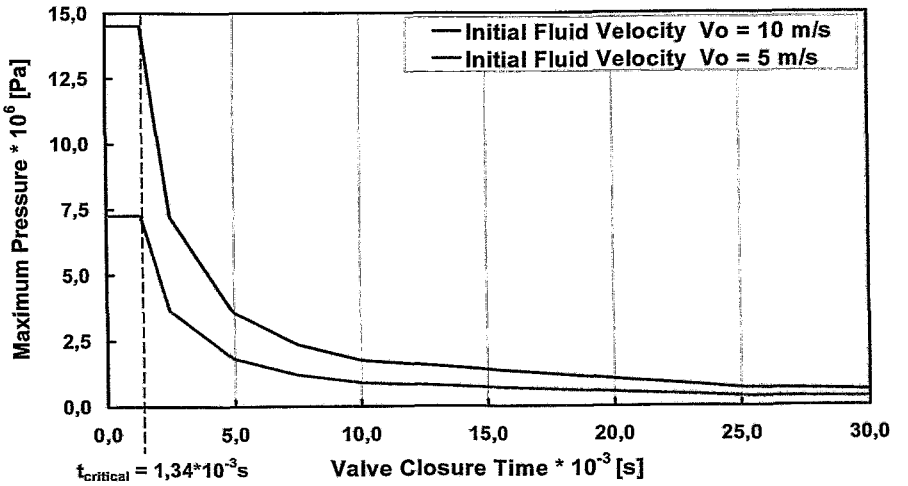

Fig. 7: Pressure versus valve closure time for two initial velocities

5. Conclusions

The simulations show that an overall good agreement is found for the average pressure amplitude of a straight pipe in comparison to the analytical results obtained with the extended

Joukowsky equation. In case of the bended pipe the pressure amplitude of the extended Joukowsky equation seems to be too conservative. In general the average pressure decreases with fluid-structure interaction. But sometimes pressure peaks may appear nearly as high as without FSI. Fluid-structure interaction may locally lead to higher stresses than obtained with common calculation methods. In case of the bended pipe the maximum stress is significantly higher than the static stress which is predicted by a static structural simulation using the pressure amplitude obtained by the extended Joukowsky equation as load.

6. Outlook

The future work is to investigate how the necessity to consider FSI changes with changing geometric parameters of the pipe (straight and bended). The influence of the wall thickness at higher pressure levels will be analyzed and also nonlinear material behavior shall be considered if large deformations and stresses are predicted. The results of the simulations will be compared to one-dimensional simulations (Krepper [6]). Cavitation simulations with pressure dependent density shall be made. Also the influence of an elastically supported valve on the FSI will be examined. Finally, if possible, the material properties shall be changed from slightly compressible water to a fully compressible medium to simulate waterhammer due to cavitation and sudden condensation, which may occur even at slower closure processes. Such simulations could be compared with measurements performed by UMSICHT and FZR (Dudlik, Schlüter and Prasser [7]).

References

[1] Sicherheitstechnische Regeln des Kerntechnischen Ausschusses (KTA) für den Primär- und Sekundärkreislauf, 3200 ff, aktuelle Version

[2] Handbuch Reaktorsicherheit und Strahlenschutz, Abschnitt 4: Empfehlungen der Reaktorsicherheitskommission, Herausgeber: Der Bundesminister für Umwelt, Naturschutz und Reaktorsicherheit, aktuelle Version

[3] F. Borchsenius, J.-Th. Bornemann (1998), Entwicklungen bei fluiddynamischen Berechnungen im atomrechtlichen Aufsichts- und Genehmigungsverfahren, Tagungsbericht der Jahrestagung Kerntechnik 1998, München, ISSN 0720-9207

[4] A. S. Tijsseling (1993), Fluid-structure interaction in case of waterhammer with cavitation, Ph. D. Thesis, Delft University of Technology, Faculty of Civil Engineering, Communications on Hydraulic and Geotechnical Engineering, Report No. 93-6, Delft, The Netherlands, 1993, ISSN 0169-6548

[5] ADINA R & D Inc. (1997), Theory and Modeling Guide, Volume II: ADINA-T and ADINA-F, Report ARD 97-8

[6] E. Krepper (1998), Hausmitteilung: Wasserhammer-Simulationen mit Athlet®, Forschungszentrum Rossendorf (FZR)

[7] A. Dudlik, S. Schlüter und H.-M. Prasser (1997), Transiente Strömungsvorgänge in Rohrleitungen, Visualisierung und Berechnung von Kavitation in Rohrleitungen hinter schnell schließenden Regelklappen, Workshop „Meßtechnik für stationäre und transiente Mehrphasenströmungen", Forschungszentrum Rossendorf (FZR)

INCREASING THE ACCURACY OF NEUTRON LOAD DETERMINATION FOR VVER REACTOR COMPONENTS

Bertram Böhmer, Gennady Borodkin[1], Ernst Brodkin[2], Victor Gorbunov[1], Gennadie Manturov[3], Anatoli Tsiboulia[3], Sergei Zaritsky[2]

1. Introduction

The loss of ductility of the reactor pressure vessel (RPV) due to neutron irradiation and the possibly resulting brittle fracture of the vessel initiated by PTS is the most serious potential accident of VVER type reactors. In order to derive measures to reduce related risks a detailed knowledge of the neutron load is needed. Therefore, in the framework of the BMBF Reactor Safety Research Program (item "Component Safety and Quality Assurance") a project was financed aiming at an increase of the reliability of the determination of the neutron load of VVER reactor components. This project complemented the BMBF project "Development of an improved methodology for the determination of the neutron load of the pressure vessel steel of VVER-1000 type reactors" (1/1996 - 12/1997) [1]. The intention was to support powerful research groups working in Russia in the field of reactor safety and to strengthen existing cooperation. Three research groups were involved, each consisting of two Russian scientists, working in three Russian research centres, namely the Scientific and Engineering Centre for Nuclear and Radiation Safety of Russian GOSATOMNADZOR (SEC NRS) Moscow, the Russian Research Centre "Kurchatov Institute" (RRC) Moscow and the Institute of Physics and Power Engineering (IPPE) Obninsk. The objectives of the project were:

- the further development and testing of neutron data bases for fluence calculations
- providing reliable data for the evaluation of activation experiments at VVER reactors and formulation of the reactor models
- assessment and further development of methods for verifying and adjusting the calculations by means of experiments
- testing and further improvement of transport calculations with Russian data and codes
- proposals for a safer operation of VVER reactors.

In the following a short description of the obtained results will be presented. A detailed report is given in [2].

2. Further development and testing of data for neutron fluence calculations

Owing to advances of calculational methods and computer capacity nowadays the uncertainty of nuclear data remains as major obstacle to further increasing the accuracy of neutron fluence calculations. At the same time, scientific research capacities in the neutron data field have been reduced worldwide to a very low level although the knowledge about many neutron data is still unsatisfactory. Therefore, it seemed worthwhile to assess the neutron data libraries available for calculations in the outer region of the reactor, to improve existing data libraries by including new data and increasing their energy resolution, and to evaluate the covariances of the calculated

[1] SEC for Nuclear and Radiation Safety of Russian GOSATOMNADZOR, Moscow, Russia
[2] Russian Research Centre "Kurchatov Institute", Moscow, Russia
[3] Institute of Physics and Power Engineering, Obninsk, Russia

group fluences. These covariances are needed to get a more reliable basis for evaluating the uncertainties of calculational results and for the adjustment of calculated fluence spectra to experimental data.

The IPPE Obninsk is one of the leading institutes in nuclear data libraries. The ABBN data library is particularly well-known. It found worldwide application to fast reactors but is used now also for thermal reactor calculations in Russia and other countries. In the framework of this project an urgently necessary completion and testing of the ABBN/MULTIC data set with a tenfold increased number of neutron groups could be accomplished:

- For simple shielding benchmarks on iron spheres of different diameters (20, 30, 40, 50, 60 and 70 cm) around a ^{252}Cf-source measured energy spectra of leakage neutrons and photons were compared with calculations done with 28 and 299 neutron groups and with 11 gamma groups. The found agreements between the two calculations and between experiment and calculations were reasonable.
- Neutron and gamma fluence spectra were calculated with the S_N transport code TWOTRAN at 4 different positions (core, downcomer, 1/4 thickness position of the pressure vessel and concrete shield) for a one-dimensional model of a typical pressure vessel. Results obtained from ABBN libraries with 28, 81 and 299 neutron groups were compared with each other and with results obtained from the ENDF/B-VI based VITAMIN-B6 199 group library. The ABBN 299 group spectra are very close to the VITAMIN-B6 spectra and also the spectra obtained with different ABBN group numbers are in good agreement. Differences are found in the low energy region, where probably the thermalization process is not properly described in the VITAMIN-B6 calculations. In the photon case the ABBN results are higher than the VITAMIN-B6 ones, because the ABBN-93 photon production group cross sections do not only include prompt but also delayed gamma yields. The photon spectra differ significantly for the 3 ABBN libraries, as only the 299-group library ensures the needed detailed representation of the thermal region.
- Cross section covariances calculated with the code NJOY91.91 from ENDF/B-VI nuclear data files have been compared for some important cases with covariances based on Obninsk evaluations. The agreement was reasonable. In cooperation with Forschungszentrum Rossendorf covariances of neutron fluence group spectra were calculated for the VVER-1000 pressure vessel using a one-dimensional reactor model and the Obninsk data system ABBN-93/INDECS. The fluence covariance matrix obtained for the outer boundary of the pressure vessel was compared with typical approximations used in spectrum adjustment procedures. The influence of these approximations on the adjustment results was evaluated.
- The data library ABBN/MULTIC has been extended by addition of new data, especially for the thermal region. Some errors were corrected in the data preparation code system CONSYST2 and new algorithms for calculations of P_N scattering matrices in the thermal region have been added. The library and CONSYST2 have been tested in international benchmarks by two-dimensional calculations with the code TWODANT and by three-dimensional Monte Carlo calculations with the code KENO-Va. In all considered cases the agreement with the experiments was similar or better as with ENDF/B-VI based libraries.

3. Development of reactor models for precise calculations of the neutron fluence at the pressure vessels of two VVER-1000 reactors

Based on ex-vessel activation experiments at the reactors Rovno-3 (7th cycle) and Balakovo-3 (5th cycle) reactor models for neutron transport calculations have been prepared in the SEC NRS of the Russian GOZATOMNADZOR.

These models include:

- the description of the design of the reactors
- the description of the experiments
- the azimuthal-radial geometrical approximation of the reactor
- the axial-radial geometrical approximation
- material compositions and nuclear densities of model zones
- reactor operating data during the detector irradiation times (total power history, 2D assembly power distributions, coolant temperature variations)
- the description of time-dependent fission sources, including
    - 2D and 3D assembly power and burnup distributions
    - 3D pin-to-pin power and burnup distributions in the peripheral assemblies
    - heavy metal concentrations in the assemblies
    - the burnup dependence of the neutron emission.

The source data were based on neutron physical calculations of reactor cores, operational system measurements and other data compiled by the NPP staff and SEC NRS. For Balakovo-3 the data were given inside a 60° symmetry sector. For Rovno-3 a 30° sector proved sufficient. The formulated models allow three-dimensional Monte Carlo or S_N calculations as well as calculations with the method of 2D-1D synthesis.

The obtained data show the necessity of a pin-wise description of sources in the outer assemblies since the radial decline of the source strength over the peripheral assemblies approaches a factor 3. The computational models of the VVER-1000 reactors Rovno-3 (cycle 7) and Balakovo-3 (cycle 5) are the most comprehensive VVER reactor models ever made available and used for detailed 3D-neutron transport calculations in the ex-core region. The prepared data were used for S_N calculations and for Monte Carlo calculations with the FZR code TRAMO.

4. Verification and Improvement of Methods of Neutron Fluence Calculations for the Pressure Vessel Region

The calculational problem is characterized by the necessity

- to determine the neutron transport through thick layers of water and steel, whereas the neutron source is located in the core,
- to determine a detailed neutron spectrum above 0.1 MeV,
- to take into account the space and time dependence of the neutron source.

To solve this problem a 3-dimensional flux density function $\varphi(r,\theta,z,E)$ was synthesized from two- and one-dimensional density functions in the following way:

$$\varphi(r,\theta,z,E) = \varphi(r,\theta,E)\, K(r,z,E)$$

$$\text{with} \qquad K(r,z,E) = \varphi(r,z,E) \,/\, \varphi(r,E),$$

where $\varphi(r,\theta,E)$ and $\varphi(r,z,E)$ are results of two-dimensional calculations with the code DOT-3 and $\varphi(r,E)$ is a one-dimensional solution obtained with the code ANISN. In first work steps an evaluation of the effect of different data libraries was made and the influence of different assumptions about the decrease of the source strength in the outer fuel elements on the calculated fluences was investigated. Finally, a special code was developed allowing the

transformation of the pin-wise source geometry to a fine (r, θ)-grid. The obtained results for the 5th cycle of Balakovo-3 and the 7th cycle of Rovno-3 have been compared with experiments and results of different calculations. As example, Tab. 1 compares results from 2D-1D synthesis calculations of RRC, FRAMATOME/SEC NRS (FRAM) and results from high precision Monte Carlo calculations of FZR.

Table 1: Flux integrals above E [MeV] in n/cm^2/s, spectral indices SI=$\varphi_{>0.5MeV}/\varphi_{>3.0MeV}$ and relations between different results

θ	Origin of data	E				SI
		0.1 MeV	0.5 MeV	1.0 MeV	3.0 MeV	
Max. Flux	RRC	$1.14 \cdot 10^{+10}$	$5.08 \cdot 10^{+9}$	$1.70 \cdot 10^{+9}$	$2.29 \cdot 10^{+8}$	22.2
	FRAM	$1.13 \cdot 10^{+10}$	$4.92 \cdot 10^{+9}$	$1.67 \cdot 10^{+9}$	-	-
	FZR	$1.18 \cdot 10^{+10}$	$4.90 \cdot 10^{+9}$	$1.60 \cdot 10^{+9}$	$2.12 \cdot 10^{+8}$	23.1
	RRC / FRAM	1.01	1.03	1.02	-	-
	RRC / FZR	0.97	1.04	1.06	1.08	0.96
	FRAM/ FZR	0.96	1.00	1.04	-	-
Min. Flux	RRC	$6.72 \cdot 10^{+9}$	$2.68 \cdot 10^{+9}$	$8.26 \cdot 10^{+8}$	$1.06 \cdot 10^{+8}$	25.3
	FRAM	$6.59 \cdot 10^{+9}$	$2.50 \cdot 10^{+9}$	$7.70 \cdot 10^{+8}$	-	-
	FZR	$6.59 \cdot 10^{+9}$	$2.61 \cdot 10^{+9}$	$7.33 \cdot 10^{+8}$	$9.41 \cdot 10^{+7}$	27.7
	RRC/FRAM	1.02	1.07	1.07	-	-
	RRC / FZR	1.02	1.03	1.13	1.13	0.91
	FRAM/FZR	1.00	0.96	1.05	-	-

The presented calculation results agree well with each other, the maximum difference reaching 13%. In several cases it is convenient to calculate influence functions, defined as contributions of single assemblies to the neutron flux density at points of special interest at the pressure vessel. Whereas the source distribution is changing substantially due to different enrichment and burnup, the neutron transport properties of a given reactor remain practically unchanged. Obviously, once the contributions of different assemblies are calculated for a certain flux value, the flux value for any source distribution can be obtained as a simple sum of products (fuel assemblies contribution method).

Table 2: Relative contributions of 8 outer assemblies to the neutron fluence at E>0.5 MeV for equidistant angular positions θ° at the inner surface of a VVER-1000 pressure vessel

θ°	Number of assembly								Sum
	6	7	12	13	16	17	18	19	
0	0.005	0.103	0.039	0.786	0.005	0.053	0.0	0.003	0.994
5	0.005	0.079	0.037	0.789	0.005	0.075	0.001	0.006	0.997
10	0.004	0.045	0.035	0.723	0.009	0.161	0.001	0.018	0.996
15	0.003	0.026	0.035	0.532	0.016	0.311	0.003	0.068	0.994
20	0.002	0.013	0.030	0.275	0.026	0.418	0.010	0.222	0.996
25	0.001	0.005	0.019	0.102	0.035	0.325	0.021	0.490	0.998
30	0.001	0.003	0.012	0.042	0.037	0.221	0.027	0.56	0.999

5. Evaluation of the Experiments performed at Rovno-3 and Balakovo-3

Activation detectors of the SEC NRS using the reactions $^{93}Nb(n,n')^{93m}Nb$, $^{237}Np(n,f)$, $^{238}U(n,f)$, $^{58}Ni(n,p)^{58}Co$, $^{54}Fe(n,p)^{54}Mn$, $^{46}Ti(n,p)^{46}Sc$, $^{63}Cu(n,\alpha)^{60}Co$, $^{55}Mn(n,2n)^{54}Mn$ and $^{59}Co(n,\gamma)^{60}Co$ were irradiated during the 7th cycle of unit 3 of the Rovno NPP and during the 5th cycle of unit 3 of the Balakovo NPP in cavities at the outer walls of the pressure vessels. Additionally, detectors of the FZR had been irradiated. In the case of Balakovo-3 also detectors of four further Russian institutes, of ECN Petten and SKODA Plzen had been applied. The irradiation and the comparison of the experimental results were done in the framework of the Balakovo-3 Interlaboratory Experiment [3]. This project covers a part of the evaluation of the Interlaboratory Experiment.

Reaction rates and spectral indices averaged over the time of irradiation were derived from the measured activities. The preliminary comparison during the Balakovo-3 Workshop in Rossendorf showed, that the independent measurement results of different participants agreed well for the $^{54}Fe(n,p)$ monitor reaction and that there were greater differences for some other reactions and some radiation positions. A particularly interesting result of the SEC investigations was the azimuthal variation of the spectral index $a=RR(^{237}Np(n,f)) / RR(^{54}Fe(n,p)^{54}Mn)$, indicating a substantial azimuthal variation of the neutron fluence spectrum.

6. Comparison of Experiments with Neutron Transport Calculations

A selection from the different comparisons described in [2] is given in tables 3 and 4.

Table 3: Comparison of RRC calculation results and SEC NRS experimental results for the azimuthal distribution of the $^{54}Fe(n,p)$ -reaction rate at 149 cm above the core bottom

Data	θ°										
	6.8	9.4	15.6	23.4	32.0	37.0	47.0	50.8	55.8	58.4	62.1
C_{RRC}/E_{SEC}	1.14	1.15	1.17	1.18	1.14	1.13	1.08	1.07	1.08	1.10	1.11

Table 4: Comparison of calculated and measured results of RRC, SEC NRS and FZR for different azimuthal angles θ at 149 cm above the core bottom

θ °	Data (C - Calcul. E - Exper.)	Detector reactions							
		$^{237}Np(n,f)$	$^{238}U(n,f)$	$^{93}Nb(n,n^1)$	$^{54}Fe(n,p)$	$^{58}Ni(n,p)$	$^{46}Ti(n,p)$	$^{60}Ni(n,p)$	$^{63}Cu(n,\alpha)$
9.4	C_{RRC}/C_{FZR}	-	-	1.02	1.02	1.02	1.06	-	0.97
	C_{FZR}/E_{FZR}	-	-	1.01	1.02	1.08	1.00	-	1.02
	C_{RRC}/E_{FZR}	-	-	1.03	1.04	1.10	1.06	-	0.99
	C_{RRC}/E_{SEC}	0.87	-	-	1.15	1.13	-	0.88	1.06
32	C_{RRC}/C_{FZR}	-	-	1.09	1.08	1.08	1.12	-	1.00
	C_{FZR}/E_{FZR}	-	-	0.85	0.97	1.00	0.91	-	0.96
	C_{RRC}/E_{FZR}	-	-	0.93	1.05	1.08	1.02	-	0.96
	C_{RRC}/E_{SEC}	0.85	0.99	-	1.14	1.14	-	0.84	1.05
55.8	C_{RRC}/E_{SEC}	0.83	0.91	-	1.08	1.08	-	0.85	1.04

The RRC calculations coincide within 10% with the FZR calculations and measurements, whereas their differences with the SEC NRS measurements are somewhat larger for some detector types and irradiation positions. The participants of the Balakovo-3 Workshop in Rossendorf recommended to define a benchmark for the verification of fluence calculation methods based on the results of the Balakovo-3 Interlaboratory Experiment.

7. Summary and Proposals

By formulating calculational models and providing data for the evaluation of ex-vessel neutron activation experiments a reliable basis has been established for the neutron load assessment of VVER-1000 reactors.
The leading Russian nuclear data library ABBN/MULTIC has been improved and tested. The uncertainties affecting the calculations of the fluence spectrum at the outer boundary of the pressure vessel have been analyzed and a spectrum covariance matrix has been derived.
The methodologies for the measurement of activation rates and for calculations of fluence spectra and activation rates have been further developed and tested by interlaboratory comparisons. It was demonstrated, that ex-vessel dosimetry in connection with advanced calculational methods can contribute substantially to a reliable determination of the pressure vessel neutron load.

To contribute to a safer operation of VVER type reactors it is proposed

- to create a full-scale 3D ex-vessel fluence benchmark for the standard VVER-1000 RPV on the basis of the Balakovo-3 Experiments results,
- to use ex-vessel dosimetry experiments to validate the calculational assessment of the RPV neutron load,
- to use routinely the method of fuel assemblies contributions (Greens´ function method) for fuel cycle optimization in order to minimize the RPV neutron load.

References

[1] H.-U. Barz, B. Boehmer, J. Konheiser and I. Stephan (1998), Entwicklung einer fortgeschrittenen Methodik zur Bestimmung der Neutronenbelastung des Druckbehältermaterials vom Reaktor des Typs VVER-1000, Final Report BMBF Project 1501022, Report FZR-222

[2] B. Böhmer, G. I. Borodkin, E. B. Brodkin, V. P. Gorbunov, G. N. Manturov, A. M. Tsiboulia, S. M. Zaritsky (1998), Erhöhung der Zuverlässigkeit der Bestimmung der Neutronenbelastung von VVER-Reaktorkomponenten zwecks Ableitung von Vorschlägen für eine sicherere Betriebsführung von VVER-Reaktoren, Final Report BMBF Project 1501021, Report FZR-220

[3] G. Borodkin, O. Kovalevich (1996), Interlaboratory VVER-1000 Ex-Vessel Experiment at Balakovo-3 NPP, Proceedings of the Ninth International Symposium on Reactor Dosimetry, Prag Sept. 2-6, 1996, Eds H. Aït Abderrahim, P. D'hondt, B. Osmera, World Scientific Publishing, Singapore (1998) ISBN 981-02-3346-9, pp 294-301

COMPUTATION OF FUSION PRODUCT DISTRIBUTIONS IN GDT EXPERIMENTS

Andrey V. Anikeev[1], Klaus Noack, Gerlind Otto

1. Introduction

The Budker Institute of Nuclear Physics Novosibirsk (Russia) has proposed a Neutron Source on the base of a Gas-Dynamic Trap (GDT) dedicated to fusion material research [1,2]. Currently, at the GDT facility of the Budker Institute an experimental research program is running to establish the physical data base of this project proposal. One of the crucial issues of the project proposal is the confinement of the fast (energetic) ion population which is generated by neutral beam injection (NBI). Therefore, the study of the fast ion behaviour is one of the key subjects of the GDT research program. In recent experiments with high-power NBI of hydrogen the following global parameters were achieved: mean energy of the fast ions in the range of 5-8 keV, maximum ion density almost 10^{13} cm^{-3}, and total plasma-ß up to 30% [3]. Fig. 1 depicts the layout of the facility.

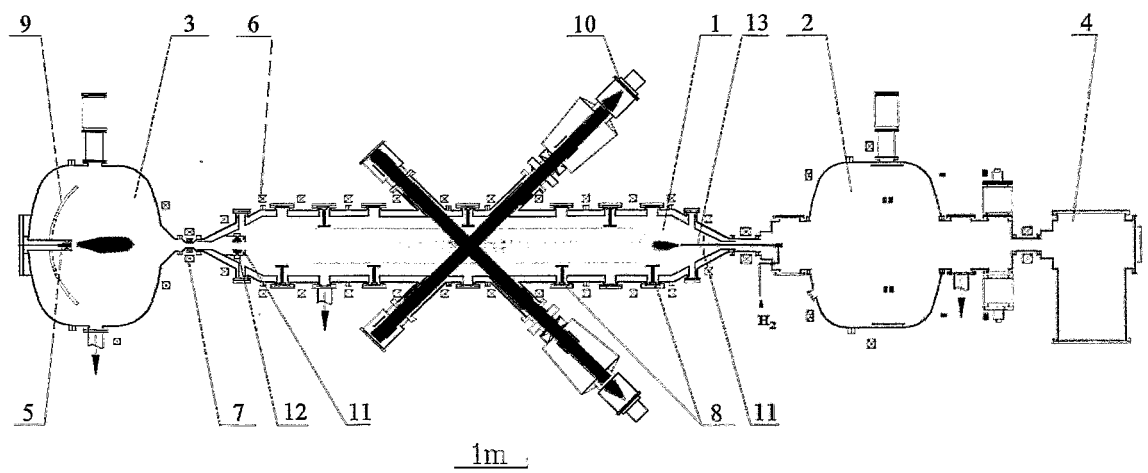

Fig. 1: The GDT layout.
1 - central cell, 2 - cusp cell, 3 - expander cell, 4 - end-tank, 5 - plasma gun, 6 – solenoid coils, 7 - mirror plug, 8 - Ti-evaporators, 9 - plasma dump, 10 – neutral beam injectors, 11 - limiters, 12 - gas-box, 13 - gas inlet tube;
■ high-energetic neutral beams, warm target plasma, ▨ fast ions.

In recent experiments for the first time D-D fusion regimes were realised in the GDT by high-power deuterium beam injection [4]. In these experiments the axial distribution of the fast ions may be directly measured by monitoring the 2.45 MeV neutrons and 3.02 MeV protons produced in D-D fusion reactions. So, this type of measurements gives a good opportunity for code verification. For that reason the Monte Carlo Fast Ion Transport code FIT that has been developed by Forschungszentrum Rossendorf [5] has been upgraded recently, to include the

[1] Budker Institute of Nuclear Physics Novosibirsk (Russia)

computation of source and flux distributions of fusion products inside the GDT during a shot. After a brief outline of the conception of FIT, the paper illustrates the variety of numerical results which have been newly introduced, points out their direct connection to measurement quantities, and compares some of them with values that were measured in first GDT experiments with deuterium neutral beam injection.

2. Conception of the FIT code

The Monte Carlo Fast Ion Transport code FIT simulates the transport of energetic ions in given magnetic field and target plasma. It has been developed:

- to simulate the fast ion transport in the classical transport approach and to consider the three-dimensional space, energy, and time dependencies of the relevant phenomena,
- to take into account a maximum of detailed information on the GDT system and
- to produce a maximum of results per run.

The general scheme of the code is of the standard Monte Carlo type: statistically independent fast ion histories are generated in course of which the quantities of interest are obtained by summing up contributions to well-defined estimators. Having simulated N particle histories a final result for each quantity is computed as the average of the single estimates and its statistical error is calculated from the mean quadratic deviation of the individual estimates from their mean value. The main disadvantage of the method is the slow convergence of the statistical errors according to $N^{1/2}$. The main components of the code are:

- generation of neutral atoms emitted from the neutral beam injectors;
- ionisation of the NBI atoms by charge exchange, electron and ion impact;
- interaction-free flight of the fast ions in a given magnetic field;
- their interaction with the target plasma (energy loss and angular scattering);
- their interaction with the neutral gas and generation of fast atoms;
- the production of neutrons and protons in fusion reactions with fast target ions.

The generation of fusion products has been introduced by the last upgrade of FIT. Additionally to magnetic field, neutral gas and warm plasma now the simulation of the fusion reactions demands also the input of information about fast target ions (deuterons) which play the part of the reaction partners inside the volume of the simulated fast ion transport (deuterons for D-D and tritons for D-T fusion). Their space, energy and pitch angle distributions during an experiment were derived from a FIT pre-calculation. Currently the code is being revised to allow the computation of such non-linear reaction rates in an iterative manner. Except for the fusion reactions the code has been undergone an extensive verification by comparing with results from several well-defined GDT experiments [3,6,7,8].

FIT offers a great spectrum of physical quantities that may be calculated. The results represent the quantities of interest as discrete distributions over a user-defined phase space grid over a sequence of time intervals. The main of them are: the fast ion energy content, NB trapped power, charge-exchange loss power, electron drag power, fusion neutron production rate, uncollided neutron/proton fluxes at user-defined space points, energy and pitch angle distribution functions of the fast ions in a magnetic flux tube defined by a radial interval on the vertical midplane. FIT is written in standard FORTRAN 77, is optimised with regard to vectorisa-

tion and parallelisation and is running under PVM and under the PARIX operation system for *Parsytec* parallel computers [9]. The code is described in detail in [5].

3. Results of Simulations

The numerical studies of D-D fusion experiments in GDT were made for the basic regime of the GDT-facility [3]. The experimental data of the warm plasma and of the NBI system were used as input parameters for the calculations. The neutral gas was calculated by means of the codes TUBE [10] and NEUSI [11]. A first FIT calculation gave the necessary distributions of the fast target deuterons. In the final FIT simulation both channels of the fusion reaction were considered:

$$D + D \rightarrow {}^{3}He\ (0.82\ MeV) + n\ (2.45\ MeV)$$
$$D + D \rightarrow T\ (1.01\ MeV) + p\ (3.02\ MeV)$$

The cross-sections were taken from [12].

The calculated distributions of the fast deuteron density along the Z-axis for several times during a shot are shown in Fig. 2. The time axis is associated with the start of the neutral beam injection. One can see the typical fast ion density distribution in the GDT mirror machine. The maximum densities appear in the regions of the turning points of the sloshing fast deuterons. The ratio between maximum deuteron density and that in the midplane is about 3-4. Unfortunately, the available fast ion diagnostics does not allow to observe this density distribution directly.

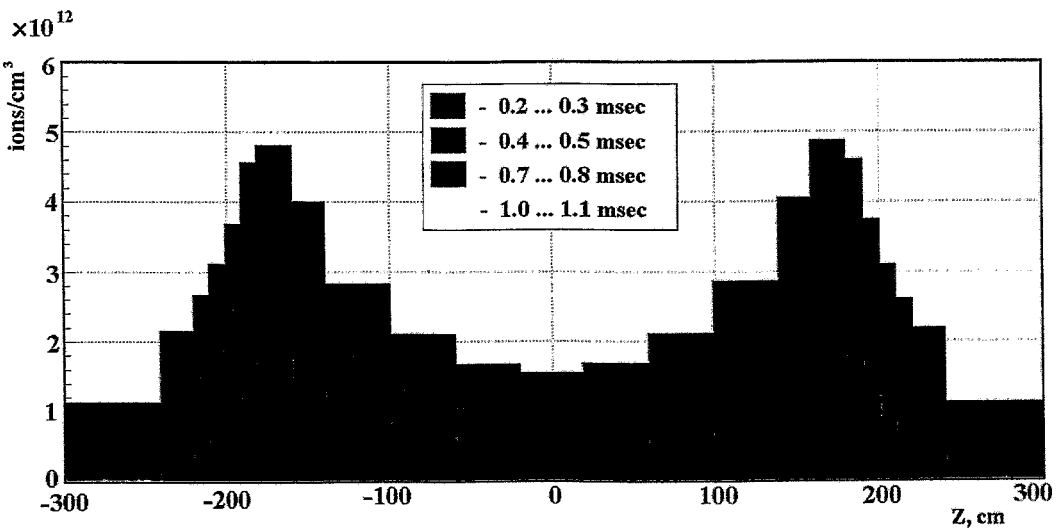

Fig. 2: On-axis density distributions of fast deuterons for several time intervals.

The axial distributions of the linear specific yield of 2.45 MeV neutrons for different moments are shown in Fig. 3. The ratio between the values in the midplane and in the turning point regions is now about 10-12 what corresponds to the square of the density ratio. Fig. 2 and Fig. 3 illustrate the basic principle of the GDT based neutron source project: the density peaks formed by high-energetic deuterons and tritons sloshing between the mirrors will produce the source of 14 MeV neutrons from the fusion reaction. Fig. 4 shows the calculated total neutron

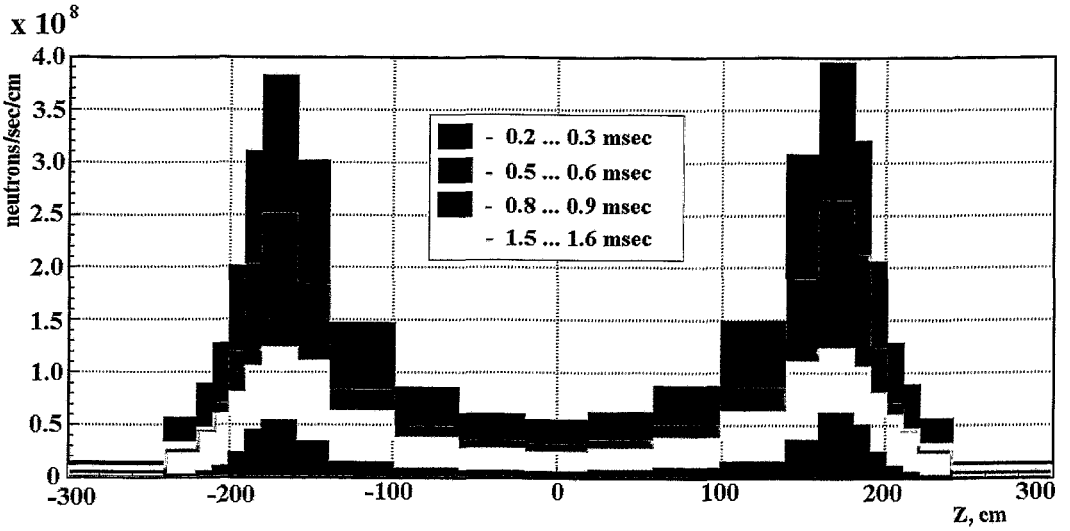

Fig. 3: Linear specific yield of D-D fusion neutrons for several time intervals.

production rates during GDT shots with deuterium injection and with the corresponding injection of a D-T mixture instead of D gas. As consequence of the higher cross-section for the D-T fusion compared with the D-D reaction the maximum neutron production rate turns out to be about sixty times higher.

In addition to neutron and proton production rates in discrete dependencies on space and time FIT offers the capability to calculate the uncollided particle fluxes at user-defined space points, e. g. at detector positions or on the first wall. So, measured particle fluxes can be directly compared with the numerical values [4]. As example Fig. 5 depicts the time evolutions of fusion proton fluxes in four detector positions inside the GDT chamber as calculated by FIT for the present experimental regime with deuterium injection. The positions are:
1 - r = 35.4 cm, z = 11.0 cm,
2 - r = 34.2 cm, z = 112.9 cm,
3 - r = 34.2 cm, z = 169.9 cm,
4 - r = 34.2 cm, z = 226.0 cm.

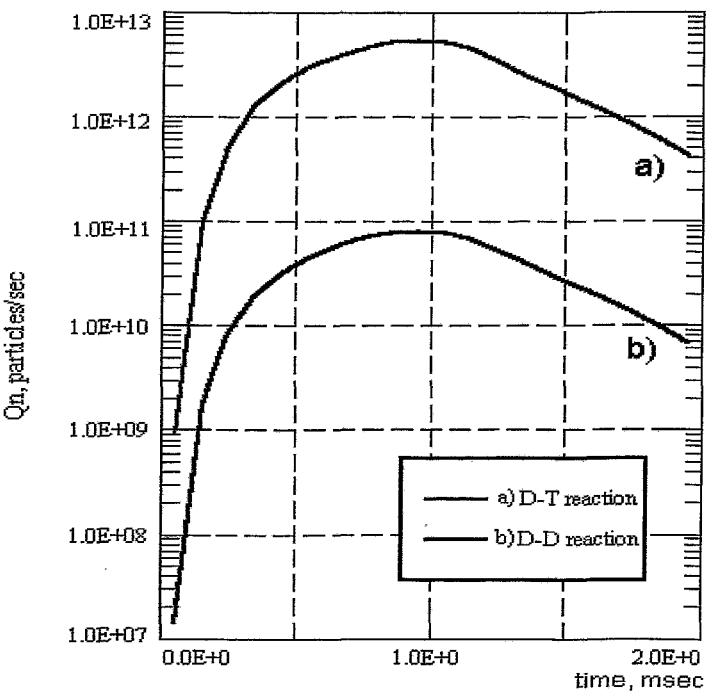

Fig. 4: Total neutron production rates.

Fig. 6 compares the calculated axial distribution of the fusion proton flux with data measured by detector plates located at the specified positions. The values belong to the time of maxi-

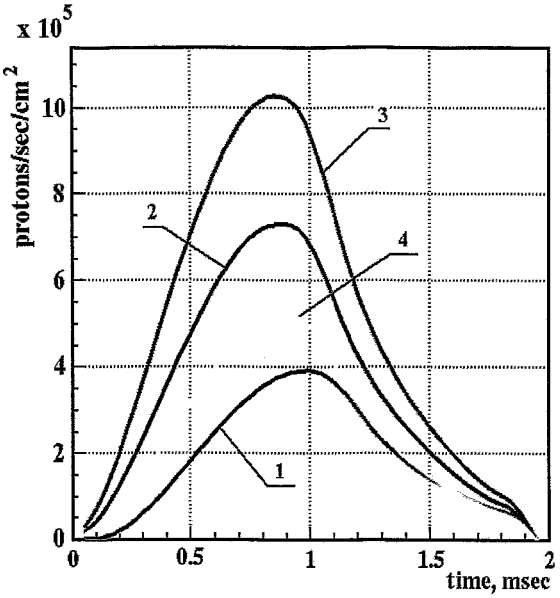

Fig. 5: D-D fusion proton fluxes in various detector postions.

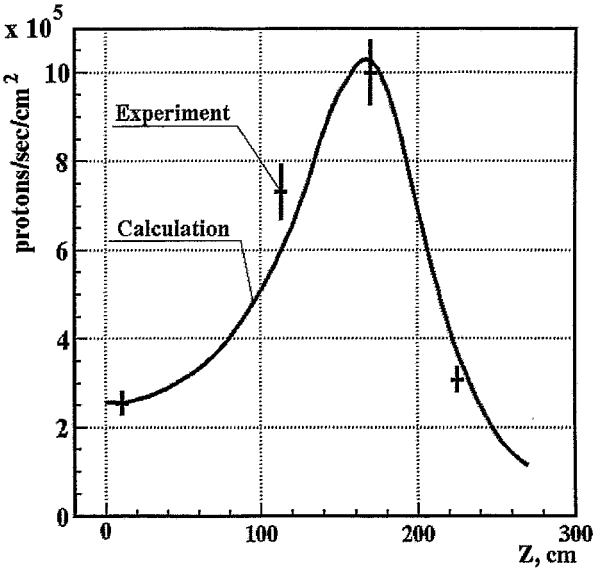

Fig. 6: Calculated and measured proton fluxes.

mum deuteron density. To measure the axial distributions of the specific linear proton yield in GDT fusion experiments the detector plates were equipped with a collimator leaving open a narrow axial window only. Fig. 7 shows the experimental results and the calculated linear specific proton yield.

4. Conclusions

Recently, the Monte Carlo Fast Ion Transport code FIT has been extended to offer the computation of neutron and proton source and flux distributions in GDT experiments using neutral beam injection with deuterium and possibly tritium. This development runs parallel with the experimental research program which is directed towards a highly intense 14 MeV neutron source. The next step of this research project is the "hydrogen-prototype" which is being constructed by the Budker Institute [13]. The FIT code is foreseen as a software tool to perform investigations to prepare and to accompany the research at this facility. In this respect the fusion product calculations of the D-D experiments at the GDT give an advantageous approach for further code verification. The presented results of the first FIT calculations of that type and their comparison with first experimental results have illustrated that

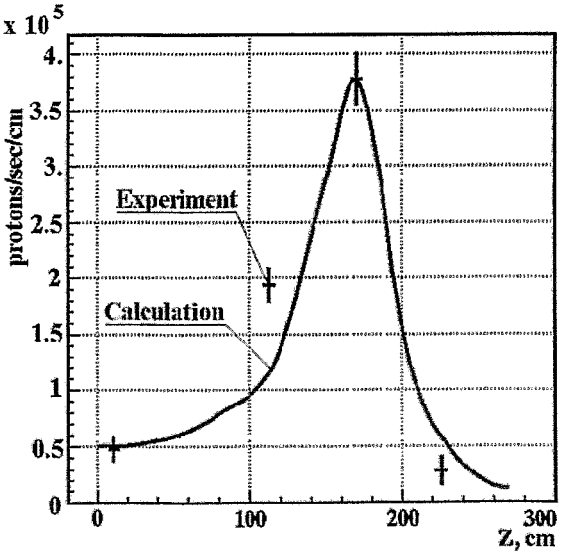

Fig. 7: Calculated and measured linear specific proton yield.

- the new FIT results are well-suited for comparison with measured fusion product source and flux distributions as well as to study dependencies of the fusion rate on various system parameters and that
- the reasonable agreement between numerical and measured results support the conclusion which has been drawn from the code verification by fast ion measurements: the physical models used by FIT adequately describe the physics of the fast ion transport in GDT experiments under the present conditions.

Acknowledgements
The co-author A. V. Anikeev would like to thank Alexander von Humboldt Foundation for supporting his research stay at Forschungszentrum Rossendorf.

References

[1] A. A. Ivanov and D. D. Ryutov (1990), Mirror-Based Neutron Sources for Fusion Technology Studies, Nuclear Science and Engineering, 106, 235
[2] A. A. Ivanov et al. (1992), A Plasma Type Neutron Source for Fusion Materials Irradiation Testing, Proceedings of the 17th Symposium on Fusion Technology, (2, p.1394), Rome, Italy
[3] P. A. Bagryansky et al. (1999), Recent Results of Experiments on the Gas Dynamic Trap, Transactions of Fusion Technology, 35, 79
[4] A. V. Anikeev, K. Noack, G. Otto (1999), Numerical Studies of Neutron Distributions in GDT Experiments, 26th EPS Conference on Controlled Fusion and Plasma Physics, Maastricht, 14-18 June, 1999, The Netherlands
[5] K. Noack, G. Otto, S. Collatz (1999), Transport Simulations of Fast Ion and Neutral Gas Dynamics During GDT Experiments, Transactions of Fusion Technology, 35, 218
[6] A. A. Ivanov et al. (1996), Improved Version of a Mirror-Based 14 MeV Neutron Source, Proceedings of the 16th IAEA Fusion Energy Conference, 7-11 October, 1996, (III, p.667), Montreal, Canada
[7] A. N. Karpushov et al. (1999), Energy Confinement of the High-ß Two-Component Plasma in the Gas Dynamic Trap, Transactions of Fusion Technology, 35, 190
[8] A. V. Anikeev et al. (1999), Study of Hot-Ion Plasma Confinement in the Gas Dynamic Trap, 26th EPS Conference on Controlled Fusion and Plasma Physics, Maastricht, 14-18 June, 1999, The Netherlands
[9] K. Noack, G. Otto (1995), Parallel Particle Transport Simulations on a PowerXplorer™, Rossendorf, Institute for Safety Research, Annual Report
[10] P. A. Bagryansky et al. (1999), Effect of Fast Ti-Deposition on Gas Recycling at the First Wall and on Fast Ion Losses in the GDT Experiment, Journal of Nuclear Materials, 265, 124
[11] S. Collatz, K. Noack (1999), NEUSI – A Code for the Calculation of Neutral Particle Densities Inside the Plasma Region of the GDT, Transactions of Fusion Technology, 35, 375
[12] D. L. Book (1990), NRL Plasma Formulary, Naval Research Laboratory, Washington, NRL Publication 177-4405
[13] A. I. Gorbovsky et al. (1995), Hydrogen Prototype of a Plasma Neutron Source, INTAS Research Project No. 1010-CT-0013, Novosibirsk, Report BudkerINP 95-90

REACTIVE TRANSPORT MODELLING OF A MIXED EQUILIBRIUM-KINETIC SYSTEM

Roland Küchler and Klaus Noack

1. Introduction

A computer code was developed for the description of the reactive transport of chemicals in the unsaturated zone. The processes modelled by this code can be assigned to three categories: motion of water, chemical interactions, and species transport. Each part is a separate sub-model within the code. This contribution addresses the issue of the chemical weathering of pyrite, calcite and uraninite, and the transport of these weathering products downwards through a 10 m thick soil matrix. Transport equations can be derived for chemical species carried with the water. The solute transport system which is used to simulate this process incorporates the effects of hydrodynamic dispersion, non-linear reaction equations and kinetic chemical interaction between aqueous and solid phases (chemical weathering). At each time step, the Richards equation (sub-model water motion) and the transport equations are first solved by an implicit difference method. The chemical equilibrium sub-model is then called to calculate the distribution of chemical species. These two steps are repeated until the solution is obtained. The water motion is described in detail in the annual reports 1996,1997. For the annual motion of water through two soils, sandy silt (A) and silty sand (B), the transport system is solved numerically.

2. Transport of reacting solutes

In order to reach the aquifer, water from precipitation infiltrates through the ground surface and percolates downwards through the unsaturated zone. The same is true for chemical species carried with the water. These species may be already present in the water reaching the ground surface or they may be added and removed to/from the water by dissolution, adsorption, and chemical reactions along its path from the ground surface to the underlying aquifer. Simplified models for solute transport in the unsaturated zone lump the effects of several processes. This can be illustrated best in the one-dimensional convective-dispersive solute transport equation [1] written as,

$$w\frac{\partial C_i}{\partial t} = -v\frac{\partial C_i}{\partial z} + \frac{\partial}{\partial z}\left\{\alpha_L |v| \frac{\partial C_i}{\partial z}\right\} + q_i(z,t,pH) + \sum_{j=1}^{n} S_{ij}(C_1,...,C_n), \qquad i = 1,..,n \qquad (1)$$

Here w is the volumetric water content of the soil and v is the water flow per unit area (Darcy-velocity) (m / h). For the flow through the unsaturated soil horizon w and v are not constants, but are functions of the negative pressure of matrix suction of soil. $C_i(z,t)$ is the solute concentration (mol / L), $q_i = q_i(z,t,pH)$ is a production function (mol / L / h), and α_L is the dispersivity of the medium (m). $\sum S_{ij}$ represents the chemical reactions, which take place in the water path and n is the number of components and species. This term can be viewed as the rate to maintain the reaction in equilibrium (see Table 1). The boundary conditions are as follows:

- At the ground surface a mixed von-Neumann / Dirichlet boundary condition is valid specifying the solute flux: $v(0,t)C_i - \alpha_L \mid v(0,t) \mid \frac{\partial C_i}{\partial z} = v_0(0,t)C_i^{rain}$ (e. g. $i = CO_2$).
- The free outflow at the outlet (z_0=10 m) is described by the boundary condition: $\frac{\partial C_i(z \approx 1{,}2z_0)}{\partial z} = 0$.

2. 1. Simulation of a mixed equilibrium-kinetic system by kinetic formulation

The underlying model for representing the chemistry in waters is the assumption that the interactions between ions results in the formation of ion pairs through ion association. In other words, the model relies on being able to describe the association of any chemical species with a limited set of other species in solution, known as components, according to the general equation:

$$\nu_A A + \nu_B B \Leftrightarrow \nu_C C,$$

where capitals are used for the chemical entities and the ν_k for their stoichiometric coefficients. For the formation of an ion pair, Gulldberg and Waage's Law of Mass Action is valid:

$$a_A^{\nu_A} \cdot a_B^{\nu_B} = K \cdot a_C^{\nu_C},$$

where a_k is the thermodynamic activity of the *k*th component or specie and K is known as the equilibrium constant for the formation of species, C.

Table. 1: Aqueous reactions and their equilibrium conditions

Chemical Reaction	Mass action law
$H^+ + OH^- \Leftrightarrow H_2O$	$a_{H^+}a_{OH^-} = 10^{-7,99}$
$H^+ + HSO_4^- \Leftrightarrow H_2SO$	$a_{H^+}a_{HSO_4^-} = 10^{6}\ a_{H_2SO_4}$
$H^+ + SO_4^{2-} \Leftrightarrow HSO_4^-$	$a_{H^+}\ a_{SO_4^{2-}} = 10^{1,08}\ a_{HSO_4^-}$
$H^+ + CO_3^{2-} \Leftrightarrow HCO_3^-$	$a_{H^+}a_{CO_3^{2-}} = 10^{-7,33}\ a_{HCO_3^-}$
$H^+ + HCO_3^- \Leftrightarrow H_2CO_3$	$a_H\ a_{HCO_3^-} = 10^{-3,35}\ a_{H_2CO_3}$
$Ca^{2+} + SO_4^{2-} \Leftrightarrow CaSO_4$	$a_{Ca^{2+}}a_{SO_4^{2-}} = 10^{0,69}\ a_{CaSO_4}$
$Ca^{2+} + CO_3^{2-} \Leftrightarrow CaCO_3$	$a_{Ca^{2+}}a_{CO_3^{2-}} = 10^{-0,15}\ a_{CaCO_3}$
$UO_2^{2+} + e^- \Leftrightarrow UO_2^+$	$a_{UO_2^{2+}}a_{e^-} = 10^{-0,58}\ a_{UO_2^+}$
$UO_2^{2+} + SO_4^{2-} \Leftrightarrow UO_2SO_4$	$a_{UO^{2+}}a_{SO_4^{2-}} = 10^{-0,15}\ a_{UO_2SO_4}$
$UO_2^{2+} + CO_3^{2-} \Leftrightarrow UO_2CO_3$	$a_{UO^{2+}}a_{CO_3^{2-}} = 10^{-7,09}\ a_{UO_2CO_3}$
$Ca^{2+} + SO_4^{2-} + H_2O \Leftrightarrow CaSO_4 \cdot H_2O$	$a_{Ca^{2+}}a_{SO_4^{2-}} = 10^{1,5}$

All a_k in mmol / L, $k = H^+, \ldots, UO_2^+$

To do the calculation it is assumed that the following homogeneous reactions assembled in Table 1 take place in the aqueous phase, and it is additionally assumed that the macroscopic flow processes are slow enough to allow local equilibrium to be achieved by the reactions. This assumption makes it possible to solve the transport equation and the set of equilibrium chemistry equations separately, with iterations in between. At each time step the Richards equation provides w, v and the chemical transport equations are solved first by implicit difference methods described in [2]. The equilibrium chemistry calculations are then carried out to determine the chemical speciation and reaction mass transfer in each space element. The Newton-Raphson method is employed to solve the set of chemical non-linear algebraic equations (Table 1). Iterations between transport and chemistry yield the common solution. The iteration is continued until the errors are less than a prescribed limit. In order to eliminate the arbitrary initial conditions of the differential equations the calculation is repeated until the quasi steady state appears. Within this loop the initial condition is replaced by the distribution of the preceding step. In the case A the stationary state is achieved after 4 years and in case B after 3 years, respectively.

For aqueous species, activities and concentrations C are related to each other by means of an activity coefficient γ. The activity coefficients γ_k are functions of all aqueous concentrations. The Davies equation [3]

$$\lg \gamma_k = -\alpha \cdot z_k^2 \left(\frac{\sqrt{I}}{1+\sqrt{I}} - 0{,}3 \cdot I \right) \tag{2}$$

is one possibility for such a function, but there are more. With this equation the γ_k were calculated. In (2) z_k is the change of the kth aqueous chemical ion, α is a constant depending on the dielectric constant of the solvent and temperature ($\alpha = 0{,}5$ for $T = 25°C$), and I is the ionic strength, defined as

$$I = 0.5 \cdot \sum_{k=1}^{N_{species}} z_k^2 C_k . \tag{3}$$

Chemical reactions take place in heterogeneous systems, where different phases are in contact with each other. Thus, solutes often react with the surfaces of the water-conducting channels along which they are transported. The reaction may be for example in the form of mineral dissolution (chemical weathering) leading to changes of the reacting solutes. The results of these reactions are the sources of radio-elements and heavy metals. For these reactions chemical equilibrium cannot be assumed, and kinetic laws have to be applied to represent the real processes. Heterogeneous reactions involving minerals are generally slow compared to aqueous homogeneous reactions. Several options are available if a kinetic condition is specified. Almost all kinetic models are based on the assumption that the reaction rate depends on the surface area of the mineral.

The dissolution of pyrite (oxidation) involved in the chemical weathering is considered as:

$$FeS_2(\text{solid}) + 3^3/_4 O_2\ (\text{aqueous}) + 3^1/_2 H_2O \rightarrow Fe(OH)_3(\text{solid}) + 2\ H_2SO_4(\text{aqueous}).$$

That means, a dissolution of 1 mol of FeS_2(solid) (needs $3^3/_4$ mol solved oxygen) will supply 1 mol $Fe(OH)_3$ (ferrihydrite) and 2 mol H_2SO_4(aqueous). This reaction is extremely exothermic, releasing –1,468 kJ of heat per mole of pyrite oxidized. The source term for H_2SO_4(aq) by dissolution of pyrite can be expressed in the form [4]:

$$q^s_{H_2SO_4} = q^0_{H_2SO_4} \cdot U(pH) \cdot \sqrt{p_{O_2}(z) / p_{O_2}(0)}, \quad q^0_{H_2SO_4} = 8{,}3 \cdot 10^{-7} \text{ mmol/cm}^2/\text{s},$$
$$U(pH) = 1{,}29 / (1 + 10^{2{,}5-pH} + 10^{pH-4.0}) + 0.048 = 1{,}29 / (1 + 0{,}316 \cdot a_{H^+} + 0{,}1 / a_{H^+}) + 0.048. \quad (4)$$

Here p_{O_2} is the partial oxygen pressure. It is assumed that the chemical and biological oxygen uptake can be described by a stationary diffusion profile of the partial pressure:

$$p_{O_2}(z) = 0{,}198(1+z)^{-3} - 0{,}524(1+z)^{-2} + 0{,}537(1+z)^{-1} \ . \quad (5)$$

$U(pH)$ has the shape of a Gaussian distribution the peak being at $pH = 3{,}2$. The rate of the pyrite oxidation (4) is catalysed by bacteria.

The dissolution rate for calcite is described in terms of the following rate law [4]

$$q^s_{CaCO_3} = q^0_{CaCO_3}(a_{H^+} + \gamma_1 a_{H_2CO_3} + \gamma_2(1 - a_{Ca^{2+}} a_{CO_3^{2-}})), \quad (6)$$

with $q^0_{CaCO_3} = \exp(0{,}456 - 1022/T)$ mmol/cm^2/s, $\gamma_1 = \exp(6{,}083 - 3991/T)$.
The reaction for this process is: $CaCO_3(\text{solid}) \rightarrow Ca^{2+}(\text{aqueous}) + CO_3^{2-}(\text{aqueous})$.
Formula (6) is taken from Plummer et al [5] and is the most comprehensive one, as it is based on dissolution studies over a wide range of pH (2-7) and CO_2-pressure (35 Pa –100 kPa). The last term in Eq. (5) is only important close to the carbonate equilibrium.

The kinetic rate law for the uraninite-water interaction is used as given by Bruno et al [6]:

$$q^s_{UO_2} = q^0_{UO_2}(1{,}4 \cdot a^{0{,}53}_{H^+} + 10^{-4}), \quad q^0_{UO_2} = 10^{-9} \text{ mmol/cm}^2/\text{s}. \quad (7)$$

In order to get the production function q in (1), q^s has to be multiplied by the reactive surface area of mineral m per unit volume ($q_m = S_m / V \cdot q^s_m = r_m \cdot q^s_m$). $S_m / V (= r_m)$ can roughly be approximated by assuming the porous medium consist of equal-grain-sized spherical particles with radius r by $r_m \approx 3r^{-1}(1-n)\zeta_m$ where n is the porosity and ζ_m is the volume fraction of mineral m in the solid phase.
For the simulation the following rate constants were chosen: $q_{tracer} = 10^{-3}$ mmol/L/h, $q^0_{FeS_2} \cdot r_{FeS_2} = 1.5 \cdot 10^{-3}$ mmol/L/h, $q^0_{CaCO_3} \cdot r_{CaCO_3} = 2 \cdot 10^{-3}$ mmol/L/h and $q^0_{UO_2} \cdot r_{UO_2} = 7 \cdot 10^{-5}$ .mmol/L/h

3. Results and discussion

For the annual motion of water through the different soils, sandy silt (A) and silty sand (B), the above reactive transport system (1) is solved numerically.
Figures 1 (sandy silt) and 2 (silty sand) show the computed profiles of pyrite, calcite and uraninite (UO_2) dissolution and the distribution of a tracer after 3, 6, 9 and 12 months. In the figures the red curves represent the case of a constant source: $q_{tracer} = 0.001$ mmol/L/h. They show the strong dependence of the tracer concentration on the water content and water motion. With constant values w and v these curves would be straight lines. The faster motion of water in case B causes the stronger curvature of the tracer profiles.

In a depth of more than seven meters the concentration of H_2CO_3 falls off in comparison to the tracer concentration. This is due to the decrease of oxygen with the depth whereby the source term (4) becomes weaker. Depending on the water motion the concentrations of Ca^{2+} and SO_4^{2-} achieve the solubility of gypsum in a depth from 0.5 to 2.5 meters so that gypsum precipitates. The straight lines therefore indicate also the presents of unsolved gypsum. The concentrations of Ca^{2+} and SO_4^{2-} do not differ (see Figures 1, 2). The reason for this identity is that the equations of the law of mass action adjust the pH-value in such a way that the source terms of SO_4^{2-} (Eq. (4)) and Ca^{2+} (Eq. (6)) become equal. In other words, an increase in the hydrogen and sulfate concentration will be immediately restricted by an increase solution of calcite. Therefore an nearly stable pH-value (~3.2) adjusts if all H^+ ions of the pyrite source and CO_3^{2-} ions of the calcite source form carbonic acid. Thus no further H^+ ions can increase the activity of the sources. Only if the volume fraction of pyrite reaches values which lead to a pH smaller than 2.5 it comes to a clear separation of both curves.

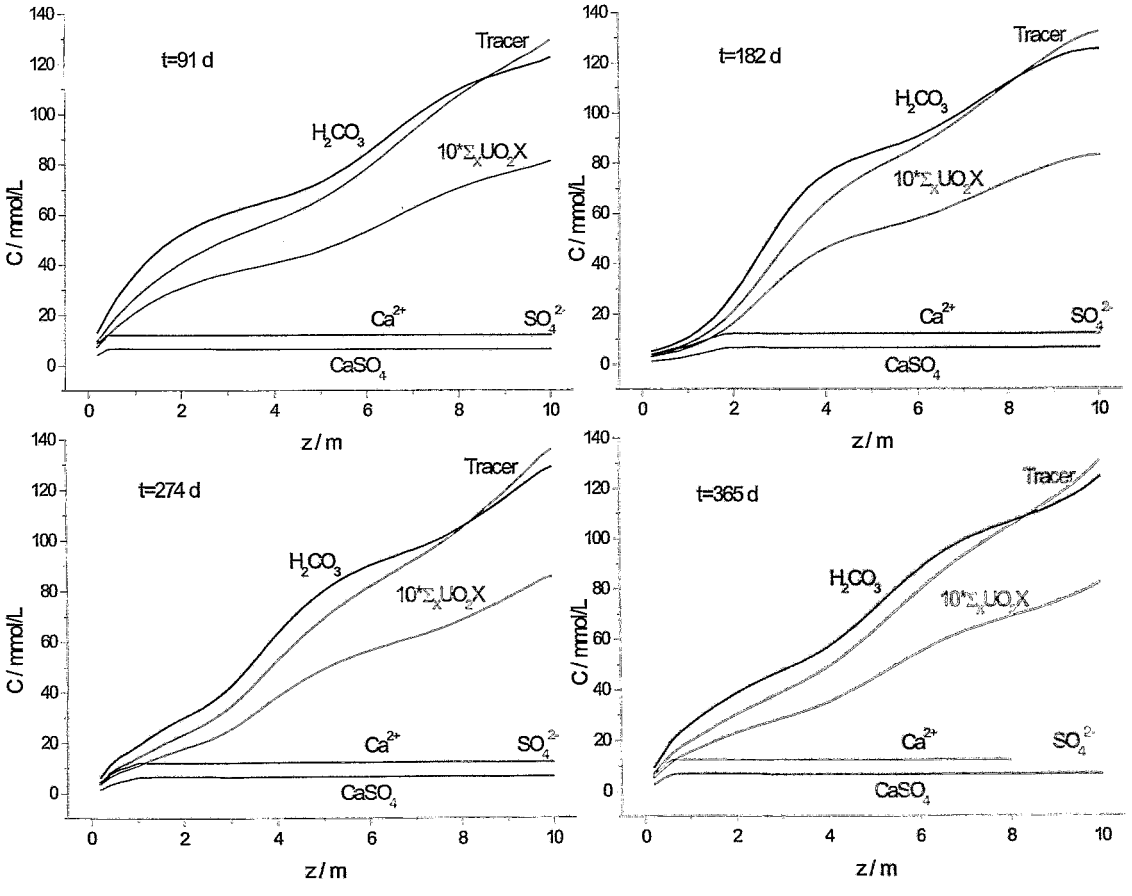

Fig. 1: Selected concentrations of the products of pyrite, calcite and uraninite dissolution for sandy silt at times 3, 6, 9 and 12 months.

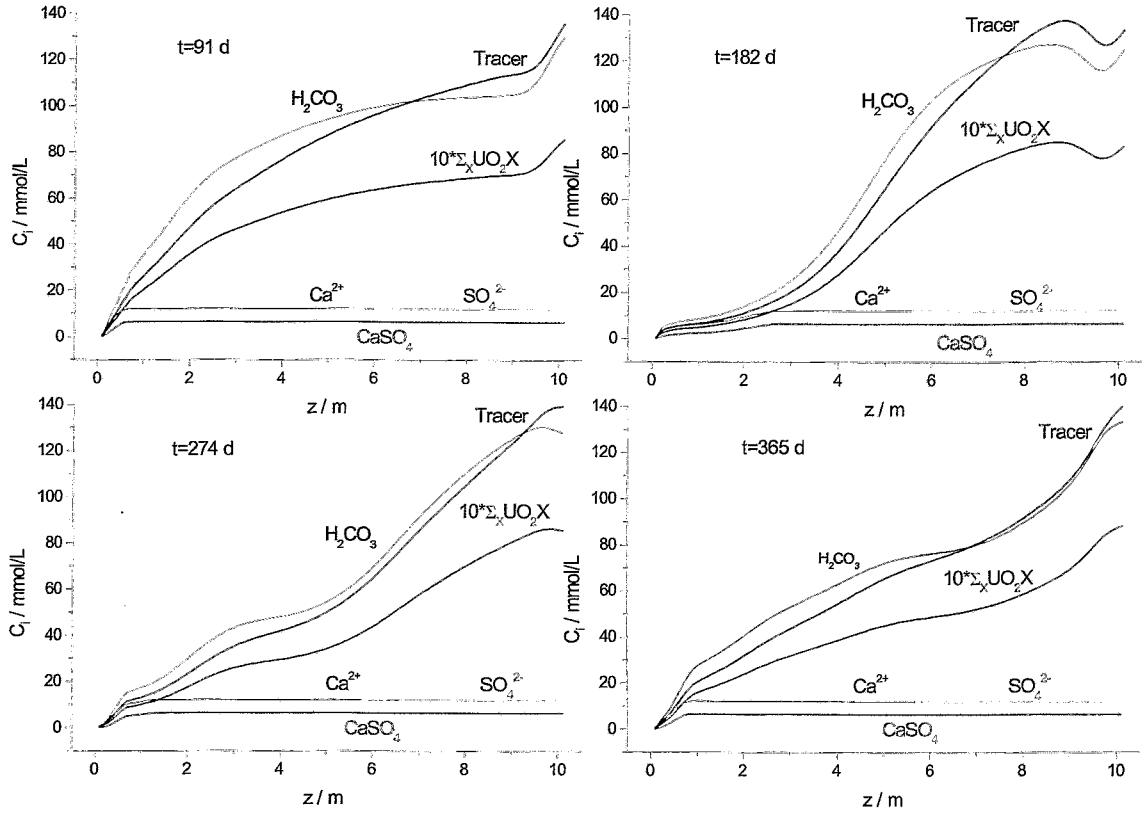

Fig. 2: Selected concentrations of the products of pyrite, calcite and uraninite dissolution for silty sand at times 3, 6, 9 and 12 months.

The time integral $I_k = \int (vC_k - \alpha_L |v| \frac{\partial C_k}{\partial z})_{z=z_0} dt$, which in the integration interval determines the mass transfer per unit area into the groundwater is of more significance than the distribution of species. Results of these integrals are listed in Table 2. These values show much better the effects of the water motion than the species distribution, as well as the effects of the contributions of the source terms given by Eq.(4-7). The influence of water motion on the concentrations is seen from the quarterly integrals.

As expected, the fluctuation in the concentrations in case B is greater than in case A because the saturated hydraulic conductivity of silty sand is a factor of ten greater than for sandy silt. In case of a non-reactive tracer emitted by the constant source q_{Tracer} the integral must provide $I_{Tracer} = 0{,}001\, mmol/h/L * 10\, m * 8760\, h\, (1\, year) = 87.6\, mol/m^2$ in the quasi steady state independently on w and v ($w(w \neq 0,\ min(w) = w_R)$. This is correct, as without sinks the number of particles per volume and unit time produced by the constant source is always identical. The deviation from this value yields the relative numerical error 2.2% for case A and

0.2% for case B, respectively. In both calculations the time step was 3 hours and the spatial step is 0.2 m in case A and 0.1 m in case B, respectively. It should be noted that the reason for the difference in the errors is not only determined by the difference in the spatial steps.
The comparison of both calculations shows no significant differences at the end of year (period). This means that a changes of water flow, water content, and in the dispersivity ($\alpha_L = 0{,}1 \ldots 1\,m$), too, has no significant effect on the total release rate. This behaviour is plausible, because the nearly constant pH value also generates nearly constant sources .

Table. 2: Release rates per quarter (year) I_i

Solid class	Δ t day	I_{Tracer} mol/m^2	I_{H^+} mol/m^2	$I_{SO_4^{2-}}$ mol/m^2	$I_{Ca^{2+}}$ mol/m^2	$I_{HSO_4^-}$ mol/m^2	$I_{H_2CO_3}$ mol/m^2	$\sum_X I_{UO_2X}$ mol/m^2
Sandy Silt	91-0	21.74	0.060	2.07	2.07	0.028	20.70	1.37
	182-91	17.63	0.048	1.66	1.66	0.023	16.77	1.11
	274-182	24.51	0.065	2.21	2.22	0.03	23.29	1.54
	365-274	25.69	0.069	2.38	2.38	0.033	24.53	1.62
	$\sum I_{sp} =$	89.57	0.242	8.32	8.33	0.114	85.29	5.64
Silty Sand	91-0	16.71	0.044	1.52	1.52	0.021	16.22	1.06
	182-91	13.51	0.037	1.27	1.27	0.017	12.77	0.85
	274-182	34.56	0.092	3.11	3.12	0.043	31.66	2.13
	365-274	23.04	0.059	2.01	2.01	0.027	21.95	1.45
	$\sum I_{sp} =$	87.82	0.232	7.91	7.92	0.108	82.60	5.49

The obtained results also show that the time depending local fluctuating concentrations do not correlate with the release rates. That means for example, that concentration measurements in mining dumps do not result in values for the pollutant release into the ground water.
Further work will proceed along two broad lines: The first one is the validation of the models and numerical tools against well reproducible experiments. The second one is the model extension to consider temperature influences, so that the important temperature effect on the kinetic and equilibrium processes can also be taken into account.

References

[1] L. Luckner und W. M. Schestakow (1991), Migration Processes in the Soil and Groundwater Zone, Leipzig, Verlag für Grundstoffindustrie

[2] R. Küchler, K. Noack (1996), Migration of pollutants in mining dumps, FZ Rossendorf, Institute for Safety Research, Annual Report 1996

[3] S. Pfeiffer, K. Pecher (1997), Experimentelle aquatische Chemie, Heidelberg, Berlin, Oxford, Spektrum, Akad. Verl.

[4] R. Münze, B. Ullrich (1997), Beschreibung und Bewertung geochemischer Zustände, die eine Verringerung der Niederschlagsinfiltration in Halden erfordern, Vortrag zum Workshop Sanierung der Hinterlassenschaften des Uranbergbaus, 10 April 1997

[5] D. L. Suarez and J. Simunek (1996), Solute Transport Modeling Under Variably Saturated Water Flow Conditions, in P. C. Lichtner, C. I. Steefel and E. H. Oelkers (Ed.),

Reactive Transport in Porous Media, Reviews in Mineralogy Vol. 34

[6] J. Bruno, I. Casas, and I. Puidoménech (1991), The kinetics of dissolution of UO_2 under reducing condition and the influence of an oxidized surface layer (UO_{2+x}), Application of a continuous flow-through reactor, Geochimica et Cosmochimica Acta, 55, 647-658

ELECTROMAGNETIC CONTROL OF FLOW SEPARATION

Tom Weier, Gerd Mutschke, Uwe Fey, Vjatcheslav Avilov, Gunter Gerbeth

1. Introduction

The performance of fluid mechanical devices is often limited by flow separation. The form drag of cars, the efficiency of diffusers and the stall on airfoils are only some examples. Control of flow separation by suction was first demonstrated by Ludwig Prandtl [1] when he presented his boundary layer theory. Flow separation occurs when fluid decelerated by friction forces is exposed to an adverse pressure gradient which is stronger than the remaining kinetic energy of the fluid. Due to separation, form drag increases and possible lift decreases. To prevent separation, the momentum deficit of the boundary layer has to be overcome and the pressure gradient of the outer flow has to be balanced.

Numerous different techniques as, e.g. suction, blowing, and wall motion have been developed and many practical applications exist today e.g. in aerodynamics.
If the fluid is electrically conducting, an additional control possibility is given by the application of a Lorentz force **f**. This electromagnetic body force results from the vector product of the magnetic induction **B** and the current density **j**:

$$\boldsymbol{F} = \boldsymbol{j} \times \boldsymbol{B} \tag{1}$$

The current density is given by Ohm's law

$$\boldsymbol{J} = \sigma(\boldsymbol{E} + \boldsymbol{U} \times \boldsymbol{B}); \tag{2}$$

where **E** denotes the electric field, **U** the velocity and σ the electrical conductivity, respectively. Depending on the conductivity of the fluid, different control strategies exist. In case of low-conducting fluids as electrolytes or seawater ($\sigma \approx 10$ S/m), which will be considered in the following, induced currents $\sigma(\mathbf{U}\times\mathbf{B})$ alone are too small, and external electric fields have to be applied in order to control the flow. Therefore, also time-dependend forces might easily be established by supplying AC-voltage feeding of the electrodes. However, electrochemical aspects like the production of electrolytic bubbles have to be considered.

The following paper gives an overview about recent experimental results on separation control at inclined plates and airfoils. For that a simple geometry of alternating stripwise electrodes and magnets attached to the surface of the body (see Fig. 1) was used. This arrangement generates a surface-parallel Lorentz force which is exponentially decreasing in wall-normal direction. Singularities at the corners of the electrodes and magnets additionally cause a slight spanwise variation of the Lorentz force in regions very close to the surface (see Fig. 2). The exact force distribution, integrated over the spanwise coordinate z, is

$$F = \frac{\pi}{8} j_0 M_0 e^{-\frac{\pi}{a}y} \tag{3}$$

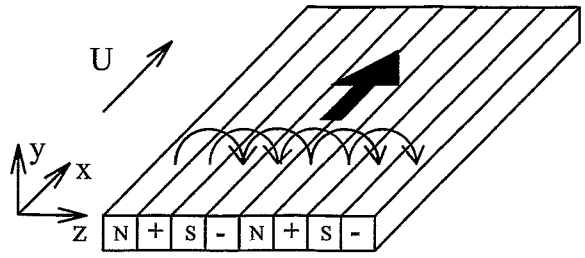

Fig.1: Sketch of the electric (green) and magnetic (blue) field lines and the resulting Lorentz force (red arrow) over a flat plate

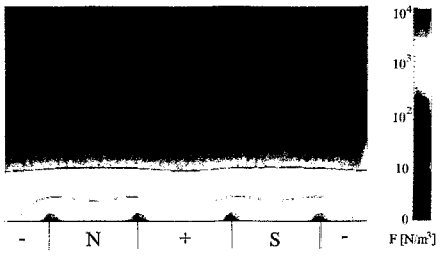

Fig. 2: Calculated Lorentz –force distribution

where M_0 denotes the magnetization of the magnets. Both electrodes and magnets are assumed to have the same width a.

The idea to influence the boundary layer flow of a low conducting fluid by electromagnetic forces dates back to the 1960s [2] and has recently attracted new attention for controlling turbulent boundary layers [3-6]. The first concept of Gailitis and Lielausis [2] used a streamwise Lorentz force for stabilizing a flat plate boundary layer. A tremendous reduction of skin friction will result from transition delay, since turbulent skin friction in general is orders of magnitude larger than laminar one. Following the approach of Tsinober and Shtern [8], the non-dimensional parameter

$$Z = \frac{1}{8\pi}\frac{j_0 M_0 a^2}{\rho U_0 \nu} \tag{4}$$

is obtained ("Tsinober-Shtern" parameter) by normalizing the boundary layer equations with the electromagnetic force term (3). Z describes the ratio of electromagnetic to viscous forces. ν, ρ and U_0 denote the kinematic viscosity, density and freestream velocity of the fluid, respectively. For the canonical case of a flat plate boundary layer, the streamwise pressure gradient dp/dx vanishes. Provided $Z = 1$, the boundary layer thickness reaches an asymptotic value. That means, the momentum loss due to the wall friction is just balanced by the momentum gain caused by the electromagnetic force. As consequence, an exponential boundary layer profile develops

$$\frac{u}{U_0} = 1 - e^{-\frac{\pi}{a}y} \tag{5}$$

comparable to the asymptotic suction profile. This profile has a critical Reynolds number which is two orders of magnitude higher than the one for the Blasius profile, i.e. transition will be delayed considerably.
The normalization of the Navier-Stokes equation leads to an additional non-dimensional parameter

$$N = \frac{j_0 B_0 L}{\rho U_0^2} \tag{6}$$

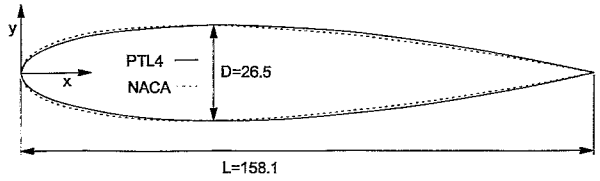

Fig.3: PTL-IV hydrofoil in comparison to a NACA-0017 airfoil

N is the so-called interaction parameter defining the ratio of electromagnetic to inertial forces. B_0 is the surface magnetization of the permanent magnets and L is a characteristic length. Obviously, N and Z are not independent, since $Z/N \sim Re$.

2. Experimental Apparatus

Flat plate boundary layer measurements and the investigation of the flow around a hydrofoil were carried out in a closed loop filled with the sodium chloride electrolyte at the Hamburg Ship Model Basin (HSVA). LDA measurements at the flat plate were performed on the upper plate side because of the electrolytic bubble production, but both sides of the plate were equipped with electrodes and magnets. The plate has 25 electrodes and 25 magnet strips, each 10 mm in width. The magnet/electrode array starts at 100 mm from the leading edge of the plate and has a length of 400 mm. The whole plate is 500mm×590mm in size and 18mm thick. Leading edge and trailing edge are rounded. The magnets generate an induction of 0.35T at their surface and consist of neodymium-iron-boron (NdFeB). The electrodes are made from stainless steel.
Separation prevention by electromagnetic forces has been studied on an additional small flat plate and two hydrofoils at different angles of attack.

The small flat plate is 130mm×140mm and 6mm thick. Electrodes and magnets cover the plate at 3mm from the leading edge and extend up to 37mm from the trailing edge. The width of the electrodes and magnets is a=10mm. Stainless steel has been used as electrode material in combination with a sodium hydroxide solution in the open channel. The permanent NdFeB magnets surface induction is B_0 = 0.4T. The hydrogen bubble technique has been applied to visualize the flow.

To verify the influence of separation prevention on the lift and the drag of a body, force measurements on two hydrofoils have been carried out at HSVA's Arctic Environmental Test Basin. Fig. 3 shows the geometry of the hydrofoil PTL-IV in comparison to a NACA 0017 airfoil. The hydrofoils with a span s of 360mm and additional end plates were mounted on a Kempf&Remmers force balance. All signals (drag, lift, angle of attack, pitching moment) were recorded by a standard PC.

The Arctic Environmental Test Basin is an open channel 30m long and 1.2m deep filled with the same aqueous sodium chloride. The maximum speed is about 1m/s. The two hydrofoils differ in their electromagnetic system. One has an electrode spacing of a = 5mm, the other of a=10mm. The magnets of the first hydrofoil have a surface induction of B_0 = 0.2T, those of the second one B_0 = 0.4T.

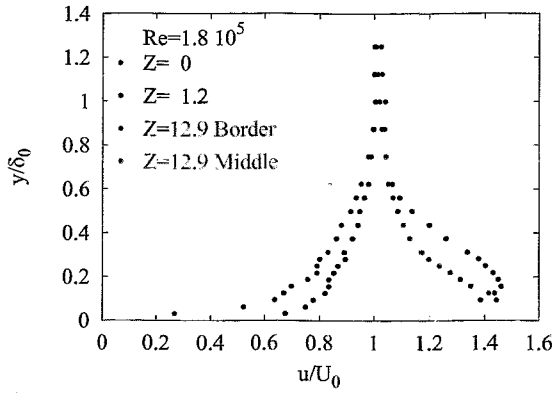

Fig. 4: Mean velocity profiles for the flat plate boundary layer in parallel flow

3. Results

3.1. Flat Plate

The effect of a streamwise Lorentz force on the mean velocity profile of a flat plate boundary layer is shown in Fig. 4. This profile was measured at the end of the electrode/magnet array, i.e. at x=500mm measured from the leading edge. A Reynolds number $Re=U_0x/\nu$ of $1.8\cdot10^5$ slightly below the theoretical transition value characterizes the flow. As can be seen from the fluctuating velocities without the Lorentz force (Z=0), the boundary layer flow is not laminar as it could be expected for such non-optimized conditions. A similar conclusion can be drawn by looking closer at the mean velocity profile. It is an intermediate profile between a Blasius and a logarithmic one. This early transition of the boundary layer is probably caused by the high turbulence level of 2% in the cavitation tunnel.

Thus the streamwise Lorentz force is, in contrast to the theory, applied to a turbulent boundary layer. For Z=1.2 the influence of the force on the flow consists in a moderate acceleration of the near wall fluid. The velocity profile becomes more convex near the wall, but ist shape is not an exponential one. Mainly three reasons could be responsible for this behavior. At first, the early transition of the boundary layer causes conditions not considered in the theory. Second, in order to establish the asymptotic profile, a certain evolution length has to be covered. A rough estimate can be given by looking at the definition of the dimensionless streamwise coordinate $x'=\nu\pi^2/(a^2U_0)$ which should at least be in the order of one to allow the asymptotic profile to develop. An integration of the boundary layer equations shows that at x'=7 the boundary layer profile for Z=1 has still a mean deviation of 1% from the exponential shape. The profiles in Fig. 4 are taken at x'= 0.13, i.e. at a position far from the required one. Third, the real force distribution differs from the ideal one. Their z modulations could have a destabilizing effect instead of the desired stabilizing one by possibly triggering transition due to secondary instabilities.

At a Tsinober-Shtern parameter of Z=12.9 the mean velocity profile shows the form of a wall jet, demonstrating the strong accelerating effect of the Lorentz-force. Fig. 4 gives the flow profile at two distinct positions in the spanwise coordinate z, at the border of a magnet and an

Fig. 5: Inclined plate: Lorentz force off

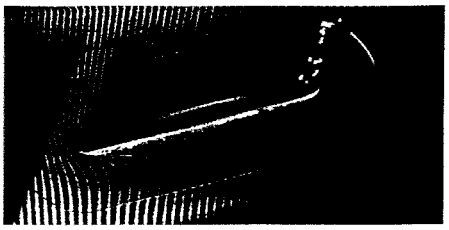

Fig. 6: Inclined plate: Lorentz force on

electrode and over the middle of a magnet. The result of the spanwise modulations on the velocity distribution is clearly to be seen. The flow is stronger accelerated at the force maxima, i.e. at the borders between electrodes and magnets (see Fig.2), than at the minima.

The wall jet in Fig.4 at Z=12.9 indicates the strong momentum increase in the boundary layer due to the Lorentz force. Since boundary layer separation occurs owing to an energy deficit of the near wall fluid, the streamwise Lorentz force should be able to counteract separation.

3.2. Inclined flat plate and hydrofoils

Visualizations of the flow around an inclined flat plate are given in Figs. 5 and 6. The electrolyte flows from the left to the right. Fig. 5 shows the flow around the plate without Lorentz force at an angle of attack α=15°. Since the Reynolds number based on the plate length is small (Re=1.24·10^4), the flow separates laminar at the leading edge without reattachment. Because of the leading edge separation, the flow should be influenced already at the nose of the plate. Consequently the magnet/electrode-array is placed just behind the half cylinder forming the leading edge of the plate.

The flow situation under the influence of a Lorentz force of N=6.87 is shown in Fig. 6. As the bubble strips indicate, the boundary layer is attached over the whole length of the plate. Due to the pressure rise in the outer flow, the boundary layer fluid is strongly decelerated at the leading edge. By the Lorentz force, the near wall fluid is subjected to an acceleration while passing the plate. This can be seen by looking at the shape of the hydrogen bubble stripes near the plate.

Separation of flow causes a form or pressure drag on the moving body simply due to the pressure difference between forward and backward stagnation point. This form drag determines practically the total drag of bluff bodies at higher Reynolds numbers. Separation prevention can reduce the form drag to zero. The application of a streamwise Lorentz force for separation prevention has two additional consequences on the drag. On the one hand due to the exponential force distribution the velocity gradient at the wall and therefore wall friction is increased. On the other hand the force exerts thrust on the body. At high enough forcing parameters a configuration is possible, where thrust overcomes drag.

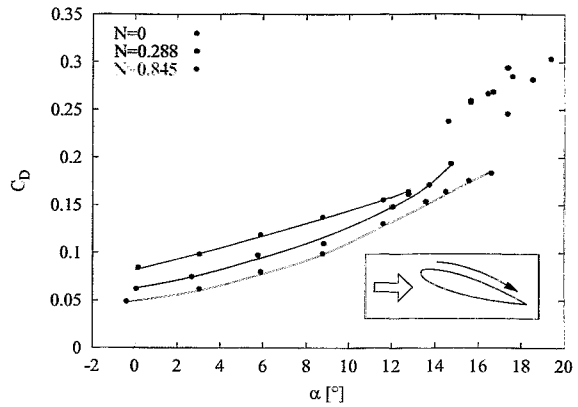

Fig. 7: C_D versus α for Re=4·10^4, a/L=0.03 and different interaction parameter

In Fig. 7 drag values of the PTL-IV hydrofoil with a/L=0.03 are presented for a Reynolds number Re=4·10^4 and different values of N versus the angle of attack α. The drag coefficient is defined in the usual way as

$$C_D = \frac{F_D}{\frac{\rho}{2} U_0^2 A} \tag{7}$$

with F_D denoting the total force in streamwise direction as obtained directly from the force balance measurements and A giving the wing area. The Lorentz force in Fig. 7 acts on the suction side of the hydrofoil only. At the low Reynolds number considered here, separation occurs for N=0 like at the flat plate as leading edge separation but at an higher inclination angle of 13°. Since the separation occurs abruptly a sudden increase of the drag coefficient is obtained. The application of the Lorentz force at the suction side results at small angles of attack, i.e. in a situation without separation, in a decrease of the drag coefficient due to the momentum gain caused by the force. The drag reduction is relatively moderate (ΔC_D=0.024 at N=0.288 and ΔC_D=0.037 at N=0.845). A larger effect on the drag results from the separation delay. At N=0.288 separation is delayed to α=14.7°, thereby reducing drag by ΔC_D=0.044. At N=0.845 separation occurs first at α=16.6°, resulting in a ΔC_D=0.084. The actual drag values are always compared to the values of the natural flow at the same angle of attack.

Thinking about drag reduction implies, of course, the question about the overall energetical balance. The small conductivity of typical electrolytes leads to large losses caused by Joule heating. It is clear that the drag reduction should overcompensate at least these Joule losses. Some hopes and estimates still exist for that based on the stabilization of a laminar boundary layer [2]; but to the best of the authors knowledge, no energetically efficient electromagnetic drag reduction has been demonstrated up to now.

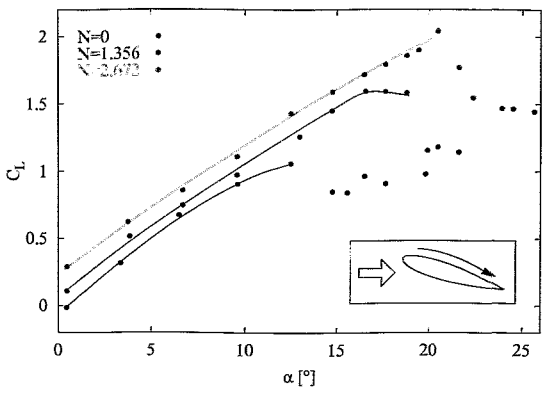

Fig. 8: C_L versus α for Re=2.9·10^4, a/L=0.06 and different interaction parameter

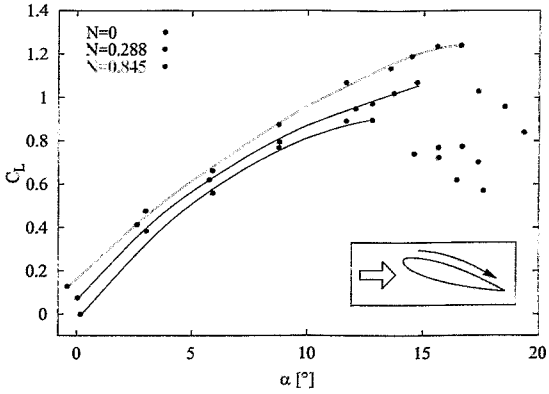

Fig. 9: C_L versus α for Re=4·10^4, a/L=0.03 and different interaction parameter

Especially on a hydrofoil, separation doesn't influence the drag alone, but also the lift. Figs. 8 and 9 show the lift development with the angle of attack at different N for the two hydrofoils. The lift coefficient is defined in analogy to the drag coefficient as

$$C_L = \frac{F_L}{\frac{\rho}{2} U_0^2 A} \tag{8}$$

Here F_L denotes the force on the hydrofoil in the direction normal to the liquid flow. Fig. 8 gives experimental values obtained at Re=2.9·10^4 and a/L=0.06, Fig. 10 for Re=4·10^4 and a/L=0.03. As in Fig. 7, the Lorentz force is applied at the suction side only. At N=0 separation takes place at α=13° leading to an abrupt lift decrease. If the Lorentz force is switched on, already at small angles of attack a lift increase can be seen. This lift increase results from the additional circulation caused by the acceleration of the suction side flow. Corresponding to the drag reduction at small angles of attack, also the lift increase due to enhanced circulation is of moderate size. Nevertheless it is possible to obtain a lift force even without an inclination of the hydrofoil.

A much larger lift increase results from the delayed separation of the suction side flow at high angles of attack. The lift coefficient increases further monotonically with the angle of attack up to a point, where the Lorentz-force cannot any longer withstand the pressure gradient of the outer flow. From Fig. 8 one can detect, that for the hydrofoil with a/L=0.06 at Re =2.9·10^4 and N=2.67 stall can be delayed up to α=21°. This results in an increase of the lift coefficient by 92% in comparison to the unforced flow. The same scenario is shown in Fig. 9 but for the hydrofoil with a/L=0.03 at Re =4·10^4 and N=0.84. Due to the lower interaction parameter, the hydrofoil stalls at α=17°, the maximum lift increases by 43%.

4. Conclusions

Experimental demonstration of separation prevention on a circular cylinder by means of a streamwise Lorentz force with accompanying numerical simulations have been given in [9].

The influence of a streamwise Lorentz force on the flow along a flat plate has been studied in a saltwater flow. The experiments show a strong acceleration of the near wall flow if electromagnetic forces of sufficient strength are applied. The application of the streamwise force to the control of separation at an inclined plate and two hydrofoils has been successfully demonstrated. Stall is delayed to higher angles of attack resulting in an increase of maximum lift and a decrease of total drag of the hydrofoils.

Acknowledgments

Financial support from VDI under Grant NLD-FKZ 13N7134/1 is gratefully acknowledged. We would also like to thank the measuring crew from HSVA and Prof. Lielausis from IoP Riga for preparing a plate and an airfoil.

References

[1] L. Prandtl (1904), Über Flüssigkeitsbewegung bei sehr kleiner Reibung, Verhandlg. III. Intern. Math. Kongr. (pp.484-491), Heidelberg

[2] A. Gailitis and O. Lielausis (1961), On a possibility to reduce the hydrodynamical resistance of a plate in an electrolyte, Applied Magnetohydrodynamics. Reports of the Physics Institute 12 (pp. 143-146), Riga (in Russian)

[3] C. Henoch and J. Stace (1995), Experimental investigation of a salt water turbulent boundary layer modified by an applied streamwise magnetohydrodynamic body force, Phys. Fluids, 7, 1371

[4] C.H. Crawford and G.E. Karniadakis (1997), Reynolds stress analysis of EMHD-controlled wall turbulence. Part I. Streamwise forcing, Phys. Fluids, 9, 788

[5] J.C.S. Meng (1994), Seawater Electromagnetics: A new Frontier, Magnetohydrodynamics, 30, 401

[6] D.M. Nosenchuck and G. Brown (1993), Discrete spatial control of wall shear stress in a turbulent boundary layer, in R.M.C. So, C.G. Speziale and B.E. Launder (Ed.), Near-Wall Turbulent Flows (pp.689-698), Elsevier

[7] E. Grienberg (1961), On determination of properties of some potential fields, Applied Magnetohydrodynamics. Reports of the Physics Institute 12 (pp. 147-154), Riga (in Russian)

[8] A.B. Tsinober and A.G. Shtern (1967), On the possibility to increase the stability of the flow in the boundary layer by means of crossed electric and magnetic fields, Magnitnaya Gidrodinamica, 152

[9] T. Weier, G. Gerbeth, G. Mutschke, E. Platacis, O. Lielausis (1998), Experiments on cylinder wake stabilization in an electrolyte solution by means of electromagnetic forces localized on the cylinder surface. Experimental Thermal and Fluid Science, 16, 84

SI-CZOCHRALKSI CRYSTAL GROWTH MELT FLOW CONTROL BY MEANS OF MAGNETIC FIELDS

Vladimir Galindo and Gunter Gerbeth

1. Introduction

A contact-less melt flow control is important for the convective motions in many crystal growth technologies. Typically steady magnetic fields are used to damp such flows. Surprisingly, active flow driving forces due to alternating magnetic fields can be of stabilising character, too. We present numerical results for the combined action of steady and alternating magnetic fields for the Czochralski growth process of silicon crystals. Not only the thermal convection and rotation of crystal and crucible are taken into account, but also the influence of driving and/or damping electromagnetic forces, the effects related to the induced electrical current in the melt and the thermo-capillary driven flow at the free melt surface. We apply a two equations low Reynolds number turbulence model since a weak turbulence slightly above the transition values is characteristic for the melt motion.

2. Geometry

The geometry used to compute the flow is shown in Fig. 1. The dimensions are given in mm and were taken according to a Czochralski single crystal growth furnace with a crucible having a diameter of 14 inches. The problem is assumed to exhibit symmetry about the z-axis – that is, all field quantities are supposed to be independent of the polar angle θ. That makes possible to consider the problem as axis-symmetric and to reduce the computation mesh to the meridional plane $r - z$.

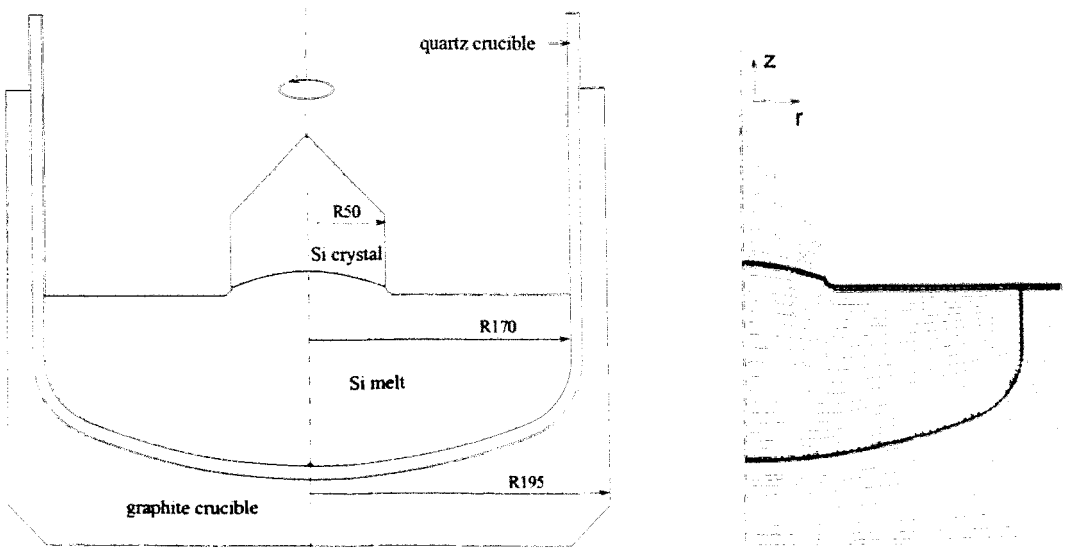

Fig. 1: Sketch of the geometry (left) and coarse computation mesh (right)

3. Governing equations and boundary conditions

With reference to Fig. 1, we consider axi-symmetric, steady, buoyancy-, thermo-capillary-, and electromagnetically induced flow and heat transfer within a crucible that is heated from the sides and from the bottom. Assuming that the fluid is incompressible and that the Boussinesq approximation is valid, the time averaged momentum, continuity, and energy equations are as follows:

Navier-Stokes (momentum) equation with electromagnetic force term:

$$\rho\left(\frac{\partial\vec{v}}{\partial t}+(\vec{v}\cdot\nabla)\vec{v}\right)=-\nabla p+\eta\nabla^2\vec{v}-\rho\,\vec{g}\,\beta\,(T-T_0)+\vec{j}\times\vec{B} \tag{1}$$

where $\vec{v}$ is the velocity vector field, p the pressure, ρ the reference density, η the dynamic viscosity, β the coefficient of volume expansion, g the gravity acceleration constant, $\vec{j}$ the electric current density and $\vec{B}$ is the magnetic field induction. For its specification see chapter 5.

Mass conservation and energy transport equations:

$$\nabla\cdot\vec{v}=0 \tag{2}$$

$$\rho\,c_p\left(\frac{\partial T}{\partial t}+(\vec{v}\cdot\nabla)T\right)=\nabla\cdot(k\nabla T) \tag{3}$$

where T s the temperature and c_p is the specific heat. The heat conductivity is designated as k.

Boundary conditions:

- no-slip at the crucible walls and interface crystal/melt
- melting temperature at the interface crystal/melt
- fixed heat flux distribution at the external graphite crucible walls (taken from a thermal global modelling)
- thermo-capillary conditions at the free melt surface
- gray body radiation condition at the melt surface and crystal side (with an "effective" emissivity $\epsilon(\vec{r})$ distribution computed from the thermal global modelling, where σ_S denotes the Stefan-Boltzmann constant)

$$-k\,\frac{\partial T}{\partial n}=\epsilon\,\sigma_S\left(T^4-T_0^4\right)=\epsilon(\vec{r})\,\sigma_S\,T^4$$

In order to define a smooth heat boundary condition at the external graphite crucible walls, we made a polynomial fit of the values provided by the thermal global modelling.

4. Numerical method

The governing equations for the computation of the flow, the temperature and the electrical stream function were solved numerically by a finite element method. We applied the commercial code FIDAP. Because the characteristic numbers (like the Reynolds and Grashof numbers) are near critical values (but not so large, that a fully developed turbulence exists) we used the Wilcox's Low-Reynolds turbulence model (see [1]). This model belongs to the so-called two-equation group of turbulence models and is therefore closely related to the $k-\epsilon$ type models. An important advantage of this model is that it can be used to directly predict low-Re ($Re \leq 10^5$) effects on the turbulence field in the near wall regions and does not need any (artificial) wall functions.

The two dimensional computational domain, contained in the plane $r-z$, has been discretized into a mesh of quadrilateral finite elements, with a finer spacing near the melt boundaries, but specially near the interface melt/crystal.

A typical velocity vector plot is shown in Fig. 2. It shows the predominance of the crucible and crystal rotation.

It is worth to assert that the Ekmann layer (depth: $\delta_E \approx 0.7mm$) caused by the crystal rotation at the interface is very thin and it turns out to be crucial for griding of the computational domain. A very high grid refinement is necessary in this region. It is necessary to find a compromise between memory usage, computational time and the need to find a grid independent solution. After the analysis of the grid dependency of the solution, we decided to use a grid with 22300 elements for all further calculations. Whitin this grid resolution, a complete converged flow and heat transfer simulation needs approximately $20h$ cpu time on a SGI Origin 2000 workstation.

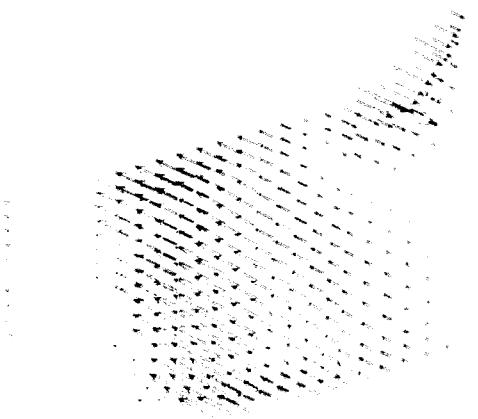

Fig. 2: Typical velocity vector plot.

5. Magnetic fields

The magnetic induction field distribution and, in the case of non-steady magnetic fields, the distribution of the electromagnetic force density $\vec{f}_L = \vec{j} \times \vec{B}$ were computed using the electromagnetic commercial solver OPERA. The geometry is assumed to be axi-symmetric.

5.1. Steady magnetic field

In the case of a steady magnetic field, the induction law reduces to $\nabla \times \vec{E} = 0$. It means that an electrical potential can be introduced: $\vec{E} = -\nabla\Phi$

Taking into account the Ohm's law (where σ denotes the electrical conductivity)

$$\vec{j} = \sigma\left(-\nabla\Phi + \vec{v} \times \vec{B}\right)$$

and the Kirchhoff's law $\nabla \cdot \vec{j} = 0$ we obtain the following equation for the electric potential:

$$\Delta\Phi = div\left(\vec{v} \times \vec{B}\right) = \vec{B} \cdot (\nabla \times \vec{v})$$

This relation shows that in vorticity regions potential differences exist creating a local electric field which can balance the electromotive field and allow the electric current lines to close. The relation above couples the electric potential, the magnetic induction and the vorticity distribution. This equation is solved numerically in order to determine how the DC magnetic fields act.

In this paper, results for numerical studies are presented concerning 2 types of steady magnetic fields: an axial homogeneous and a cusp field.

In order to generate a *homogeneous axial magnetic field* which has a main component in the direction of the symmetry axis, we presumed to have 2 direct current coils in the way connected, that the electric current is flowing in the same direction. For the calculations with OPERA we assumed a current density flowing through the coil of approximately $10^7\ A/m^2$ what provides a maximum magnetic induction of $400\ mT$.

The so called *cusp magnetic field* can be generated by means of two coil systems carrying electric currents in opposite direction. The distribution of the field in the region containing the melt is very inhomogeneous. The cusp magnetic field induction distribution shows (see Fig. 3) that the field strength growths in the melt from zero at the symmetry axis up to approximately 1/30 of the maximal value of the corresponding axial field strength at the crucible walls.

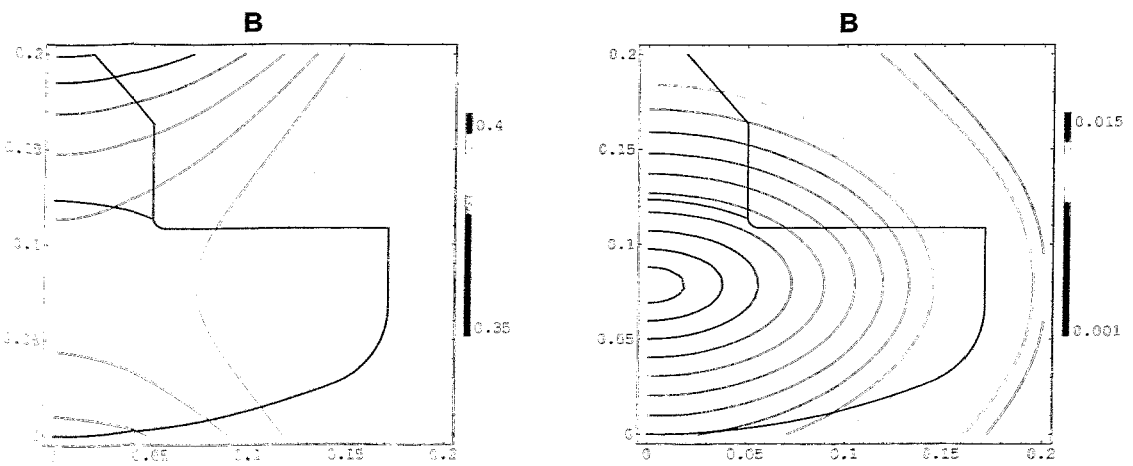

Fig. 3: Homogeneous (left) and cusp (right) steady magnetic induction distribution in Tesla.

5.2. Alternating magnetic field

The alternating magnetic field is induced using a set of windings fed by an external power supply with an alternating current (AC). This time dependent magnetic field induces an electric current in the conducting melt. Because of the skin effect, the magnetic lines penetrate into the conducting material up to a skin depth of the order $\delta = (\mu\,\sigma\,\omega)^{-1/2}$, where μ is the magnetic permeability, and ω the frequency of the pulsating field.

The Lorentz force $f_L = \vec{j} \times \vec{B}$ averaged over one period has a time-independent component since both $\vec{j}$ and $\vec{B}$ vary harmonically in time with the same frequency.

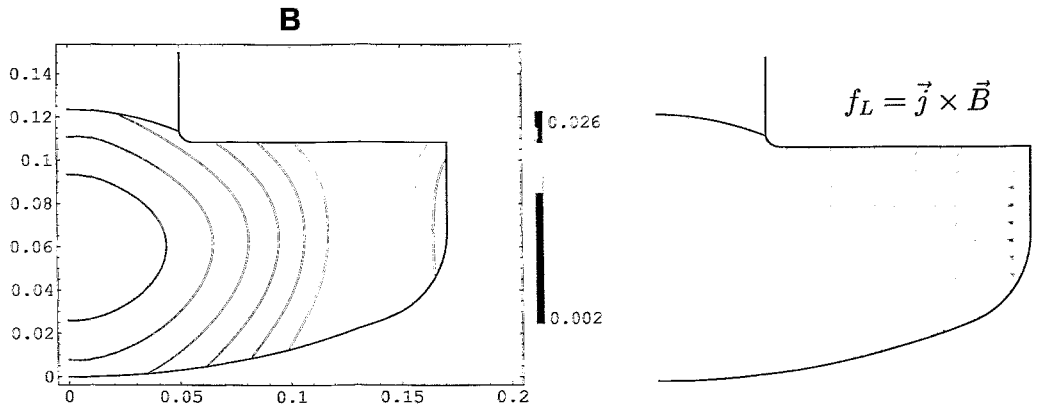

Fig. 4: Alternating magnet field distribution (left) and Lorentz force vector plot (right).

6. Results

Typical results of the magnetic field actions are shown in Fig. 5. The main action of the AC-field consists in a flow driving mechanism which may superimpose the buoyancy convection in the meridional plane. This can lead to an opposite flow direction at the free melt surface if the AC-field amplitude is sufficiently strong. Without magnetic fields the meridional flow is mainly determined by buoyancy with a strong vortex resulting in a melt flow direction from the crucible to the crystal at the free surface of the melt (not shown in Fig. 5). The AC-field primarily creates a jet at mid-height of the crucible as can be seen from the Lorentz force distribution in Fig. 4. This Lorentz force creates a double vortex structure in the melt causing the melt at the free surface to flow from the crystal to the crucible wall, i.e. against the basic buoyant flow direction. Depending on the strength of the AC field this may change drastically the heat- and mass transport in the meridional plane. The DC-fields have in general a stabilising influence on the melt flow. It results in a general weakening of the convective velocities, and (not shown in Fig. 5) in a reduction of the turbulent velocity and temperature fluctuations. A better homogeneous damping effect is found for the cusp magnetic field since it provides no preferred direction to the flow field. In case of a vertical homogeneous magnetic field additional instabilities may arise due to the fact that vorticity parallel to the preferred magnetic field direction is not influenced by such type of DC-fields.

The different magnetic fields offer a large variety of control possibilities for a contact-less optimization of the heat and mass transfer processes in the silicon melt.

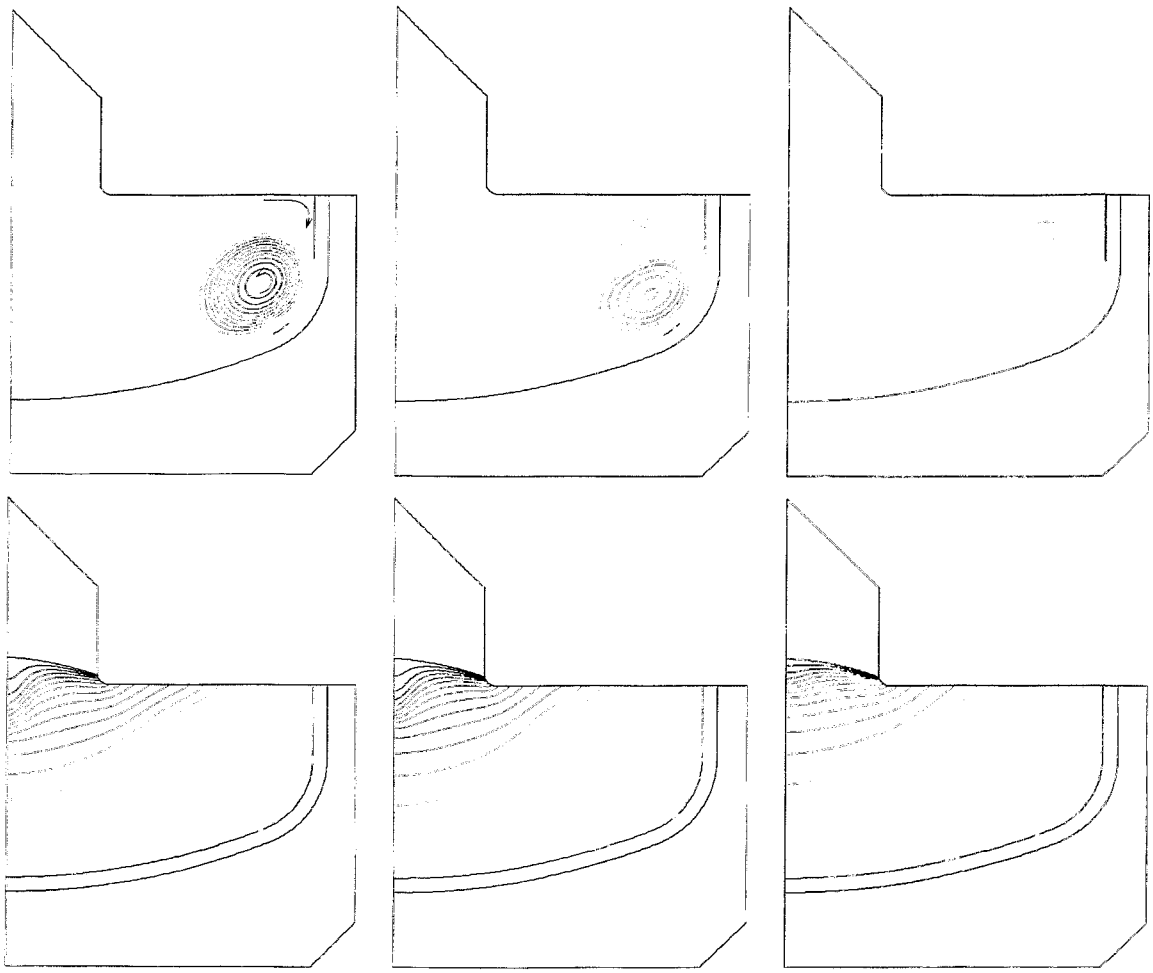

$B_c = 32\ mT$ $B_c = 128\ mT$ $B_c = 256\ mT$

Fig. 5: Flow streamlines (above) and isotherm distribution (below) by the combined action of alternating ($B_{ac} = 12\ mT$) and cusp ($B_c = 32, 128$ and $256\ mT$) magnetic fields.

References

[1] D. C. Wilcox (1993), Turbulence Modelling for CFD, DCW Industries, Inc.

MEASUREMENT TECHNIQUES TO DETERMINE LOCAL QUANTITIES IN LIQUID METAL FLOWS

Sven Eckert, Willy Witke, Gunter Gerbeth

1. Introduction

In the last few decades magnetohydrodynamic (MHD) effects have attracted growing interest because of its potential impact on numerous industrial technologies such as metallurgy, crystal growth, electron or laser beam melting/evaporation of surfaces, etc.. In processes involving electrically conducting liquids, the application of an external magnetic field offers efficient opportunities for a contactless flow control and fluid handling.

However, for a well-aimed optimisation of the flow structure local information about flow quantities like velocity, pressure, temperature, concentration or void fraction are necessary. The techniques of local and instantaneous measurements in liquid metals are known to be much more difficult than in classical fluids like water or air. Whatever diagnostic method is used, two categories of problems have to be solved: those due to the nature of the fluid (opaque, hot, chemical aggressive) and, in addition, due to the presence of electromagnetic fields. Almost all conventional measuring techniques used for ordinary flows, for instance LDA or hot-wire anemometry, totally fail in liquid metal MHD flows or their applicability is strongly limited. As a consequence, no commercial measuring systems are available.

During the last years activities of the MHD department are focussed to develop and to qualify techniques to measure the velocity of the liquid metal and two-phase flow characteristics such as void fraction, bubble velocity and bubble size, respectively. In liquid metal model experiments local sensors as well as integral methods have been tested and applied.

2. Measurements of the liquid metal velocity

2.1 Potential-difference Probe

The potential-difference probe (sometimes also called conductance anemometer) can already be considered as standard technique in MHD experiments (see Branover [1]). The problem to be solved here was the development of special sensors being capable of working reliably in liquid sodium.

If a flow is exposed to a sufficiently strong magnetic field the measured electric potential drop $\Delta\varphi$ between the electrodes is essentially determined by the $\vec{u}\times\vec{B}$ term [2] (see figure 1), resulting in a linear dependance on the flow velocity. The following advantages promote the use of such kind of probes:

- The geometry of the probe is very simple (two isolated electrodes). Therefore, a good minimisation of the sensor size is possible to reduce the flow disturbances caused by the probe itself.

- The sensor is reliable and robust in liquid sodium at temperatures up to 320°C.
- The relation between the voltage signal and the fluid velocity is linear for a wide parameter range.
- The sensor responds promptly and guarantees the suitability to measure the turbulent velocity fluctuations.

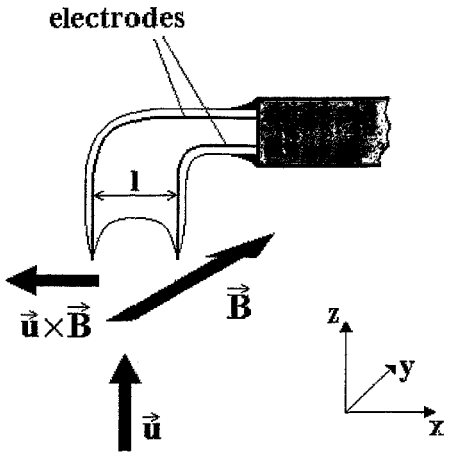

Fig. 1: Principle of the potential probe

However, the use of the potential probe is combined with some serious limitations and difficulties. The measuring principle requires the application of a steady magnetic field, whereas the velocity component parallel to magnetic field lines cannot be determined. To measure the velocity fluctuations one has to deal with very small signals (some μV), which can be disturbed by a significant level of electric noise arising from components of the experimental facility (electromagnetic pump, heating elements). Moreover, the linear relation between output signal and velocity is not valid if the flows is bounded by highly conducting walls or influenced by changes of the magnetic field, the cross sectional area or the wall conductance [2].

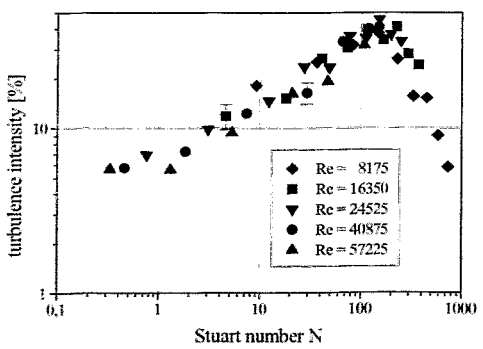

Fig. 2: Turbulence intensity as a function of Stuart number N

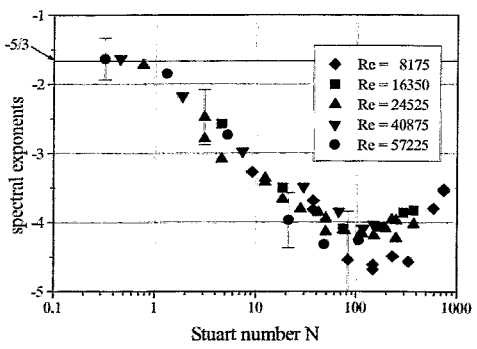

Fig. 3: Slope of the spectral energy versus Stuart number N

Potential probes have been employed to characterise the local, turbulent properties of liquid sodium channel flows by the determination of the turbulence intensities and the power spectra [2]. Some interesting effects have been revealed, for instance, the increase of the turbulence intensity with increasing Stuart number $N=\frac{\sigma B^2 L}{\rho u}$ (see Figure 2) or the steeper slope of the spectral energy in the inertial range with increasing Stuart number starting from a $k^{-5/3}$-behaviour for $N \leq 1$ and reaching a k^{-4} -scaling at $N \approx 100$, which becomes obvious in Fig. 3.

2.2 Mechano-optical probe

A new measuring system based on a mechano-optical principle has been developed to determine local flow velocities. Our intention was to meet the following requirements:

- The sensor should be able to work in opaque fluids at high temperatures.
- The resolution should be sufficient to measure also velocities below 0.1 m/s.
- The system should be characterised by good spatial resolution.
- Flow disturbances caused by the sensor should be negligible.
- An influence of external electromagnetic fields or electric noise on the signal should be avoided.

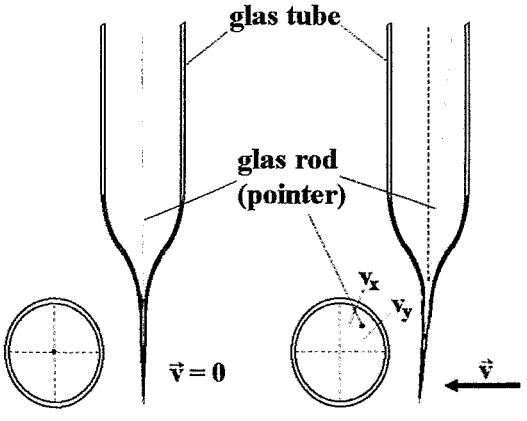

Fig. 4: Measuring principle of the mechano-optical sensor

The sensitive part of the probe is a glass tube formed to a thin conical tip which is in direct contact to the fluid (see figure 4). A small glass rod, the so-called pointer, is positioned inside this glass tube and connected with the sensor tip only at the front point. The interaction with the flow causes a deformation of the sensor tip resulting in a displacement of the pointer. The flow velocity can be derived from this observed displacement. A detailed description of the measuring principle and the equipment is given by Eckert et al. [3]. The authors also modelled the drag force acting on the sensor in the fluid. From those estimates the rod displacement shows a parabolic dependence on the flow velocity. Such a qualitative behaviour has been confirmed by first experimental investigations, where the sensors have been calibrated in a circular rotating channel.
The sensors have been tested in water and InGaSn at room temperature as well as in SnPb and PbBi at temperatures up to 300 °C. The suitability of the sensor in this temperature range was

demonstrated. A further increase of the temperature can be questionable, because the elastic module of the borosilicate glass becomes then a function of the temperature. The transformation temperature of this type of glass is approximately 650 °C. To use the measuring system at higher temperatures, for instance in aluminium at about 700 °C, the probe tip has to be manufactured from different material. A possible alternative is quartz glass with a transformation temperature above 1200 °C. The adaptation of the existing technology for the sensor production to quartz glass is the present subject of investigation.

The measuring system has already been used to determine the local flow structures in real experimental flows. In our lab swirling flows of InGaSn alloy in a circular box created by the application of time-variable (travelling and/or rotating) magnetic fields have been investigated. The interest is focussed on geometry and parameters relevant for crystal growth technologies. Measured profiles of the azimuthal velocity obtained at different frequencies and field amplitudes are displayed in Figure 5. In case of low frequency the increase of the velocity starting from the centre to the boundary seems to be linear. This indicates that the flow structure of the melt can be associated with a solid body rotation. The application of a magnetic field rotating with a significantly higher frequency results in an evident variation of the profiles. The enhancement of the velocity maximum near the boundary corresponds to the above-mentioned skin effect of the concentration of the field action in the boundary region.

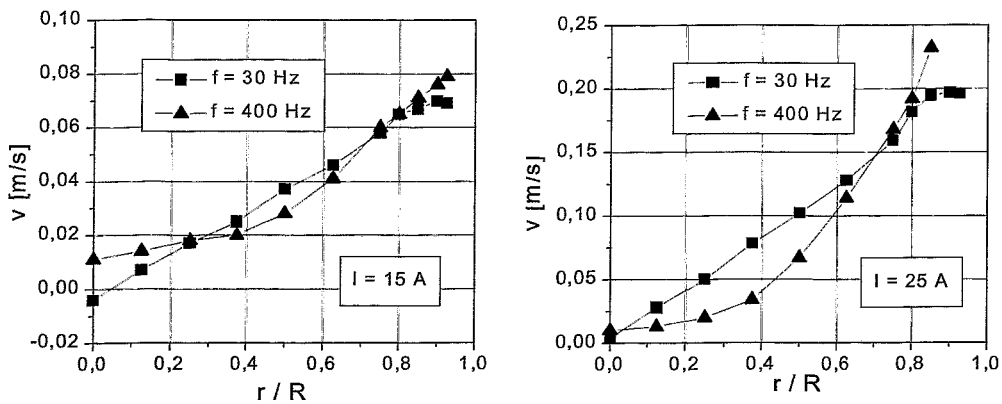

Fig. 5: Radial profiles of the azimuthal velocity in a cylindrical flow driven by a rotating magnetic field

Another application will be the channel flow of liquid sodium at the experimental sodium loop of FZR. It is planned to measure the velocity profiles in the channel cross section with and without transverse magnetic field. The obtained results shall be compared with the existing data of the potential probe. Moreover, first measurements have been confirmed in co-operation with industrial partners.

2.3 Ultrasound-Doppler method

The instantaneous velocity profile which is one of the most fundamental quantities in fluid flow phenomena can be obtained by the Ultrasound-Doppler technique [4]. Main advantages are the ability to investigate flows of opaque liquids in a non-intrusive way and to deliver complete velocity profiles in real-time. The principle of this method is to utilise the pulsed

echo technique of ultrasound and to detect the Doppler shift of the ultrasound wave reflected from moving particles suspended in the fluid.

The general feasibility of velocity profile measurements has already be shown in low temperature liquid metals like mercury [5] and gallium [6]. However, the technology reveals severe limitations regarding the practicability of measurements at high temperatures and the useable velocity range. Therefore, activities have been started to develop this technique for high temperature liquid metal applications. First tests have already been performed at the sodium facility of FZR. At the present status the following main problems have been identified:

- Limitation of the temperature range of the ultrasonic transducer: The transducer can be used up to a maximum working temperature of 150°C. Moreover, the efficiency at temperatures close to this maximum is low.
- Coupling of the ultrasound into the fluid: Due to the high temperatures and the chemical properties of liquid sodium the transducer was installed at the outer channel wall. Therefore, an excellent wetting of the liquid metal at the inner surface of the wall is required to get a small acoustic impedance at the interface steel - liquid metal.
- Availability of tracers in the flow: The sensitivity and accuracy of the method depends on the occurrence of flow tracers reflecting the ultrasonic beam. If the amount of naturally existing impurities is not high enough, additional scattering particles have to be added to the flow.

3. Measurements of two-phase flow parameters

3.1 Resistance probes

The single-wire resistance probes are local sensors to measure the local void fraction well-known from the applications in ordinary two-phase flows (see Jones & Delhaye [7], Prasser [8]). There is an electrically conducting tip (Cr/Ni wire, ∅ 0.1 mm) in direct contact with the liquid metal. The probe is supplied with an alternating current (1-10 kHz), which results in an electric current flowing from the probe tip to the cladding pipe acting as the other electrode. The gas contact at the sensitive wire is detected by an interruption of the current. Due to the huge differences in the electrical conductivity between the gas and the liquid metal we obtain very sharp signals easy to evaluate by a threshold method.

An extensive survey about a number of two-phase flow measurements carried out by several kinds of local sensors characterised by different tip sizes and probe shapes is provided by Cartellier & Achard [9]. As a rough estimation it may be generalised, that bubbles with a minimal size being about 10 times higher as compared to the probe wire can be detected by the sensor. In our experiments single-wire conductance probes with wire diameters of 25 μm and 100 μm have been used.

Double-wire resistance probes have been used to measure gas velocity and bubble size by detecting the time delay of the bubble contact between two wires arranged closely together in flow direction. But, such a sensor configuration enhances seriously the tip size of the probe. In fact, reliable measurements of bubble diameters less than 1 mm by means of local conductance probes have to be considered as doubtful. Despite of measuring errors of bubble

velocities and chord lengths up to about 20 % for bubble diameters of a few mm also measurements by means of double-wire probes provide useful information about the structure of the two-phase flow.

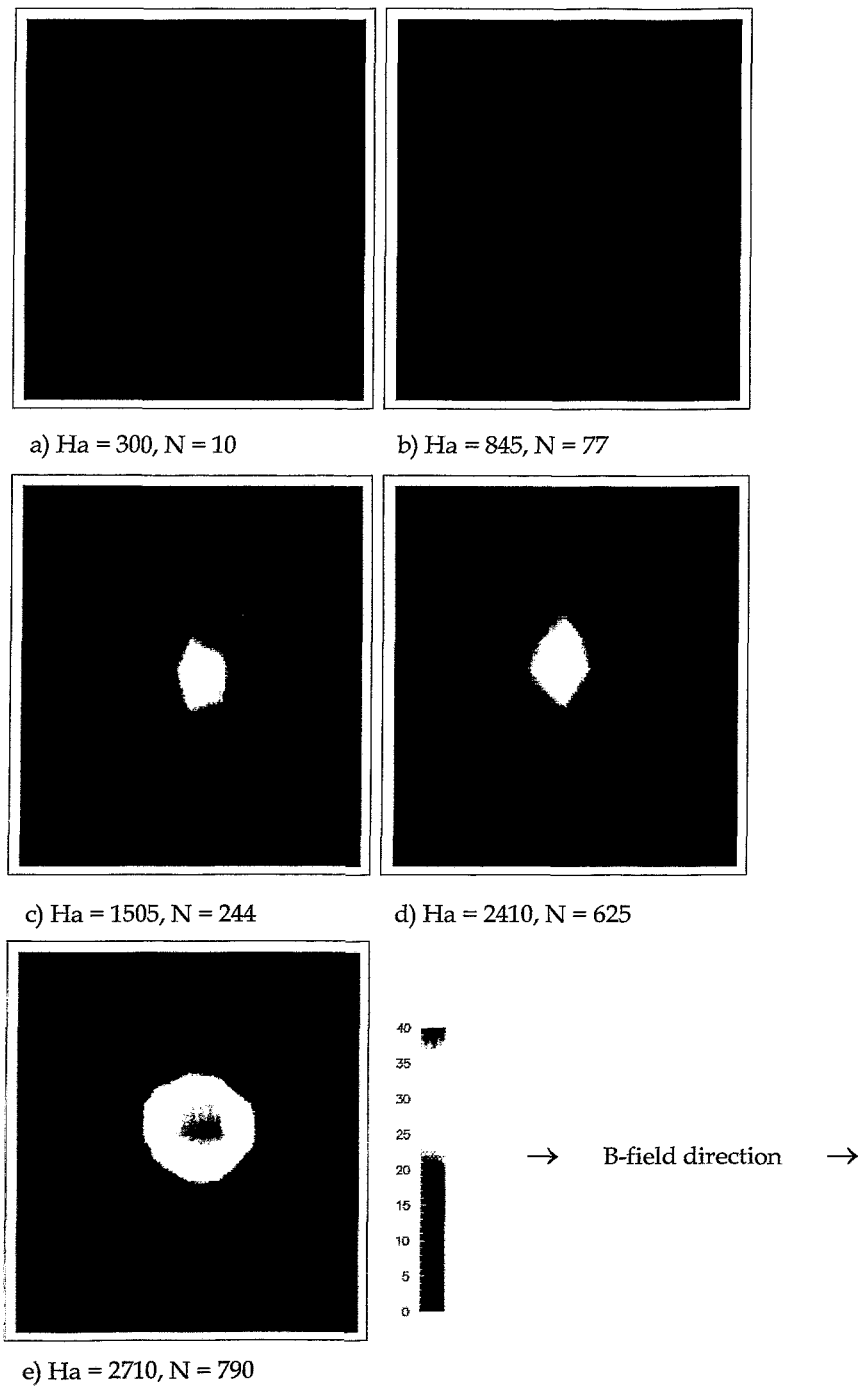

Fig. 6: Local distributions of the void fraction α [%] in a turbulent sodium channel flow exposed to a transverse magnetic field (Re = 9300)

Figure 6 shows some representative isoplots of the void fraction distribution in the cross sectional area of a MHD channel flow obtained at different Reynolds numbers and different

values of the magnetic field by Eckert et al. [10]. In the case of a transverse field direction an anisotropic distribution is observed indicating the existence of quasi-two-dimensional vortices as typical for turbulent MHD flows.

3.2 X-ray measurements

A direct observation of gas bubbles in non-transparent liquid metals is impossible by optical means. Despite of the substantial technical effort, the use of high energy radiation allows also investigations of liquid metal two-phase flows. X-ray measurements can be used to directly observe gas bubbles rising in liquid metals. However, due to the high attenuation in the liquid the experiment is restricted to narrow flow domains. The thickness of the fluid, which can be screened by X-ray, depends of the atomic number of the liquid metal.

Experiments with mercury and InGaSn, respectively, have been performed at the X-ray facility of the FZ Jülich. A 450kV industrial X-ray tube was employed for the inspection of liquid metal contained in rectangular cell made from Perspex. A sketch of the experimental configuration is depicted in Figure 7. For a detailed description of the experimental technique the reader is referred to Stechemesser et al. [11]. Flow sequences were recorded in mercury layers with a depth of 6 mm at 450 kV and 10 mm for InGaSn at 147 kV. Experiments with InGaSn would allow an enlargement of the fluid domain, whereas for mercury the limit has been reached. The resolution of the X-ray screening technique is restricted to a bubble diameter of about 1 mm. The decrease of the X-ray absorption inside the liquid volume due to smaller gas bubbles is not sufficient to produce a corresponding image with a reliable contrast.

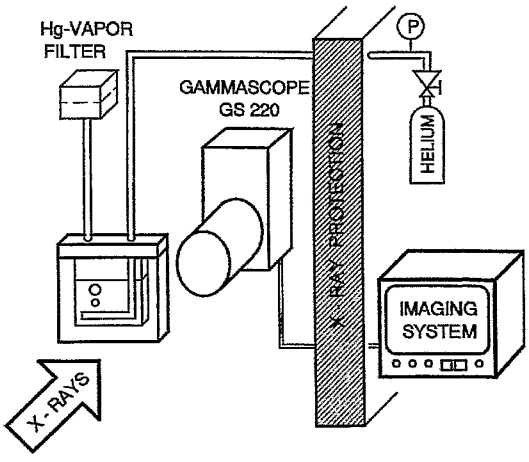

Fig. 7: Experimental configuration of the X-ray screening technique

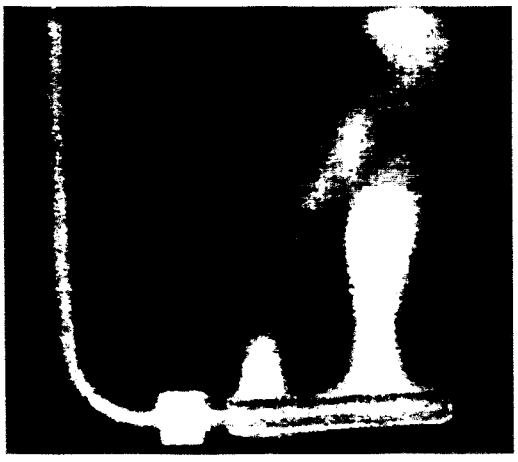

Fig. 8: Gas injection through a nonwetted sintered metal tube into mercury (observed by X-ray technique)

The features of a gas injection into mercury by means of miscellaneous gas injectors for the case, if the surface of the injector is not wetted by the liquid metal, has been demonstrated [12]. Among other types of gas injectors a bent stainless steel tube has been used completed with a sintered metal body at the end having a mean pore diameter of 4 μm. The gas flow can escape from the injector only at the upper surface. Nevertheless, it becomes obvious in Figure

8 that instead of a bubble formation directly at the end of the pores, a gas layer is growing around the injector until the buoyancy force will be high enough to promote the release of particular, large bubbles. However, in this situation the size of the generated bubbles does not depend on the typical diameter of the injection pores.

References

[1] H. Branover (1978), Magnetohydrodynamic Flow in Ducts, New York, Toronto, John Wiley & Sons

[2] S. Eckert (1998), Experimentelle Untersuchung turbulenter Flüssigmetall- und Flüssigmetall-Gas-Strömungen in einem äußeren Magnetfeld, Rossendorf, Report FZR-219

[3] S. Eckert, W. Witke and G. Gerbeth (1999), A new mechano-optical technique to measure local velocities in opaque fluids, submitted to: Flow Measurement and Instrumentation

[4] Y. Takeda (1991), Development of an ultrasound velocity profile monitor, Nuclear Engineering and Design, 126, 277

[5] Y. Takeda, H. Kikura and G. Bauer (1998), Flow Measurement in a SINQ Mockup Target using Mercury, Proc. of ASME FED Summer Meeting, Washington D.C.

[6] P. Cardin, H.-C. Nataf, B. Pascal and J. C. Attiach (1996), Velocity measurements in a vortex of liquid Gallium, 1st Int. Symposium on Ultrasound Doppler Methods for Fluid Mechanics and Fluid Engineering, Villigen PSI

[7] O. C. Jones and J.-M. Delhaye (1976), Transient and statistical measurement techniques for two-phase flows: A critical review, J. Fluid Mech.,147, 89

[8] H. M. Prasser (1997), Leitfähigkeitssensoren für die Bestimmung von Parametern in einer Zweiphasenströmung, Workshop "Meßtechnik für stationäre und transiente Mehrphasenströmungen", Rossendorf

[9] A. Cartellier and J. L. Achard (1991), Local phase detection probes in fluid/fluid two-phase flows, Rev. Sci. Instrum., 62, 279

[10] S. Eckert, G. Gerbeth and O. Lielausis (1998), The behaviour of gas bubbles in a turbulent liquid metal MHD flow - Part I: Dispersion in quasi-two-dimensional MHD turbulence, submitted to: Int. J. Multiphase Flow

[11] H. Stechemesser, G. Schröder, Ch. Sauerwein and W. Nuding (1998), Gas injection experiments in static Hg: Real-time observations with X-rays, ESS report 98-68-T

[12] S. Eckert, G. Gerbeth, B. Guttek and H. Stechemesser (1998), Bubble formation in heavy liquid metals: Evaluation of conventional gas injection methods with respect to a suitability under ESS relevant conditions, ESS Report 98-72-T

The projects summarised in this report are funded by Deutsche Forschungsgemeinschaft under grant No. Ge 682/3-4 and in frame of the DFG-Innovationskolleg Magnetofluiddynamik.

Short Contributions

Accident Analysis

U. Grundmann,
S. Kliem,
S. Mittag,
U. Rohde,
A. Seidel,
as guest scientist:
I. Reiche

Development, validation and application of the code complex DYN3D - ATHLET

Concerning the validation of the coupled 3D neutron kinetics/ thermohydraulic code complex DYN3D-ATHLET, a new quality was reached by participation in international benchmarks and comparison of calculations with measurement data from real transients in NPPs. The benchmarks comprise the analyses of 2 main steam line break scenarios. Due to the overcooling of the reactor connected with positive reactivity insertion, recriticality and return to power of the shut down reactor can occur. 5 organisations from 5 countries participated in the benchmark exercise for VVER-440 type reactors, which was defined by FZR. The other exercise for a Western PWR is organized by OECD/CSNI.

In the framework of an EU PHARE project under the leadership of FZR in which institutions from 3 EU member states and 5 East European countries take part, measurement data on transients in nuclear power plants with VVER type reactors have been collected and documented. Two transients, the power drop of one generator down to house load level at NPP Loviisa (VVER-440) and turning off one of two working feedwater pumps at NPP Balakovo (VVER-1000), were selected for the analysis using different coupled code systems. It is the first international validation of coupled codes against measuring data from NPPs.

A new, original nodal expansion method was developed leading to enhanced accuracy of the neutron flux calculation in DYN3D. In cooperation with IPPE Obninsk (Russia), DYN3D has been coupled to the internationally widely used thermohydraulic system code RELAP.

Using the 2D neutron transport code HELIOS, effective macroscopic cross sections for the absorber elements of VVER-440 type reactors were generated. A methodology has been developed to ensure the equivalence of the neutron diffusion theory which is applied in DYN3D to transport calculations.

supported by BMBF, BMU, and EU

E. Krepper,
F. Schäfer

Validation of thermohydraulic system codes

The activities were focused on the validation of the thermoydraulic code ATHLET (developed by Gesellschaft für Anlagen- und Reaktorsicherheit) against experiments performed at thermohydraulic integral test facilities. Post test analysis calculations of two experiments were carried out, which were performed at the french integral test facility BETHSY. In the experiment 5.2c, the accident management procedure was investigated in case of the total loss of steam generator feedwater. The experiment should show the possibility of emergency core cooling by primary bleed and feed. In the test 9.3, the consequences of the failure of the emergency feedwater and high pressure safety injection systems after

a steam generator tube rupture were investigated. Primary and secondary side depressurization to activate the low pressure emergency core cooling system was shown to be an appropriate accident management measure.

Calculations were performed for two large break LOCA experiments with cold and hot leg safety injection into the primary circuit. The tests were done at the Japanese test facility CCTF. Significant counter current flow of steam and water occured during these experiments. The analyses aim at the validation of an improved ATHLET model for phase interaction.

funded by BMBF

E. Krepper, A. Krüssenberg, T. Höhne, M. Kliem

Computational fluid dynamics simulations of one and two-phase flow

At the Rossendorf coolant mixing test facility ROCOM, experiments were performed on the mixing of a plug of salt water simulating a temperature or boron concentration perturbation in one of the loops under steady-state conditions and during the start-up of the first pump. CFD calculations show a good agreement of the velocity distribution in the downcomer with data obtained in the experiment by laser Doppler anemometry. Comparative numerical studies on the flow field in the downcomer of KONVOI and VVER-440 type reactors were done confirming a simplified mixing model for VVER-440 as it is used in the code DYN3D.

Experiments on the convection in externally heated storage tanks were done together with VKTA Rossendorf. The temperature and void fraction were measured at different locations in the tank. The formation of stable temperature layers during the heat-up of the tank was observed in the case of heating from the side, while in the case of heating from the bottom the fluid is homogeneously mixed. The measurement data will be taken for the validation of CFD codes.

Using the code CFX-4, experiments carried out at the Rossendorf two-phase flow test loop were numerically simulated. Velocity and void fraction profiles of water and air flows were measured with different gas and liquid superficial velocities in the tube using high resolution two-phase instrumentation (wire mesh sensor). Taking into account different forces acting on the bubbles in a two-phase flow, typical radial velocity and void fraction profiles were simulated.

partially funded by BMBF (know how conservation program)

D. Lucas, H.-M. Prasser

Pressure relief of chemical reactions

The code BRICK, a new one-dimensional simulation tool for multiphase flow in batches and tanks, was improved and extended by additional single effect models, e.g. for phase transition under non-equlibrium conditions and the kinetics of chemical reactions. The code was validated against numerous depressurization experiments with different reaction systems, where the pressure builds up mainly due to evaporation (esterification of methanol and acetic anhydride), gas re-

supporteded by Volkswagen-Stiftung

lease from the chemical reaction (decomposition of ammonium peroxydisulphate) or both mechanisms (thermal decomposition of hydrogen peroxide). In charge of an industrieal partner, BRICK was used for the assessment of a pressure relief system.

Thermo-Fluiddynamics

A. Böttger
G. Grunwald
T. Höhne
H.-M. Prasser
K.-H. Richter
J. Zschau

Coolant mixing in pressurised water reactors

The mixing test facility ROCOM modelling the German KONVOI type pressurised water reactor in the scale of 1:5 was constructed and put into operation. It is aimed at studying the mixing during boron dilution and steam line break transients. The main purpose is the generation of high-resolution data for the validation of 3D CFD codes. The facility disposes of four individually controllable loops. It is equipped with several mesh-sensors used for the measurement of the tracer salt concentration in the downcomer and at the core entrance.

A. Böttger
H.-M. Prasser
J. Zschau
C. Zippe
W. Zippe

Development and calibration of two-phase flow measurement techniques

The qualification of the diversified level indication system for boiling water reactors developed by FZR was started according to the German reactor safety regulations. The qualification procedure and the series production will be accomplished by an industrial supplier of measurement instrumentation. FZR contributes as a scientific consultant.

An extensive calibration of different kinds of two-phase flow instrumentation was performed at the two-phase test loop in Rossendorf. A gamma-densitometer was used as reference measurement. Void fractions obtained by the wire-mesh sensor and the needle probes developed by FZR are in good agreement with the readings of the gamma-densitometer in the entire void range between 0 and 100 %.

In co-operation with the Technical University of Nishny Novgorod (Russia) a new ultrasonic mesh sensor was developed. The work is part of a TRANSFORM project financed by the BMBF. The sensor is based on a system of crossing ultrasonic wave-guides. It is complementary to the electrical wire-mesh sensors of FZR, because it can be applied to non-conducting fluids. The sensor was tested at the Rossendorf two-phase flow test loop.

For the investigation of transport processes in bubble columns and foam layers, a PET detector is under construction. The scanner will allow to measure the distribution of a tracer marked by a positron emitting nuclide with a time resolution of better than 1 s. It consists of 8 axial layers with 16 BGO detectors each. The spatial resolution will be in the range of a centimetre.

T. Kern
D. Lucas
H.-M. Prasser

Basic studies of two-phase flows with foam production

The thermal decomposition of hydrogen peroxide was used as a model reaction for a runaway in a batch reactor. Experiments were carried out at a 2 l autoclave. The strong exothermal reaction leads to a combined degassing-evaporation process, which is very valuable for the validation of computer models, like the code BRICK, developed by FZR.

Needle shaped conductivity probes were applied to foams. The reason for the underestimation of the gas fraction in the foam layer was clarified by observing the interaction of the probe tip with the flowing foam. It was found, that the foam cells trend to orient their Plateau borders along the probe, which leads to unrealisticly long contact times with the liquid. A method to eliminate this effect by evaluating the time derivate of the probe signal is under development.

A. Grahn

Thermoconvection and instabilities at the boundary layer of two non-miscible liquid reacting components

During the neutralisation of carbonic acids dissolved in the organic phase with sodium hydroxide in the aqueous phase, a double-diffusive convection flow regime was discovered. In a capillary gap the regime is characterised by fingering in the heavier aqueous phase. Characteristic wave lengths and the time behaviour of the growth of the fingers were studied as a function of the reacting species and the gap width.

E. Krepper,
H.-M. Prasser,
A. Schaffrath,
C. Zippe,
W. Zippe

Transient two-phase flows in pipelines

The wire-mesh sensor for fast gas fraction measurements in two-phase flows was used to study the transient flow pattern in an air-water flow in a vertical pipe. Experiments were carried out by varying the superficial velocities of both phases in a wide range, so that bubble, slug and annular flow regimes were covered.

Besides the high-speed flow visualisation and the analysis of gas fraction profiles, the sensor data were used to get bubble size distributions. For this purpose, a special signal evaluation algorithm was developed. In the transition region between bubble and slug flow, a change from a monomodal to a bimodal bubble size distribution was found at growing superficial liquid velocity, which can be taken as a quantitative criterion for the onset of bubble coalescence. When the maximum bubble diameter exceeds the inner diameter of the pipe this is an indication that bubble-to-slug transition has occured. Several flow maps from the literature were compared to the new criterion. The best agreement was found with the flow map after Taitel, Bornea & Dukler.

Further, the evolution of the flow pattern along a vertical pipeline was studied. In a servies of experiments, the axial distance between the air injection and the wire-mesh sensor was successively increased. Three differnt air injection modes were used. Beside the void fraction profiles, the development of the bubble size distribution was obtained. This allows the development of models for bubble coalescence and fragmenta-

tion. The inlet length necessary to establish equilibrium profiles and bubble size distributions strongly depends on the superficial velocities. In some cases, even at the end of the entire test section (70 L/D) the influence of the air injection was still recognisable.

A. Schaffrath

Condensation models for horizontal pipelines

In co-operation with the HTWS Zittau/Görlitz the condensation models KONWAR (FZJ) and HOTKON (HTWS) were validated by cross-checking against experimental data from the HORUS test facility. Despite the fact, that the models were developed for different working parameters, both models implemented in ATHLET, describe the condensation process in horizontal steam generator tubes of VVER type reactors very well. GRS, as the developer, intends to include KONWAR into the standard version of ATHLET.

Materials and Components Safety

H.-W. Viehrig, H. Richter, J. Böhmert

Mechanical tests of reactor pressure vessel steel from the irradiation programme Rheinsberg

After the licence for the operation of the radionuclide material testing laboratory became valid at the end of 1997, a comprehensive test programme was performed with unirradiated materials to prove the practicable, correct and reliable operation of the equipment. The programme proved that the installed devices and used techniques meet the requirements. In the laboratory both conventional mechanical and fracture mechanics parameters can be measured. It has been used for the specimens from the irradiation programme Rheinsberg, which is part of the German Russian scientific cooperation. The programme comprised instrumented Charpy impact tests and quasi-static 3-point bending tests. The shift of the Charpy transition temperature due to irradiation and the recovery by annealing were determined. Additionally, the fracture toughness K_{IC} was measured and evaluated using the master curve concept. In general, the results were consistent with the prediction according to the Russian guides. In the case of a VVER 1000-type weld metal a surprisingly high embritttlement was detected.

supported by BMWi

H.-W. Viehrig, H. Richter, J. Böhmert

Correlation between mechanical and fracture mechanics parameters for irradiated reactor pressure vessel steels

In order to gain a broad data base, unirradiated materials were additionally investigated. For that purpose a heat of ASTM A533 B cl 1 pressure vessel steel was selected which is often used as IAEA reference material. The correlation between the Charpy transition temperature and the reference temperature according to the master curve concept is significant but scatters considerably. The large variations result from material inhomogeneities (segregations). As consequence of this scattering, neither the Charpy transition temperature nor the reference temperature could be determined with satisfactory accuracy if the tests were done according to the standards. New testing concepts are de-

supported by BMWi

signed and examined. They include tests at different temperatures and an increased number of specimens.

M. Große, A. Ulbricht, J. Böhmert

Microstructural analyses of irradiated VVER pressure vessel steels

Microstructural analyses of irradiated reactor pressure vessel steels were carried out using different techniques, such as transmission electron microscopy and small angle scattering with neutrons and X-rays. Transmission electron microscopy is not suitable to detect and characterize the weakly structured nano-defects produced by irradiation. Small angle neutron scattering clearly indicated irradiation-induced effects. Unfortunately, the interpretation of the measuring effects is difficult for a such highly complex material system like the pressure vessel steel. Therefore, additional techniques were applied to gain in formation about the type and composition of the irradiation defects.

The methods of contrast variation (anomalous X-ray scattering, ratio between magnetic and nuclear small angle neutron scattering) were combined with annealing experiments and model calculations of the scattering intensity of hypothetical defect structures. In this way, it could be shown that the irradiation defects can be interpreted as clusters from vacancies, iron, and solute atoms. Their volume fraction but not their size depends on the fluence. By annealing the defects can almost entirely be annihilated.

supported by BMWi

H.-W. Viehrig, S. Schneider

Radionuclide laboratory for the preparation of specimens from radioactive material

The second stage of the construction of the radionuclide laboratory for testing of radioactive materials shall allow the preparation of specimens from materials cut from the components of nuclear power plants. The most essential equipment is a CNC-controlled electric discharge cutting machine. The machine had to be modified for operation under semihot cell conditions. New or modified components were developed and tested. The design and the civil work for the laboratory are finished. The containment that houses the radioactive parts is just being constructed.

H.-G. Willschütz, E. Altstadt, T. Mössner, G. Müller

Behaviour of components under extreme mechanical and thermal loads

The investigation concentrated on the in-vessel and ex-vessel behaviour of core melt. As a first step the FZR has participated in a benchmark regarding the long-term behaviour of spread melt in the core catcher. The benchmark was defined by GRS together with Battelle Ingenieurtechnik. FZR contributed finite-element calculations with the code ANSYS/FLOTRAN. Using the standard k-ϵ-turbulence model and assuming a motionless superheated melt in the initial state, large convection rolls establish within the melt pool. The temperatures at the surface do not drop to solid temperatures due to the enhanced convection heat transfer. The temperature gradients at the surface are rela-

tively flat while there are steep gradients at the interface to the substratum where the no-slip condition was applied. However, even at the ground no solidification is observed. In general, good agreement of the results in comparison to the other participating finite volume codes could be stated.

To investigate the convection flow of a two component melt in the lower head of a PWR an axisymmetric finite-element model is developed using the code ANSYS/Multiphysics. The temperature field achieved with the fluid-dynamic calculation was imposed to a strucural mechanical model of the lower head. First calculations on the creep of the lower head were realized. For that, a user routine for the FE-code ANSYS was developed which allows to model the creep behaviour of metals at high temperatures (up to 1200 °C). This new creep law is based on high temperature tests performed by MPA Stuttgart. The ablation at the RPV wall is simulated by removing such elements which reach the melt temperature. The calculations show that the RPV does not even fail after about 24h after core slumping although a high internal pressure was assumed.

T. Repp, E. Altstadt

Calculation of the loads in pipelines due to waterhammers

The pressure waves induced by a sudden slow down of the fluid flow in a pipeline are modelled on the base of the finite element method. Special attention is put on the influence of fluid-structure interaction if the pipe diameter is relatively large in comparison with the wall thickness. The FE-code ADINA is used for modelling. The transient velocity and pressure distribution was calculated in a straight pipe and in a 90° elbow assuming a slightly compressible fluid. The coupling between the elastic pipe wall and the fluid is realized by boundary elements. It is shown that there are local stresses in the elbow which are higher than those calculated with the conventional uncoupled calculations.

supported by VDEW

E. Altstadt

Structural dynamic modelling of BWR components

During a hypothetical break of a BWR feed water line, the feed water distributor (FWD) inside the RPV is subjected to a high pressure load for a short time (10 ms). Due to the sudden coolant release from the inner volume of the FWD there is a pressure difference between the inner and outer surface. It is conservatively assumed that the pressure difference can nearly reach the operating pressure. The distributor box and the ring line of the feed water distributor are modelled with shell and volume elements that can be used for large strain analyses with elastic-plastic material behaviour. By non-linear static calculations (without consideration of the inertia of the material) it is demonstrated that a buckling instability occurs at about 60% to 80% of the maximum pressure load. The arc-length method is used for the numerical solution to overcome these points of instability. To evaluate the influence of the dynamics of the process a non-linear transient analysis was done showing that the maximum strain occurs with a time delay to the

pressure peak. The maximum plastic strain differs only insignificantly between static and transient solution. Inspite of the large strains the mechanical integrity is maintained during the hypothetical event.

M. Werner,
S. Perov,
E. Altstadt

Vibration modelling of VVER-1000 light water reactors

The work is to contribute to the efficient early failure of VVER-1000 primary circuit components. For that purpose, a finite element model for the simulation of mechanical vibrations of all primary circuit components of the VVER-1000 was established. With the adjusted model it is possible to clarify how hypothetical damages of reactor internals influence the vibration signature of the primary circuit. For a better recognition and analysis of damages at VVER-1000 reactors it is intended to integrate the simulation results into a catalogue of spectral signatures. Moreover, damage simulation is an appropriate means to find sensitive measuring positions for on-line monitoring and to define physically based threshold values for frequency shifts and amplitude changes.

The influence of fluid-structure interaction (FSI) on vibration modes was especially investigated. The method of modelling FSI was verifyed comparing the results obtained by finite-element calculations with the exact analytical solution of a simple fluid-shell test system. It was shown that the method of coupling between structural and fluid elements is important for the exact simulation of the eigenfrequencies. The vibration modes were calculated of the reactor pressure vessel and its internals. The FSI causes a considerable down shift of the shell mode frequencies of the pressure vessel, core barrel and thermal shield. Some bending modes which exhibit a relative displacement between pressure vessel and core barrel or between core barrel and thermal shield are significantly affected, too.

support by BMBF

M. Beyer,
H. Carl

Monitoring NPP in the Ukraine

A system was designed and constructed in analogy to the pilot project for the fifth unit of the Zaporozhye NPP (VVER-1000/V-320) to improve the operational monitoring for both VVER-440/V-213 units in Rovno. For that, 55 relevant-to-safety parameters per unit and 7 specific parameters of the NPP-site are made available to the on-site inspector at the NPP and to the Supervisory Authority in Kiev for collection and assessment. These parameters are transferred on-line by modern technical facilities once a minute. Within functional tests between the end of 1998 and the beginning of 1999 data records from the local area network of the Rovno NPP were correctly transferred to Kiev and displayed on a computer at the Information- and Crisis Centre.

Simulation of Particle and Radiation Fields

R. Küchler, K. Noack

Transport of reacting solutes through unsaturated soil

Unsaturated flows within subsurface regions control many large-scaled hydrological and environmental processes. The work aims at the development of a transport code system for the calculation of the migration of various radionuclides that models the relevant phenomena in maximum possible detail. The present code was used to compute the water flow and the reactive transport of several chemical species produced by the weathering of pyrite, calcite and uraninite through a soil matrix. The water motion was calculated for three different soil classes and for a typical annual precipitation. The code module which calculates the transport of the species incorporates the effect of hydrodynamic dispersion, nonlinear chemical equilibrium reactions, and kinetic chemical interactions between aqueous and solid phases. The obtained results have already demonstrated the relevance of the code system with regard to two aspects: it may serve as tool allowing a deep analysis and, so , the understanding of the interactin of the single processes and it can produce results which are of practical significance.

H.-U. Barz, B. Böhmer, J. Konheiser

Neutron dosimetry of reactor pressure vessels

The BMBF project "Development of an Advanced Method for Determination of the Neutron Load on VVER-1000 Reactor Pressure Vessel Material" was completed. The developed methodology allows to calculate pressure vessel fluences for VVER-1000 type reactors with high accuracy. By covariance analyses and spectral adjustment of the calculated fluence spectra, the theoretical results could be further improved in accuracy and consistency with the measurements.

The EU TACIS project "Development of Advanced Methods for the Evaluation of Irradiation Embrittlement of VVER-1000/320 Type RPVs" was started with the FZR as member of the leading consortium. Within the scope of this EU project, measurements and calculations for an international dosimetry experiment at the Russian irradiation facility KORPUS in Dimitroffgrad have been done. A calculational model was developed including all details about geometry, material composition of the facility, and the experiment. First TRAMO test calculations were performed with this model.

The Rossendorf Monte Carlo code TRAMO, so far intended only for neutron transport, is now being extended to allow also gamma transport calculations coupled to the neutron transport by neutron-gamma reactions. The needed additional nuclear data files have been generated. The adjustment code COSA2 was extended to allow simultaneous adjustment of several correlated spectra with activation detectors at different positions.

supported by BMBF and EU

H. Kumpf

Recriticality calculations for uraniumdioxide-water system

An important question of reactor safety is whether recritical constellations of fuel and moderator might appear in the course of a core melt accident. In this connection, some fundamental aspects of the recriti cality of water-uraniumdioxide mixtures were elucidated. Stochastic geometric arrangements of fuel and water were modeled and their neutron multiplication was determined by MCNP. It turned out, that these arrangements can be characterised globally by two parameters, the fuel chord length and the fuel/moderator volume ratio. The worst case with respect to recriticality has been identified still exhibiting mechanical stability.

H.-U. Barz, B. Böhmer

Transport of high energy ions and of fragmentation products

The development of the Monto-Carlo-Code IONTRA allowing the simulation of the transport of ions with initial energies from some ten to some hundred MeV/nucleon and of their daughter products has been completed. A Russian code based on different nuclear reaction models that treats the fragmentation as a stochastic process can now be used alternatively for a description of the reaction cross sections by phenomenological formula adjusted to the experiments. A comparison of both approaches with measured cross sections showed considerable differences. The agreement with experiments is better if the phenomenological approach is used, but there is a potential to improve the microscopic approach by adjusting selected input parameters of the nuclear reaction models.

R. Küchler, K. Noack

Model calibration and verification

A computer code has been developed to simulate the reactive transport of various chemicals in the unsaturated soil. For the calibration and verification of the code and of its mathematical models the following data from a natural field are neccessary: chemical concentrations, rate constants and equilibrium coefficients of the involved chemical reactions. However, field data can be obtained only with great expenses so that they are often replaced by data from column experiments. Therefore, it is planned to perform systematic model experiments with unsaturated columns to verify the modelling of the diverse processes by the code as best as possible. The construction of the column experiments is running parallel to the development and verification of hydraulic measurement techniques.

H.-U. Barz, B.Böhmer, J. Konheiser

Increasing the accuracy of neutron fluence determination

The Rossendorf Monte Carlo code TRAMO is being upgraded. The geometrical module now allows to define oblique cylinders and permits different geometrical structures in different horizontal layers. A new procedure for the treatment of elastic scattering using equiprobable angular intervals was included. In contrast to the formerly used Legendre polynomial expansion, the new procedure allows to apply any number of energy groups without loss of accuracy or significant increase of calculation time.

Fluence calculations for two irradiation positions in the KORPUS facility have been performed using different versions of reactor models and numbers of energy groups. Comparing the results obtained with different versions, the uncertainties of fluences caused by model deficiencies and group approximations could be evaluated. They were found to be smaller than 10%. A comparison between measured and calculated activation reaction rates and an adjustment of the calculated fluence spectra to the measured reaction rates has been carried out with the code COSA3. The calculations and measurements agree within the error boundaries.

supportes by BMBF and EU

Safety and Efficiency of Chemical Processes

G. Hessel, W. Schmitt, N. Tefera, K. van der Vorst, F.-P. Weiß

Early detection of dangerous operation states in chemical plants

The research project "Application of new computer-aided diagnostic methods to identify dangerous operational states in chemical plants" was completed. The catalytic esterification of acetic anhydride and methanol was chosen as prototypical exothermal reaction. In the lab scale, it was shown that neural networks are capable of reliably identifying dangerous states in reactors operating in the batch or semibatch mode.

Further, to increase the operational safety of batch and semibatch reactions, on-line concentration measurements were accomplished in the reaction calorimeter RC1 using a Fourier-Transform Infrared-Spectrometer. In case of the hydrogenation of an aromatic nitro compound the in-situ measured concentration profiles of reactant, intermediates, by-products, and products could not only be used to clarify the reaction mechanisms, but allowed also to provide more accurate kinetic data of this strongly exothermic reaction. For example, it was possible not only to determine the formal kinetics, but also the kinetic data of partial reactions.

supported by BMBF

G. Hessel, H. Kryk, W. Schmitt, T. Seiler, F.-P. Weiß

Environmentally safe process control and state diagnostics in chemical plants using neural networks

In this interdisciplinary project, the Fraunhofer Institute for Environmental, Safety, and Energy Technology UMSICHT, the Arzneimittelwerk Dresden (AWD) and the Institute of Safety Research of Forschungszentrum Rossendorf have collaborated since August 1998. The project aims at the development of neural networks for the diagnosis of discontinuous chemical processes and their test application in a production plant. It is the goal to achieve an early detection of deviations from the optimum, environmentally safe operation of a chemical plant. Besides the conception of the state-identification method and the process data interface, detailed studies of the kinetics and the mass transfer in heterogeneous, exothermal hydrogenation reactions (hydrogenation of nitro-aromatics) were accomplished. These reactions were chosen

as a model reaction for the prototype test in a real production plant of AWD. In co-operation with AWD, the necessary input parameters for a process simulation tool (UMSICHT) were obtained. With the help of the simulator, data will be generated for training the neural networks with operational states beyond normal operation. Further, the investigation of the mass transfer in the AWD plant was started to enable scalable disturbance and runaway tests in the laboratory reactors of FZR, which can be used to train neural networks.

supported by BMBF

G. Hessel, H. Kryk, W. Schmitt, N. Tefera, F.-P. Weiß, T. Willms

Experiments and numerical simulations of exothermic chemical reactions

A two-year research programm "Grignard reactions" was started in June 1998 in co-operation with AWD. The molar reaction enthalpy of a Grignard reaction was measured in a closed reaction calorimeter as a function of temperature. The investigation of the spontaneous behaviour has shown that the initiation of the Grignard formation can be detected by a FTIR spectrometer much earlier than by using the temperature or the pressure signals. Further, by dosing the organic halide with different feed rates, reproducible induction times as a function of the concentrations were obtained, what is very important for a safe initiation (i.e. without runaway) of Grignard reactions.

supported by industry

The institute took part in the international benchmark DAKAPO (data acquisition by calorimetry for polymerisation reactions) and has in this way broadened the scope of activities by including polymerisation reactions. The benchmark aimed at establishing a standard polymerisation reaction and at the assessment of the accuracy of the calorimeters. The evaluation of the benchmark is still pending.

Liquid Metal Magneto Hydrodynamics

W. Witke, S. Eckert, G. Gerbeth, V. Kolevzon, T. Weier, U. Fey

Measuring techniques for liquid metal test facilities

Liquid metals are non-transparent, typically hot and aggressive. There is almost no commercial measuring technique available for the determination of local velocities or pressure. A mechano-optical velocity probe was developed which is able to measure two components of the local velocity. It is calibrated and tested in different melts like InGaSn, SnPb, SnBi, and PbBi. The measuring principle consists in the velocity induced elongation of a glass rod which is encapsulated in a glass capillary. This elongation is then measured by optical means using an endoscope and a camera. Due to its measuring principle the probe is independent of any electromagnetic fields. It is now developed and tested up to temperatures of about 700°C.

A laser light scattering technique was applied in order to investigate the phenomena at free liquid metal surfaces. The experiments with

molten gallium show that the observed frequencies and damping constants differ strongly from the classical description of the gallium surface as that of a normal liquid. The results are explained in terms of surface layering possessing visco-elastic properties.

supported by DFG, BMBF, GIF

J.Priede, G.Gerbeth

Theoretical studies on Marangoni flows in a magnetic field

The model configuration of a plane liquid metal layer exposed to a horizontal temperature gradient and a vertical staedy magnetic field has been studied. The basic two-dimensional flow due to the thermocapillary effect (Marangoni convection) becomes oscillatory in a three-dimensional way if the applied temperature gradient increases. The magnetic field provokes a basic boundary layer type flow and an efficient suppression of the first instabilities. The threshold of instability increases as square of the magnetic field strength.

supported by DARA

V. Galindo, G. Gerbeth, R. Mößner, Th. Jung, E. Zienicke

Numerical simulation of flow and heat transfer in crystal growth

Numerical codes have been developed and used for melt flow and heat transport calculations of crystal growth problems. For the Czochralski growth of silicon commercial codes were used in order to simulate the melt control by means of different magnetic fields. The calculations were compared with model experiments and real growth experiments of silicon single crystals. Parameter regions have been identified where the growth process and the grown crystal show clear improvements. Meanwhile the corresponding magnetic systems are successfully introduced into industrial growth facilities. For simulations of transport phenomena and magnetic field influences on growth processes in ampulla, an own spectral code was developed. These results are compared with InAs growth experiments performed at Bergakademie Freiberg where a rotating magnetic field is installed in order to enhance the convective transport within the melt.

supported by DFG, SMWK and industry

F. Stefani, A.Gailitis, G.Gerbeth

Participation at the Riga Dynamo experiment

The experimental verification of a magnetic field selfexcitation at the IoP in Riga was supported by numerical investigations. The measured water experiment profiles have been checked with respect to their critical magnetic Reynolds numbers. In an iterative procedure between the pump designers and the Riga water experiments the profiles have finally been adjusted in such a way that selfexcitation should be possible. As a particular result of the magnetic field calculations, additional pre- and post-propeller blades were installed at the Riga facility in order to improve the velocity profiles. Moreover, optimum measuring sites for the excited magnetic field have been fixed on the basis of the computer simulations.

supported by DFG

T. Weier, G. Mutschke, U. Fey, G. Gerbeth

Electromagnetic boundary layer control for saltwater

The flow of saltwater around bodies can be controlled by electromagnetic forces localized directly on the surface of the body even though the elctromagnetic forces penetrate only slightly into the low-

conducting fluid. With suitable arrangements of electrodes and permanent magnets Lorentz forces can be produced which for instance accelerate the fluid motion parallel to the body surface. This results in a stabilized flow, drag reduction of the body, and prevention of flow separation. All these effects have been convincingly demonstrated during a set of plate experiments performed at the Shipbuilding Test Basin Hamburg in a saltwater flow. A significant drag reduction of about 80% was measured.

supported by VDI and DFG

J. Priede, G. Gerbeth

Levitation of metallic samples

Electromagnetic levitation is a well-known method in order to support and fix metallic samples without any contact to wall. However, these samples typically show a strong tendency to instabilities resulting in rotation or oscillation of the body. The physical reason of such instabilities has been analysed. A frequency dependent threshold has been identified as main result of the theoretical investigations. Model experiments were performed clearly confirming the theoretical results.

supported by DARA

Based on these investigations a method to stabilize the levitated samples by means of steady magnetic fields is developed.

S. Eckert, G. Gerbeth. C.Guttek, H. Stechemesser

Experiments on gas injection for the liquid metal target of a spallation source

The next generation of spallation sources will require a mercury target instead of solid targets being used today. The strong energy input due to the proton beam pulses will cause shock waves in the target which may lead to serious structure problems. These shock waves shall be suppressed by adding of gas bubbles to the mercury, thus making the fluid slightly compressible. Basic experimental studies have been performed in order to analyse the possibilities of gas bubbles injection and their measurement. X-ray visualizations of gas bubble motions in liquid metals show the strong influence of wetting and surface tension phenomena. A homogeneous distribution of tiny bubbles was obtained by injecting the gas through a wetted porous body.

supported by FZ Jülich

A.Cramer, G.Gerbeth, Yu.Gelfgat, A.Bojarevics, G. Stephani

Melt extraction of metallic fibres

In cooperation with the Fraunhofer institute IFAM-Dresden the stabilization of an inductively stirred melt surface by means of an external magnetic field was studied. A solenoid was installed at the semi-industrial facility of the Fraunhofer institute under realistic boundary conditions: vacuum, strong induction heater and a crucible with hot melts (up to 1800°C) close to the solenoid. The magnetic field lead to a stabilization of the melt surface which improved the process significantly. A model experiment has been built up using the lower melting fluid SnPb in order to study the effects at the wheel meniscus in more detail. First measurements with a high-speed camera show that the oscillating meniscus has a strong influence on the diamter distribution of the extracted fibres.

supported by DFG

Yu.Gelfgat,
O.Lielausis,
G.Gerbeth

Applications of electromagnetic stirring

Electromagnetic stirring of solidifying melts is an attractive approach in order to prevent dendritic solidification. It is of increasing application in light metals casting. An electromagnetic stirrer was installed at the continuous casting facility of University Leoben in Austria. First results of copper solidification with magnetic field stirring show the expected benefits.

Theoretical studies were performed for the electromagnetic stirring of magnesium alloys with the primary goal to prevent segregation of heavier components.

Publications

Publications in Scientific and Technical Journals and in Conference Proceedings

Altstadt, E., F.-P. Weiß, M. Werner, H.-G. Willschütz
Finite element based stress analysis of BWR internals exposed to accident loads
Proceedings of the 6th International Conference on Nuclear Engineering (ICONE-6),
CD-ROM, paper 6508
San Diego, May 10-15, 1998

Altstadt, E., F.-P. Weiss, M. Werner, H.-G. Willschütz
Stress analysis of BWR components under accident loads using finite elements
Proceedings of TOPSAFE'98, CD-ROM, Session TSD-1
Valencia (Spain), April 15-17, 1998

Altstadt, E. and F.-P. Weiss
Finite element based vibration analysis of WWER-440 reactors
Proceedings of the 6th International Conference on Nuclear Engineering (ICONE-6)
CD-ROM, paper 6507
San Diego, May 10-15, 1998

Altstadt, E., H. Ohlmeyer, F. Otremba, F.-P. Weiß
Elastic plastic finite element analysis of a BWR feed water distributor exposed to an extreme pressure load
Proc. of the 15th International Conference on Structural Mechanics in Nuclear Technology,
Vol. VII, p. 177
Seoul (Korea), August 15-20, 1999

Altstadt, E., H. Ohlmeyer, F. Otremba, F.-P. Weiss
Finite element analysis of a BWR feed water distributor under extreme transient pressure load
Proc. of the 7th International Conference on Nuclear Engineering (ICONE-7)
CD-ROM, paper 7073
Tokyo (Japan), April 19-23, 1999

Altstadt, E., F.-P. Weiss
Finite-element based vibration analyses of WWER-440 type reactors.
Annals of Nuclear Energy 26 (1999) 1037-1052

Anikeev, A. V., K. Noack, G. Otto
Numerical studies of neutron source distributions in GDT experiments
Proc. of the 26th EPS Conference on Controlled Fusion and Plasma Physics
Maastricht (The Netherlands), June 14-18, 1999

Anikeev, A. V., P. A. Bagryansky, A. A. Ivanov, A. N. Karpushov, V. N. Kornilov, V. V. Maximov, S. V. Murakhtin, K. Noack, A. Yu. Smirnov
Study of hot-ion plasma confinement in the gas-dynamic trap
Proc. of the 26th EPS Conference on Controlled Fusion and Plasma Physics
Maastricht (The Netherland), June 14-18, 1999

Aszodi, A., E. Krepper, H.-M. Prasser
Investigation of heating up and evaporation processes of fluids in storage tanks by experiments and by numerical simulation
2nd International Symposium on Two-Phase Flow Modelling and Experimentation
Proc. Vol. 3, pp. 1667-1674
Pisa (Italy), May 23-25, 1999

Aszodi, A., Krepper, E., Schaffrath, A.
Numerical simulation of the emergency condenser of the SWR 1000
Ninth International Topical Meeting on Nuclear Reactor Thermal Hydraulics (NURETH-9)
San Fancisco (California), October 3 - 8, 1999

Aszodi, A., E. Krepper, H.-M. Prasser
Experimental and numerical investigation of one and two-phase natural convection in storage tanks
Eurotherm Seminar No. 63, Single and Two-Phase Natural Circulations
Genua, September 6-8, 1999

Bagryansky, P. A., E. D. Bender, A. A. Ivanov, A. N. Karpushov, K. Noack, St. Krahl. S. Collatz
Effect of fast Ti-deposition on gas recycling at the first wall and on fast ion losses in GDT experiments
Journal of Nuclear Materials 265 (1999) 124

Bagryansky, P. A., A. V. Anikeev, S. Collatz, P. P. Deichuli, A. A. Ivanov, A. N. Karpushov, A. A. Lizunov, V. V. Maximov, S. V. Murachtin, I. V. Shikhovtsev, A. N. Shukaev, N. V. Stupishin, K. Noack, G. Otto, K. N. Saunichev, S. A. Korepanov
Recent results of experiments on the gas-dynamic trap
Transactions of Fusion Technology 35 (1999) 79

Barz, H.-U., B. Böhmer, J. Konheiser, I. Stephan
High-precision monte carlo calculations, experimental verification and adjustment of fluences in the pressure vessel cavity of a VVER-1000
Proc. of the ANS Radiation Protection and Shielding Division Topical Conference
Vol. 1, p. 447-454
Nashville, Tennesse (USA), April 19-23, 1998

Barz, H.-U., J. Konheiser
Influence of the number of energy groups on the accuracy of neutron fluence calculations
Nuclear Science and Engineering, submitted

Barz, H.-U., B. Böhmer, J. Konheiser, I. Stephan
Monte Carlo calculations of neutron fluence spectra, activation measurements, uncertainty analysis and spectrum adjustment for the KORPUS Benchmark
10th Int. Symposium on Reactor Dosimetry,
Osaka (Japan), Sept. 12-17, 1999

Bergner, F., M. Schaper, U. Bergmann
Analyse von Rißschließvorgängen mit Ultraschallverfahren
30. Tagung des DVM-Arbeitskreises Bruchvorgänge
DVM-Bericht 230, S. 151-160
Dresden, 17.-18.02.1998

Beyer, M., H. Carl, P. Schumann, A. Seidel, F.-P. Weiß, J. Zschau, K. Nowak
Ein modernes technisches System zur verbesserten betrieblichen Überwachung des ukrainischen Kernkraftwerkes Saporoshje
atomwirtschaft-atomtechnik atw 43 (1998) 230

Beyer, M., H.Carl, P. Schumann, V.A. Chernousov
Aufbau, Bestandteile, Struktur und Funktionsprinzipien eines technischen Systems zur betrieblichen Überwachung von Kernkraftwerken (in Russ.)
Uprawljajemye Maschiny i Sistemy, (Ukraine), eingereicht

Beyer, M., H.Carl, P. Schumann, A. Seidel
Fernüberwachung ukrainischer Kernkraftwerke (in Russ.)
Atomnaja Energija, Rußland, eingereicht

Böhmer, B., G. Manturov
Neutron spectrum covariances and their influence on results of pressure vessel neutron spectrum adjustments
Voprosy Atomnoi Nauki i Techniki, Seriya Jadernye Konstanty, 1998
Vypusk 1, p. 28-34, Ed. ZNIIatominform, Moscow

Böhmer, B., G. I. Borodkin, G. N. Manturov
Improved covariance analysis and spectrum adjustment for VVER-1000 pressure vessel fluences
10th Int. Symposium on Reactor Dosimetry
Osaka (Japan), Sept. 12-17, 1999

Böhmert, J., M. Große
Nanoscale precipitates in Russian reactor pressure vessel steel after irradiation and annealing
Jahrestagung Kerntechnik 1998, Tagungsbericht S. 631
München, 26.-28. Mai 1998

Böhmert, J., A. Kryukov, Yu. A. Nikolaev, D., Yu. Erak
Einfluss von Kupfer, Phosphor und Nickel auf die Neutronenversprödung von Eisenlegierungen
Jahrestagung Kerntechnik '99, Tagungsbericht, S. 663
Karlsruhe, 18.-21. Mai 1999

Böhmert, J.
Consideration of environmental degradation of reactor pressure vessel steels for the safety assessment
Environmental Degradation of Engineering Materials
Gdansk-Jurata (Poland), 19-23 September 1999

Böhmert, J.
Irradiation-induced structural changes in surveillance material of VVER 440-type welt metal
Journal of Nuclear Materials (1999), accepted

Collatz, S., K. Noack
NEUSI - A code for the calculation of neutral particle densities inside the plasma region of the GDT
Transactions of Fusion Technology 35 (1999) 375

Cramer, A., A. Bojarevics, G. Gerbeth, Yu. Gelfgat
Stabilisation of the melt extraction process with a magnetic field
accepted at: El-Kaddah (Ed.): Fluid Flow Phenomena in Metals Processing, San Diego (USA)

Dudlik, A., H.-M. Prasser, St. Schlüter
Visualisation of cavitating liquid flow behind fast acting valve
2nd European congress of Chemical Engineering ECCE2
Le Corum, Montpellier (France), 5-7 October, 1999

Eckert, S., G. Gerbeth, B. Guttek, H. Stechemesser
Bubble formation heavy liquid metals: Evaluation of conventional gas injection methods with respect to a suitability under ESS relevant conditions, (ESS-European Spallation Source)
ESS 98-72-T, August 1998

Eckert, K., A. Grahn
Plume and finger regimes driven by an exothermic interfacial reaction
Physical Review Letters 82 (1999) 4436-4439

Eckert, S., G. Gerbeth, O. Lielausis
The behaviour of gas bubbles in a turbulent liquid metal MHD flow
Part I: Dispersion in quasi-two-dimensional MHD tubulence
Part: II. Magnetic field influence on the slipratio
International Journal of Multiphase Flow, accepted

Eckert, S., W. Witke, G. Gerbeth
A new mechano-optical technique to measure local velocities in opaque fluids
Flow Measurement and Instrumentation, submitted

Erge, Th., V. U. Hoffmann, K. Kiefer, E. Rössler, U. Rindelhardt, G. Teichmann, B. Decker, J. Grochowski, G. Heilscher, M. Schneider, G. Blaesser, H. Osserbrink, H. Becker, W. Vaaßen. B. Genennig, H. Rieß, P. Sprau
The German 1000-roofs-pv-programme - a resume of the 5 years pioneer project for small grid-connected pv-systems
Proc. of the 2nd World Conference and Exhibition on Photovoltaic Solar Energy Conversion
Vol. III, p. 2648
Vienna (Austria), 6 - 10 July 1998

Fethke, M., A. Schaffrath, L. Rossner, H. Jaegers, E. F. Hicken
Experimental investigation of the operation mode of passive safety systems
ENS Bern (Ed.): Transactions of the ENC `98 World Nuclear Congress, Vol. III, S. 403-407
Nizza, (France) 25-28 Oct. 1998

Fey, U., T. Weier, G. Gerbeth, G. Mutschke, M. Gad-el-Hak
Separation control using Lorentz forces: recent experimental and numerical results
51th APS Meeting Philadelphia, 22.-24.11.98
Bulletin of the American Physical Society 43 (1998) 2024

Franke, K., U. Rindelhardt
Die räumliche und zeitliche Korrelation der Globalstrahlung auf beliebig orientierten Flächen in Sachsen
11. Internationales Sonnenforum 1998, Tagungsband S. 881
Köln, 26.-30. Juli 1998

Futterschneider, H., U. Rindelhardt, G. Teichmann
Modul-Untersuchungen im FZR-Testfeld
SONNENENERGIE 5/1998, S. 36

Gerbeth, G., J. Priede
Spin-up instability of electromagnetically levitated spherical bodies
IEEE Transactions on Magnetics, USA, submitted

Grants, I. G. Gerbeth
Linearized solution of quasisteady Stefan problem in vertical gradient freeze configuration
Journal of Crystal Growth Elsevier, Elsevier, accepted

Große, M., J. Böhmert
Irradiation damage structure in VVER-440 steels after irradiation at different temperatures and post-irradiation annealing
19th International Symposium "Effects of Radiation on Materials", Seattle (USA), June 1998
ASTM STP 1366

Große, M., J. Böhmert, Ch. Riekel
Investigations of the structural changes ahead of a crack tip in ductile aluminium using scanning micro-beam small angle x-ray scattering
J. Material Science Letters 17 (1998) 1631

Große, M., J. Böhmert, R. Gilles
Small angle neutron scattering investigations of the microstructure of VVER 440-type reactor pressure vessel steel after irradiation at 60 °C
Journal of Nuclear Materials, 254 (1998) 143-150

Große, M.
Additional information about the chemistry of precipitates by variation of the scattering contrast in the SANS and SAXS experiments
Proc. International School and Symposium on Small-Angle Scattering
Matrahaza (Hungary), Oct. 1998

Große, M.
SAXS experiments with high lateral resolution by using of an X-ray micro beam
Proc. International School and Symposium on Small-Angle Scattering
Matrahaza (Hungary), Oct. 1998

Große, M., A. Hempel, R. Gilles
SANS investigations of the irradiation and annealing behaviour of the VVER-type reactor pressure vessel steel 15Xh2MFA
BENSC Experimental Reports 1997, HMI-B552 (1998), S. 244

Große, M., V. Denner, J. Böhmert, G. Goerigk
ASAXS-investigations of the structural changes in the reactor pressure vessel steel 15Kh2MFA after electron irradiation
Jahresbericht HASYLAB 1997, Hamburg (1998)

Große, M., V. Denner, J. Böhmert
Irradiation-induced structural changes in surveillance material of the VVER-440-type welt metal Sv-10KhMFT
Journal of Nuclear Material, accepted

Große, M., A. Gokhmann, J. Böhmert
Dependence of the ratio between magnetic and nuclear small angle neutron scattering on the size of the heterogeneities
Nuclear Instruments & Methods in Physics Research Section B, Beam Interaction with Materials and Atoms NIMB, submitted

Große, M., P. Nitzsche, J. Böhmert, G. Brauer
Investigation of the development of irradiation-induced precipitates in VVER-440-type reactor pressure vessel steels and weld metals during irradiation and annealing
18th International Symposium "Effects of Radiation on Materials",
R.K. Nanstad, M.L. Hamilton, F.A. Garner and A.S. Kumar, (Eds.): ASTM STP 1325(1999) p.346

Grundmann, U.
HEXNEM - A nodal method for the solution of the neutron diffusion equation in hexagonal geometry
M & C `99 - Madrid International Conference on Mathematics and Computation, Reactor Physics and Environmental Analysis in Nuclear Applications
Madrid (Spain), 27 - 30 September, 1999

Grundmann, U.
3D nodal expansion method HEXNEM for solution of the neutron diffusion equation in hexagonal geometry
Jahrestagung Kerntechnik `99, Tagungsbericht S. 15-18
Karlsruhe, 18. - 20. Mai 1999

Grundmann, U., S. Kliem, U. Rohde
Analysis of the exercise 2 of the OECD - MSLB benchmark with the code DYN3D/R
M & C `99 - Madrid International Conference on Mathematics and Computation, Reactor Physics and Environmental Analysis in Nuclear Applications
Madrid (Spain), 27 - 30 September, 1999

Grundmann, U., F. Hollstein
A two-dimensional intranodal flux expansion method for hexagonal geometry
Nuclear Science and Engineering 133 (1999), accepted

Hensel, F., U. Rohde
Measurement and simulation of the turbulent dispersion of a radioactive tracer in a two-phase flow system
Advances in Fluid Mechanics II (AFM98), Udine (Italy), May 13-15, 1998
M. Rahman, C. A. Brebbia, G. Comini (Hrsg.): Advances in Fluid Mechanics II
Southampton 1998, S. 283-294

Heilscher, G., M. Schneider, H. Becker, U. Rindelhardt
Ermittlung der Fehlertoleranz bei Kennlinienmessungen in Vorortuntersuchungen
13. Symposium Photovoltaische Solarenergie, Tagungsband S. 323
Staffelstein, 11. - 13. März 1998

Hessel, G., W. Schmitt, N. Tefera, K. v.d. Vorst, F.-P. Weiß, J. Neumann, S. Schlüter
Identifying dangerous states in chemical plants using neural networks
Proc. of the 6th European Congress on Intelligent Techniques and Soft Computing EUFIT'98, Vol. II, 1237
Aachen, Sept.- 7-10, 1998

Hoppe, D.
Ein akustisches Verfahren zur Klassifikation von Füllständen
Technisches Messen 66 (1999) 244-247

Ivanov, K. N., U. Grundmann, S. Mittag, U. Rohde
Comparative study of a boron dilution scenario in VVER reactors
Annals of Nuclear Energy 26 (1999) 1331-1339

Karpushov, A. N., A. V. Anikeev, P. A. Baryansky, A. A. Ivanov, S. A. Korepanov, A. A. Lizunov, V. V. Maximov, S. V. Murakhtin, K. Noack, K. N. Saunichev
Energy confinement of the high-ß two-component plasma in the gas-dynamic trap
Transactions of Fusion Technology 35 (1999) 190

Kern, T.
Gasgehaltsmessung mit nadelförmigen Leitfähigkeitssonden in schäumenden Medien
DECHEMA Jahrestagung 1998, Fachtreffen Sicherheitstechnik, Tagungsband II, S. 163-164
Wiesbaden, 26.-28. Mai 1998

Kern, T.
Quantifizierung der hydrodynamischen Parameter in kurzlebigen Schäumen
4. Fachtagung „Anlagen-, Arbeits- und Umweltsicherheit", Preprint P10
Köthen, 5./6. November 1998

Kern, T.
Void fraction measurement in foams using needle shaped conductivity probes
2nd European congress of Chemical Engineering ECCE2
Le Corum, Montpellier (France), 5-7 October, 1999

Kliem, S.
Analysis and calculation of an accident with delayed scram at NPP Greifswald using the coupled code DYN3D/ATHLET
1998 International Conference on the Physics of Nuclear Science and Technology
Proceedings pp. 486-491, ANS
La Grange Park, IL (1998)

Kliem, S.
Solution of the fifth dynamic AER benchmark using the coupled code DYN3D/ATHLET
Proceeding of the 8th AER-Symposium, pp. 357-367
KFKI Atomic Energy Research Institute, Budapest (1998)

Kliem, S.
Comparison of the results of the fifth dynamic AER benchmark-a benchmark for coupled thermohydraulic system/three-dimensional hexagonal neutron kinetic core models
Proceeding of the 8th AER-Symposium, pp. 429-469
KFKI Atomic Energy Research Institute, Budapest (1998)

Kliem S., U.Grundmann, U. Rohde
Main steam line break analysis of a NPP with VVER by means of the coupled code DYN3D/ATHLET
Tagungsbericht Jahrestagung Kerntechnik '98, pp. 15-19
München, 26. - 28. Mai 1998

Kliem. S., U.Grundmann, U. Rohde
Main steam line break analysis of a NPP with VVER by means of the coupled code DYN3D/ATHLET
Proc. TOPSAFE '98, CD-ROM, Session TSC-1a,
Valencia (Spain), April 15-17, 1998

Kliem, S., S. Danilin, R. Kyrki-Rajamäki, J. Hadek, A. Kereszturi, P. Siltanen
A benchmark for coupled 3D neutron kinetics/thermohydraulics system codes - main steam header break in a NPP with VVER-440 reactor
M & C '99 - Madrid International Conference on Mathematics and Computation, Reactor Physics and Environmental Analysis in Nuclear Applications
Madrid (Spain), 27 -30 September, 1999

Kliem, S., T. Höhne, U. Rohde, F.-P. Weiß
Main steam line break analysis of a VVER-440 reactor using the coupled thermohydraulic system/3D-neutron kinetic code DYN3D/ATHLET in combination with the CFD code CFX4
Ninth International Topical Meeting on Nuclear Reactor Thermal Hydraulics (NURETH-9)
San Fancisco (California), October 3 - 8, 1999

Knebel, J. U., G. Grötzbach, W. Lischke, U. Rohde, A. Schaffrath
Technische Sitzungen der Sektion 2 (Thermo- und Fluiddynamik) der Jahrestagung Kerntechnik 1999
atomwirtschaft - atomtechnik 44 (1999) 419-423

Krepper, E.
Natural circulation experiments at the ISB-VVER integral test facility and calculations using the code ATHLET
Proc. TOPSAFE'98, CD_ROM, Session TP-1
Valencia (Spain), April 15-17, 1998

Krepper, E.
Pre- and posttest calculations to natural circulation experiments at the integral test facility ISB-VVER using the thermalhydraulic codes ATHLET
Nuclear Engineering and Design 190 (1999) 341-346

Krepper, E., H.-M. Prasser
Natural circulation experiments at the ISB-VVER integral test facility and calculations using the thermalhydraulic code ATHLET
Nuclear Technology, submitted

Krepper, E.
Natural circulation experiments at the ISB-VVER integral test facility and calculations using the thermalhydraulic code ATHLET
Ninth International Topical Meeting on Nuclear Reactor Thermal Hydraulics (NURETH-9)
San Fancisco (California), October 3 - 8, 1999

Krepper, E., H.-G. Willschütz, F.-P. Weiß
Solution of a mixed convection flow benchmark using computational fluid dynamic codes
Proc. of the7th International Conference on Nuclear Engineering (ICONE 7),CD-ROM, paper 7072
Tokyo (Japan), April 19-23, 1999

Krepper, E., F. Schäfer
Post-Test analysis of the BETHSY experiment 5.2c - total loss of feedwater
Jahrestagung Kerntechnik, Tagungsbericht, S. 99-102
Karlsruhe, 18.-21. Mai 1999

Krepper, E., F. Schäfer
Post-Test analysis of the BETHSY 9.3 experiment - steam generator tube rupture with failure of both the high pressure safety injection and auxiliary feedwater systems
Jahrestagung Kerntechnik, Tagungsbericht, S.103-106
Karlsruhe, 18.-21. Mai 1999

Krepper, E., A. Schaffrath, A. Aszodi
Numerical simulation of the emergency condenser of the SWR 1000
Kerntechnik, accepted

Krepper, E., H.-G. Willschütz, F.-P. Weiß
Calculation at a mixed convection flow benchmark using different CFD codes
Jahrestagung Kerntechnik, Tagungsbericht, S. 135-138
Karlsruhe, 18.-20. Mai 1999

Krepper, E., A. Schaffrath, A. Aszodi
Numerical simulation of the emergency condenser of the SWR 1000
Nuclear Science and Engineering, submitted

Krepper, E., H.-G. Willschütz, F.-P. Weiß
Simulation of a buoyancy influenced forced fluid flow using a finite volume and a finite element code
Eurotherm Seminar No. 63, Single and Two-Phase Natural Circulations
Genua, September 6-8, 1999

Krepper, E., A. Krüssenberg, H.-M. Prasser, A. Schaffrath
High resolution void fraction measurements for the validation of flow maps and CFD codes
2nd International Symposium on Two-Phase Flow Modelling and Experimentation
Proc. Vol. 3, pp. 1371-1378
Pisa (Italy), May, 23-25, 1999

Kruber, St., H. Schöne
The application of decision analysis in the remediation sector
Environmental Engineering and Policy 1998

Krüssenberg, A.-K., E. F. Hicken
Neue Rechnungen zu Lufteinbruchstörfällen bei Fusionsreaktoren mit einer Beschichtung des Reaktorraums aus CFC-Material
Jahrestagung Kerntechnik, Tagungsbericht S. 573-576
München, 26. - 28. Mai 1998

Krüssenberg, A..-K., R. Moormann, H. K. Hinssen, M. Hofmann, C. H. Wu
Investigation of oxidation resistance of carbon based first-wall liner material aerosol AO5
Journal of Nuclear Materials 258-263 (1998) 770-776

Krüssenberg, A.-K., Schaffrath, A., Prasser, H.-M.
A new criterion for the bubble slug transition in vertical tubes
Ninth International Topical Meeting on Nuclear Reactor Thermal Hydraulics (NURETH-9)
San Francisco (California), October 3- 8, 1999

Lucas, D., H.-M. Prasser
Einfluß der Abblaseleitung auf die Notentspannung von Reaktoren
DECHEMA Jahrestagung '98, Tagungsband S. 158-159
Wiesbaden, 26. - 28.05.1998

Lucas, D.
BRICK - ein Simulationstool für Mehrphasenströmungen in Behältern auf der Basis einer Partikelmethode
GVC-Jahrestagung '98, Kurzfassung in Chemie-Ingenieur-Technik 70 (1998) 1139
Freiburg, 30.09. -02.10.1998

Lucas, D., H.-M. Prasser, T. Kern
Die thermische Zersetzung von Wasserstoffperoxid als Modellreaktion für die Druckentlastung
4. Fachtagung Anlagen, Arbeits- und Umweltsicherheit, Preprint P 9
Köthen, 5./6. Nov. 1998

Lucas, D.
BRICK - a 1-D tool for transient multiphase vessel flow simulations based on a new particle method
2nd International Symposium on Two-Phase Flow Modelling and Experimentation
Proc., Vol. 3, pp. 1657-1664
Pisa (Italy), May 23-25, 1999

Lucas, D.
A new one-dimensional particle-in-cell model for multiphase vessel flow
Journal of Thermal Sciences, accepted

Lucas, D.
BRICK - ein Simulationstool für Mehrphasenströmungen in Behältern
Chemie Ingenieur Technik 71(1999) 713-717

Moormann, R., S. Alberici, H.-K. Hinssen, A.-K. Krüssenberg, C. H. Wu
Oxidation behaviour of carbon-based materials used for high-temperature gas-cooled reactors and fusion reactors
9th International Conference on Modern Materials & Technologies
Florence, Italy 14.-19.06.1998
Advances in Science and Technology 24 (1999) 331

Mößner, R., G. Gerbeth
Buoyant melt flows under the influence of steady and rotating magnetic fields
Journal of Crystal Growth 197 (1999) 341-354

Murachtin, S. V., P. A. Bagryansky, E. D. Bender, A. A. Ivanov, A. N. Karpushov, K. Noack, St. Krahl, S. Collatz,
Wall conditioning and neutral gas transport at the GDT facility
Transactions of Fusion Technology 35 (1999) 370

Mutschke, G., V. Shatrov, G. Gerbeth
Cylinder wake control by magnetics fields in liquid metals flows
Experimental Thermal and Fluid Science 16 (1998) 92-99

Noack, K., G. Otto, S. Collatz
Transport simulations of fast ion and neutral gas dynamics during GDT experiments
Transactions of Fusion Technology 35 (1999) 218

Perov, S., E. Altstadt, M. Werner
The influence of fluid-structure interaction upon the vibration of WWER-1000 type reactors
Journal of Fluid and Structure, submitted

Prasser, H.-M., A. Böttger, J. Zschau
A new electrode-mesh tomograph for gas-liquid flows
Journal Flow Measurement & Instrumentation 9 (1998) 111-119

Prasser, H.-M.
Measurement of gas fraction, gas velocity and volume flow by electrode mesh sensors
2nd European Congress of Chemical Engineering, ECCE2
Le Corum, Montpellier (France), October 5 - 7, 1999

Prasser, H.-M., W. Zippe, J. Zschau
Evolution der Zweiphasenströmung in einer senkrechten Rohrleitung - Ausprägung von Gasgehaltsprofilen und Blasengrößenverteilungen entlang des Strömungsweges
GVC-Jahrestagung 1999
Leipzig, 29.09-01.10.1999

Priede, J., G. Gerbeth
Spin-up instability of electromagnetically levitated spherical bodies
accepted at: Journal IEEE Transactions on Magnetics
Washington (USA), Oct. 1998

Priede, J., G. Gerbeth
Oscillatory instability of electromagnetically levitated solid bodies
submitted to: IEEE Transactions of Magnetics
Washington (USA), Oct. 1998

Priede, J., G. Gerbeth
Hydrothermal wave instability of thermocapillary-driven convection in a transverse magnetic field
submitted to: Journal of Fluid Mechanics
Cambridge (UK), June 1998

Priede, J., G. Gerbeth
Oscillatory and rotational instabilities in electromagnetic levitation
accepted at: El-Kaddah (Ed.): Fluid-Flow Phenomena in Metals Processing,
TMS, San Diego (USA)

Priede, J., A. Cramer, A.Y. Gelfgat, P.Z. Bar-Yuseph, A.L.Yari, G. Gerbeth
Experimental and numerical study of an anomalous thermocapillary convection in liquid gallium
submitted to: Physics of Fluids, American Institute of Physics
New York (USA), September 1998

Priede, J., G. Gerbeth
Oscillatory instability of electromagnetically levitated solid bodies
IEEE Transactions on Magnetics, USA, submitted

Priede, J., A. Cramer, Y. M. Gelfgat, P. Z. Bar-Yoseph, A. L. Yarin, G. Gerbeth
Experimental and numerical study of an anomalous thermocapillary convection in liquid gallium
Physics of Fluids, accepted

Richter, H.,. J. Böhmert, H.-W. Viehrig
The use of acoustic emission to determine characteristic dynamic strength and toughness properties of steel
Nuclear Engineering and Design 188 (1999) 241-254

Rindelhardt, U., G. Teichmann
Netzgekoppelte Photovoltaik-Anlagen: Erfahrungen und Perspektiven
Elektrizitätswirtschaft 24 (1998) 36

Rindelhardt, U.
Auslegung und Erträge von netzgekoppelten Photovoltaik-Anlagen
Energie und Umwelt `99, Tagungsband S. 81
Freiberg, 24./25. März 1999

Rohde, U.
The modeling of fuel behaviour under RIA conditions in the code DYN3D
Proceedings of the 8th AER-Symposium, pp. 721-740
KFKI Atomic Energy Research Institute, Budapest (1998)

Rohde, U., S. Langenbuch
Gekoppelte Berechnungen von Thermohydraulik und Neutronenkinetik
Jahrestagung Kerntechnik
Karlsruhe, 18.-20. Mai 1999

Schaffrath, A., H.-M. Prasser
Meßtechnik für stationäre und transiente Mehrphasenströmungen
atomwirtschaft-atomtechnik atw 43 (1998) 706-708

Schaffrath, A., H.-M. Prasser
Workshop on „Measuring techniques for steady state and transient multiphase flows"
Kerntechnik 63 (1998) S. 300-302

Schaffrath, A., P. Dumaz
Post test calculations of NOKO experiments within the framework of a European research programm
Kerntechnik 63 (1998)113-119

Schaffrath, A., E. F. Hicken, H. Jaegers, H.-M. Prasser
Results of experiments at the NOKO pilot plant
VGB-Power Tech 78 (1998), Nr. 5, S. 79-84

Schaffrath, A., E. F. Hicken, H. Jaegers, H.-M. Prasser
Experimentelle Ergebnisse mit der NOKO-Versuchsanlage
VGB-Kraftwerkstechnik 78 (1998), Nr. 5, S. 90-96

Schaffrath, A., P. Dumaz
Calculation of the NOKO-Test B6-4
Jahrestagung Kerntechnik '98, Tagungsbericht S. 87-90
München, 26. - 28. Mai 1998

Schaffrath, A.
Post test calculations of NOKO bundle experiments
Proceedings TOPSAFE 98, CD-ROM, Session TSC4-b
Valencia (Spain), April 15-17,1998

Schaffrath, A., P. Dumaz
Post test calculations of NOKO emergency condenser experiments
Proceedings of the 6th International Conference on Nuclear Engineering (ICONE-6)
CD-ROM, paper 6382
San Diego, May 10-15, 1998

Schaffrath, A., H.-M. Prasser, A. Böttger
Sonderuntersuchungen zu Strömungsformen am NOKO Einzelrohr
Jahrestagung Kerntechnik '98, Tagungsbericht S. 83-86
München, 26. - 28. Mai 1998

Schaffrath, A., A. Fjodorow, U. Gocht, A.-K. Krüssenberg
Vergleich von Modellen zur Berechnung der Kondensation in horizontalen Rohren
Jahrestagung Kerntechnik, Tagungsbericht S. 111-115
Karlsruhe, 18.-21. Mai 1999

Schaffrath, A., Krüssenberg, A.-K., Fjodorow, A., Gocht, U., Lischke, W.
Modelling of condensation in horizontal tubes
Ninth International Topical Meeting on Nuclear Hydraulics (NURETH-9)
San Francisco (California), October 3- 8, 1999

Schaffrath, A., E. F. Hicken, H. Jaegers, H.-M. Prasser
Operation conditions of the emergency condenser of the SWR 1000
Nuclear Engineering and Design 188 (1999) 303-318

Schaffrath, A., M. Fethke, H. Ringel
Experimentelle Untersuchungen zu passiven Komponenten des SWR 1000
atomwirtschaft-atomtechnik 44 (1999) 35-36

Schaffrath, A., E. F. Hicken, H. Jaegers, H.-M. Prasser
Experimental and analytical investigation of the operation mode of the emergency condenser of the SWR 1000
Nuclear Technology 126 (1999) 123-142

Schaffrath, A., A.-K. Krüssenberg, W. Lischke, U. Gocht, A. Fjodorow
Comparative assessment of condensation models for horizontal tubes
Kerntechnik, accepted

Schneider, C.
Fluid mechanics of electrolytic cells
2nd International Symposium on Two-Phase Flow Modeling and Experimentation
Proc. Vol. 2, pp. 1085-1992
Pisa (Italy), May 23-25, 1999

Schneider, C.
Two-phase flow in the anode chamber of alkaline chloride electrolysis cells
2nd European Congress of Chemical Engineering, ECCE2
Le Corum, Montpellier (France), October 5 - 7, 1999

Stephan, I., D. Gawlik, W. Gatschke
Bestimmung der Neutronenflußdichten in den Bestrahlungseinrichtungen des BER II bei der HEU-LEU-Umstellung
Jahrestagung Kerntechnik 1998, Tagungsbericht, S. 631
München, 26.-28. Mai 1998

Stephan, I., I. Mönch, A. Köthe
High-purity niobium for neutron activation detectors
Proc. of the Symposium on Ultra High Purity Metals
Sendai (Japan), May 31, 1999

Stefani, F., G. Gerbeth, A. Galitis
Velocity profile optimization for the Riga dynamo experiment
A. Alemany, Ph. Marty, J.P. Thibault (Eds.): Transfer Phenomena in Magnetohydrodynamic and Electroconducting Flows, Kluwer, 1998, pp. 31-44

Stefani, F., G. Gerbeth
Velocitiy reconstruction in conduction fluids from magnetic and electric potential measerements
Inverse Problems 15 (1999) 771-786

Stefani, F., G. Gerbeth
On the uniqueness of velocity reconstruction in conducting fluids from measurements of induced electromagnetic fields
Inverse Problems, submitted

Thess, A., G. Gerbeth
Magnetohydrodynamik
Physikalische Blätter 54, S. 125
Februar 1998

Viehrig, H.-W., J. Böhmert
Specimen reconstitution technique and verification testing for charpy size SENB specimens. small specimen test techniques,
W.R. Corwin, S.T. Rosinski, E. van Walle, (Eds.): ASTM STP 1329
American Society for Testing and Materials, July 1998, pp. 420

Viehrig, H.-W., J. Böhmert
Anwendung des Master-Curve-Konzeptes zur bruchmechanischen Charakterisierung von Reaktordruckbehälterstählen,
Deutscher Verband für Materialforschung und -prüfung e.V., Tagungsberichte "Werkstoffprüfung 1998", S. 353

Viehrig, H.-W., J. Böhmert
Die Radionuklidlaboratorien zur Untersuchung bestrahlter Werkstoffproben im Institut für Sicherheitsforschung des FZR
Jahrestagung Kerntechnik '99, Tagungsberichte S. 687
Karlsruhe, 18.-20. Mai 1999

Viehrig, H.-W., J. Böhmert
Some issues by using the master curve concept
Proc. of the 15th International Conference on Structural Mechanics in Reaktor Technology, Vol. V, 383
Seoul (Korea), August 15-20, 1999

Viehrig, H.-W., J. Böhmert, H. Richter
Common German/Russian irradiation experiment at Rheinsberg NPP - results of the mechanical testing
Proc. of the IAEA Specialists Meeting Neutron Embrittlement and Mitigation
Madrid (Spain), April 26-29, 1999

Viehrig, H.-W., J. Böhmert, H. Richter, M. Valo
Use of instrumented charpy test for determination of ductile crack initiation toughness
ASTM Symposium on Pendulum Impact Testing: A Century of Progress
T. Siewert ans M. P. Manahan, Sr., (Eds): ASTM STP 1380
American Society for Testing and Materials,West Conshohocken (PA), 1999

Weier, T., G. Gerbeth, G. Muschke, U. Fey, O. Posdziech, O.Lielausis, E.
Some results on electromagnetic control of flow around bodies
Proc. of the International Symposium on SEAWATER DRAG REDUCTION, pp. 395-400
Newport, Rhode Island (USA), 22.-24. Juli 1998

Weier, T., G. Gerbeth, G. Mutschke, E. Platacis, O. Lielausis
Experiments on cylinder wake stabilization in an electrolyte by means of electromagnetic forces localized on the cylinder surface
Experimental Thermal and Fluid Science 16 (1998) 84-91

Weier, T., U. Fey, G. Gerbeth, G. Mutschke, O. Lielausis, E. Platacis
Electromagnetic control of flow separation
2nd International Conference on Marine Electromagnetics
Brest (France), July 5-7, 1999

Weier, T., U. Fey, G. Gerbeth, G. Mutschke, O. Lielausis, E. Platacis
Electromagnetic flow control for drag reduction and separation prevention
11th European Drag Reduction Working Meeting
Prague, September 15-17, 1999

Weiß, F.-P, U. Rohde, H.-M. Prasser, E. Altstadt, J. Böhmert, B. Böhmer, H. Carl
Forschungsüberblick Reaktorsicherheitsforschung im Institut für Sicherheitsforschung des Forschungszentrums Rossendorf
atomwirtschaft atw 44 (1999) 348-353

Oral Conference Contributions

Aszodi, A.,E. Krepper
Simulation of the single phase natural circulation at the secondary side of an emergency condenser (NOKO facility) using the CFD-code CFX-4
ENC-Conference, CD-ROM, poster 2.05
Nizza, Oktober 1998

Böhmert, J. G. Müller, H.-W. Viehrig
Einfluß von Seigerungen in dickwandigen Teilen aus Druckbehälterstählen auf die Zähigkeitskennwerte
Tagung "Gefüge und Bruch", Internationale Werkstofftagung
Bochum, 17.-19. März 1999

Bojarevics, A. , Yu.Gelfgat, G. Gerbeth, A. Cramer
The effect of a superimposed steady magnetic field on nonstationary flow driven by a high frequency AC magnetic in an open cavity
Workshop „The Use of Magnetic Fields in Crystal Growth and Metals Casting"
Frankfurt a. M., 1.-2. April 1998

Cramer, A., A. Bojarevics, G. Gerbeth, Y. Gelfgat
Stabilisation of the melt extraction progress with a magnetic field
128th TMS Annual Meeting & Exhibition: Fluid Flow Phenomena in Metals Processing
San Diego, CA, February 28 - March 4 1999

Dudlik, A., H.-M. Prasser, S. Schlüter
Verhinderung des Kavitationsschlages beim schnellen Absperren einer Flüssigkeitsleitung
Vortrag 4. VDI-Fachtagung „Anlagen-, Arbeits- und Umweltsicherheit"
Köthen, 5.-6. Nov. 1998

Dumaz, P., A. Schaffrath
Analysis of the NOKO emergency condenser experiments
Vortrag, Seminare Systemes REP No 2
Cadarache, 19. März 1998

Galindo, V., G. Gerbeth
Numerical studies on crystal growth melt flow control using different magnetic fields
SIAM Annual Meeting
University of Toronto (Canada), July 13-17, 1998

Galindo, V., G. Gerbeth
Crystal growth melt flow control by means of magnetic fields
Workshop SOLFIDAP, IKZ Berlin
Berlin-Adlershof , 25.-27. Mai 1998

Gerbeth, G., V. Galindo
Einsatz von Magnetfeldern bei der Silizium-Czochalski-Kristallzüchtung
Berg und Hüttenmännischer Tag
TU Bergakademie Freiberg, 18.06.1998

Gerbeth, G.
Fundamentals of technical applications of MHD
Workshop "The use of Magnetic Fields in Crystal Growth an Metals Casting"
Frankfurt a. M., 1.-2. April 1998

Gerbeth, G.
Influence of magnetic fields on surface driven flows
Workshop "Applications of magnetic fields in materials processing under microgravity conditions"
Erlangen, Nov. 11-12, 1998

Große, M.
Type and annealing behaviour of irradiation defects in surveillance materials of the VVER-type weld metal Sv-10KhMFT
Table Ronde LLB
Saclay (Frankreich), Nov.1998

Grundmann, U., F. Hollstein
HEXNEM2 - a new nodal method for hexagonal geometry
AER Working Group D Meeting
Rez (Czech Republic), May 18-20, 1998

Grundmann, U., S. Mittag, U. Rohde
The 3-dimensional core model DYN3D
Safety Analysis for NPPs of VVER and RBMK Type
Obninsk, 26.-30. October 1998

Fey, U., T. Weier, G. Lammers
Elektromagnetische Grenzschichtkontrolle - Experimente an der Hamburgischen Schiffbauversuchsanstalt
Statusseminar Nichtlineare Dynamik
Frankfurt, 23./24.02.1999

Fietz, J.
Rolle und Akzeptanz der Kernenergie in einem gesicherten Stromversorgungskonzept
VDI-KTG-Seminar
Dresden, 17. Juni 1999

Gerbeth, G.
Elektromagnetic control of flow around bodies
Einladungsvortrag am LEGI
Grenoble, 04.02.1999

Gerbeth, G.
Kontrolle der Nichtlinearen Dynamik von Strömungsgrenzschichten - Anwendung bei Schiffen
Statusseminar Nichtlineare Dynamik
Frankfurt, 23./24.02.1999

Hensel, F., H.-M. Prasser
SchaumPET - A setup for positron emission tomography (PET) investigation of foam in a bubble column
4th Topical Meeting on Industrial Radiation and Radioisotope Measurement Applications - IRRMA '99. Raleigh (USA), October 3-7, 1999

Hensel, F.
Investigation of a density measurement technique using positron radiation
4th Topical Meeting on Industrial Radiation and Radioisotope Measurement Applications - IRRMA '99. Raleigh (USA), October 3-7, 1999

Höhne, T., G. Grunwald, U. Rohde
Coolant mixing in pressurized water reactors
8th AER Symposium on VVER Reactor Physics and Reactor Safety
Bytrice nad Pernstejnem, Czech Republic (Sept. 21-25, 1998)

Höhne, T.
1:5 scaled plexiglas mixing model of the PWR Konvoi
7th International Conference on Nuclear Engineering (ICONE-7)
Tokyo (Japan), April 19-23, 1999

Höhne, T.
Numerical simulation of the coolant flow in pressurized water reactors
CFX International Users Conference
Friedrichshafen, June 19-24, 1999

Kliem, S.
Fifth dynamic AER Benchmark - a benchmark for coupled thermohydraulic system/3D hexagonal neutron kinetic core models - comparison of results - level 1
AER Working Group D Meeting
Rez (Czech Republic), May 18-20, 1998

Kliem. S.
OECD PWR MSLB benchmark - dependence of the results from several parameters
2nd PWR MSLB Workshop CIEMAT
Madrid (Spain), June 22-23, 1998

Krepper, E., H.-M. Prasser
Measurements and CFX-simulation of a bubbly flow in a vertical pipe
CFX International Users Conference
Friedrichshafen, 21.-24. Juni 1999

Lindau, B.
Anwendung wissensbasierter Methoden auf der Grundlage von Insitu-Messung und Online Modellierung zur Optimierung von Schüttguthandhabungstechniken am Beispiel des Dosierens
FA „Agglomerations- und Schüttguttechnik" der VDI-Gesellschaft
Magdeburg 30.03. - 01.04.1998

Lindau, B.
Anwendung wissensbasierter Methoden auf der Grundlage von Insitu-Messung und qualitativer Modellierung zur Optimierung von Schüttguthandhabungstechniken am Beispiel des Dosierens
49. Berg- und Hüttenmännischer Tag 1998
TU Bergakademie Freiberg, 18.06.1998

Lucas, D.
BRICK - ein Simulationstool für Mehrphasenströmungen in Behältern auf der Basis einer Partikelmethode
1. Chemnitzer Verfahrenstechnisches Kolloqium
TU Chemnitz, 25.-26.11.1998

Lucas, D., H.-M. Prasser, T. Kern
Einfluß von Zusätzen niedermolekularer oberflächenaktiver Stoffe auf den Massenaustrag bei der Druckentlastung eines verdampfenden Stoffsystems
GVC-Fachausschuß-Sitzung "Mehrphasenströmungen"
Aachen, 02.-06.03.98

Lucas, D.
Erste Nachrechnungen von Druckentlastungsexperimente bei durchgehender Reaktion mit dem Programm BRICK
47. Sitzung des DECHEMA/GVC-Arbeitsausschusses "Sicherheitsgerechtes Auslegen von Chemieapparaten
Frankfurt a. M., 9./10. März 1999

Lucas, D.
Investigations on pressure reliefs at Forschungszentrum Rossendorf
Presentation at the DIERS User Group meeting
Las Vegas (NV), April 14-16, 1999

Mutschke, G., G. Gerbeth, V. Shatrov
Bluff body wake control by magnetic fields
SIAM Annual Meeting
University of Toronto (Canada), July 13-17, 1998

Mutschke, G., V. Avilov, G. Gerbeth
Elektromagnetische Grenzschichtkontrolle - Theorie und Numerik
Statusseminar Nichtlineare Dynamik
Frankfurt, 23./24.02.1999

Prasser, H.-M.
Messung von Gasgehalt, Gasgeschwindigkeit und Volumenstrom mit Gittersensoren
1. Chemnitzer Verfahrenstechnisches Kolloqium
TU Chemnitz, 25.-26.11.1998

Prasser, H.-M.
Schnelle Gittersensoren für Gasgehalt, Gasgeschwindigkeit und Volumenstrom in einer Zweiphasenströmung
Seminarvortrag Universität GH Essen, 6. Mai 1999

Prasser, H.-M.
Messtechniken in der Zweiphasenströmung
Vortrag am IKE des Forschungszentrums Karlsruhe, 4. Mai 1999

Rindelhardt, U.
Use of renewable energies in Saxony
International Forum "Alternative Energy Sources"
Lubawka (Poland), 28-29th May 1998

Rindelhardt, U.
Netzgekoppelte Photovoltaik-Anlagen - Ergebnisse des 1000-Dächer-Langzeitmeßprogramms in Sachsen
2. Merseburger Solartag, 09.06.1998

Rindelhardt, U.
Solarenergie - Photovoltaik
Tagung der Evangelischen Akademie Meißen, 12. - 14. Juni 1998

Rindelhardt, U.
Windenergienutzung in Sachsen
Einladungsvortrag, Graduiertenkolleg „Lokale innovative Energiesysteme"
14.01.1999, TU Dresden

Stefani, F., G. Gerbeth, A. Gailitis
Numerical Simulation of the Riga dynamo experiment
SIAM Annual Meeting
University of Toronto (Canada), July 13-17, 1998

Stefani, F., Gerbeth, G., A. Gailitis, O. Lielausis
Laboratory experiments on dynamo action
SIAM Annual Meeting
University of Toronto (Canada), 13.-17. July 1998

Stefani, F., G. Gerbeth, A. Gailitis
Numerical simulation of the Riga dynamo experiment
SIAM Annual Meeting
University of Toronto (Canada), 13.-17. July 1998

Stefani, F., G. Gerbeth, A. Gailitis
Numerical simulation for the Riga dynamo
Workshop / Laboratory Experiments on Dynamo Action
Riga, 14.-16. June 1998

FZR-Reports and Other Publications

Barz, H.-U., J. Konheiser
Monte-Carlo Programm TRAMO - Möglichkeiten und Anleitung zur Nutzung
FZR-245, Dezember 1998

Barz, H.-U. , B. Böhmer, J. Konheiser, I. Stephan
Entwicklung einer fortgeschrittenen Methodik zur Bestimmung der Neutronenbelastung des Druckbehältermaterials vom Reaktor des Typs WWER-1000,
Final Report BMBF-Projekt 1501022
FZR-222, Mai 1998

Beyer, M., H. Carl, J. Kriks, K. Nowak, P. Schumann, A. Seidel
Unterstützung der ukrainischen Genehmigungsbehörde NARU beim Aufbau eines technischen Systems zur verbesserten betrieblichen Überwachung des KKW Saporoshje
(4. Realisierungsstufe)
FZR-259, Mai 1999

Beyer, M., H. Carl, J. Kriks
Unterstützung der ukrainischen Genehmigungs- und Aufsichtsbehörde bei der Einrichtung einer verbesserten betrieblichen Überwachung für das KKW Rovno
(5. Realisierungsstufe)
FZR-260, Mai 1999

Böhmert, J., M. Große
Anwendung von Kleinwinkelstreuverfahren zum Nachweis verformungsbedingter Strukturschädigung
FZR-229, Juli 1998

Böhmert, J., A.. Kryukov, Yu. Nikolaev, Yu. N. Korolev, D. Yu. Erak, S. Gerashenko
Einfluss der Zusammenssetzung auf die Strahlenversprödung von Eisenlegierungen
FZR-255, Februar 1999

Eckert, S.
Experimentelle Untersuchung turbulenter Flüssigmetall- und Flüssigmetall-Gas-Strömungen in einem äußeren Magnetfeld
FZR-219, April 1998

Fiorini, G. L., E.Friesen, T. v. D. Hagen, J. Lopez Jimenez, P. Meloni, U. Rindelhardt
BWR physics and thermalhydraulic complementary actions to the IPSS-BWR R&D cluster,
Final report, CEA Cadarache: RT DER/SIS/LSS 98/32-1, Februar 1998

Gerbeth, G.
Marangoni-Konvektion in einer seitlich beheizten ebenen Flüssigmetallschicht unter dem Einfluß eines Magnetfeldes
Schlussbericht, Juli 1998

Gerbeth, G., A. Alemany, V. Shatrov, E. Krasilnikov
Magnetohydrodynamic flow around bluff bodies
Final Report: Januar 1995 – Dezember 1997
Dresden, September 1998, Reference number: INTAS-94-1504

Große, M., A. Ulbricht
SANS-investigation of the irradiation-induced changes in reactor pressure vessel steels
Rapport de Experience 1998, LLB Saclay

Grundmann, U., S. Kliem, E. Krepper, S. Mittag, U. Rohde, F. Schäfer, A. Seidel
Qualifizierung des Kernmodells DYN3D im Komplex mit dem Störfallcode ATHLET als fortgeschrittenes Werkzeug für die Störfallanalyse von WWER-Reaktoren
FZR-216, März 1998

Hensel, F.
Methodische Untersuchungen zum Einsatz von Positronenemittern für die Dichtebestimmung in leichten Medien
FZR-254, Februar 1999

Hessel, G., D. Hoppe, W. Schmitt, N. Tefera, K. van der Vorst, F.-P. Weiß
Anwendungsmöglichkeiten neuartiger EDV-gestützter Erkennungmethoden zur Identifizierung gefährlicher Betriebszustände in Chemieanlagen (I)
FZR-223, Juni 1998

Hoppe, D.
Nutzung der statischen Informationstheorie und eines tensororienten Klassifikationsverfahrens zur Signalerkennung an einem chemischen Prozeß
FZR-225, Juni 1998

Hoppe, D.
Modellbildung durch Auswertung von Fehlerdimensionen
FZR-244, Dezember 1998

Hoppe, D.
Die Verknüpfung von Teilmodellen auf der Grundlage der Dimensionsanalyse
FZR-263, Juni 1999

Höhne, T.
Vergleich von Kühlmittelströmungen und -vermischung in einem skalierten Modell des DWR Konvoi mit den Vorgängen im Originalreaktor
FZR-210, Februar 1998

Höhne, T., G. Grunwald, U. Rohde
Coolant mixing in pressurized water reactor
FZR-237, Oktober 1998

Krepper, E., F. Schäfer
Verifikation des ATHLET-Rechenprogramms im Rahmen der externen Verifikationsgruppe ATHLET BETHSY Test 5.2c - Totalverlust des Speisewassers
FZR-231, August 1998

Krepper, E., F. Schäfer
Verifikation des ATHLET-Rechenprogramms im Rahmen der externen Verifikationsgruppe ATHLET BETHSY Test 9.3c - Heizrohrbruch mit Versagen der Hochdruck-Noteinspeisung
FZR-232, August 1998

Meyer, K., F. Hollstein
Analytisches Modell zur Berechnung der Übertragungsfunktionen für das Neutronenflussrauschen in WWER-440-Reaktoren bei stochastischen Schwingungen der Regelelementunterteile
FZR-205, Januar 1998

Prasser, H.-M. (Ed.)
Workshop „Meßtechnik für stationäre und transiente Mehrphasenströmungen"
24.-25. September 1998 in Rossendorf
FZR-241, November 1998

Prasser, H.-M., A. Böttger, J. Zschau
Entwicklung von Zweiphasenmeßtechnik für vergleichende Untersuchungen zur Beschreibung von transienten Strömungen in Rohrleitungen
Abschlußbericht zum Vorhaben 11ZF9504/1
FZR-233, Februar 1999

Prigarin, S. M., K. Noack
About the influence of randomnes of hydraulic conductivity on solute transport in saturated soil: numerical experiments
FZR-243, Dezember 1998

Richter, H., J. Böhmert, M. Valo, H.-W. Viehrig
Detektion von duktiler Rißinitiierung durch Schallemission
FZR-230, August 1998

Rindelhardt, U., G. Teichmann, H. Futterschneider
Langzeituntersuchungen an netzgekoppelten Photovoltaikanlagen in Sachsen
FZR-221, Mai 1998

Schaffrath, A., H.-M. Prasser
Theoretical support to the NOKO experiments
FZR-224, Juni 1998

Walle, E. van, M. Valo, H.-W. Viehrig, G. Gage, M. Wootton, E. Keim, L. Debarberis, M. Horsten
Reconstitution techniques qualification & evaluation to study ageing phenomena of nuclear pressure vessel materials - Resque, Contract FI4SCT960038,
Yearly Progress Report 1997, European Commission, Euratom Research Framework Programme 1994-1998 "Nuclear Fission Safety", June 1998, AGE-Resque(98)-P003

Walle, E. van, R. Chaouadi, J.L. Puzzolante, M. Scibetta, J. van de Velde, H.-W. Viehrig
SCK.CEN Progress Report on RESQUE, Report R-3411
Mol (Belgium), März 1999

Willschütz, H.-G.
CFD-calculation to a core catcher benchmark
FZR-257, April 1999

Meetings and Workshops

Meetings and Workshops

Composition Effects on Neutron Embrittlement
Rossendorf, 20.-21. Januar 1998

Laboratory Experiments on Dynamo Action (LEDA)
International Workshop
Jurmala (Lettland), June 14-16, 1998

2. Workshop
Messtechnik für stationäre und transiente Mehrphasenströmungen
Rossendorf, 24.-25. September 1998

FE-Modelling of VVER-type reactors
Project in the frame of WTZ Deutschland-Rußland with DIAPROM (Rußland)
Rossendorf, October 26-28, 1998

AER Work Group Meeting
Rossendorf, 10.-12. Mai 1999

3.Arbeitstreffen EU-Projekt "RESQUE"
Rossendorf, 27.-28. Mai 1999

CONDOR-Projekt
Meeting zum 5th EU-FWP
Rossendorf. 31. Mai - 01. Juni 1999

Workshop Fernüberwachung KKW Saporoshje
Rossendorf, 07.-11. Juni 1999

Measuring Techniques for Liquid Metal Flows (MTLM)
Rossendorf, 11.-13. Oktober 1999

3. Workshop
Messtechnik für stationäre und transiente Mehrphasenströmungen
Rossendorf, 14.-15. Oktober 1999

Patents

Patents

1. B. Lindau
   Verfahren zur Bestimmung der Festigkeit von dispersem Material
   Patent DE 198 13 065.1
   Anmeldung 25.03.1998

2. H.-M. Prasser, J. Zschau, A. Böttger
   Anordnung zur Verhinderung eines Kavitationsschlages beim schnellen Absperren einer zum Transport von Flüssigkeiten genutzten Rohrleitung
   Patent DE 198 15 232.6
   Anmeldung 04.04.1998

3. D. Hoppe, H.-D. Giera
   Anordnung und Verfahren zur akustischen Volumenbestimmung
   Patent DE 198 30 442.0
   Anmeldung 08.07.1998

4. H.-M. Prasser, S. Schlüter, A. Dudlik
   Anordnung zum druckstoßfreien Absperren einer flüssigkeitsfördernden Rohrleitung
   Patent DE 198 40 961.3
   Anmeldung 08.09.1998

5. B. Lindau
   Vorrichtung zum Fördern von Schüttgut mittels Vibrationsförderung
   Patent DE 198 35 530.0
   Anmeldung 06.08.1998

6. U. Rindelhardt, G. Teichmann
   Verfahren und Schaltungsanordnung zur Maximum-Power-Point-Steuerung von Solargeneratoren
   Patent DE 199 04 561.5
   Anmeldung 04.02.1999

7. F. Stefani, G. Gerbeth, J. Priede, A. Thess, S. Eckert
   Verfahren und Anordnung zur Bestimmung von räumlichen Geschwindigkeitsverteilungen in elektrisch leitfähigen Flüssigkeiten
   Patent DE 199 22 311.4
   Anmeldung 14.05.1999

8. W. Witke, S. Eckert, G. Gerbeth
   Einrichtung zur lokalen Messung von Strömungsgeschwindigkeiten
   Patent DE 199 13 484.7
   Anmeldung 25.03.1999

Seminars of the Institute

Seminars

Dr. A. Polte
Modellierung und Bewertung von Störfallauswirkungen technischer Anlagen in urbanen Gebieten im Rahmen der Entscheidungsanalyse für öffentliche Entscheidungen
15.01. 1998

T. Reitz (TU Dresden)
Visuelle Ansätze der Wissensrepräsentation im Altlastenbewertungssystem XUMA/GEFA
22.01.1998

Dr. R. Koch
Programme zur Berechnung von Neutronenfeldern
12.02.1998

Dr. R. Küchler
Migration von Schadstoffen in Bergbauhalden
26.02.1998

Dr. A. Schaffrath
Stand der Arbeiten zu TOPFLOW
12.03.1998

Dr. E. Altstadt
Nichtlineare Finite-Elemente-Analyse von Schalenstrukturen
26.03.1998

Dr. J. Böhmert, Holger Richter
Nachweis der dynamischen Rißinitiierung - eine kritische Methodenbewertung
09.04.1998

PD Dr. U. Rindelhardt, G. Teichmann
Netzgekoppelte Photovoltaikanlagen inSachsen
- Ergebnisse des 1000-Dächer-Programmes -
14.05.1998

Dr. Unholzer (TU Dresden)
Neutronen- und Photonenflußspektren in einem ITER-Mockup
19.05.1998

Dr. S. Eckert, Dr. G. Gerbeth
Flüssigmetall-Zwei-Phasen-Untersuchungen für das Target einer Neutronen-Spallationsquelle
04.06.1998

R. Beck (Siemens KWU)
Modellierung der Fluidkräfte bei der Erdbebenauslegung von Kompaktlagerstellen
19.06.1998

Prof. Dr. J. Wagschal (Hebrew University of Jerusalem)
Cross Section Adjustment Revisited
08.07.1998

Dr. A. Polte
Wertesystem bei der Beurteilung störfallrelevanter technischer Anlagen
23.07.1998

Prof. Gokhmann (Universität Odessa)
Interpretation of small angle curves of neutron-irradiation Cr-Mo-V-steels
27.08.1998

Dr. B. Lindau
Prozeßführung beim Feststoffdosieren
03.09.1998

Dr. H.-M. Prasser
Visualisierung von Kavitation in Rohrleitungen mit Gittersensor
11.09.1998

Dr. V. Galindo
Einsatz von Magnetfeldern in der SI-Einkristallzüchtung
01.10.1998

Dr. E. Krepper, F. Schäfer
Verifikation des Programmes ATHLET anhand der Nachrechnungen von BETHSY-Experimenten
08.10.1998

Dr. W. Schmitt, G.Hessel
Identifizierung gefährlicher Betriebszustände in Chemieanlagen
22.10.1998

M. Fethke (FZ Jülich)
Berechnung des Gebäudekondensators des SWR-1000 mit RALOC
29.10.1998

Dr. W. Ferse
Angewandte Entscheidungsanalyse
- Ein Überblick der Arbeiten im FZR -
30.10.1998

Dr. M. Werner
WWER-1000-Schwingungsmodellierung mittels finiter Elemente
05.11.1998

Dr. K. Noack
Stand und Perspektiven des Themas "Reaktordosimetrie" in der Abteilung FWST
19.11.1998

Dr. F. Stefani
Ergebnisse zum Rigaer Dynamoexperiment
10.12.1998

Dr. N. Tefera
Reaktions- und sicherheitstechnische Untersuchungen von exothermen chemischen Reaktionen
16.12.1998

Dr. J. U. Knebel (Forschungszentrum Karlsruhe)
Stand der Arbeiten zu einer beschleunigergetriebenen Anlage (ADS) am Forschungszentrum Karlsruhe zur Transmutation von Aktiniden
14. 01. 99

Dr. P. Hübner (Bergakademie Freiberg)
Korrelation zwischen Kerbschlagarbeit und bruchmechanischen Kennwerten
28. 01. 99

M. Große
Beiträge zur Charakterisierung von bestrahlungsinduzierten Ausscheidungen in RDB-Stählen
11. 02. 99

Dr. D. Hoppe
Modellbildung durch Auswertung von Fehlerdimensionen
25. 02. 99

Dr. E. Franke, Dr. I. Reiche (VKTA Rossendorf)
Neutronentransportrechnungen für Reaktorkerne vom Typ WWER-440 mit dem Code Helios
11. 03. 99

Dr. D. Lucas
BRICK – ein 1D Simulationstool für Mehrphasenströmungen in Behältern
25. 03. 99

Dr. D. Parker (University Birmingham)
Application of PET and other positron tracer techniques in engineering and the physical sciences
31. 03. 99

D. Klotz (Gesellschaft für Strahlenforschung Neuherberg)
Experimente zum Schadstofftransport
08. 04. 99

Dr. Steinwarz (Siempelkamp Nuklear- und Umwelttechnik GmbH & Co, Krefeld)
Repräsentative Experimente zur Beherrschung von Kernschmelzunfällen
20. 04. 99

Prof. F. Wagner (Max-Planck-Institut für Plasmaphysik, Greifswald)
Die physikalischen Grundlagen des Fusionsprojektes Wendelstein - 7X
22. 04. 99

Dr. U. Fey
Experimente zur elektromagnetisch kontrollierten Körperumströmung
06. 05. 99

Dr. G. Grunwald
Experimente zur Kühlmittelvermischung in Druckwasserreaktoren
03. 06. 99

T. Willms
Kalorimetrische Untersuchungen zur Kinetik der Alkoholyse von Acylchloriden
15. 06. 99

H.-G. Willschütz
Simulation der Thermofluiddynamik einer segregierten Metall-Oxid-Schmelze
17. 06. 99

Lecture Courses

Lectures

F.-P. Weiß
Zuverlässigkeit und Sicherheit technischer Systeme
TU Dresden, Fakultät Maschinenwesen
SS 98 und WS 98

U. Rindelhardt
Erneuerbare Energien I und II
Universität Leipzig, Fakultät für Physik und Geowissenschaften
SS 98 und WS 98

F.-P. Weiß
Zuverlässigkeit und Sicherheit technischer Systeme
TU Dresden, Fakultät Maschinenwesen
SS 99

U. Rindelhardt
Erneuerbare Energien I
Universität Leipzig, Fakultät für Physik und Geowissenschaften
SS 99

Departments of the Institute

Institute of Safety Research

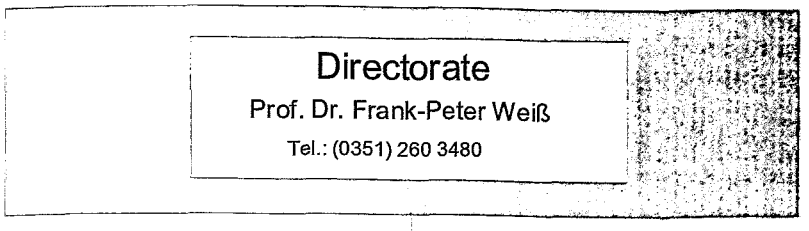

Dpt.

Accident Analysis

Dr. U. Rohde
Tel.: (0351) 260 3460

Dpt.

Particle and Radiation Transport

Dr. K. Noack
Tel.: (0351) 260 3239

Dpt.

Materials and Components Safety

Dr. J. Böhmert
Tel.: (0351) 260 3186

Dpt.

Magneto-Hydrodynamics

Dr. G. Gerbeth
Tel.: (0351) 260 3484

Dpt.

Experimental Thermal Fluid Dynamics

Dr. H.-M. Prasser
Tel.: (0351) 260 3460

Forschungszentrum Rossendorf e.V.
Institute of Safety Research
PF 51 01 19

D-01314 Dresden

Organigram
11.11.1998

Personnel

Director:
Prof. Dr. F.-P. Weiß

Scientific Staff
Altstadt, Eberhard Dr.
Barz, Hansulrich Dr.
Beyer, Matthias
Böhmer, Bertram
Böhmert, Jürgen Dr.
Carl, Helmar Dr.
Cramer, Andreas Dr.
Eckert, Sven Dr.
Ferse, Wolfgang Dr.
Fey, Uwe, Dr.
Fietz, Jürgen Dr.
Galindo, Vladimir Dr.
Gerbeth, Gunter Dr.
Grants, Ilmars Dr.
Große, Mirco
Grundmann, Ulrich Dr.
Grunwald, Gerhard Dr.
Gundrum, Thomas
Hensel, Frank Dr.
Hessel, Günter
Hoppe, Dietrich Dr.
Hüller, Jürgen Dr.
Jung, Thomas Dr.
Kliem, Sören
Koch, Reinhard Dr.
Konheiser, Jörg
Krepper, Eckhard Dr.
Kruber, Stefan Dr.
Krüssenberg, Anne-K. Dr.
Kryk, Holger Dr.
Kumpf, Hermann Dr.
Küchler, Roland Dr.
Lindau, Bernd Dr.
Lucas, Dirk Dr.
Mittag, Siegfried Dr.
Mößner, Ralph, Dr.
Mössner, Thomas
Müller, Gudrun, Dr.
Mutschke, Gerd
Noack, Klaus Dr.
Prasser, Horst-Michael Dr.
Priede, Janis Dr.
Reitz, Thomas
Richter, Holger
Rindelhardt, Udo PD Dr.
Rohde, Ulrich Dr.
Schaffrath, Andreas Dr.
Schäfer, Frank
Schmitt, Wilfried Dr.
Scholz, Thomas
Schumann, Peter Dr.
Seidel, Andre
Seiler, Torsten
Stephan, Ingrid Dr.
Stephani, Frank Dr.
Teichmann, Günther
Tefera, Nurelegne Dr.
Viehrig, Hans-Werner Dr.
Werner, Matthias Dr.
Willms, Thomas, Dr.
Willschütz, Hans-Georg
Witke, Willy
Zschau, Jochen Dr.
Zienicke, Egbert Dr.
Zippe, Cornelius Dr.

PhD Students
Batic, Davide
Beckert, Carsten
Grahn, Alexander
Höhne, Thomas
Kern, Tommy
Kliem, Margarita
Repp, Thomas
Schneider, Carola
Ulbricht, Andreas
Weier, Tom

Technical Staff
Baldauf, Dieter
Behrens, Sieglinde
Blumentritt, Thea
Bombis, Doris
Borchardt, Steffen
Böttger, Arnd
Eichhorn, Christine
Erlebach, Stephan
Forker, Klaus
Futterschneider, Hein
Heinze, Gerda
Kaule, Christian
Kunadt, Heiko
Leonhardt, Wolf-Dietrich
Leuner, Bernd
Losinski, Claudia
Mansel, Catrin
Möller, Falk
Nowak, Bernd
Opitz, Ruth
Otto, Gerlind
Pietzsch, Jens
Richter, Annett
Richter, Henry
Richter, Joachim
Richter, Karl-Heinz
Richter, Petra
Rott, Sonja
Russig, Heiko
Schleßiger, Heike
Schneider, Gisela
Schütz, Peter
Seidler, Christa
Skorupa, Ulrich
Tamme, Marko
Tamme, Günther
Trepte, Manuel
Utke, Holger
Webersinke, Steffen
Weiß, Rainer
Zimmermann, Wilfried
Zippe, Winfried Dr.